A Stochastic Imaging Technique for Spatio-Spectral Characterization of Special Nuclear Material

by

Michael C. Hamel

A dissertation submitted in partial fulfillment
of the requirements for the degree of
Doctor of Philosophy
(Nuclear Engineering and Radiological Sciences)
in The University of Michigan
2017

Doctoral Committee:

Professor Sara A. Pozzi, Chair
Associate Research Scientist Shaun D. Clarke
Professor Jeffrey A. Fessler
Professor Igor Jovanovic

And forever, Go Blue.

Michael C. Hamel

mchamel@umich.edu

ORCID iD: 0000-0002-4293-1685

Dedication

For my family.

Mom and Dad, you have provided me with the love and incredible support necessary to complete this degree.

And to Brett and Griffin, my partners in crime and the best of friends.

Acknowledgments

A great many people helped contribute to the work presented in this dissertation. First, I want to thank Alexis and Kyle, two people that worked side-by-side with me for years. Alexis, you were my first mentor when I started as a UROP student in DNNG. Kyle joined us a year later and the three of us shared an office, as well as the many ups and downs that came with the PhD process. You two were great co-workers and remain even better friends.

Next I want to thank Professor Pozzi. At my first project meeting with her I forgot to bring a pad of paper to take notes. After making many comments on the work I presented, she asked me, "Did you get all that?" I've never forgotten a notebook since. None of this work would have been possible without your guidance and belief in me. You were a great mentor to me beginning as a junior in undergrad, through my Master's, and now PhD. Thanks for always having confidence in me and my work!

To Shaun, you have also been a great mentor since I started with the group. You've always made yourself available when I have questions and greatly improved my ability to tell a story through writing and presentation. On the other-hand, your fantasy football advice has been a bit more suspect.

There are too many other people to thank, including all of the other students in the department and DNNG that have supported me, my friends in Ann Arbor and elsewhere who provided me with a release from the rigors of school, and my family who has been there for me throughout the entire process. By now they have perfected the ability to politely nod

when I excitedly explain a new algorithm or concept I am working on. Unfortunately for them, this will continue after my PhD.

Thank you to my other committee members Dr. Jovanovic and Dr. Fessler. I greatly appreciate you taking your time to serve on my committee and want to thank you for the valuble feedback you provided to improve this dissertation.

I also want to thank the sponsors. This work was supported in-part by the National Nuclear Security Administration through NA-22 funding opportunity DE-FOA-0000568. It is also funded in-part by the Consortium for Verification Technology under Department of Energy National Nuclear Security Administration award number DE-NA0002534. I was funded in-part by the University of Michigan/Sandia National Laboratories Excellence in Engineering Fellowship. This fellowship was supported in part by the Laboratory Directed Research Development (LDRD) Program at Sandia National Laboratories (project 17-0884). The prototype system was funded in-part by the Department of Energy, Nuclear Energy University Program, award number DE-NE0000324. This work also utilized the National Criticality Experiments Research Center supported by the Department of Energy's Nuclear Criticality Safety program with financial support from the National Nuclear Security Administration's Office of the Chief of Defense Nuclear Safety, NA-511.

Table of Contents

List of Figures

List of Tables

List of Appendices

List of Abbreviations

DAF ..... Device Assembly Facility

DD ..... Deuterium deuterium

DT ..... Deuterium tritium

DPI ..... Dual-particle imager

DU ..... Depleted uranium

FM ..... Fissile material

HE ..... High explosive

HEU ..... Highly enriched uranium

IAEA ..... International Atomic Energy Agency

INF ..... Intermediate-range Nuclear Forces Treaty

LEU ..... Low enriched uranium

MCMC ..... Markov chain Monte Carlo

MDA ..... Minnimum detectable activity

MLEM ..... Maximum-likelihood expectation-maximization

NORM ..... Normally occurring radioactive material

NPT ..... Treaty on the Non-Proliferation of Nuclear Weapons

PDF ..... Probability density function

PoliMi ..... MCNPX-PoliMi

PSD ..... Pulse shape discrimination

SNL ..... Sandia National Laboratories

SNM ..... Special nuclear material

SNR ..... Signal-to-noise ratio

TOF ..... Time-of-flight

WGPu ..... Weapons grade plutonium

WGU ..... Weapons grade uranium

Abstract

Radiation imaging is advantageous for detecting, locating and characterizing special nuclear material (SNM) in complex environments. A dual-particle imager (DPI) has been designed that is capable of detecting gamma-ray and neutron signatures from shielded SNM. The system combines liquid organic and NaI(Tl) scintillators to form a combined Compton and neutron scatter camera. Effective image reconstruction of detected particles is a crucial component for maximizing the performance of the system; however, a key deficiency exists in the widely used list-mode maximum-likelihood estimation-maximization (MLEM) image reconstruction technique. The steady-state solution produced by this iterative method will have poor quality compared to solutions produced with fewer iterations. A stopping condition is required to achieve a better solution but these conditions fail to achieve maximum image quality. Stochastic origin ensembles (SOE) imaging is a good candidate to address this problem as it uses Markov chain Monte Carlo to reach a stochastic steady-state solution that has image quality comparable to the best MLEM solution. The application of SOE to the DPI is presented in this work.

SOE was originally applied in medical imaging applications with no mechanism to isolate spectral information based on location. This capability is critical for non-proliferation applications as complex radiation environments with multiple sources are often encountered. This dissertation extends the SOE algorithm to produce spatially dependent spectra and presents experimental result showing that the technique was effective for isolating a 4.1-kg mass of weapons grade plutonium (WGPu) when other neutron and gamma-ray sources were

present.

This work also demonstrates the DPI as an effective tool for localizing and characterizing highly enriched uranium (HEU). A series of experiments were performed with the DPI using a deuterium-deuterium (DD) and deuterium-tritium (DT) neutron generator, as well as AmLi, to interrogate a 13.7-kg sphere of HEU. In all cases, the neutrons and gamma rays produced from induced fission were successfully discriminated from the interrogating particles to localize the HEU. For characterization, the fast neutron and gamma-ray spectra were recorded from multiple HEU configurations with low-Z and high-Z moderation. Further characterization of the configurations used the measured neutron lifetime to show that the DPI can be used to infer multiplication.

Chapter 1

Introduction

The use of nuclear material for non-peaceful purposes represents one of society's greatest present concerns. It is a problem that demands solutions to effectively control nuclear material and verify its appropriate usage. The control and accountancy of nuclear material is critical in all phases of the non-proliferation effort, including security, safeguards and nuclear arms control. After the use of atomic weapons to end World War II, many nations have sought international treaties to control nuclear material and help ensure its peaceful use. The evolution and implementation of these treaties have motivated the science and engineering work presented in this dissertation.

1.1 Radiation detection for treaty verification

Verification of declared nuclear material usage is at the forefront of many non-proliferation treaties. These treaties present many opportunities for verification including nuclear warhead deployment in arm-control treaties and confirmation of nuclear fuel properties in safeguards agreements. Nuclear material emits ionizing radiation as a characteristic signature. Neutrons and gamma ray are the most penetrating particles emitted, presenting an opportunity for detection that can characterize and identify the originating material.

The nuclear materials most relevant to non-proliferation treaties are weapons grade plu-

tonium (WGPu) and highly enriched uranium (HEU). Increased masses of these materials present a greater risk, and are given special designations by organizations such as the US Nuclear Regulatory Commission and the International Atomic Energy Agency (IAEA), known as *category-I strategic special nuclear material* (SNM) and a *significant quantity* respectively [1, 2].

To date, radiation detection has been deployed to a much greater extent in nuclear safeguards applications compared to arms control. Only two arms-control treaties have called for radiation detection technologies, the Intermediate-range Nuclear Forces (INF) treaty and the New Strategic Arms Reduction Treaty (New START) [3, 4]. Nuclear safeguards, implemented through the Treaty on the Non-Proliferation of Nuclear Weapons (NPT) rely more heavily on radiation detection to enforce comprehensive safeguards agreements between the IAEA and non-nuclear weapons member states [5]. A short introduction to radiation detection techniques used in treaty verification follows.

1.1.1 Radiation detection in arms-control

To this point, radiation detection has played a very limited role in arms-control treaties. The INF treaty used ^{3}He neutron detectors to verify that the treaty-limited Soviet SS-20 missile was not concealed within an SS-25 missile (not limited by the treaty) [3, 6]. A grid with pre-arranged measurement positions was placed near the warheads and used to map count rates at each position. The count-rate profiles differed between the SS-20 and SS-25 allowing this count mapping technique to discriminate between the two. This use of radiation detection is the only example in an arm-controls treaty to verify a declared nuclear item.

The New START also permits the use of radiation detectors [4]; however, in this case, detection is limited to confirming the non-nuclear nature of items. The treaty stipulates that neutron counting detectors can be used for this purpose. In Part Five, Section II of the Annex on Inspection Activities, the United States is permitted to use a ^{3}He system with

count times from 5 to 150 seconds. The Russian detector type is not specified but is also limited to detecting count rates.

Verifying warhead contents and dismantlement

Introducing more radiation detection techniques in future arms-control treaties would create added complexity in defining treaty accountable items. Currently, the New START uses delivery vehicles such as silos, submarines, and bombers to count deployed warheads [7]. Moving to a treaty that seeks to verify individual nuclear warheads directly would require a definition allowing for confirmation or rejection based on properties of a nuclear warhead.

Fetter et al. offer a look at components that are included in typical nuclear warheads, which provides a basis for possible definitions [8]. Their study uses a hypothetical weapon that includes a fissile core of WGPu or weapons grade uranium (WGU) surrounded by a reflector, tamper, high explosive and an aluminum case. While the reflector, tamper, and casing may differ, the fissile core surrounded by high explosive is a defining characteristic of a nuclear warhead.

Seeking to verify the nuclear warhead by identifying characteristics of the fissile material (FM) and high explosive (HE) would represent an *attributes* based approach. In contrast, a *template* based approach would use a pre-determined, unique signature of a specific nuclear warhead as a comparison for other inspected warheads [7]. Characteristics that can be directly measured or produce a unique fingerprint include material properties such as isotopic composition and density. Radiation emitted from the fissile material in the form of neutrons and gamma rays can provide characteristics such as spectral and multiplicity information.

Verifying nuclear warhead dismantlement is another challenge that demands similar verification methods. In this case however, confirming that the FM has been separated from the HE is required. A joint report from the United States and United Kingdom outlines five possible measurements to verify dismantlement [9]:

1. *to confirm the presence of the FM in the "FM" container*
2. *to confirm the absence of HE in the "FM" container*
3. *to confirm the presence of HE in the "HE" container*
4. *to confirm the absence of FM in the "HE" container*
5. *to confirm that all of the FM is in the "FM" container*

This approach would require defined attributes or a template for both the FM and HE. Measurement numbers one, four, and five, present opportunities for radiation detection. Simply confirming the presence or absence of FM could use the approaches from the INF treaty and New START, which deployed neutron counting detectors. However, measurement number five requires a more sophisticated technique to identify the fissile mass of WGPu or WGU such as neutron coincidence counting or gamma-ray spectroscopy. Developing systems capable of characterizing FM could be used to provide better verification in future arms control treaties.

1.1.2 Radiation detection in support of the NPT

The IAEA uses a wide array of radiation detection techniques to support the NPT. All non-weapons states that are party to the NPT are required to complete a Comprehensive Safeguards Agreement that allows the IAEA to implement safeguards on all special fissionable material within the state and ensure that it is not diverted to nuclear weapons use [10].

Detection capabilities include hand-held gamma-ray spectrometers that can be used for uranium enrichment and plutonium isotopic calculation [11, 12]. The detector types employed for these applications include NaI(Tl), CdZnTe, and high-purity germanium. Neutron detectors also play a large role in safeguards and are primarily used to verify isotopic

mass through neutron coincidence counting. Passive neutron detection applications seek to verify the mass of plutonium in nuclear fuel or hold-up in a nuclear facility. A technique for verifying ^{235}U content in HEU or low-enriched uranium (LEU), known as active neutron coincidence counting, uses an interrogating source such as AmLi to induce fission in a sample. [11, 13].

Another type of detection tool that the IAEA is looking to implement in the future is a radiation imaging device. Radiation imaging creates a visual representation of radiation detected by the system. IAEA inspectors could use radiation imaging to quickly locate declared or undeclared sources of radiation. Appendix A contains an excerpt of a document providing contextual usage scenarios for which the IAEA may benefit from gamma ray imaging [14].

1.2 Radiation imaging: Technologies and benefits

Most of the radiation detection techniques described above for nuclear arms control and safeguards use counting techniques, which do not provide source localization. In this case, radiation coming from another source, or environmental background, could inhibit the verification of the item of interest. As such, radiation imaging techniques, that reconstruct the distribution of radiation in space, can be applied to assist many of the non-proliferation challenges.

Radiation imaging has long been developed for the fields of astronomy, to detect cosmic particles, and medical imaging to detect the location of radioactive tracers in the body. For these particular applications of gamma-ray detection, the Compton scatter camera was developed [15–20]. However, with the threat of nuclear terrorism and the demand for non-proliferation becoming more prevalent, development of radiation detection systems has become important to address these issues. For example, Compton cameras developed for

non-proliferation applications have included higher resolution detectors [21] and added an ability to localize thermal neutrons [22].

The demand for imaging systems designed to detect SNM led to the development of neutron scatter cameras [16, 23–26]. These devices are analogous to Compton scatter cameras but have neutron sensitivity. A combined neutron and gamma-ray imager was first proposed in [16] and a current system under development using the same concept for emergency response is described in [27]. However, these systems relied on an approximation to calculate the incident gamma-ray energy instead of measuring it directly.

Other concepts have been developed to image neutrons and gamma rays. For example, a coded aperture imaging system relies on a mask pattern that shields parts of the detection system to localize the source. These systems have been proposed to image both gamma rays and neutrons from SNM [28–31]. Another method is known as time-encoded imaging. The technique has been applied for gamma rays in [32] and more recently to neutrons [33] and both particle types [34].

Radiation imaging provides localization capabilities for all or a subset of detected particles. While localizing a source is important for search applications, imaging also provides other benefits such as increased signal-to-background. In a typical scenario, contributions from environmental background will occur from all locations, while the sources of radiation will only emit particles from one or several locations. If aggregated, the contribution of counts from the source may not exceed background fluctuations; however, if the background contribution is only considered at the location of the source, the contribution is much less compared to the contribution from all space. Thus, the signal-to-background will be increased because the source is concentrated while the background is spread throughout the imaging space. Radiation imaging also allows for the localization of other information about the source or sources. For example, techniques have been demonstrated that localize the energy of detected particles for different locations in the image [35–39]. These techniques

can be used to discriminate between sources or interest and naturally occurring radioactive material (NORM).

1.3 The Dual-particle imager

In this work, the Dual-particle Imager (DPI) is used to exploit the benefits of radiation imaging for SNM detection. The concept for the DPI was first presented in [40] as the three plane DPI, and was later condensed to a two plane design [41]. Another system using a three plane design and similar physics concepts to the DPI was presented later in [42, 43].

The DPI uses arrays of liquid organic scintillators and NaI(Tl) scintillators to create a combined Compton and neutron scatter camera. The system uses the liquid organic scintillators, with their excellent pulse shape discrimination capabilities, as the scatter plane for both particles. The Compton camera is completed by having the NaI(Tl) scintillators absorb scattered gamma rays in the back plane, alongside more liquid organic scintillators to detect scattered neutrons. The information collected by the system allows for the reconstruction of separate neutron and gamma-ray images and spectra. The design of the DPI and its application to locating SNM is the basis for this thesis.

1.4 Contributions of this work

The goal of this dissertation was to extend the capabilities of the DPI for localizing and characterizing SNM; however, the design and development of the system was also a large portion of the work. System design and optimization was required to evaluate more advanced image reconstruction techniques and have adequate system performance in the high count rate environments required for SNM detection. The system development was documented extensively in [44]. As such, this thesis only briefly covers the design and

construction of the DPI, but that work constitutes a large contribution and foundation of the work presented here. System design parameters and initial simulated and experimental results were published in [45–47].

To effectively image SNM and other sources of radiation, statistical image reconstruction techniques must be applied to the basic kinematic localization. The maximum-likelihood estimation-maximization (MLEM) method is seen as the gold standard for image reconstruction in not only scatter cameras but other types of imaging devices as well [48]; however, the image quality produced by this iterative technique is highly dependent on the number of iterations performed and over-iteration will degrade image quality significantly. Defining a stopping condition to avoid over-iteration is not a trivial problem and often will not produce the optimal solution [49, 50]. To address this problem, an image reconstruction method that provided good image quality without a heavy dependence on the number of iterations performed was sought.

The stochastic origin ensemble (SOE) technique, found in medical imaging literature for computed tomography possessed the desired characteristics [51]. An application for use with the Compton camera was given in [52]. However, at the time of initial implementation to the DPI, the literature provided only simulated results for small Compton cameras in medical imaging settings [52, 53]. Following application of SOE to the DPI, an additional experiment result from the medical imaging field was published, which implemented the method for measured gamma-ray data [54].

This dissertation details the first application of the SOE image reconstruction technique to non-proliferation applications. It details how the method was implemented for the DPI and used in neutron scatter camera reconstruction for the first time. The results presented in this work demonstrate that SOE produces improved image quality compared to MLEM reconstruction without heavy dependence on a stopping condition. The technique is used to reconstruct neutron and gamma-ray images for a single point-source, two point sources, and

discusses a modification made to the algorithm to improve extended source reconstruction. The initial application of SOE to the DPI was published in [55].

Application of SOE to non-proliferation problems necessitated the ability to localize energy spectra if multiple sources of radiation were present. The SOE literature did not provide a means to accomplish this, as medical applications use radioactive tracers with know energy spectra. This work presents an extension to the SOE method that allows for spectral isolation from different locations in the image. This technique is demonstrated for an experiment with category-I WGPu and two other non-SNM sources. The extended SOE method successfully shows that the neutron and gamma-ray spectra from the WGPu can be differentiated from the other two sources. Experimental results detailing spectrum isolation with SOE were published in [56].

While using the DPI for passive radiation detection can effectively localize and characterize WGPu, HEU does not emit enough neutrons or high-energy gamma rays to effectively detect the material. To increase the emission from HEU, other radiation sources can be used to interrogate the HEU by inducing fission reactions. Most work on this subject simply uses count-rate analysis to determine if fissionable material is present. In this work, the DPI is used with neutron interrogation from AmLi and a neutron generator to show that HEU can be localized. Characterization of the HEU is also demonstrated by examining neutron and gamma-ray spectra as well as neutron lifetime. Experiments using the DPI with a portable DT neutron generator to interrogate a 13.7-kg HEU sphere show that this method could be effective for treaty-verification applications.

1.5 Organization of this thesis

The work contained in this thesis is presented over several chapters that build on the basic theories of radiation detection and imaging to address the challenges of detecting and

characterizing SNM. Chapter 2 details the basic principles and design of the DPI. Basic image and spectral reconstruction is discussed as well as the system components that compose the DPI such as radiation detectors, digitizers, and data-processing algorithms.

Chapter 3 then builds on the basic image reconstruction techniques by showing that the application of SOE to the DPI effectively reconstructs neutron and gamma-ray images. The specific parameters used for this image reconstruction technique are discussed at length. Finally, the image quality of SOE reconstructions is directly compared to the popular MLEM method implemented on the same data. Multiple source distributions were used to demonstrate the versatility of the SOE method.

After demonstrating the image reconstruction qualities of SOE, the extension of the method to include spectral isolation is documented in Chapter 4. Several experiments are discussed to evaluate the spectral isolation qualities of the extended SOE method for gamma rays using ^{22}Na and ^{137}Cs sources, and neutrons with ^{252}Cf and PuBe sources. Finally, the spectrum isolation technique is demonstrated on a measurement of a 4.1-kg WGPu sphere, ^{252}Cf, and AmBe. Discrimination of the WGPu is shown through spectral isolation of the neutrons and gamma rays.

While WGPu is easy to detect passively, Chapter 5 tackles the challenges associated with imaging HEU using active interrogation. Experiments using three different neutrons sources to actively interrogate a 13.7-kg sphere of HEU are detailed. The neutron sources included: AmLi, a deuterium-deuterium (DD) neutron generator, and a deuterium-tritium (DT) neutron generator. Localization, as well as spectra and neutron lifetime are evaluated for the bare HEU sphere and moderated configurations with polyethylene and tungsten.

Finally, Chapter 6 provides conclusions drawn from this work and ideas for how this work can be extended in the future to improve localization and characterization of SNM.

Chapter 2

Design and operation of a dual-particle imager

The previous chapter spoke to the need for development of imaging solutions for various non-proliferation challenges. This chapter will describe how the DPI was designed to address these challenges and detail the physics principles involved in its construction.

2.1 Advantages of dual-particle imaging

Perhaps the most difficult challenge facing passive radiation detection is the possible presence of intervening material. Commonly referred to as shielding, radiation will interact in this material, which will change several key properties of the signal. For example, the number of particles reaching the detector or detection system will be reduced due to the material attenuating particles through scattering or capture. Shielding will also distort the energy spectrum of a source, which is a key signature for identification. These factors are difficult to characterize because they are heavily dependent on the type of radiation, the shielding material, and the amount of shielding.

Fortunately, some of these effects can be mitigated by expanding the detection capabilities of a system to detect neutrons and gamma rays, both a key signature of SNM. The dual-particle sensitivity of the DPI makes the system more robust to a variety of shielding material,

that could be used to hide a source. Using a common example, a high-Z material such as lead will attenuate the gamma-ray signal but will not significantly alter the neutron flux through the material. In contrast, a low-Z material such as plastic will have the opposite effect, significantly altering the neutron signal passing through the material while having little effect on the gamma rays.

Other important factors involved in the detection of SNM motivated the design of DPI as well. The system needed a large field-of-view to effectively search for SNM outdoors or in a large nuclear facility. The system also had to be capable of handling high count rates while still providing a useful signal for. This includes a signal in which the gamma-ray flux may dominate the neutron flux [57]. The isotopes in SNM can often emit x-rays and gamma rays with a flux at least an order of magnitude larger than the neutron flux. The characteristics of emitted radiation from SNM dictated that excellent discrimination capabilities were needed for neutrons and gamma rays.

What follows is a short overview of the overall system before explaining the choice of the components and the underlying principles that led to their inclusion. Other design characteristics such as the choice of a scatter camera and how events are detected and analyzed is also detailed.

2.2 DPI system overview

The DPI was formed by combing a Compton and neutron scatter camera [40, 41, 44–46, 58–62]. It has a two-plane design with the front plane acting as a joint scatter plane for neutrons and gamma rays. The back plane acts as a second scatter plane to complete the neutron scatter camera as well as an absorption plane for the Compton scatter camera. A picture of the system is shown in Figure 2.1.

Two different types of scintillators, EJ-309 organic liquid and NaI(Tl), are used for the

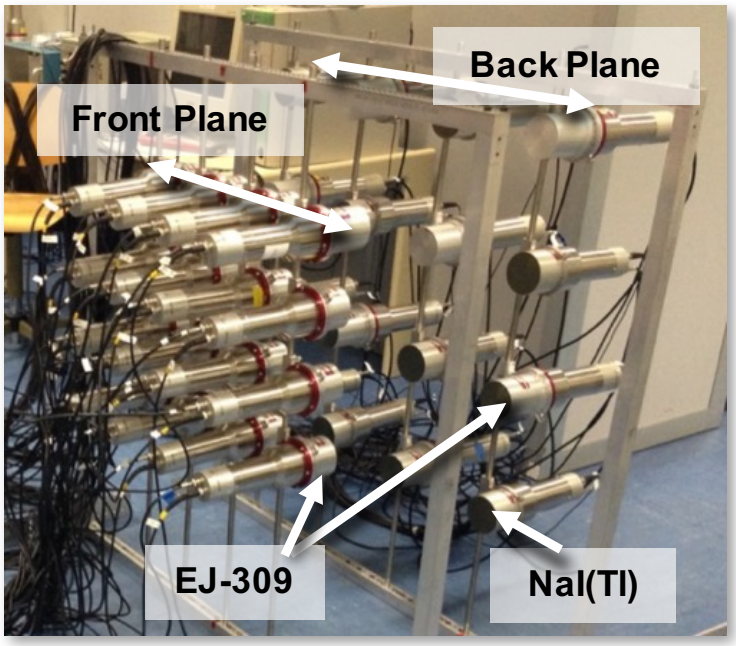

Figure 2.1: A photo of the dual-particle imager.

DPI. The front plane is a 4×4 array of cylindrical liquid scintillators each with a thickness of 5.1 cm and a diameter of 7.6 cm. The backplane is also a 4×4 array but consists of eight liquid scintillators and eight NaI(Tl) scintillators. All back plane detectors are cylindrical with a 7.6-cm thickness and 7.6-cm diameter. The backplane has both detector types arranged in a checkerboard pattern.

2.3 Basic principles of operation

The DPI operates as a scatter camera. For a scatter camera to achieve information about the origin of a particle, the particle must be detected at least twice in the system. In the DPI, this requirement amounts to a particle being detected in at least two different detectors, one in the front plane and another in the back plane; this is referred to as a correlated count or score in the system.

2.3.1 Neutron imaging

For a neutron to score in the DPI, it must first undergo elastic scattering in a front plane liquid scintillator followed by a subsequent scatter in a back plane liquid scintillator. The incident energy of the neutron, $E_{0,n}$, can be reconstructed by summing the energy deposited in the first scatter, $E_{1,n}$, and remaining energy of the neutron, E_{TOF} using

$$E_{0,n} = E_{1,n} + E_{TOF}\,. \tag{2.1}$$

E_{TOF} is calculated from the time-of-flight, TOF, and the velocity of the scattered neutron, v_n,

$$E_{TOF} = \frac{1}{2} m_n v_n^2\,. \tag{2.2}$$

v_n is calculated using

$$v_n = \frac{d}{TOF}\,, \tag{2.3}$$

where d is the distance between the two detectors recording events. Combining Equations (2.2) and (2.3) gives

$$E_{TOF} = \frac{1}{2} m_n \left(\frac{d}{TOF}\right)^2\,. \tag{2.4}$$

The energy deposited in the first scatter is transferred from the neutron to the recoil nucleus, which is either hydrogen or carbon in a liquid scintillator. The angle of the elastic scattering event, θ_n, and the mass of the recoil nucleus, A, provide a unique solution for the energy deposited [63]

$$E_{1,n} = \frac{4A}{(1+A)^2}(\cos^2\theta_n) E_{0,n}\,. \tag{2.5}$$

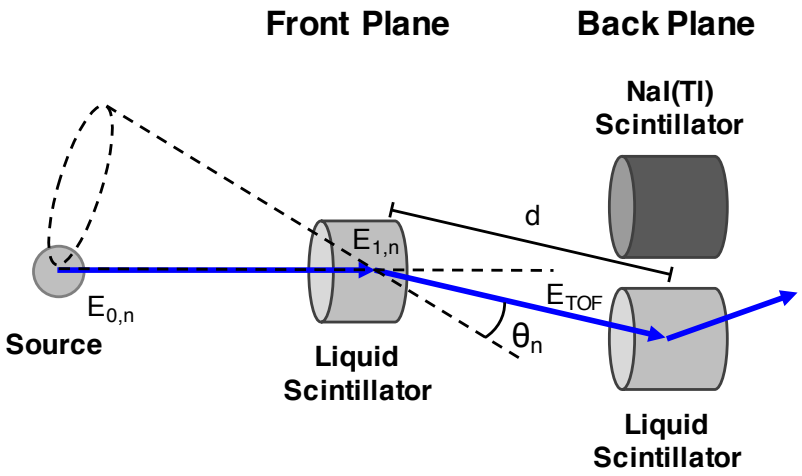

Figure 2.2: Example of an ideal neutron event in the DPI.

When $A = 1$, Equation (2.5) can be simplified and solved for θ_n

$$\theta_n = \cos^{-1}\sqrt{\frac{E_{1,n}}{E_{0,n}}}\,. \tag{2.6}$$

The calculated scatter angle θ_n and the vector between both detectors involved in the event are used to define a cone. The surface of the cone represents all possible origins of the incident neutron on the system. Figure 2.2 shows a schematic of the DPI with the cone of possible source locations and relevant quantities depicting the detection of a neutron event.

The scenario outlined above represents an ideal sequence of events for neutron detection. However, carbon is present in the liquid scintillators and often a neutron will undergo multiple scatters in a single detector cell [64]. In cases such as these, an event may still score in the system, but the assumption made to simplify Equation (2.5) to Equation (2.6) is that a single scatter on hydrogen occurred. These events are referred to as non-ideal and can only be identified through simulation and not in actual experiments.

2.3.2 Gamma-ray imaging

A gamma-ray event is recorded in the DPI when a gamma ray undergoes Compton scattering in a front plane liquid scintillator and then interacts in a back plane NaI(Tl). Compton scattering can result from the interaction of an incident gamma ray and an electron. The energy transferred to the recoil electron, $E_{1,\gamma}$, is detected by a front-plane liquid scintillator. In a back plane NaI(Tl) scintillator the two most probable interactions that can deposit energy, $E_{2,\gamma}$, are photoelectric absorption or Compton scattering [63].

For the purpose of reconstructing the scattering angle, a photoelectric absorption is preferable. The incident energy of the gamma ray is calculated using

$$E_{0,\gamma} = E_{1,\gamma} + E_{2,\gamma}\,. \tag{2.7}$$

If a Compton scatter occurs instead of a photoelectric absorption, the full energy of the gamma ray is not deposited in the system and $E_{0,\gamma}$ will be less than the actual energy of the incident gamma ray. Once $E_{0,\gamma}$ has been calculated, the Compton equation can be used to solve for the scattering angle, θ_γ,

$$\theta_\gamma = \cos^{-1}\left[1 - \frac{m_e c^2 E_{1,\gamma}}{E_{2,\gamma}(E_{1,\gamma} + E_{2,\gamma})}\right]. \tag{2.8}$$

This equation will provide the proper angle of the incident particle providing that the event was ideal. An ideal event is defined by the gamma ray undergoing a single Compton scatter in the liquid scintillator and a photoelectric absorption in the NaI(Tl). An example of an ideal gamma-ray event is shown in Figure 2.3. The calculated angle then can be used to define a cone of possible origins for the incident gamma ray [15, 17]. This cone is analogous to the cone defined by the angle θ_n for neutrons in Section 2.3.1. The cones of possible source origins provide the backbone for the imaging methods, such as simple backprojection and stochastic origin ensembles, that will be described in later sections.

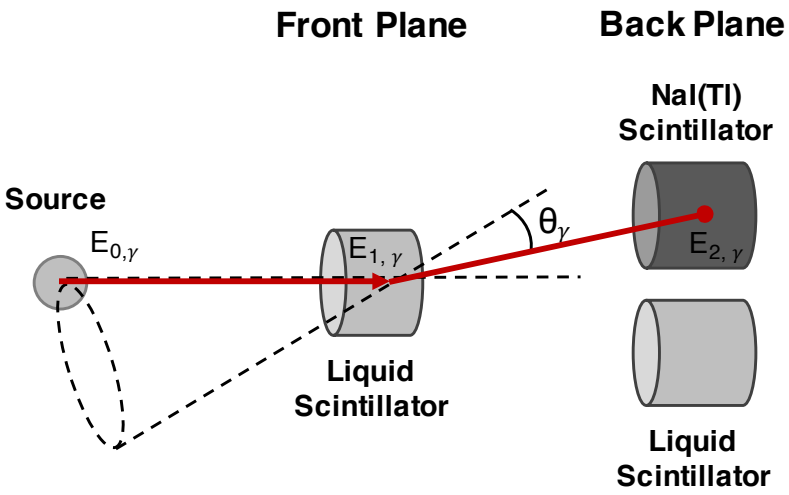

Figure 2.3: Example of an ideal gamma-ray event in the DPI.

2.4 DPI components

The individual components that makeup the DPI are worth discussing to bring further understanding of system abilities and limitations. The properties that define system performance are the two detectors types, the arrangement of the detectors, and the data acquisition hardware.

2.4.1 EJ-309 organic liquid scintillators

The response of organic liquid scintillators provide the information necessary to reconstruct the possible origins of a neutrons and gamma rays, as described in Sections 2.3.1 and 2.3.2 respectively. The version of organic liquid scintillator used by the DPI is the EJ-309. This material provides excellent pulse shape discrimination (PSD) capability, which is of the utmost important since the liquid scintillators act as the scatter plane for both neutrons and gamma rays [65–69]. Using the PSD algorithm from [70], misclassification ratios of 4.0×10^{-2} are obtainable for neutrons with a 40 keVee threshold. In short, a portion of the pulse tail is integrated and plotted against the total pulse integral. For neutrons, the tail region of

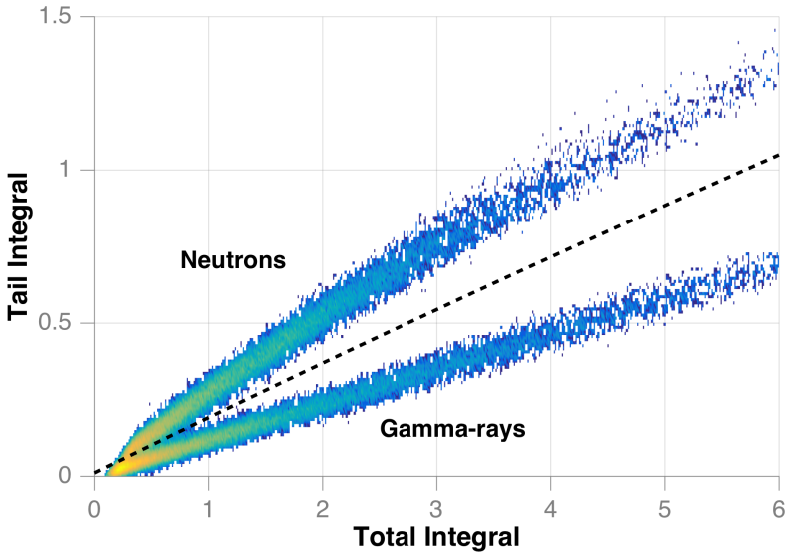

Figure 2.4: A plot of tail integral versus total integral for pulses used for pulse shape discrimination.

a pulse decays more slowly than for gamma rays due to the combined effects of increased singlet quenching, which reduces the amount of prompt light and increased triplet-triplet annihilation contributing additional delayed light [71]. An example of a tail integral versus total integral plot is shown in Figure 2.4 with a line used to discriminate the upper neutron cluster from lower gamma-ray cluster. Points above the line are classified as neutrons with points below the line classified as gamma rays.

Another important property of liquid scintillators is the difference in light creation for neutrons and gamma rays and how that affects the calculation of energy deposition. Whether a gamma ray collides on a hydrogen or carbon electron, the same amount of scintillation light is created. In this case the amount of light produced follows a linear relationship with the amount of energy deposited in the collision. For example, a gamma ray that deposits 0.3 MeV in a Compton scatter would produce a light output of 0.3 MeVee in the scintillator.

For neutron elastic scattering, the relationship between energy deposited and light created is not linear. The characterization of this relationship is a complex topic that has been

covered substantially in the literature. In this work, the relationship used is from [72]. The relationship between light output, in MeVee, and energy deposited, in MeV, is shown in Figure 2.5 for neutrons and gamma rays. The curve for neutrons lies below that of gamma rays meaning that less light is created by neutrons for an equivalent energy deposition. Over the course of this work, improvements to this relationship were made by Norwsworthy et al. in [73] based on proton stopping power in scintillator materials [74, 75]. In some cases, the relationship called *Exponential 4* in the Norsworthy et al. paper is used. When called for, the set of coefficients used will be noted.

The distinction between energy deposited, and light output, results in neutrons and gamma rays having different minimum and maximum detection thresholds. A typical measurement in this work has the minimum detection threshold set at about 40 keVee. At this threshold a gamma ray must deposit at least 40 keV to be detected while a neutron must deposit approximately 460 keV. Because a double scatter is required for an event to be recorded in the DPI, if all liquid scintillators had a threshold of 40 keVee then the minimum incident energy that a neutron must have to score in the system is 920 keV. The minimum detected energy that a gamma ray must have to record an event would be 80 keV if the threshold in the NaI(Tl) is also set at 40 keVee.

The excellent timing resolution offered by liquid scintillators is critical for calculating the time-of-flight needed for neutron events. Flight paths between liquid scintillator pairs can range from about 30 cm to 60 cm in the DPI. The flight time for a 1-MeV neutron to travel 50 cm is 36 ns. The time resolution for the liquid scintillators in the DPI is about 1-ns. The time resolution is dependent on several factors including the interaction location in the detector cell, light collection time, and pulse amplification by the PMT. To characterize the time resolution two liquid scintillators are placed face-to-face with a ^{22}Na source between them. The difference in arrival times from the correlated 511-keV gamma rays measured in each detector are calculated. For a typical pair of scintillators this distribution is Gaussian

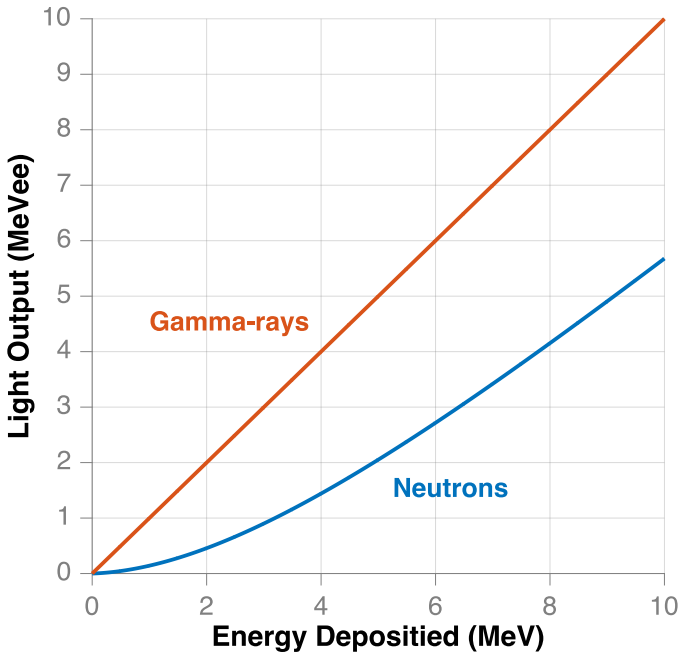

Figure 2.5: Relationship between light output and energy deposited in a liquid scintillator for neutrons and gamma rays.

with a FWHM of about 1-ns. A more in depth discussion of the timing resolution can be found in [46].

The energy resolution for the liquid scintillators was also characterized in [72]. A plot showing the resolution, which is about 20% at 0.5 MeVee and then ranges from 12-15% at light outputs greater than 1 MeVee, is reproduced in Figure 2.6. More recent work by Norsworthy et al. has shown that this function overestimates the resolution at low energies. Recent experiments showed the resolution at 44 keV to be about 46% [76].

2.4.2 NaI(Tl) scintillators

Eight NaI(Tl) scintillators form the absorption plane for the Compton camera portion of the DPI. NaI(Tl) was chosen because it offers a high detection efficiency for gamma rays and a high probability of photo electric absorption [63, 77]. The large photoelectric absorption

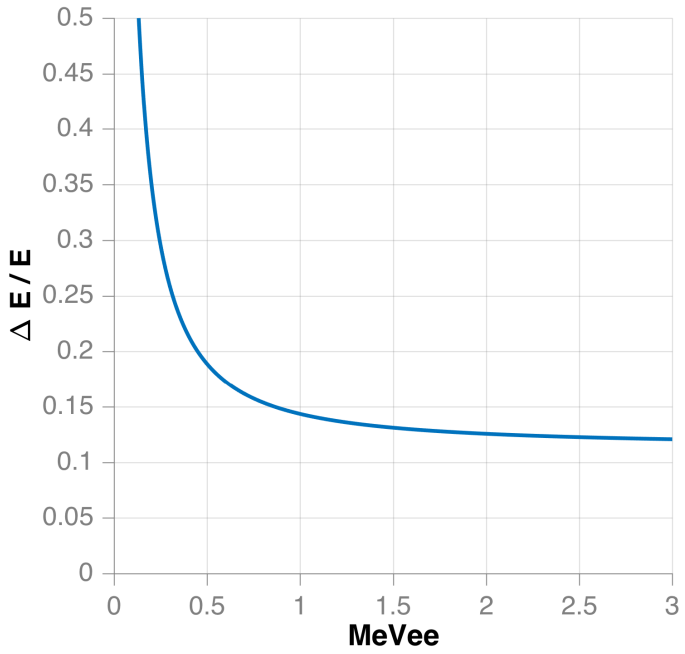

Figure 2.6: The energy resolution for a 7.6-by-7.6 cm EJ-309 liquid scintillator is plotted for a range of light outputs.

cross-section is important because it provides a full knowledge of incident gamma-ray energy. NaI(Tl) also provides acceptable energy resolution when accounting for efficiency, cost, and scalability.

To achieve the energy resolution typically associated with NaI(Tl), the pulses from the PMT are input to a pulse shaper. The shaper used in this work is the Mesytec MSCF-16 F. A shaping time of 0.125 µs was used in this work, which achieved an energy resolution of 7.6% at 662 KeV while allowing for a waveform window-size of 560 ns [78]. The time resolution when using the pulse shaper was found to be about 16 ns. Timing information is not used in the cone angle calculation for gamma rays (Equation (2.8)). It is only used for event correlation, which is described in detail in Section 2.5.2.

2.4.3 System configuration

The geometrical spacing of the individual detectors in the DPI plays a large role in defining performance. The two factors affected by the configuration are angular resolution and efficiency. Because these two factors are competing, the system configuration was chosen heuristically through Monte Carlo simulation of many configurations and evaluating the angular resolution and efficiency [47].

The angular resolution of the system has two components, the angular resolution of individual events and the overall angular resolution of an image. Individual event resolution is determined by the detector properties and spacing from one another. The overall angular resolution is determined not only by individual event resolution but also by how many detector pairs are possible for event creation, and which events are preferentially created based on the configuration of the pairs.

The resolution of an individual neutron event is determined by the uncertainties present in the first energy deposition, the time-of-flight, and interaction positions in both detectors. For gamma rays, the resolution is determined by the uncertainty in both energy depositions and interaction locations. For both particles, the uncertainty in interaction locations within detectors, referred to as spatial uncertainty, has the largest effect. [39].

The configuration of the detectors also plays a role in individual event uncertainty. Each event is assumed to have occurred in the center of the detector. Because each interaction position can be off by up to 4.6 cm in the front plane and 5.4 cm in the back plane, there is uncertainty in the actual scatter angle. Increasing the flight path of the particle by spacing the detectors further apart reduces this uncertainty.

While increasing the distance between front and back plane detectors improves individual event resolution, it lowers the efficiency of detecting correlated events. The efficiency is worse because increasing the distance of the back plane detectors from the front plane decreases the solid angle for particles that have undergone scattering in the front plane.

The second component of overall system resolution is the detector positioning. There are a possible 128 detector pairs for neutron events and another 128 pairs for gamma-ray events. The finite nature of pairs also limits possible scatter angles and flight path distances. To characterize the overall angular resolution of an image, the FWHM of the hot-spot produced in a simple backprojection image was calculated. Lower values for the FWHM provide the best overall angular resolution. Creation of backprojection images is covered in more detail in Section 2.5.3.

Due to the large number of variables possible in system optimization a few limitations were applied. The number of detectors was fixed at 16 liquid scintillators in the front plane with a checkerboard pattern of eight liquid scintillators and eight NaI(Tl) scintillators in the back plane. The detector sizes were also fixed and given in Section 2.2. The choice of detector size was based on work from [45]. Hardware for holding the detectors also dictated a two-plane design. These constraints produced three variables in the simulations: Detector spacing in the front plane, detector spacing in the back plane, and separation between the planes.

A complete description of the cases simulated and the results can be found in [47]. The configuration chosen offered a balance between efficiency and angular resolution. This configuration had a plane separation of 30 cm, which is measured between the faces of the detectors in each plane. The spacing between detector centers was 15 cm in the front plane and 25 cm in the back plane. The Monte Carlo simulations were performed with MCNPX-PoliMi. A full description of how the DPI was simulated is provided in Section 2.6.

2.4.4 Data acquisition

The DPI uses CAEN waveform digitizers to collect pulses from the detectors. The experiments presented in this dissertation used two different digitizer configurations. Four CAEN V1720 waveform digitizers were used initially, each with eight channels [79]. The digitiz-

ers were later upgraded to the CAEN V1730 model, which have 16 channels each. In this configuration only three digitizers were needed [80].

For the system using the V1720 digitizers, seen in Figure 2.7, the four boards were synchronized in time with triggers propagated from board to board. The front plane was split across two boards with the back-plane liquid scintillators occupying another and the NaI(Tl) scintillators connected to the fourth. Every channel in the system was used as a trigger, with the provided zero suppression capabilities eliminating waveforms in the time window without a pulse. This acquisition method allowed for non-correlated events, or singles, to be detected from all detectors. The V1720 had a 12 bit resolution, a 2 V dynamic range and a 250 MHz sampling rate.

With the V1730 digitizers, seen in Figure 2.7, the front plane used the first digitizer in the daisy-chain, the back-plane liquid scintillators used the second digitizer, and the back-plane NaI(Tl) scintillators used the third. The V1730 had an improved sampling rate of 500 MHz, with 14 bit resolution, and a 2 V dynamic range. Triggering logic was applied such that while the front plane detectors recorded singles, the back-plane detectors would only record events if two channels triggered above threshold in the pulse window throughout all channels. Because the NaI(Tl) scintillators have a very high efficiency, this greatly reduced the number of waveforms collected that did not result in correlated events. The downside is that a true singles spectrum was not available from the back-plane detectors. However, because some situations demand performance with very high count rates, the triggering logic was required for good system performance.

2.5 Data processing

Once waveforms have been transferred to the computer, software is used to analyze and clean the waveforms. The pulses are then correlated to look for neutron and gamma rays that

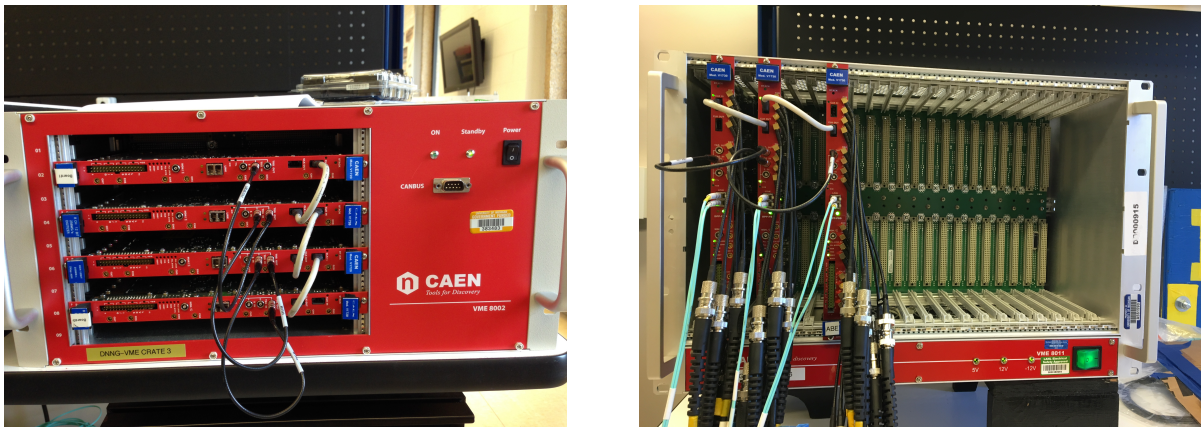

(a) (b)

Figure 2.7: Digitizer configurations for the DPI using the CAEN V1720s (a) and CAEN V1730s (b).

have possibly been detected twice in the system. These correlated events are then used to calculate the incident particle energy and reconstruct a conical surface representing possible source locations. The results include separate neutron and gamma-ray spectra, images and event data for advance imaging algorithms.

2.5.1 Pulse processing

Two distinct pulse structures are created by the liquid scintillators and NaI(Tl). The excellent timing resolution for liquid scintillators is because the pulses have a fast rise time. The decay time is also fast, making these detectors good for high count-rate applications because double pulses have a lower probability of occurrence. The difference in the pulse decay for neutron and gamma rays also allows for PSD to be applied as described in Section 2.4.1. Figure 2.8 shows an example of raw pulses from the liquid scintillators with clipped pulses removed.

The pulses from the NaI(Tl) scintillators have a different structure than those from liquid scintillators. Raw pulses collected from the NaI(Tl), after shaping and amplification, are shown in Figure 2.8 with clipped pulses removed for clarity. The pulse shaping greatly im-

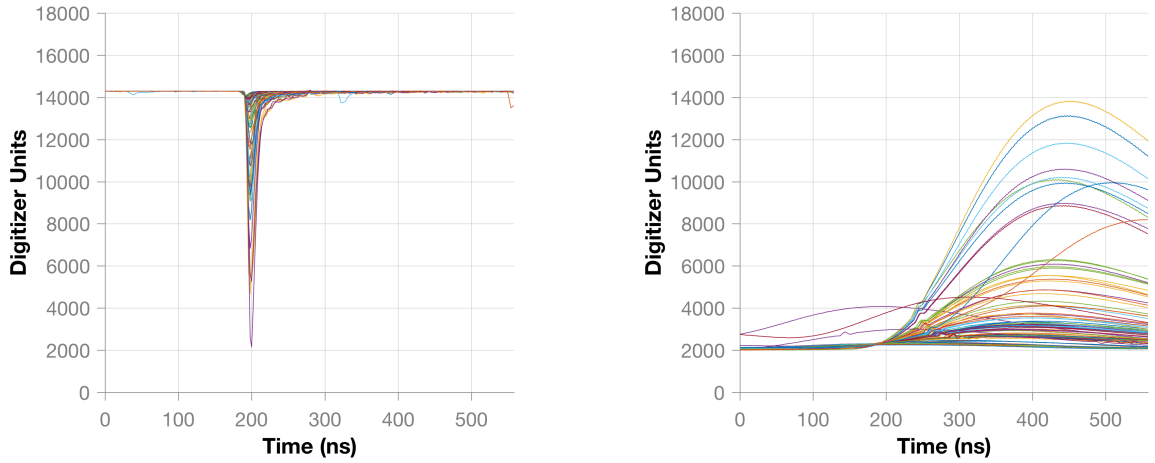

Figure 2.8: Raw waveforms from a liquid scintillator (a) and NaI(Tl) scintillator (b) using the V1730 digitizers. Clipped pulses were removed for clarity.

proves the energy resolution but extends the pulse rise time which sacrifices time resolution.

The waveforms are processed using a custom algorithm that performs pulse cleaning and PSD. The software removes clipped pulses that have exceeded the 2 V dynamic range of the digitizer and double pulses that inhibit PSD. The gain applied to the detectors defined the upper limit for observable events at approximately 2.8 MeVee. To calculate the time of the pulse, a constant fraction discriminator was set at 0.5 for both pulse types. The software provides the pulse height, time, and particle type for each pulse, which is then used to find correlated events.

2.5.2 Event correlation

The DPI relies on correlated detections of the same particle to image sources. When a particle is detected, a time window is used to look for detections occurring an another detector. The window extends both before and after the detection time of the event to account for detector time resolution. Originally, the waveforms from every channel were written to the computer from the digitizer and the events were then correlated using software. In high

count rate applications this is problematic because most of the pulses do not contribute to the desired signal, with only a small percentage of particles detected twice in the DPI. As a result, the digitizers can experience data throughput problems and not function correctly.

This problem was addressed by implementing trigger logic on the digitizers such that the many waveforms not contributing to a correlated event were not transferred to the computer. More specifically, all waveforms that produced a trigger in the front plane detectors were recorded, but the waveforms from both types of back-plane detectors were only recorded if there was a trigger present in the front-plane within the opened correlation window. The correlation window for back-plane liquid scintillators and the NaI(Tl) scintillators was 120 ns and was 400 ns respectively, both before and after the original trigger.

The algorithm used for event correlation worked from a list of pulses that were sorted by pulse time and identified as a neutron or gamma ray. For gamma rays, a time correlation window of 25 ns was opened before and after the first trigger. Due to the time resolution of the NaI(Tl) scintillators, the second event may appear to have occurred before the first. The correlation window for neutrons only occurs after the first trigger because the particles are slower and the time resolution is good enough to determine the proper order of detections. The window began 5 ns after the first trigger and extended 100 ns. An additional 5 ns window is applied to the first trigger in only the front plane to remove events in which a neutron scatters in two front plane detectors before scattering in a back-plane detector. The correlation script also does not include events that satisfy the time windows if a third trigger, of the same particle type, occurs in either the front or back plane.

2.5.3 Backprojection imaging

Once events have been correlated, their corresponding properties are used as described in Section 2.3 to calculate the scatter angle, θ, using Equations (2.6) for neutrons and (2.8) for gamma rays, which define both the opening angle for a cone of possible origins

of the particle. These known properties dictate that the particle had an equally probable chance of originating from anywhere on the conical surface. Although a single cone does not provide localization of the source, using the superposition of multiple cones will provide source localization.

To create an image, the cones must also be projected from three-dimensional to two-dimensional space. The configuration of the DPI and uncertainty associated with each cone does not provide enough information to localize the distance a source is from the system, only the angle in space relative to the system. In two-dimensional space, the probability function is the intersection of the cone and a sphere centered around the DPI. The coordinates used to define this geometry are the azimuthal angle, ranging from 0° to 360°, and the inclination, which has a range of 0° to 180° .

Two approaches can be used when defining the radius of the sphere. To create an image using the *long-distance approximation*, the radius of the sphere is set such that it is much greater than the distance between the front plane detectors. In this case, the apexes of each cone will all be located approximately at the origin of the sphere. For sources located at a large standoff from the DPI, this approximation is appropriate and will provide good image resolution. However, if a source or sources are located such that the magnitude of the standoff and detector spacing is similar, the image resolution will be poor using the long-distance approximation. In this case, the radius of the sphere must be similar to that of the source(s) to achieve good localization and resolution.

Because of uncertainty and resolution from system detectors described in Section 2.4.3, The cone-sphere intersection for each event will likely not overlap the actual source position. To account for the uncertainty in position of the cone, the intersection is broadened to a normal distribution with the mean representing the original cone-sphere intersection. The actual uncertainty of all the components contributing to the uncertainty of the cone can be propagated to define the extent of broadening. However, in an analysis by J. K. Polack in

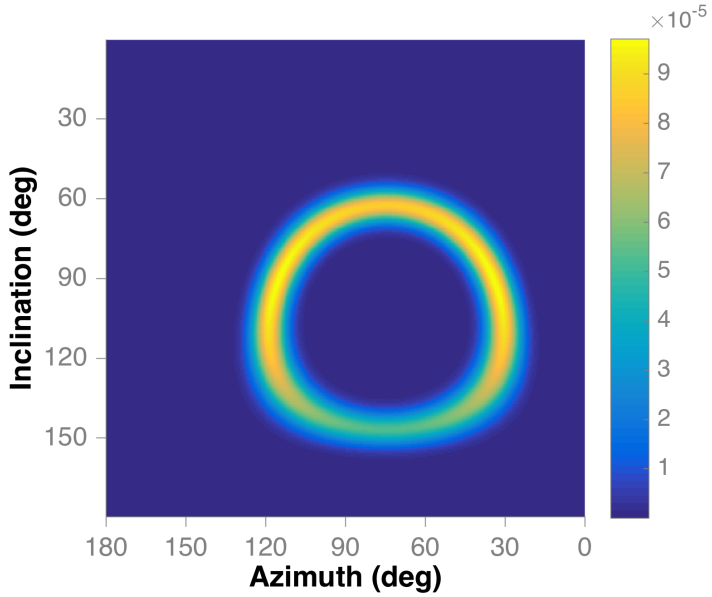

Figure 2.9: A single broadened-cone, projected onto a sphere.

[39], it was found that the resolution for neutron and gamma-ray events is dominated by spatial uncertainty and is similar regardless of incident energy. Based on the findings by J. K. Polack and empirical trials, using a broadened cone with a FWHM of 10° was a good approximation and system performance was not found to improve when using propagated uncertainties for all cones.

An example of a single broadened cone is shown in Figure 2.9. With the addition of more cones, a hot-spot in the image begins to form and with many cones the hot-spot becomes well defined. Figure 2.10 shows an image consisting of eight cones and 500 cones. This technique, projecting each cone and looking at the superposition, is typically referred to as *backprojection* or *simple-backprojection* imaging.

A separate backprojection image for neutrons and gamma rays is shown in Figure 2.11 from a ^{252}Cf source placed directly in front of the DPI at a 2 m standoff. The neutron image was made using 11,322 cones and the gamma-ray image using 135,426 cones. The long-distance approximation was used for these two images. With a standoff of only 2 m,

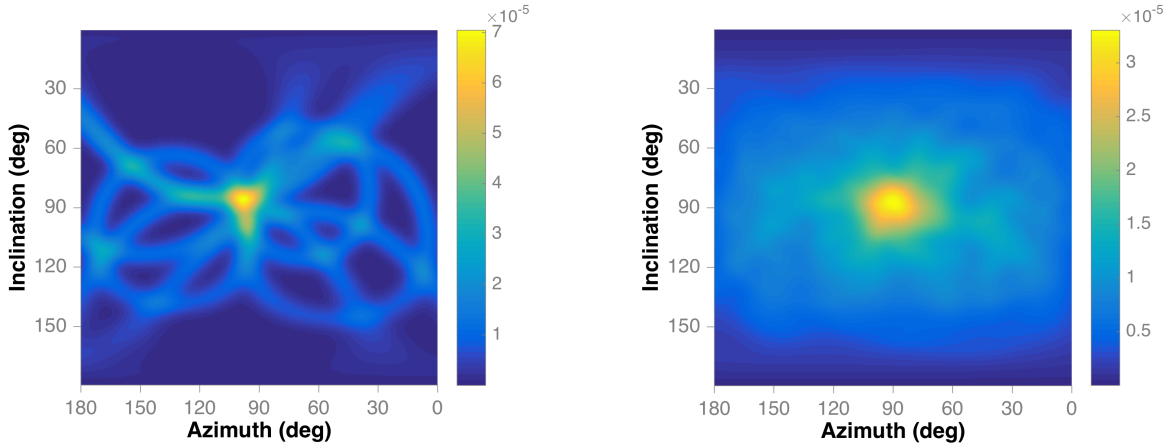

(a) (b)

Figure 2.10: Two examples of backprojection images. One image (a) was created using only eight total cones, which makes the structure of individual cones apparent in the image. The other image (b) was created using 500 cones, which blurs the structure of individual cones.

defining the sphere radius at 2 m improves the image resolution lowering the FWHM of the hot-spot from 52.3° to 40.1° along the azimuthal angle. The neutron backprojection images reconstructed with the long-distance approximation, and without, are compared in Figure 2.12. At distances greater than about 2.5 m the image quality for reconstruction with the long-distance approximation and without becomes the same.

While straightforward to create, backprojection images suffer from poor resolution and a low signal-to-noise ratio because the entire cone-sphere intersection is included as part of the image, even though only a small portion of it represents the actual source location. Other advanced imaging methods such as list-mode MLEM and bin-mode MLEM can greatly improve image resolution and the signal-to-noise ratio of hot-spots [39, 48]. Much of the work in this dissertation will focus on another advanced imaging technique known as the stochastic origin ensembles (SOE) method [51, 52]. SOE uses the same cones that create the backprojection images, but is able to eliminate much of the cone that causes the low-signal to noise ratio.

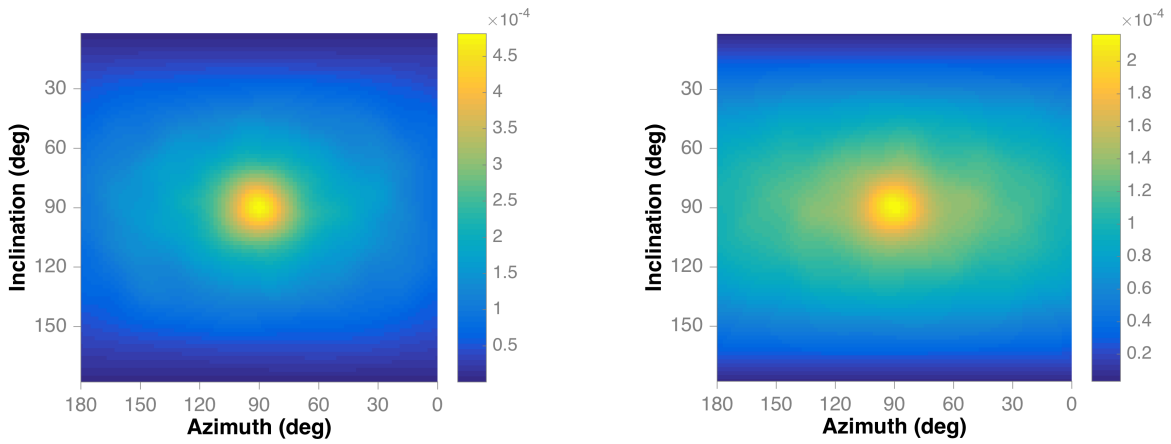

(a) (b)

Figure 2.11: Neutron (a) and gamma-ray (b) backprojection images reconstructed using the long-distance approximation from a ^{252}Cf source.

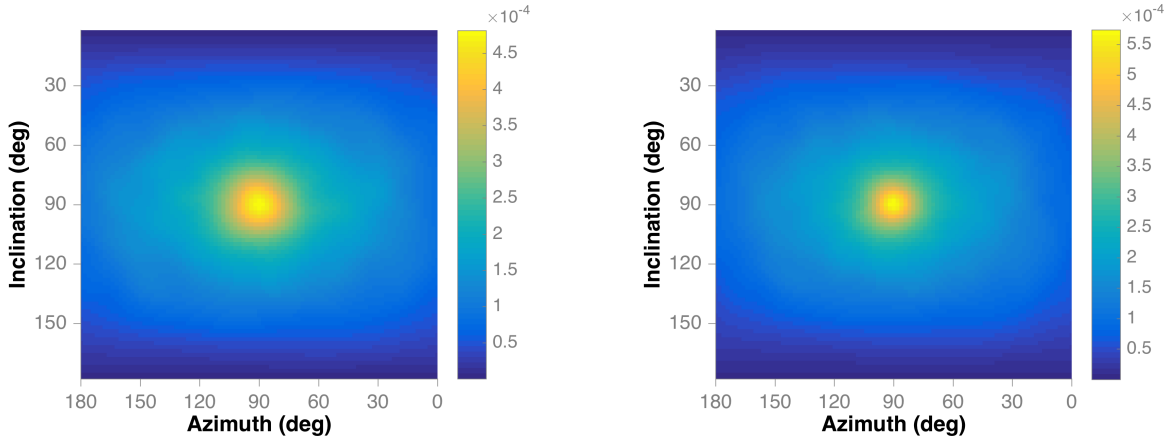

(a) (b)

Figure 2.12: A comparison of neutron backprojection images for a ^{252}Cf source at a 2 m standoff. The long-distance approximation (a) produces worse image resolution than when a sphere with a radius of 2 m is used for cone projection (b).

2.5.4 Energy spectra

The reconstructed energies for neutrons and gamma rays, calculated using Equations (2.1) and (2.7) respectively, combine to form energy spectra of all measured events. Figure 2.13 shows an example of a neutron and gamma ray spectrum from a ^{252}Cf source measured with the DPI. As is typical of most sources that emit neutrons, the gamma-ray flux emitted is usually at least an order of magnitude larger. The gamma-ray signal will contain environmental background whereas the neutron background is very low and safe to ignore.

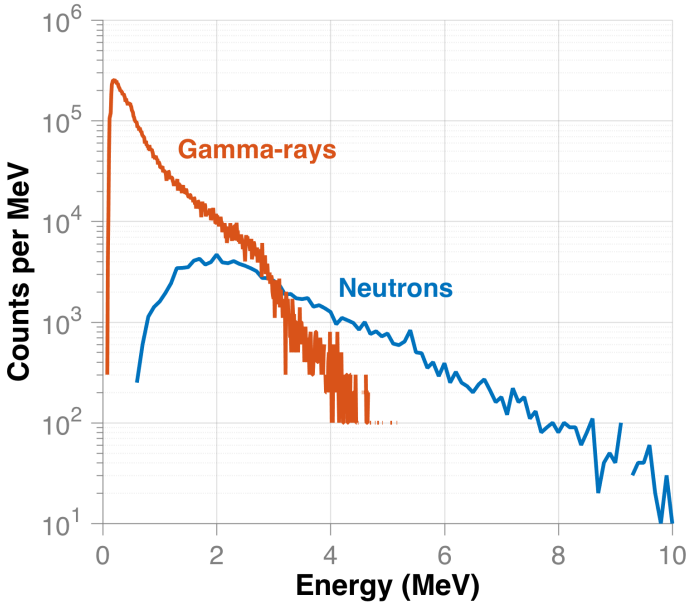

Figure 2.13: Reconstructed neutron and gamma-ray spectrum from a ^{252}Cf source.

2.6 Monte Carlo simulation of the DPI

A key capability for the development and research of the DPI was a reliable simulation method that could accurately reproduce the system response. The Monte Carlo code MCNPX-PoliMi (PoliMi), which is based on MCNPX, was used to model the DPI [81–84]. PoliMi expands on the capabilities of standard MCNPX in several ways that greatly bene-

fited this work. PoliMi provides the user with a data file that records all, or of subset, of the collisions that occurred in the simulation. Information such as the energy deposited, time, and position of the collision is recorded among other characteristics of the collision. Another feature is the treatment of fission on an event-by-event basis. Instead of producing average quantities for the number of neutrons and gamma rays produced in a fission event, PoliMi samples the known distributions and also accounts for the anisotropies of the fission neutrons. These properties have been included in many source definitions that can be called by the code. Some of the source definitions included, such as ^{252}Cf, ^{240}Pu, and AmBe, are sources used extensively in this work.

2.6.1 Simulation properties

A goal of PoliMi was to address the gaps in current versions of MCNP for simulating the response of organic scintillators. As described in Section 2.4.1, the difference in light creation, from neutron collisions on hydrogen or carbon, necessitates a more complex treatment than a pulse height tally can offer [85]. PoliMi has been extensively validated along with the collision file post-processor MPPost, to provide accurate detector response for liquid scintillators [73, 86, 87].

There were two relationships between energy deposited and light output for neutrons used in simulations. First is the relationship found by Enqvist et al.

$$L = 0.817E - 2.63\left(1 - e^{-0.297E}\right) , \tag{2.9}$$

where L is the amount of light produced in MeVee and E is the amount of energy deposited in the elastic scatter in MeV [72]. Further characterization by Norsworthy et al. found a different set of coefficients that provided better agreement [73]

$$L = 0.668E - 1.63\left(1 - e^{-0.387E^{1.05}}\right). \tag{2.10}$$

While the individual pulse height distributions were improved, other resolution effects did not show a tangible improvement in the imaging results. The results in Chapters 2, 3, and 4 were processed using Equation (2.9) and the results in Chapter 5 were processed using Equation (2.10).

The resolution of the liquid scintillator is a key property for producing accurate system response. The resolution function used in this work was

$$\frac{\Delta E}{E} = \sqrt{0.113^2 + \frac{0.065^2}{E} + \left(\frac{0.060}{E}\right)^2}. \tag{2.11}$$

The light output and resolution functions were found empirically for the 7.6-cm thick liquid scintillators used in the DPI. These functions were also used for the 5.1-cm thick liquid scintillators. The resolution function for the NaI(Tl) scintillators was

$$\frac{FWHM}{E} = \left(3.531 \times 10^{-4}E + 1.475\sqrt{E} + 14.24\right)\%, \tag{2.12}$$

with $FWHM$ being the full width at half maximum at energy E, in keV.

Time resolution was applied to the arrival time of particles in the simulations by sampling a Gaussian with a FWHM of 1 ns for liquid scintillators and 16 ns for NaI(Tl) scintillators. The mean of the sampled Gaussian was the time of the first collision in the detector. Because the PMTs do not have the ability to resolve multiple scatters in the detector by the same particle, a pulse generation time of 10 ns was applied after the first collision in the detector. Any subsequent collision occurring in the following 10 ns contributed to the same pulse with the light created being summed and then converted to energy deposited using Equation (2.9) or (2.10).

Non-active detector materials, such as the aluminum casing and PMTs were also included

in the simulations. Optical windows, responsible for aiding light collection in the liquid scintillators were composed of a borosilicate glass known as BK7, and induced many particle collisions. In simulations, events that collided in non-active detector materials or scattered more than once once in a detector, but still resulted in a detected event, could be classified as *non-ideal* events. Neutron events that underwent a single scatter on hydrogen in the front plane followed by an interaction in a back plane liquid scintillator could be classified as *ideal* events. An *ideal* gamma-ray event was classified as a single scatter in a front-plane liquid scintillator followed by an interaction in a back-plane NaI(Tl). Other examples of interactions that result in non-ideal events are the correlation of two different particles and an incorrect ordering of detections due to time resolution.

2.6.2 Simulation validation

To validate the simulation method and assumptions, it is important that the images and spectra agree with measured results. For neutron validation, a ^{252}Cf source was placed 2 m directly in front of the system. The distance was measured from the center of the gap between the front and back planes. The ^{252}Cf had a spontaneous fission activity of 5.07×10^6 fissions per second and was measured for two minutes. A count rate of 94.4 correlated neutrons per second was measured. The simulated count rate agreed well with a correlated count rate of 96.1 neutrons per second. A comparison of the reconstructed neutron spectra for the measured and simulated results is shown in Figure 2.14. The reconstructed images both locate the source with a well defined hot-spot. The images are shown in Figure 2.15.

To validate gamma-ray simulation, a ^{137}Cs point source with an activity of 86 µCi was placed 2.5 m from the system at the angular coordinates (135^o, 90^o). In a 60 minute measurement, a total of 13.4 counts per second were recorded, with 4.2 counts per second in the peak located at 662 keV. Figure 2.16 shows a comparison with the simulated spectrum, which produced a total of 10.9 counts per second, 5.8 in the peak. A comparison of the

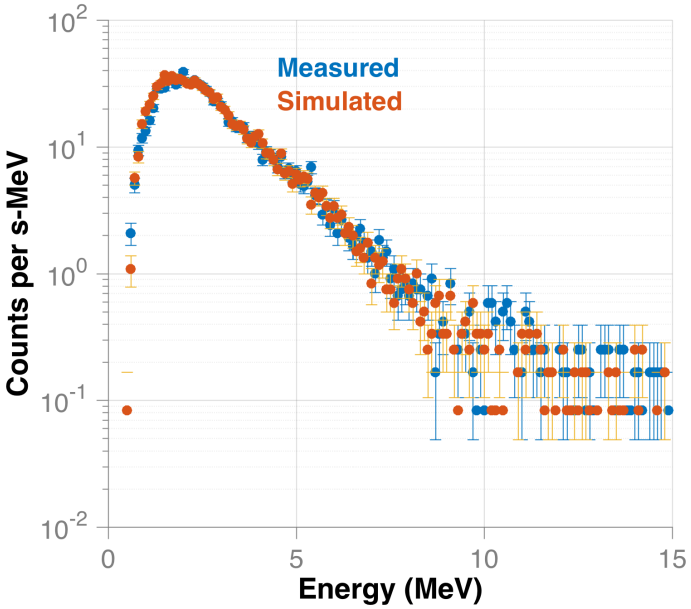

Figure 2.14: The measured and simulated reconstructed neutron spectrum from a 2 minute measurement of a ^{252}Cf source located 2 m from the DPI.

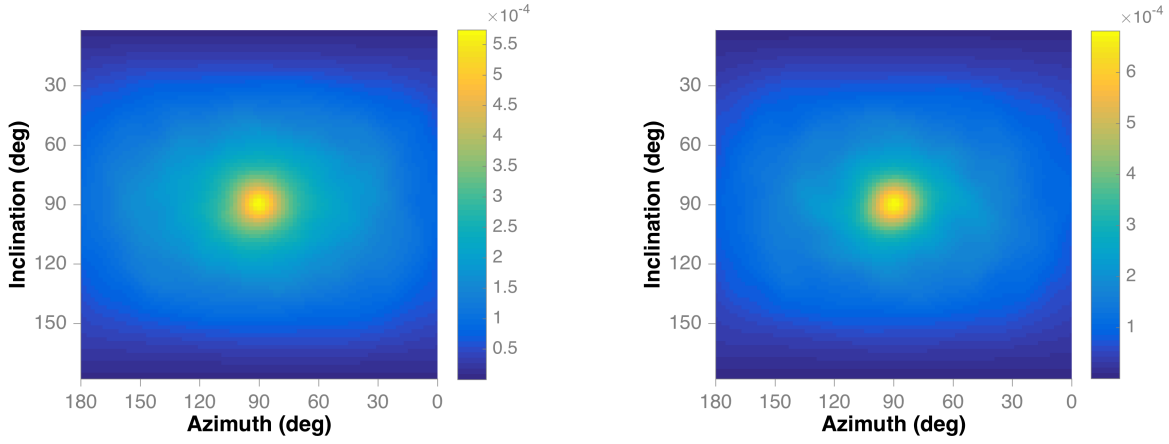

(a) (b)

Figure 2.15: Comparison of measured (a) and simulated (b) reconstructed neutron images for a ^{252}Cf source located 2 m from and directly in front of the DPI.

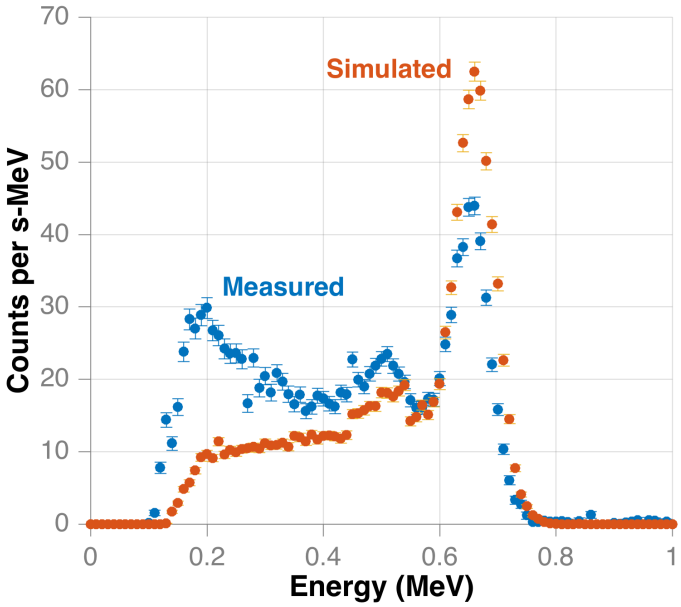

Figure 2.16: The measured and simulated reconstructed gamma-ray spectra from a one hour measurement of a ^{137}Cs source located 2.5 m from the DPI.

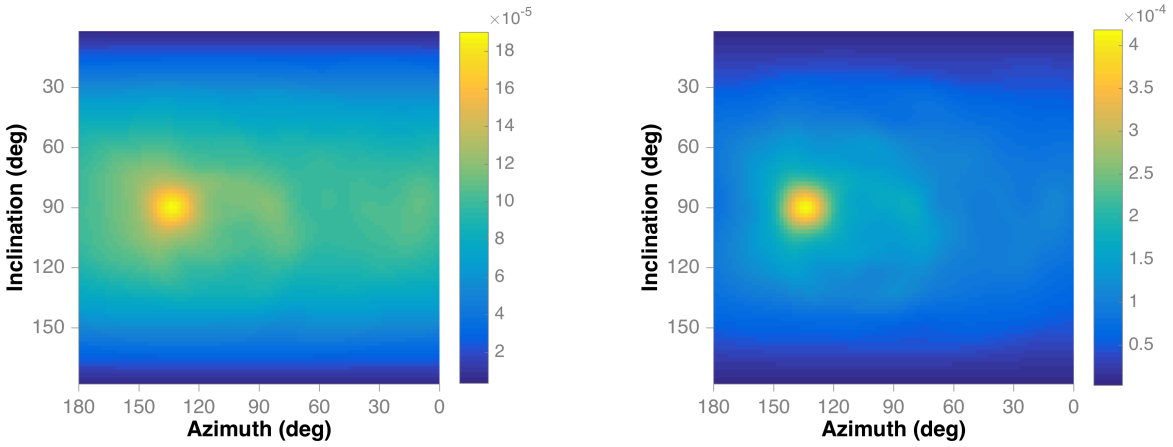

(a) (b)

Figure 2.17: Comparison of measured (a) and simulated (b) reconstructed gamma-ray images for a ^{137}Cs source located 2.5 m from the DPI.

reconstructed backprojection images is shown in Figure 2.17.

Much of the spectral mismatch may be attributable to the modeling of PMTs. Particles must pass through the front plane PMTs before detection. The PMTs in the simulation may not be attenuating enough incident particles, causing the larger simulated peak. The increased count rate at low energies is likely due to scattering on materials in the room not included in the simulation. The hot-spot in the simulated images matches the measured hot-spot well. More noise is seen in the measured image however because background radiation is present.

2.7 Conclusions

In this chapter, the motivation for and design of the DPI was presented and discussed. The system was motivated by the need to detect special nuclear material despite the presence of shielding. Choosing liquid scintillators for a combined neutron and Compton scatter camera, allowed for simultaneous detection of neutrons and gamma rays. Sensitivity for both particle types makes the system more robust to shielding that attenuates neutrons, gamma rays or both.

Organic liquid scintillators were found to provide sufficient pulse shape discrimination and timing properties to accurately correlate neutron and gamma-ray events. Using NaI(Tl) scintillators provided full energy depositions for a significant portion of the scattered gamma rays, which allowed for calculation of the incident energy. With time-of-flight information available for correlated neutron events, the DPI produced the appropriate information to create separate neutron and gamma-ray incident energy spectra.

With the appropriate incident energy information and the axis between detectors known, Equations (2.6) and (2.8) could be solved for the scatter angle of the particle. The scatter angle and axis then defined a cone of possible origins for the particle. Taking the superposi-

tion of many cones is known as backprojection imaging as was found to create hot-spots for both neutron and gamma-ray sources.

Accurate Monte Carlo simulation of the DPI was important for finding an optimized configuration. This required validation of the simulation, which were performed using MCNPX-PoliMi and post-processed using MPPost. Neutron response was validated by comparing the measurement and simulation of a ^{252}Cf source. The correlated event count rates, reconstructed spectra, and images produced from both the measurement and simulation agreed very well. For gamma rays, the simulated image located the source correctly but the spectra did not agree as well as the neutron spectra. The disagreement may be attributable to not modeling complexities of the PMTs or the full room.

Chapter 3

Applying and evaluating stochastic image reconstruction for the DPI

3.1 Motivation for stochastic image reconstruction

Reconstructing a measured source distribution from radiation scatter cameras is a difficult task with a variety of challenges. The most basic form of image reconstruction, simple backprojection (explained in Section 2.5.3), relies on only the kinematics of a particle that scores in the system. For an individual event, this method only succeeds in producing a cone, which defines all possible origins of that event. The superposition of the reconstructed cones produces images with large amounts of noise because only a single point of each cone contributes to the correct part of the image. This gives rise to many artifacts and can skew the reconstructed shape of distributed sources.

Another challenge is overcoming the effect of system resolution, which produces uncertainty in the reconstructed cones. An easy way to conceptualize this effect is by assigning each cone a thickness such that it is no longer a surface. The individual components that contribute to event resolution arise from measured quantities and system geometry. The individual components include energy and time resolution in the detectors, uncertainty of the interaction position in the detector, and the assumption of a single hydrogen scatter (for neutrons) or complete absorption in the NaI (for gamma rays) [88–90]. The summed

uncertainty of all these factors will appear Gaussian in nature due to the central limit theorem. The thickness of a cone can then be defined by a normal distribution estimating the uncertainty, where a point approximation of the mean exemplifies the highest probability of the quantity of interest, and the width of the distribution describes the uncertainty.

To improve the quality of reconstructed images, the resolution effects from the system must be mitigated. Many methods have attempted to address this problem. These include but are not limited to backprojection, filtered backprojection, maximum likelihood, and maximum a posterior [91]. One of the best performing and most widely used methods is MLEM [92]. This statistical method uses a system response matrix to estimate the true source distribution from observed data. The most commonly implemented form is *list-mode* MLEM [48]. Another type of MLEM algorithm is implemented in *bin-mode* [39, 59, 93]. Bin-mode MLEM has been thoroughly studied as a reconstruction method for the DPI with good results. The studies showed that MLEM greatly improved the image quality compared to backprojection and also allowed for the spatial isolation of spectra.

While MLEM improves upon backprojection greatly, there are several issues associated with these methods. Incomplete information in the system matrix can lead to over-fitting, which produces noise or artifacts in the solution. Another well known issue with MLEM is the heavy dependence of solution quality on the number of iterations performed. Over-iterating will produce an image with low quality [94]. While many solutions for a stopping condition have been proposed, there is no consensus [50]. Bissantz et al. propose a stopping condition that only achieves 80% of the maximal signal-to-noise ratio (SNR) [49]. This issue exists for both the list-mode and bin-mode implementations of the algorithm.

The bin-mode solution requires the inclusion of a simulated system-response matrix for image reconstruction. While it is possible to weight the system matrix created for the list-mode algorithm with the simulated response-matrix, it is not required. The simulated response-matrix is computationally intensive as the response to both particle types must be

evaluated for all energies over all space.

To address the given issues, this work proposes the application of the stochastic origin ensembles (SOE) method for image reconstruction. SOE uses Markov chain Monte Carlo (MCMC), through the Metropolis-Hasting algorithm, to reconstruct source distributions [95]. SOE is an iterative method using the reconstructed cones for each detected particle to produce a stochastic steady-state solution. The method was originally proposed by Sitek for use in computed tomography, and was then extended to Compton cameras by Andreyev et al. [51, 52]. They showed that SOE produces a solution comparable in quality to list-mode MLEM. However, a key gap in the available literature was the absence of measured results using SOE reconstruction, with the exception of [54, 96, 97], in which a Compton camera was used for range verification in proton therapy. The application of the method were generally limited to small Compton cameras for medical imaging with small source-to-detector distances [53].

The application of SOE to the DPI differs from the prior applications in several key ways. Instead of medical applications, the DPI is designed for non-proliferation applications, with the detection of SNM as the main goal. SNM produces different energy spectra depending on the type of source, as opposed to a radioactive tracer with a known energy. The system is also much larger and needs to achieve far-field two-dimensional imaging of point sources and extended sources. In this work, the application of SOE is extended to the neutron scatter mode of the DPI. Measured results are also provided for both neutrons and gamma rays, with a comparison to MLEM results. Experimental results using mixed-oxide nuclear fuel canisters, PuBe, and mono-energetic gamma-ray sources demonstrated that SOE faithfully reconstructed a stochastic steady-state solution of the expected source distributions. A direct comparison to a list-mode MLEM implementation with the same data showed that SOE produced improved quality making it a viable tool for DPI image reconstruction to locate SNM.

3.2 Theory of the stochastic origin ensemble technique

For each neutron or gamma-ray event recorded by the DPI, the knowledge of the event origin is limited to a cone. In reality, there is only a singular location, not a conical surface, that can be the origin of the event. The conical surface represents a probability density function (PDF) for each event. Due to the complex and dependent nature of the individual PDFs, a direct solution of the problem is not possible and requires an estimation method. This problem is well suited for the use of a MCMC technique because a series of states, at which probability densities can be evaluated, can be created from the individual event PDFs. In this case, a state in the Markov chain will be a proposed distribution of the location for all event origins.

A random sampling process can be described that moves between states of the Markov chain, while preferentially keeping sampled origins in areas of higher probability for the true source distribution. The Metropolis-Hastings algorithm was developed for estimating a solution based on a MCMC process. Sitek relies on this algorithm to describe the probability for transitioning from one state to another state of the Markov chain, in his work on CT reconstruction. The symbols and notation used in this section to describe the MCMC process are reproduced from his paper [51].

To preserve the properties of the Markov chain necessary to estimate a solution, the condition of detailed balance is required. The balance equation arises from the standard form of Bayes' theorem,

$$P(A|B) = \frac{P(B|A)P(A)}{P(B)}\,, \tag{3.1}$$

and allows the Markov chain to reach equilibrium. Rewritten using Y_s to represent the current state of the Markov chain, or prior, and Y_{s+1} to represent the proposed state, or posterior, the equation has the form

$$P(Y_{s+1}|Y_s) = \frac{P(Y_s|Y_{s+1})P(Y_{s+1})}{P(Y_s)}\,. \tag{3.2}$$

The conditional probability $P(Y_{s+1}|Y_s)$ is the probability of transitioning state Y_s to state Y_{s+1} and can be written as $P(Y_s \to Y_{s+1})$. Using this notation with Equation (3.2) provides the balance equation:

$$P(Y_s)P(Y_s \to Y_{s+1}) = P(Y_{s+1})P(Y_{s+1} \to Y_s)\,. \tag{3.3}$$

This equation defines a key feature of Markov chains, which states that the posterior state Y_{s+1} depends only on the prior state Y_s. The MCMC process is said to be memoryless, as the next estimation relies only the previous estimation and no others.

To define $P(Y_s)$ and $P(Y_{s+1})$ we define a PDF that accounts for the detection of all events. Starting with a single event, the PDF is the intersection of the calculated cone and a sphere surrounding the DPI, which is broadened to include system resolution. More complete explanations of individual event probabilities are described in Sections 2.3.1, 2.3.2, and 2.5.3. Next the probability density function $\pi_i(y)$, which describes the probability that a single event originated from a particular location is defined as

$$\pi_i(y) \sim \alpha_i(y) f(y)\,, \tag{3.4}$$

where α_i is the probability of detecting event i at location y and $f(y)$ is the actual number of events detected from location y. In this case y represents a direction defined by angular coordinates. This is the desired quantity that the SOE algorithm seeks to estimate for each subsection or pixel of the image. For N detected events, the probability density of a particular state can be given as

$$\Pi(Y) \sim \prod_{i=1}^{N} \alpha_i(y_i) f(y_i)\,, \tag{3.5}$$

where Y is a vector of all event locations. Substituting Equation (3.5) into Equation (3.3), the detailed balance equation takes the form

$$\frac{P(Y_s \to Y_{s+1})}{P(Y_{s+1} \to Y_s)} = \frac{\Pi(Y_{s+1})}{\Pi(Y_s)}\,. \tag{3.6}$$

The transition between states in the Markov chain consist of a new proposal for y for a single event k. Since the probability density of all other events remains the same, the ratio of the probability density between the two states, will be the same as the ratio between the probability of event k at both locations

$$\frac{\Pi(Y_{s+1})}{\Pi(Y_s)} = \frac{\pi_k(y_{k,s+1})}{\pi_k(y_{k,s})}\,. \tag{3.7}$$

Substituting Equation (3.4) then gives:

$$\frac{\Pi(Y_{s+1})}{\Pi(Y_s)} = \frac{\alpha_k(y_{k,s+1}) f(y_{k,s+1})}{\alpha_k(y_{k,s}) f(y_{k,s})}\,. \tag{3.8}$$

Combining Equations (3.7) and (3.6) gives:

$$\frac{P(Y_s \to Y_{s+1})}{P(Y_{s+1} \to Y_s)} = \frac{\alpha_k(y_{k,s+1}) f(y_{k,s+1})}{\alpha_k(y_{k,s}) f(y_{k,s})}\,. \tag{3.9}$$

Assuming a uniform prior, we can estimate that $f(y_{k,s}) \sim n_{k,s}$ where $n_{k,s}$ is the number of origins at the location of event k is state s. As stated by Andreyez et al. in [52], the term α_k is accounted for in the Monte Carlo sampling for each origin location. These considerations provide an acceptance probability for the transition between states $A(Y_s \to Y_{s+1})$ that fulfills the requirement that

$$\frac{A(Y_s \to Y_{s+1})}{A(Y_{s+1} \to Y_s)} = \frac{P(Y_s \to Y_{s+1})}{P(Y_{s+1} \to Y_s)}\,. \tag{3.10}$$

The acceptance probability is defined as

$$A(Y_s \to Y_{s+1}) = \min\left(1, \frac{n_{k,s+1}}{n_{k,s}}\right)\,, \tag{3.11}$$

which is simply the ratio of the number of origins in the locations of event k in states s and the proposed state $s+1$. The proposed state is then accepted and another state $s+2$ is proposed or the state remains at state s and a new state $s+1$ is proposed.

Another important property of the method is that every possible state in the chain is attainable thorough a series of finite moves through the chain. A chain with this property is known to be ergodic. By moving only a single event k between each state, this property is fulfilled.

The method described above will reach equilibrium after transitioning between a finite number of states. At this equilibrium, each sampled state will be an estimate of the true distribution of origins. An estimation of the equilibrium states can then be taken with an average. If image states are averaged beginning at state s through state C, the following equation represents the average of the selected states in the Markov chain

$$\hat{\Pi} = \frac{1}{C - s + 1} \sum_{c=s}^{C} \Pi(Y_c)\,. \tag{3.12}$$

As $C \to \infty$, $\hat{\Pi}$ will approach the estimate of Π asymptotically [95].

The next section will describe the algorithm as applied to the DPI using the theory described in this section.

3.3 The SOE algorithm as applied to the DPI

Implementation of the SOE algorithm begins by defining the PDF for each event detected by the DPI. Using the measured values for each event outlined in Sections 2.3.1 and 2.3.2, a cone of possible sources locations and its intersection with a sphere surrounding the system is calculated. However, uncertainty in the measured quantities must be accounted for to achieve good image reconstruction. One implementation of the SOE algorithm accounts for these sources of uncertainty, while another uses an approximation. The basic outline for the SOE algorithm was described by Andreyev et al. for application to a Compton camera, with another paper that describes how elements of system resolution can be recovered [98]. Application of the SOE to the DPI follows. The following algorithm is run separately for neutrons and gamma rays:

1. The measured parameters used to define cones of possible source locations are resampled according to probability distributions corresponding to their respective uncertainties.

    - For neutron events, sampled parameters include energy deposited in the front plane, the time-of-flight (TOF) between interactions, and the interaction position in both detectors. The energy deposited in the liquid scintillator is sampled from a normal distribution according to the energy dependent resolutions shown in Figure 2.6. The TOF is resampled from a normal distribution with a FWHM of 1 ns as described in Section 2.4.1. The interaction position within each detector is sampled uniformly throughout the cylinder.
    - The sampled quantities for gamma-ray events include the same uniform sampling throughout both cylindrical detectors as is done for neutron events. The energy deposited in the first detector is also sampled using the resolutions in Figure 2.6. The energy deposited in the NaI(Tl) is sampled using Equation (2.12).

Using the sampled quantities, a cone of possible source locations, and its intersection with a sphere surrounding the system, is calculated. The origin of the sphere is centered between the two planes of the DPI. If the long-distance approximation is used, the apex of all cones are centered at the origin of the sphere. If this approximation is not used, a radius for the sphere must be defined.

2. A single origin is sampled for each event along the cone sphere intersection calculated in Step 1. This ensemble of sampled origins is pixelated using 5° pixels and constitutes the starting image state Y_0.

3. The parameters of each event are resampled as described in Step 1. The origin locations are then resampled and the new origin locations are pixelated. This ensemble constitutes a new image state.

4. The new location for each pixel is then accepted or rejected based on the acceptance probability:

$$A(Y_s \rightarrow Y_{s+1}) = \min\left(1, \frac{N_{p',s+1}}{N_{p,s}}\right) . \tag{3.13}$$

In this equation, the pixel containing the original origin location is represented by p and the pixel containing the new location by p'. The number of origins N, in the proposed image state $s+1$ is compared to the number of origins in the prior image state s. Note that $N_{p',s+1}$ will be greater than $N_{p',s}$ by one, which represents the movement of the origin. With this probability, a proposed move will always be accepted if there are more origins in the new location. If there are fewer, the probability of acceptance is the ratio between the number of origins in the original and new pixel.

5. Steps 3 and 4 are repeated for many iterations with the number of origins in each pixel recorded at each iteration.

6. After a sufficient number of iterations have been completed, the images states from each iteration are averaged to achieve an estimation of the true source distribution.

3.3.1 Approximations

A simplification can be made to the algorithm that aids computation time and simplicity. As described in Section 2.5.3, the resolution effect that dominates uncertainty for each event is the spatial resolution of where the particle was detected in each detector. Instead of re-sampling each measured parameter to calculate the opening angle of the cone, θ, the opening angle can be sampled from a probability density function,

$$\text{PDF} = \frac{1}{\sigma\sqrt{2\pi}} \exp\left[\frac{-(x-\theta)^2}{2\sigma^2}\right], \tag{3.14}$$

using the original calculated angle as the mean with a Gaussian broadening of 10° at the FWHM ($\sigma = 4.25°$).

While sampling each individual parameter may seem like a more appropriate treatment, the resolutions of several measured parameters are difficult to quantify. For example, the energy resolution of the liquid scintillators (shown in Figure 2.6) at low light-outputs is not well known. The study used to determine the energy resolution of the liquids scintillators used a minimum light output of 250 keVee with an extrapolation to lower values [72]. With a detector threshold usually around 40-50 keVee, many correlated events will contain detections in this region. Another difficult quantity to characterize is the uncertainty associated with interaction position in the detector. If the source location is known, the interaction position could be quantified by using the mean free path of the particle within the liquid. This would require a complex characterization of estimating the source distribution initially before characterizing the uncertainty for each event and performing a second image reconstruction.

Two reconstructions of the same data were performed to compare the two methods. Both

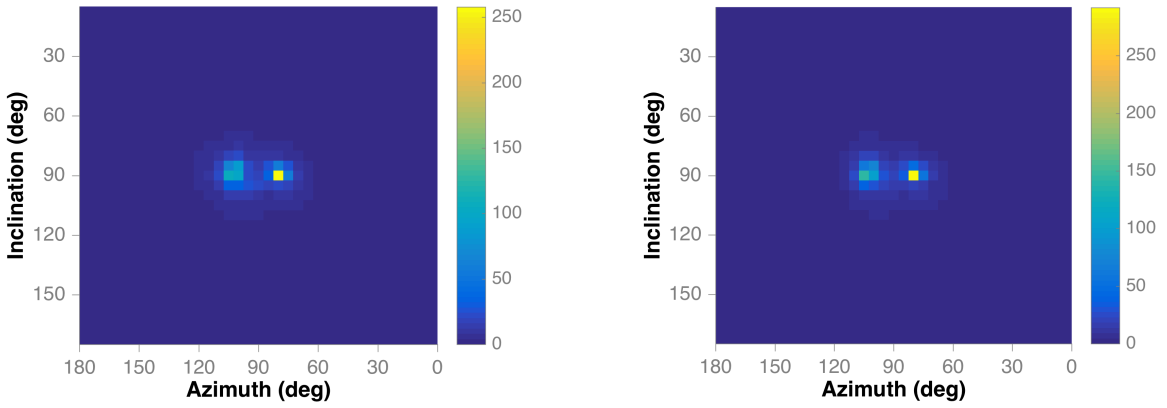

(a) (b)

Figure 3.1: An SOE reconstruction (a) created using sampled quantities for all parameters and a reconstruction (b) estimating the uncertainty of each cone angle with a 10° FWHM. The scale is in units of detected events.

images are seen in Figure 3.1. Only several pixels in the image differ by more than about 15%. Figure 3.2 shows the magnitude of the difference between the two images calculated using

$$\frac{|\text{Image}_A - \text{Image}_B|}{\text{Image}_A}, \tag{3.15}$$

where Image_A was reconstructed using sampled quantities and Image_B used the approximation. The image reconstructed with the approximation produces a slightly better SNR.

3.3.2 Burn-in period

After many iterations, each image state sampled will be an approximation of the true source distribution. This period of the Markov chain is known as equilibrium. Once equilibrium is reached, a running average of image states is taken, which composes the final estimate (Equation (3.12)). Because image states earlier in the chain have yet to reach equilibrium, they provide a worse approximation of the true source distribution. Therefore, to create

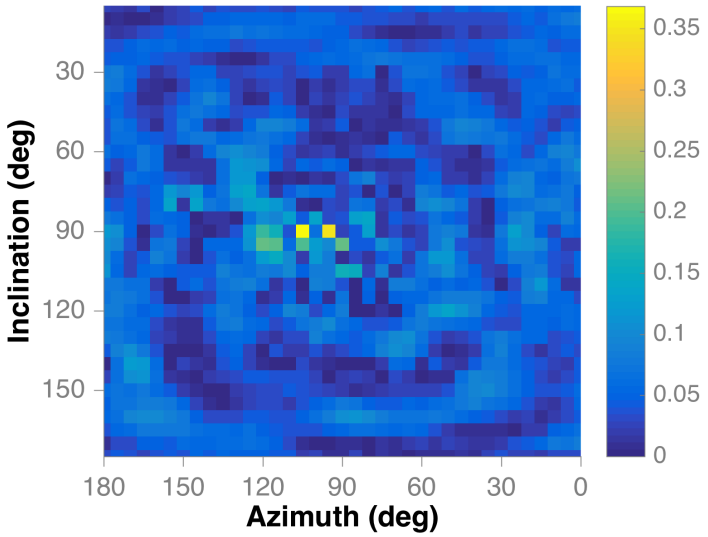

Figure 3.2: The fractional difference between the images reconstructed using sampling for all parameters and an approximated uncertainty. The magnitude of the difference in each pixel is shown.

an estimate without the bias from image states outside of the equilibrium period, they are not included in the average estimate. The image states before the Markov chain reaches equilibrium is known as burn-in.

A couple measures can be used to determine when the equilibrium state has been reached. First, the number of origins in a particular pixel can be tracked. If a pixel located within the true source distribution is considered, it will contain a number of origins in the initial image state Y_0. During the burn-in period, the number of origins located in this pixel will fluctuate, but ultimately increase, until the equilibrium is reached. At this point the number of origins within the pixel will fluctuate but have neither an increasing nor decreasing trend. An example is shown in Figure 3.3. This example is taken from an experiment with two gamma-ray emitting sources that includes total 54,541 counts. The number of origins, located within the two pixels representing both source locations, is plotted as function of iteration number. Consecutive iterations are highly correlated but large swings occur over

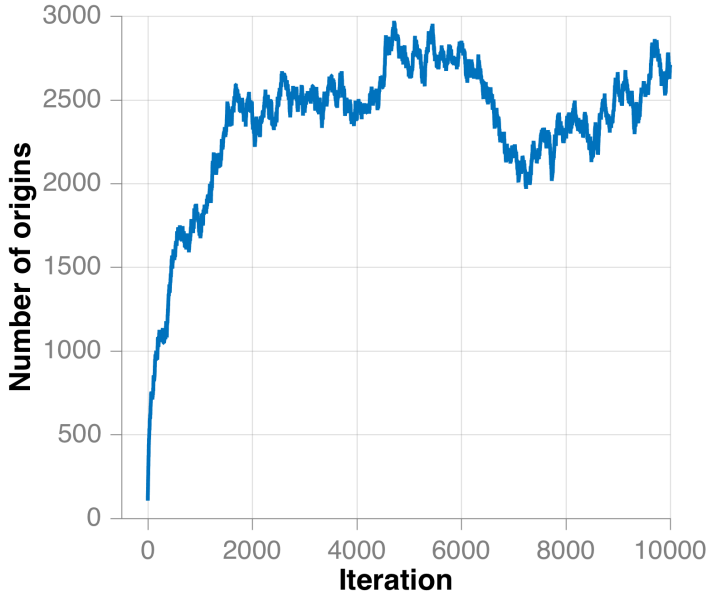

Figure 3.3: The number of origins located in the pixels representing two source locations as a function of iteration.

many iterations.

A second way to determine the length of the burn-in period does not require the choice of a particular pixel or group of pixels. When the chain has reached equilibrium, the average probability of accepting a move will remain relatively constant with little fluctuation. This parameter can be tracked by examining the fraction of moves accepted for each iteration. Figure 3.4 shows an example. It is also important to note the smaller deviations in this value than in the number of origins located within a group of pixels as shown in Figure 3.3.

The algorithm must determine, in real-time, when to begin keeping a running average of image states. A moving average, of the fraction of moves accepted, can be computed using a pre-selected sampling length; however, The equilibrium value reached for the fraction of moves accepted will differ on a case-by-case basis. A solution is desired that can be used for a general case and does not require a threshold value to determine when equilibrium has been reached.

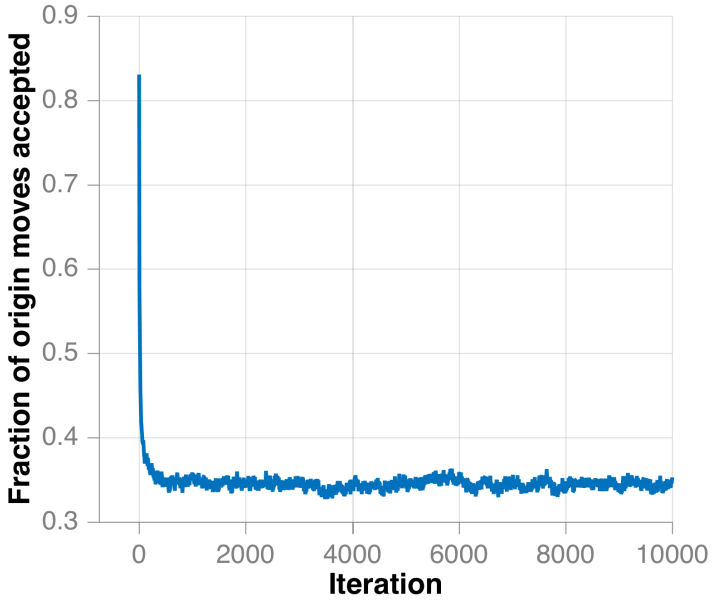

Figure 3.4: The fraction of origins moved to a new location in the image as a function of iteration.

The MCMC theory dictates that once equilibrium has been reached, the fraction of moves made should oscillate around the mean with an equal number of values above and below the mean assuming a representative sample is taken [99]. To determine when there are frequent fluctuations in sign, at each iteration n the mean of the fraction of accepted moves within a window, $\hat{F}_{n,1}$, is calculated:

$$\hat{F}_{n,1} = \frac{1}{I} \sum_{i=n-2I+1}^{n-I} F_i \,. \tag{3.16}$$

The range of the mean is $n - 2I + 1$ through $n - I$, with a pre-described window length I. A second mean is calculated for the window with the range $n - I + 1$ to n

$$\hat{F}_{n,2} = \frac{1}{I} \sum_{i=n-I+1}^{n} F_i \,. \tag{3.17}$$

The percentage difference P_n between the means of both windows is calculated for each

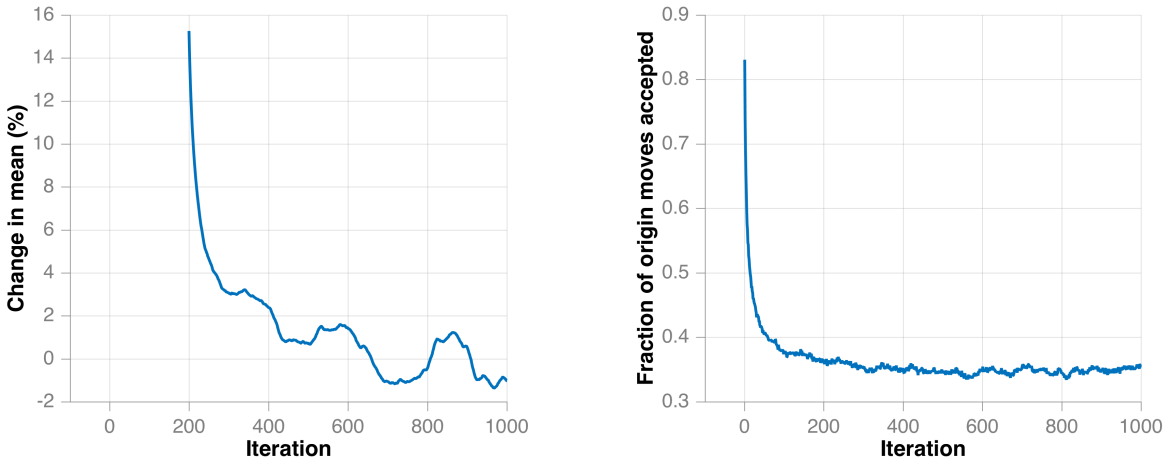

(a) (b)

Figure 3.5: The percent difference of windowed means, for origin acceptance rates, is shown at each iteration (a). A value less than zero is reached after 660 iterations, which indicates the end of the burn-in period. A plot of the origin acceptance rate (b) shows that after 660 iterations equilibrium has been reached.

iteration number $n >= 2I$ using

$$P_n = \frac{\hat{F}_{n,1} - \hat{F}_{n,2}}{\hat{F}_{n,1}} \times 100\,. \tag{3.18}$$

During the Markov chain equilibrium, P_n will fluctuate around a mean of zero. Therefore, the burn-in period is considered to have ended once P_n reaches zero for the first time. At this point, a running mean is started that will be the final solution once a sufficient number of iterations have occurred.

A window length I of 100 iterations was found to be a sufficient length for determining the burn-in period. Figure 3.5, shows P_n for the above example, as well as a zoomed in plot showing the fraction of moves accepted for the first 1,000 iterations. For this case, the first value at which P_n is less than zero is at 660 iterations.

To quantify the effect of burn-in on the final solution, two sets of image reconstructions were run, using the same random number seed, with increasing numbers of iterations. The first set set of reconstructions began averaging image states for each iteration after the

Table 3.1: Burn-in effect on reconstructed image for various numbers of iterations. Pixels included gives the number of pixels with a value greater than one. Differences $> 1\sigma$ are the number of pixels in which the difference between reconstructed images exceeds one standard-deviation. The percentage is also given.

Iterations	**Pixels included**	**Differences** $> 1\sigma$	**Percentage** $> 1\sigma$
1×10^3	1862	548	29.4%
1.5×10^3	1864	312	16.7%
2×10^3	1874	199	10.6%
5×10^3	1882	41	2.2%
1×10^4	1881	3	0.2%
2×10^4	1882	0	0.0%
5×10^4	1884	0	0.0%

calculated burn-in of 660 iterations. The second set did not account for burn-in and averaged every image state. The difference in images reconstructed with the same number of iterations, but one accounting for burn-in and the other not, were compared to quantify the effect of burn-in. The inclusion of burn-in can be considered insignificant when the difference, created by its inclusion, is insignificant compared to the overall statistical uncertainty of the image. A simple approximation for the statistical uncertainty of the image is the square-root of each pixel value because the detected particles are emitted through a Poisson process. In this analysis, only pixels with an average value of at least one in both solutions were included.

For each number of iterations, the difference between the reconstruction including burn-in and the reconstruction without was taken. The number of pixels where this difference exceeded the statistical uncertainty of 1 σwere counted. The results are shows in Table 3.1. At 1×10^4 iterations, only 0.2% of pixels fulfilled this criterion and at 2×10^4 no pixels fulfilled the criterion. The conclusion is that, in this case, the inclusion or exclusion of burn-in does not have a significant affect on the final solution after about 1×10^4 iterations.

A second case examined a neutron measurement, also of two point sources, with 2,452 total counts. A similar analysis found that the burn-in only had a significant affect on the image until about 5,000 iterations were run. It is likely that the effect of burn-in is washed out with fewer iterations in this case because fewer total origins being included in the reconstruction.

3.3.3 Iteration stopping condition

As described in section 3.2, the average of image states $\hat{\Pi}$ approaches Π asymptotically as the number of iterations goes to infinity. To efficiently compute an estimated solution, a condition must be established for when a sufficient number of iterations have been completed. The stopping condition presented, sets a threshold, below which a solution updated with more image states chain is considered unchanged [100]. At this point the solution will have reached a stochastic steady-state and subsequent iterations will not change the solution in a meaningful way.

The parameter used to describe the difference between images, $\vec{D}$, is the percent change between iterations for a subset of pixels

$$\vec{D} = \frac{\left|\hat{\Pi}_i - \hat{\Pi}_{i+1}\right|}{\hat{\Pi}_i} \times 100\,. \tag{3.19}$$

Comparing image states from subsequent iterations is problematic due to the high degree of correlation in subsequent image states. Subsequent image states produce a very small change in $\hat{\Pi}$ while a larger change is produced when comparing solutions separated by thousands of iterations. Known as *autocorrelation*, MCMC algorithms often includes *thinning* techniques to address high correlation between subsequent states [101, 102]. For example, $\hat{\Pi}$ may be computed by only including every tenth or hundredth image state in the average. While, this technique was necessary in the past to avoid computer memory and computation time

issues, Link and Eaton suggest that thinning Markov chains may reduce precision of the estimate and that thinning should only be used if computational resources require it [103]. The reconstructions in this work does not present computational issues so thinning is not used. While autocorrelation does not present a problem for estimating a final solution, the small changes occurring between subsequent states are a poor indicator of when a stochastic steady-state has been reached for $\hat{\Pi}$. A step size for calculating $\vec{D}$ must be determined such that significant changes in the solution will be included if steady state has not yet been reached.

This method for determining when steady state has been reached requires four parameters:

1. Quantity to measure change between solutions
2. Threshold at which iterations are stopped
3. Subset of pixels for which chosen quantity is evaluated
4. Step size for parameter evaluation

An empirical evaluation found the following parameters well suited to this application:

1. **Quantity to measure change between solutions:** Percent difference between solutions
$$\vec{D} = \frac{\left|\hat{\Pi}_i - \hat{\Pi}_{i+step}\right|}{\hat{\Pi}_i} \times 100 \tag{3.20}$$
2. **Threshold at which iterations are stopped:** 1%
3. **Subset of pixels for which chosen quantity is evaluated:** Pixels in both $\hat{\Pi}_i$ and $\hat{\Pi}_{i+step}$ with at least 1% of total image intensity
4. **Step size for parameter evaluation:** 10,000 iterations

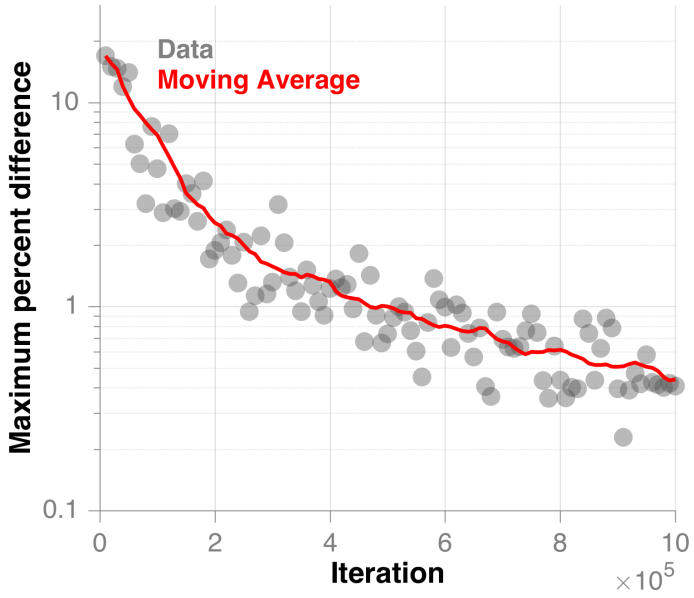

Figure 3.6: The pixel with the greatest percentage difference calculated at 10,000 iteration intervals. The cutoff for iterations is when the moving average of this value falls below 1%.

The method outlined above was applied to the two-source neutron measurement described previously in Section 3.3.2. Figure 3.6 shows the percent difference given by Equation (3.20) using the given parameters. The generated curve can be smoothed using a moving average with a span of 20 data points. Iterations are stopped when the moving average of this curve falls below 1%. In this case, iterating can be stopped after 4.8×10^5 iterations.

Reconstructed images using 1×10^4, 1×10^5, and 4.8×10^5 iterations were compared to an image reconstructed with a very large number of iterations, 1×10^7. Figure 3.7 shows the reconstructed image with 1×10^7 iterations and Figures 3.8, 3.9, and 3.10 show the comparisons respectively. Each comparison shows the reconstructed image and the magnitude of the fractional difference at each pixel. For the 4.8×10^5 case, the maximum difference between the images is 6.2% in pixel (80°, 95°). To provide context for how significant of a change this is, it can be compared to the estimated statistical uncertainty of the pixel. The statistical uncertainty of the pixel can be approximated by taking the square root. With a value of

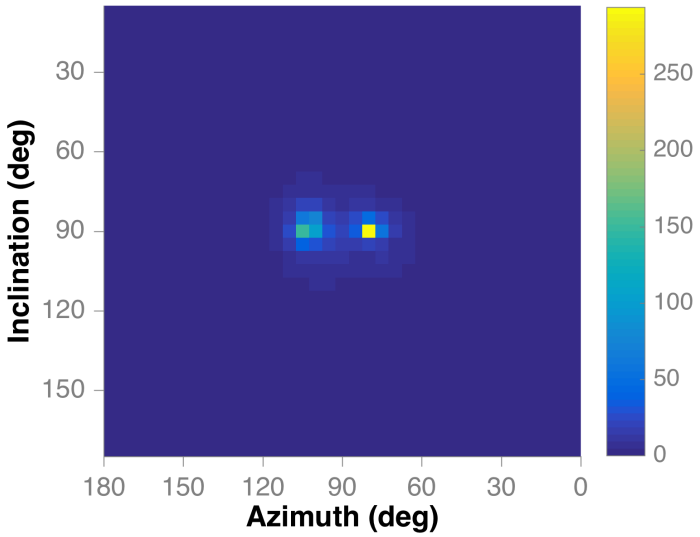

Figure 3.7: Image reconstructed using 1×10^7 iterations

21.11 in the 1×10^7 iteration reconstruction, the standard deviation is estimated to be 22%. The 6.2% difference between the two image reconstructions falls below this value, making the differences in image reconstruction less significant than the statistical uncertainty of the measurement. For 1×10^4 iterations the maximum difference is 33% and for 1×10^5 iterations is 14%.

While 14% falls below the 22% estimated standard-deviation for the pixel, adding another 1×10^4 iterations at this stage can produce a large pixel change of about 5% (From Figure 3.6). At 4.8×10^5 iterations, the change from an additional 1×10^4 iterations will be only about 1%. A more definitive answer, as to when an acceptable number of iterations have been run, would likely be application driven to balance precision with computational time. However, for the purposes of this work, the criterion described above is sufficient for evaluation SOE and drawing conclusions from experiments.

The experiment using two gamma-ray sources was also examined under these parameters. The stopping condition found 3.0×10^5 iterations to be sufficient. It was compared to a

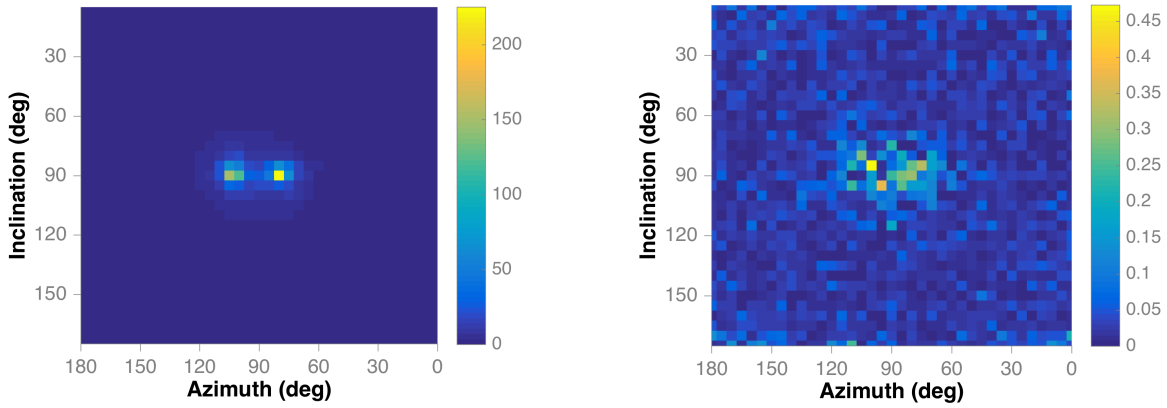

(a) (b)

Figure 3.8: Image reconstructed using 1×10^4 iterations (a) and the magnitudes of fractional differences between the images using 1×10^4 and 1×10^7 iterations (b).

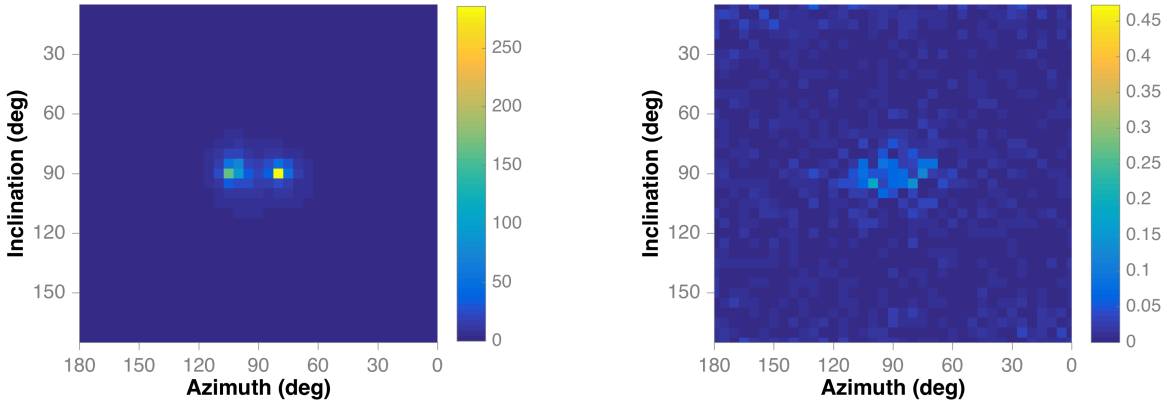

(a) (b)

Figure 3.9: Image reconstructed using 1×10^5 iterations (a) and the magnitudes of fractional differences between the images using 1×10^5 and 1×10^7 iterations (b).

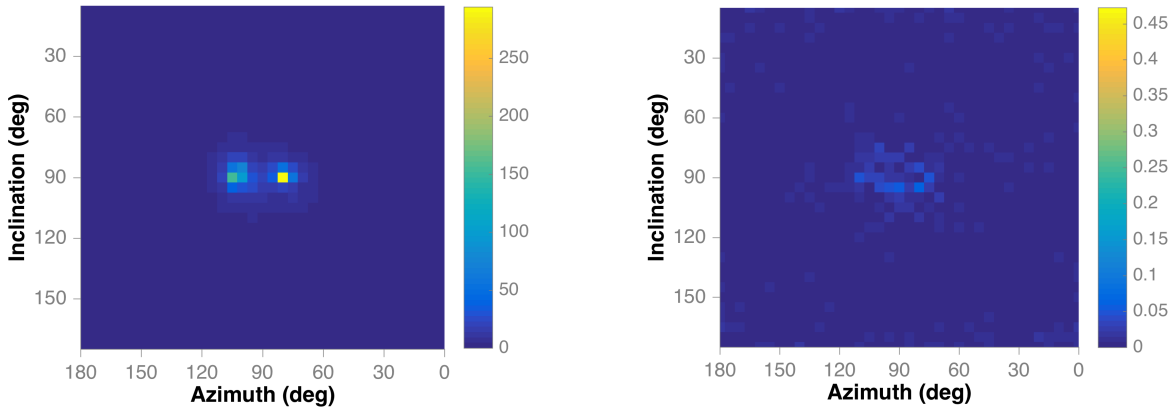

(a) (b)

Figure 3.10: Image reconstructed using 4.8×10^5 iterations (a) and the magnitudes of fractional differences between the images using 4.8×10^5 and 1×10^7 iterations (b).

reconstruction using 1×10^6 iterations. The maximum difference for a pixel was 6.3% in a pixel with an estimated standard deviation of 13.9%. This is consistent with the results seen for the neutron reconstructions.

3.4 Evaluating SOE for different source distributions

The SOE algorithm with the conditions outlined above, was applied to several test cases to determine effectiveness for different source distributions. An important conclusion to draw from this set of experiments is that the DPI and SOE can discriminate a point source, multiple point sources, and an extended source. The test cases included experiments with PuBe sources that emit neutrons and gamma rays. The goal of the experiments was to characterize the reconstructed images from three different source distributions using the reconstruction methods simple backprojection, SOE, and list-mode MLEM. The different distributions measured were a single point-source, two point-sources, and an extended line source.

3.4.1 Description of PuBe sources used for experiments

Two ^{239}PuBe sources were used for these experiments. The source MRC-PuBe-270 was used for all three test cases and emitted approximately 1.8×10^6 neutrons per second [104]. A second source, M-151, was used in the two point-source measurement and emitted about 1.3×10^6 neutrons per second [105].

3.4.2 Single point source

The PuBe was positioned 108 cm from the center of the DPI at the position (90°, 68.2°). A 10-minute measurement resulted in 21,373 total correlated neutron counts and 59,236 gamma-ray counts. The reconstructed neutron images using backprojection and SOE are shown in Figure 3.11. Both the backprojection and SOE reconstructions produced a hot-spot at the correct location. To directly compare image quality, the backprojection images were created using 5° pixels. To evaluate the quality of the reconstruction, the SNR, was calculated using the equation:

$$\text{SNR} = \frac{\mu_{ROI}}{\sigma}. \tag{3.21}$$

The pixel or pixels containing the true source location(s) are defined as the region-of-interest (ROI) with μ_{ROI} defined as the values of these pixels and σ defined as the standard deviation of all other pixels. For neutrons, the SNR was improved from 7.6 in the backprojection image to 91.0 in the SOE image. The same effect was seen in the gamma-ray images with the SNR improving from 6.0 using backprojection to 50.7 using SOE. Figure 3.12 shows a comparison of the gamma-ray images using both reconstruction methods.

The SOE gamma-ray image has more artifacts surrounding the hot-spot than the neutron image does, which is caused by environmental background. The noise appears as a course grid of relative hot and cold spots. The hot-spots likely represent areas of higher detection

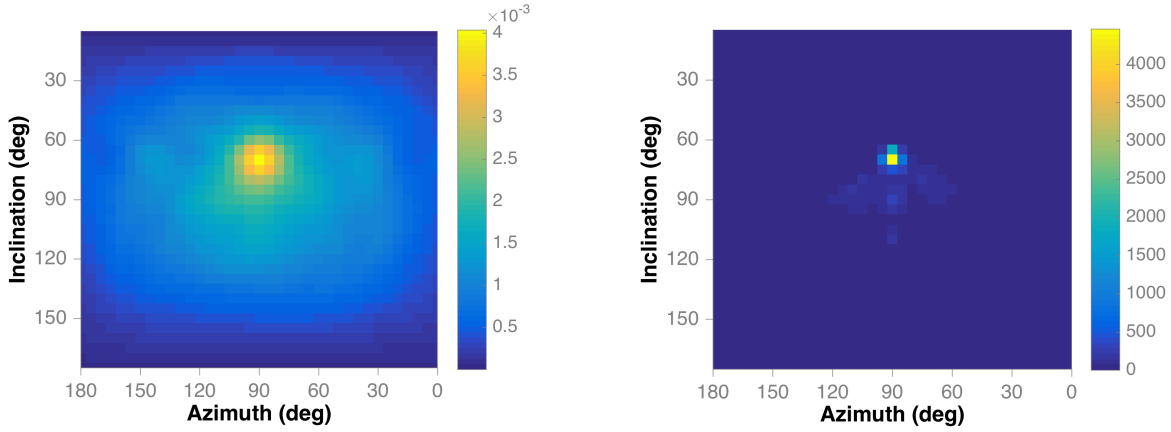

(a) (b)

Figure 3.11: The backprojection reconstruction (a) is compared to the SOE reconstruction (b) for neutrons from a PuBe point source. The hot-spot is successfully reconstructed in both images, but the SNR is much improved with the SOE reconstruction.

efficiency compared to the cold spots. The backprojection cones used for the SOE reconstructions were not adjusted for differences in spatial efficiency. Polack shows examples of DPI spatial efficiency maps for neutrons and gamma rays created using Monte Carlo simulation in [39]. The gamma-ray maps presented for several energies show spatial variation at magnitudes sufficient to create hot and cold spots in the environmental background. The gamma-ray images in the following sections display similar noise characteristics.

3.4.3 Two point-sources

To evaluate the ability of SOE to between two point-sources, both PuBe sources, described in Section 3.4.1, were placed on the same plane spaced 33 cm apart. Both were 109 cm from the center of the DPI. The angular locations of the two sources were (99.5°, 68.2°) for MRC-PuBe-270 and (80.5°, 68.2°) for M-151. This configuration was measured for 10 minutes, which produced 35,572 neutron counts and 99,457 gamma-ray counts. A comparison of the backprojection and SOE images is shown in Figure 3.13 for neutrons and

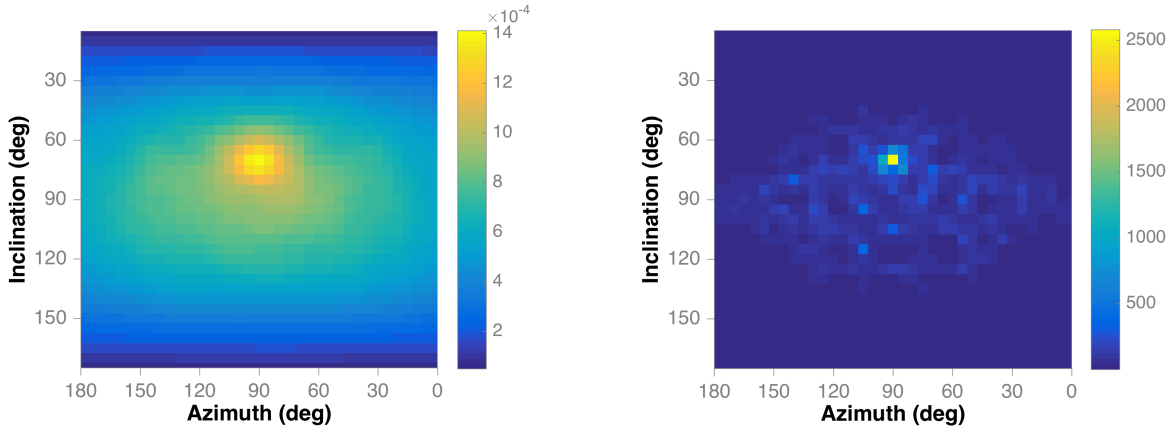

(a) (b)

Figure 3.12: The backprojection reconstruction (a) is compared to the SOE reconstruction (b) for gamma rays from a PuBe point source. The hot-spot is successfully reconstructed in both images, but the SNR is much improved with the SOE reconstruction.

Figure 3.14 for gamma rays.

For both particle types, the SOE algorithm reconstructed two distinct hot-spots in the images. This case clearly shows the advantage offered by SOE reconstruction compared to backprojection. The backprojection images reconstruct a hot-spot that appears as a single extended source. The neutron SNR improved from 11.2 to 108.1 and the gamma-ray SNR improved from 10.2 to 40.3.

3.4.4 Extended source

To create a source that would subtend multiple pixels, the PuBe was placed on a stage that moved from side-to-side azimuthally at a constant velocity throughout the measurement. The total length of the stage was 100 cm. Figure 3.15 shows the experiment setup. A 10-minute measurement produced 19,702 neutron counts and 58,126 gamma-ray counts. The center of the stage was located at (90°, 70°) and subtended a total of 53.1°. The backprojection images for neutrons (Figure 3.16) and gamma rays (Figure 3.18), both appear

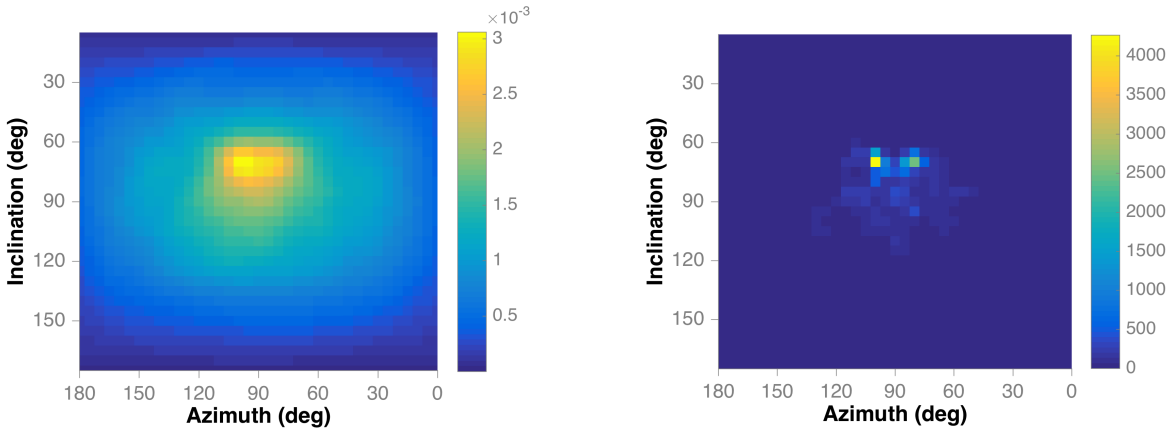

(a) (b)

Figure 3.13: The backprojection reconstruction (a) is compared to the SOE reconstruction (b) for neutrons from two PuBe point sources. The backprojection image appears to be one extended source while the SOE reconstruction shows two distinct hot-spots.

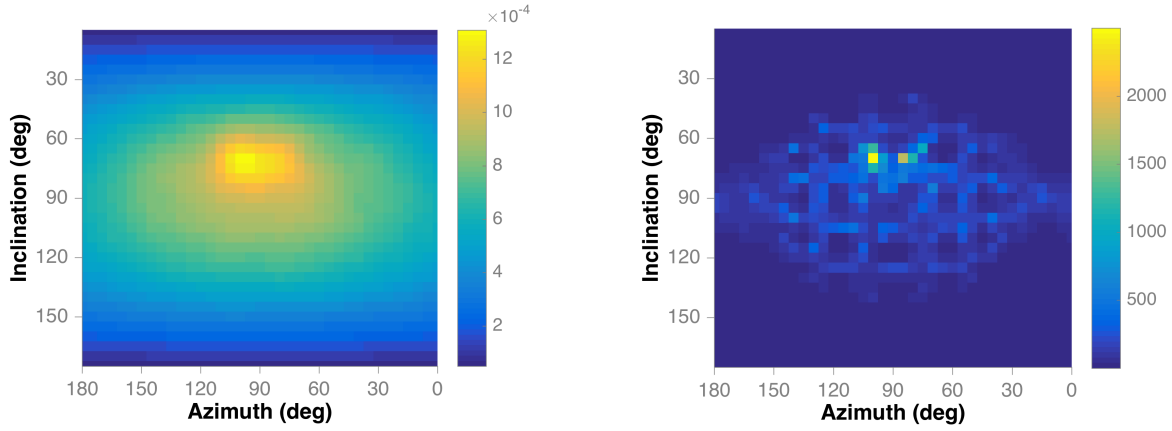

(a) (b)

Figure 3.14: The backprojection reconstruction (a) is compared to the SOE reconstruction (b) for gamma rays from two PuBe point sources. The backprojection image appears to be one extended source while the SOE reconstruction shows two distinct hot-spots.

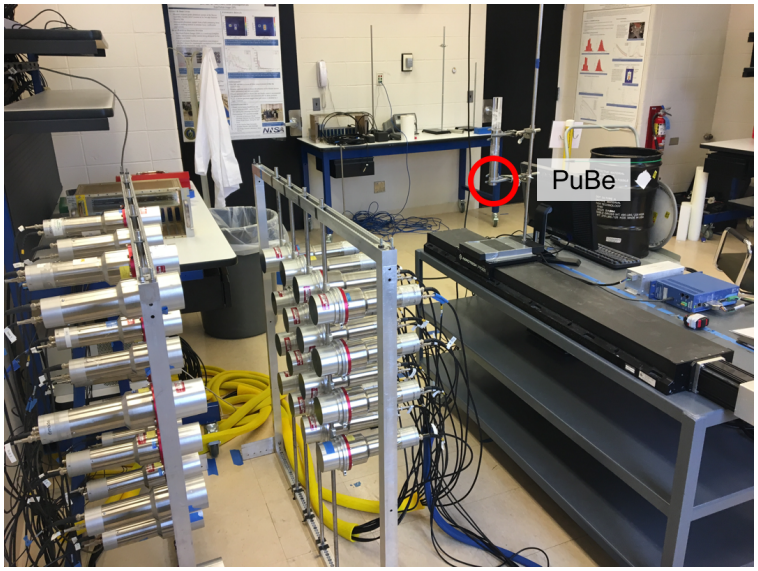

Figure 3.15: Setup showing the moving stage to create an extended source. The red circle highlights the PuBe source which moved back-and-forth along the stage at a constant velocity.

as an extended source. As described in Section 3.4.3, two point sources will also appear as an extended source when reconstructed using backprojection.

The SOE reconstruction for neutrons is compared to the backprojection in Figure 3.16. The image does not reconstruct a good representation of the source, which should appear as a continuous line. Instead, it appears that local maxima along the source have been created by the SOE reconstruction, which obscures the continuous nature of the source.

The local maxima in the source are likely caused by a poor mixing of image states in the Markov chain. To encourage more image states to be explored in the chain, the acceptance probability for a new image state, given in Equation (3.11), can be increased. A helpful way to conceptualization the effects for different acceptance probabilities, is to examine the extreme cases. In one case all moves are accepted and in the other where no moves are accepted. For the former with all moves accepted, each image state will be sampled in proportion to the backprojection image with no preference being given to locations with a larger number of origins. This is known as a Gibbs sampler and will simply reproduce the

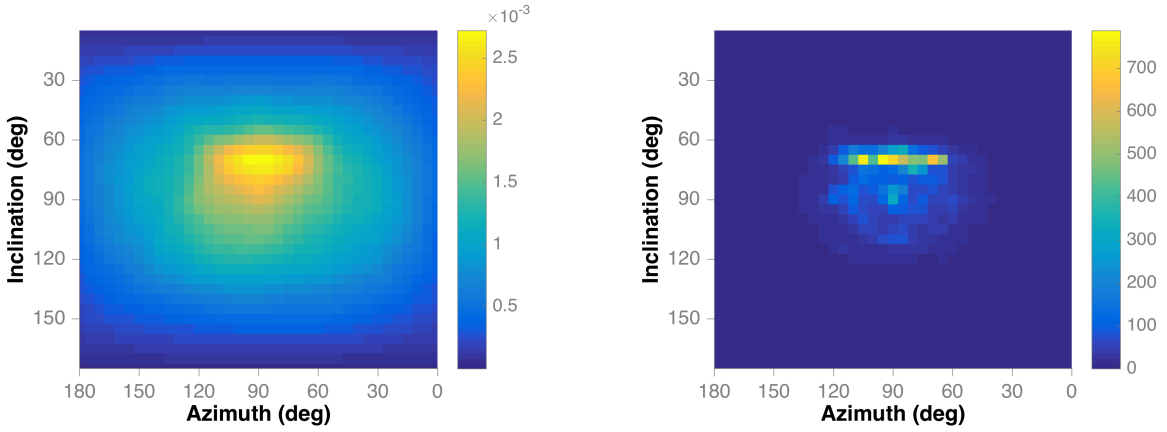

(a) (b)

Figure 3.16: The backprojection reconstruction (a) is compared to the SOE reconstruction (b) for neutrons from an extended PuBe source. The backprojection appears as an extended source but the SOE reconstruction appears discontinuous.

backprojection reconstruction. For the latter case in which no moves are accepted, the first sampled image state Y_0 will be the same as the resulting reconstruction.

To test a modified acceptance probability, Equation (3.11) was modified to include a factor, x that can increase or decrease the probability

$$A(Y_s \rightarrow Y_{s+1}) = \min\left(1, x\frac{n_{k,s+1}}{n_{k,s}}\right) . \tag{3.22}$$

With x set to 1.01 and 1.05, the resulting SOE reconstructions in Figure 3.17, appeared as a more continuous line source. The SNR remained at 226 for $x = 1.01$ and decreased to 142 for $x = 1.05$.

The measured gamma rays were reconstructed using both $x = 1.0$ and $x = 1.01$ for the acceptance probability. Figure 3.19 shows a comparison of the results. Both images show an over-weighting of the ends of the source compared to the center. A possible explanation for this feature is that gamma rays detected by the DPI have a spatially-dependent efficiency that is more non-uniform than for neutrons. This idea is supported by efficiency maps for the DPI

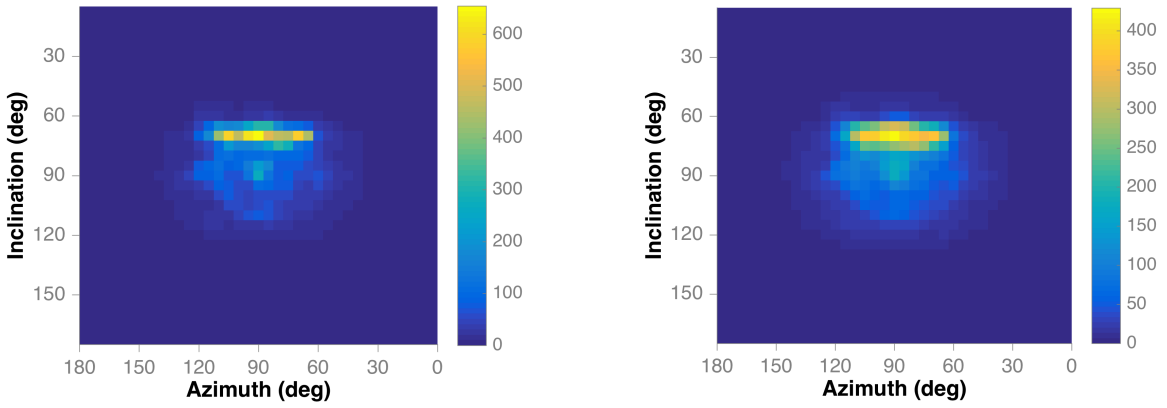

(a) (b)

Figure 3.17: A comparison of reconstructed images for an extended neutron source with increased acceptance probabilities using $x = 1.01$ (a) and $x = 1.05$ (b).

presented in [39]. The next section will examine if this feature seen in the reconstruction is due to the SOE algorithm, or to other factors, by comparing it to a list-mode MLEM reconstruction.

While increasing the acceptance probability improves reconstruction of an extended source, it is important to ensure that it does not cause the two point-source case to appear as an extended source.

Point sources with increased acceptance probability

The neutron images for the PuBe point source and two PuBe point-sources were reprocessed using Equation (3.22) with $x = 1.01$. Both images, shown in Figure 3.20, reconstruct as expected, to a point source and two point-sources. In both cases the SNR decreased from the case where $x = 1.0$. In the case of the point source, the original SNR was 91.0 and decreased to 72.9. For two point-sources, the SNR is decreased from 108.1 to 92.0.

Modifying the acceptance probability, which alters the underlying Bayesian prior, is an area of this work that demands future study. Several different models for priors are given

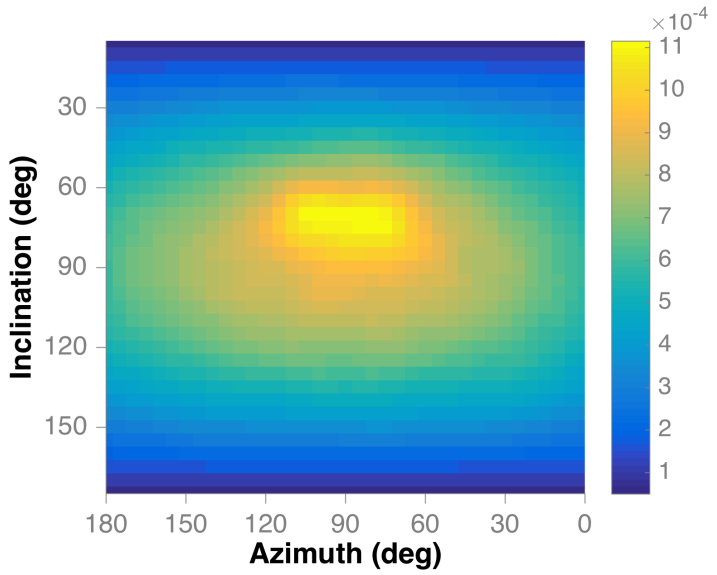

Figure 3.18: A gamma-ray backprojection image of the extended PuBe source.

by Sitek in [106] for use in MCMC algorithms. As seen by the above results, having some knowledge of the source distribution can lead to a choice of prior that provides a better reconstruction. Another parameter affecting the acceptance probability, that is not accounted for in this algorithm, is the spatially dependent detection efficiency. This is difficult to quantify and requires a complex set of Monte Carlo simulations to create an energy-dependent system-response matrix. This system response for the DPI was investigated by Polack in [39]. While including these quantities as part of the prior may improve SOE reconstruction, it removes some generality from the SOE algorithm, which as presented here is based only on scattering kinematics of the system. As such, a new energy dependent system matrix would be required for a different system configuration. The presented results have shown that spatial system response is consistent enough to provide a faithful reconstruction for sources of interest.

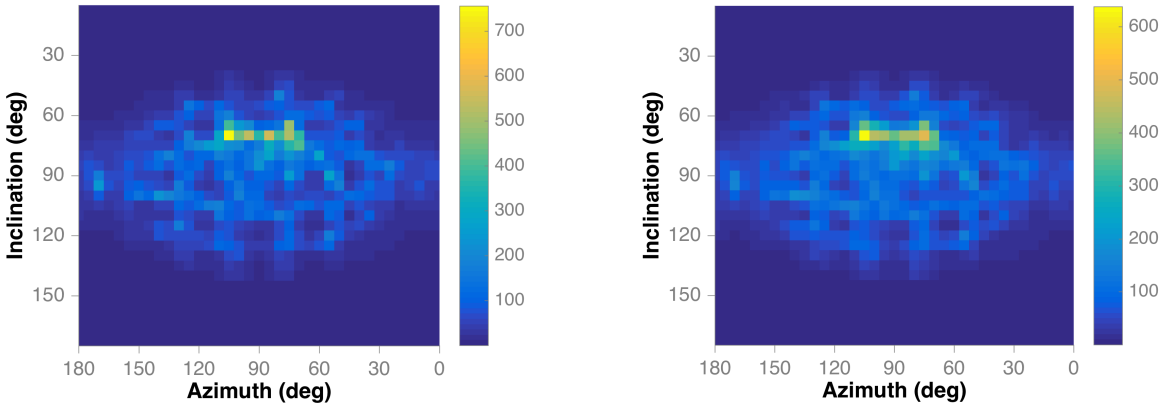

(a) (b)

Figure 3.19: A comparison of reconstructed SOE images for an extended gamma-ray source with acceptance probabilities using $x = 1.0$ (a) and $x = 1.01$ (b).

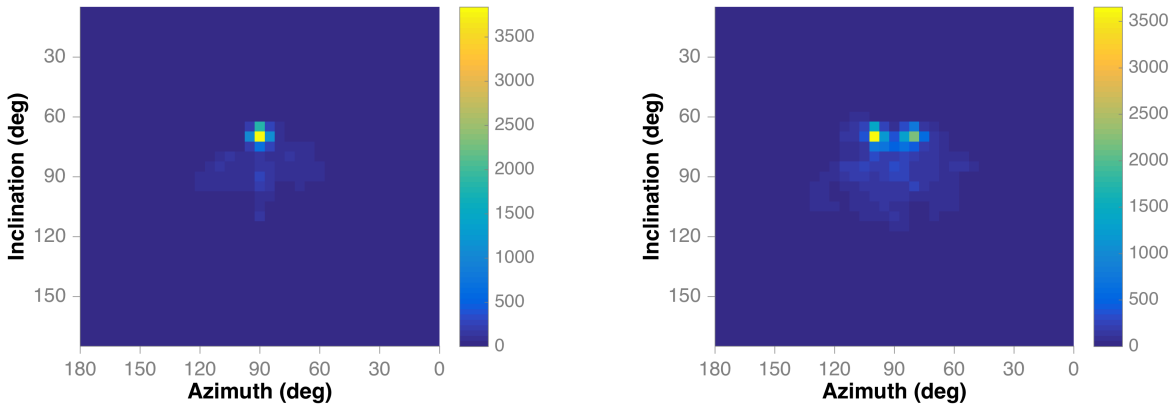

(a) (b)

Figure 3.20: Neutron images of a point source (a) and two point-sources (b) reconstructed with SOE using an increased acceptance probability with $x = 1.01$. Both sources still appear as they should despite the increased acceptance probability.

3.5 Comparison of SOE and MLEM image quality

The advantages of SOE reconstruction compared to other methods such as MLEM were outlined in Section 3.1. In this section the image quality of SOE and list-mode MLEM reconstructions are compared. A fair comparison of the methods is admittedly difficult due to the required choice of parameters for each method. For example, the choice of a stopping condition for the list-mode MLEM has a large impact on image quality. The system response matrix, used for both methods is the same. It is composed of the backprojection cones created using the method described in Sections 3.3 and 3.3.1.

For comparison, the list-mode MLEM algorithm was run multiple times with different numbers of iterations [48]. The SNR was calculated for each reconstruction, which allowed for a comparison to the SNR calculated from the SOE reconstructions.

3.5.1 Single point source

The SNR for point-source neutrons peaked at 100 iterations of MLEM. Figure 3.21 shows the SNR as a function of iteration number. The SNR for the SOE reconstructions using $x = 1.0$ and $x = 1.01$ are overlaid on the plot. With $x = 1.0$ the SOE reconstruction SNR outperforms the best MLEM SNR, 91.0 to 78.5. When $x = 1.01$ is used, the SOE SNR decreases to 72.9 which is similar to the MLEM solutions for 50 and 200 iterations.

This result shows that the SOE algorithm reconstructs a SNR that is superior to, or on par with the best possible MLEM SNR results. Figure 3.22 shows the MLEM images reconstructed using 50 and 100 iterations, which represent the solution closest to matching the SOE with $x = 1.01$ and the best SNR produced respectively.

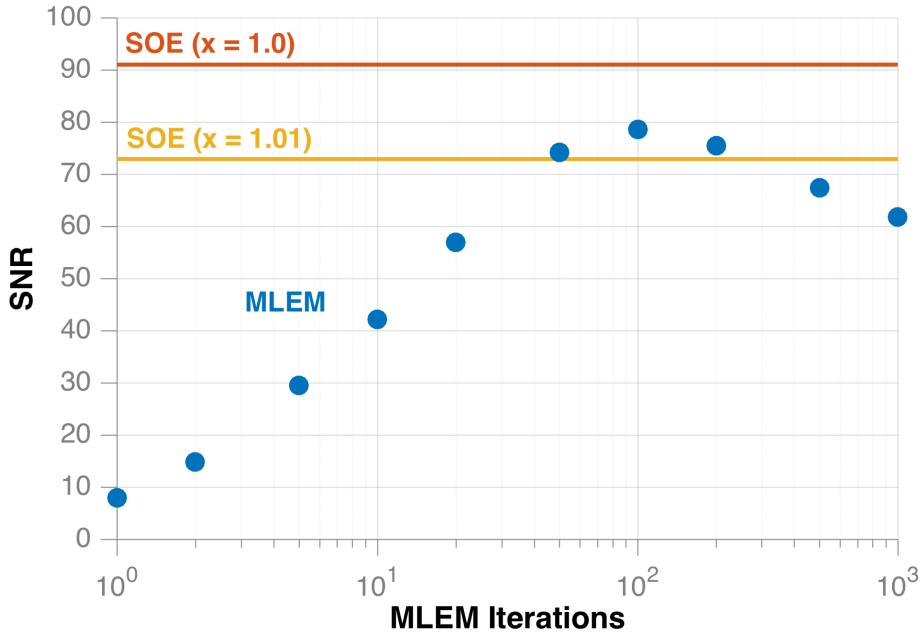

Figure 3.21: A comparison of SNRs, for a neutron point source, as a function of MLEM iterations compared to SOE solutions for $x = 1.0$ and $x = 1.01$

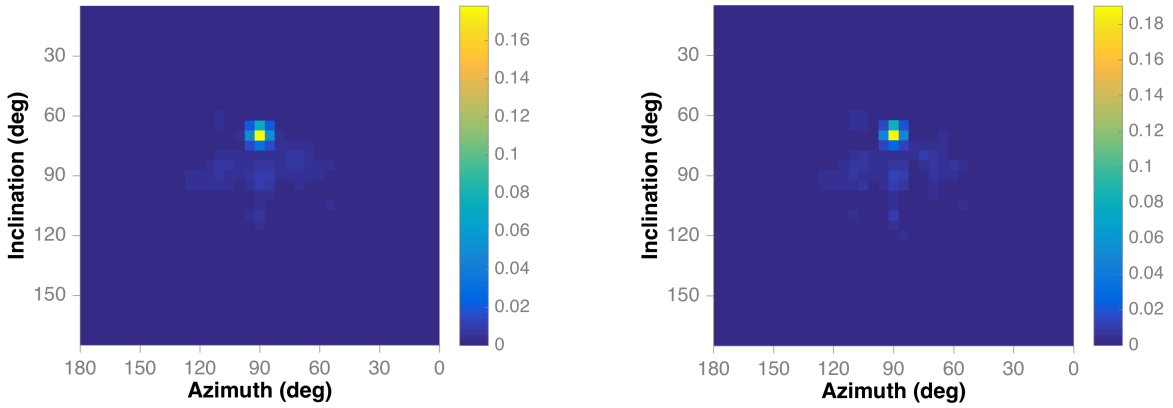

(a) (b)

Figure 3.22: MLEM reconstructions for a neutron point source using 50 (a) and 100 (b) iterations.

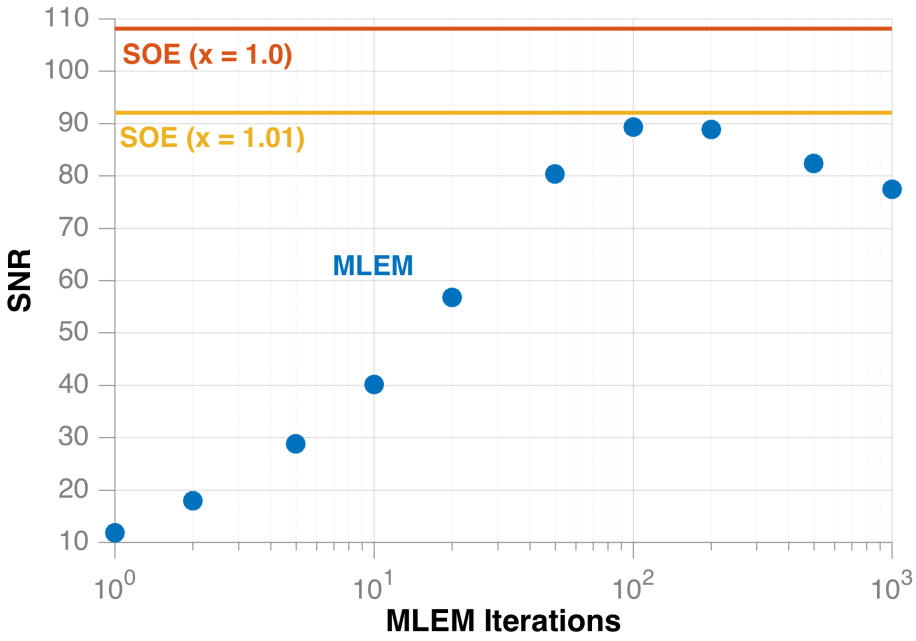

Figure 3.23: A comparison of SNRs, for neutrons from two point-sources, as a function of MLEM iterations compared to SOE solutions for $x = 1.0$ and $x = 1.01$

3.5.2 Two point sources

With two-point sources present, the MLEM SNR also peaked at 100 iterations with a value of 89.3. For both SOE cases, the SNR had values of 108.1 and 92.0 for $x = 1.0$ and $x = 1.01$ respectively. In this case, both SOE SNRs are superior to the best MLEM SNR.

3.5.3 Extended source

For the extended neutron source, the SOE reconstructions using $x = 1.0$ and $x = 1.01$ both produced a SNR of 226. This was the same SNR produced by the best MLEM solution at 100 iterations. Figure 3.24 shows the SNRs for SOE and MLEM reconstructions. Figure 3.25 shows the MLEM solution at 100 iterations, which also produced a SNR of 226.

A question raised in Section 3.4.4 was whether the MLEM solution would also overweight the ends of the extended source, as seen in the SOE reconstruction (Figure 3.19). Figure

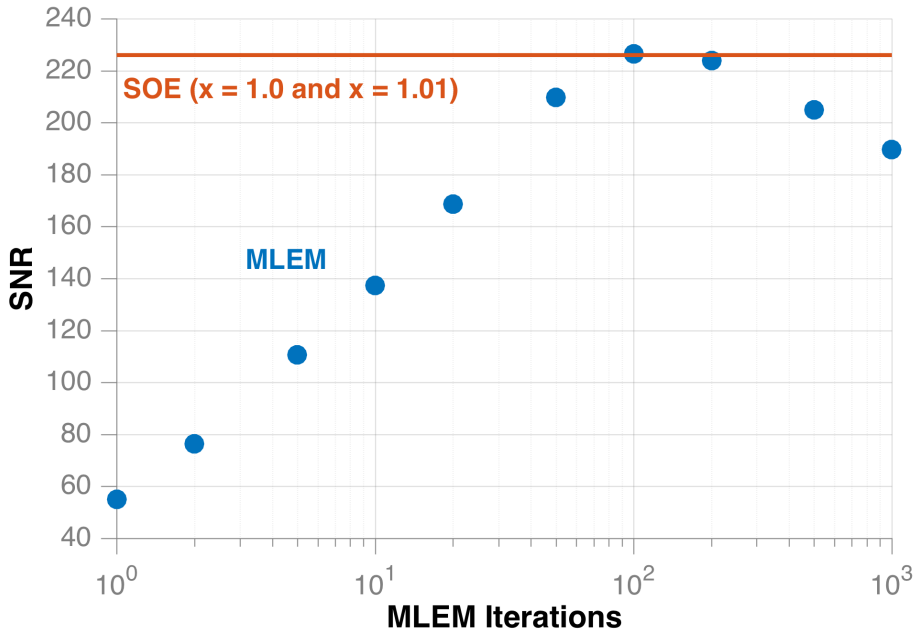

Figure 3.24: A comparison of SNRs, for an extended neutron source, as a function of MLEM iterations compared to SOE solutions for $x = 1.0$ and $x = 1.01$

3.26 shows the MLEM solution that produced the best SNR, using 50 iterations. In this reconstruction, the ends of the source are also over-weighted compared to the center. This result suggests that the cause of over-weighting is in the definition of the system matrix, rather than a result of a particular imaging method.

3.6 Image reconstruction time

The SOE reconstruction time was not a focus of this work. For reference, the images in Section 3.4 had reconstruction times ranging from 5 hours (21,373 neutron events; 380,000 iterations; Figure 3.11(b)) to 18 hours (99,457 gamma-ray events; 260,000 iterations; Figure 3.14) depending on the number of events and iterations. The stopping condition presented in Section 3.3.3 is conservative, and a higher threshold could be chosen to greatly reduce computation time without sacrificing much image quality.

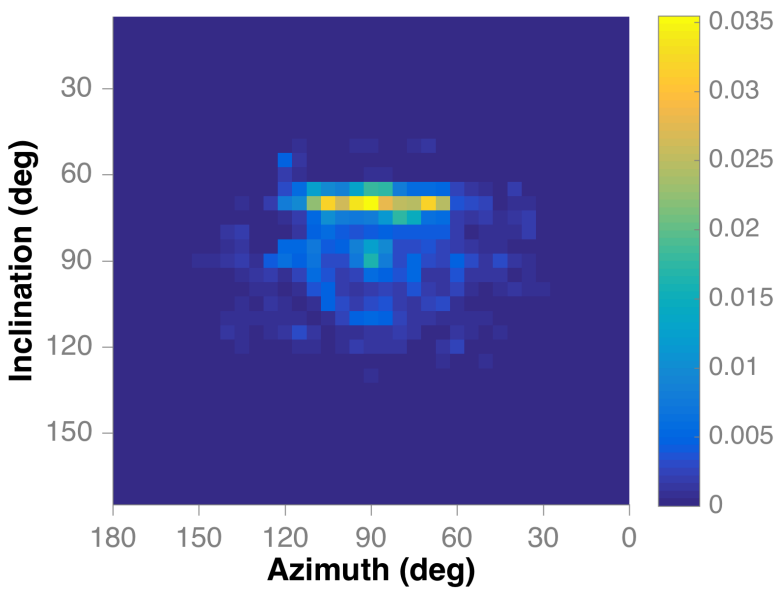

Figure 3.25: MLEM reconstruction of an extended neutron source using 100 iterations

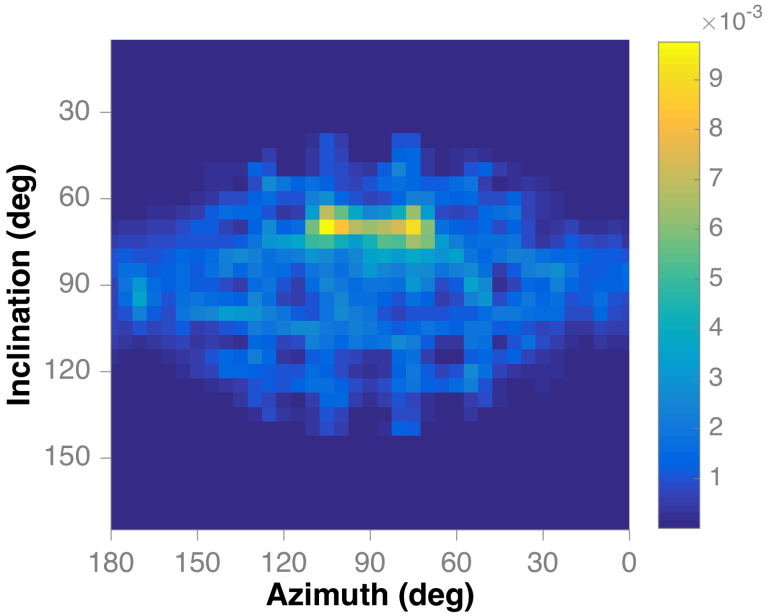

Figure 3.26: MLEM reconstruction of an extended gamma-ray source using 50 iterations

The algorithm was run using MATLAB on a 3.5 GHz, 6-core processor. No parallelization was pursued. However, past work that has examined SOE, for applications to a Compton camera, found that running a version in which all moves throughout a single iteration are performed in parallel on graphical processing units, has comparable speed to MLEM [52]. To further improve on speed if necessary, the iterations themselves could be paralyzed without losing the integrity of the supporting MCMC theory. To accomplish this, multiple chains could be run using different seeds on a machine with multiple cores or a computing cluster [107]. As long as each seed accounted properly for the burn-in period, the seeds could be averaged together for a final solution that would provide the same result as running a single chain.

3.7 Conclusions

This chapter examined the application of SOE to the DPI for reconstruction of neutron and gamma-ray images. Currently, list-mode MLEM represents the standard in advanced imaging methods but has the drawback of heavy reliance on a stopping condition, while SOE reaches a stochastic steady-state solution as the number of iterations goes to infinity. To compare the two methods, the SOE algorithm was optimized by choosing parameters for image reconstruction such as the burn-in period and the number of iterations required to reach a stochastic steady-state. Three experiments were performed using PuBe to create a point source, two point sources, and an extended source. These source configurations were used to evaluate the SOE reconstruction and make direct comparisons to the MLEM solutions using SNR.

The burn-in period of the Markov chain was determined by examining when the fraction of origins moved for each iteration became relatively constant. However, if the number of iterations run is on the order of 10^4, the burn-in period becomes insignificant in the final

solution. To determine when a stochastic steady-state has been reached, the maximum percentage change among all pixels from one solution to another must fall below 1%. The difference between solutions is calculated after every 10,000 iterations.

The test cases showed that SOE could successfully reconstruct a point source and two points-sources for both neutrons and gamma rays. However, to construct an extended source, the acceptance probability for origins had to be increased by 1%. This encouraged better mixing of the origins throughout the image space and for neutrons, displayed a continuous line as expected. The gamma-ray reconstruction for the extended source showed an over-weighting of the ends of the source compared to the middle. It was determined though that this was a systematic issue and not caused by SOE, because the MLEM result displayed the same characteristics.

In a comparison with the maximum possible SNR from MLEM reconstruction, the SNR from the SOE reconstruction was similar or larger in almost all cases. This demonstrated that SOE produces images with comparable or higher quality to MLEM, while removing a heavy dependence on the need for a stopping condition.

This chapter focused on implementation and characterization of the SOE algorithm for the DPI. The next chapter will examine ways in which the method can be extended to aid in detection of SNM. This includes isolating energy spectra from an image with multiple sources and examining how neutron and gamma-ray events can be used together in image reconstruction.

Chapter 4

Implementation of spectral localization with the SOE algorithm

4.1 Motivation for adding spectral isolation to SOE

The work presented thus far has described the development of the DPI and shown that it has the ability to image neutrons and gamma rays. The SOE algorithm was also presented as a method for image reconstruction that improves on aspects of existing techniques. Experimental data showed that SOE can faithfully reconstruct the source distributions for point sources and extended sources. While the spatial localization of sources offers an improvement on simple radiation counting techniques, further extension into localizing other information about the source offers the best solutions to non-proliferation applications.

A well-established technique for source identification is through examination of energy spectra for gamma rays and neutrons. The DPI offers spectroscopic capabilities, as described in Section 2.3.2. However, if multiple sources are present, the aggregate spectrum produced does not contain enough information to delineate which spectrum was emitted by which source. In a scenario where one source is much stronger than others present, its energy spectra may mask those of weaker sources. The literature cited in Chapter 3 dealt with applications where the energy of detected particles was not of interest. For medical imaging this is because radioactive tracers with a known energy are used and for in-situ proton-

therapy range-verification, only the location of detected gamma rays determines the range of protons, not energy of the emitted gamma rays. For application to non-proliferation missions, identification of source location and emitted energy spectra are valuable. In security applications, spectra isolation may help detect SNM masked by NORM. In safeguards or treaty-verification scenarios, the spectra can be used to determine the proper use of declared materials or detect undeclared materials.

A successful spectral isolation technique reliant on MLEM has been demonstrated using the DPI [39]. A drawback to this technique is that it relies on the pre-computation of a system response matrix through Monte Carlo simulation. The response matrix requires a computation time on the order of weeks despite using hundreds on nodes on a high performance computing cluster. The spectral isolation results also change depending on the number of iterations performed. The prior chapter showed that SOE can eliminate the heavy dependence on a stopping condition by producing similar image quality to the ideal MLEM reconstruction, without a large dependence on the number of iterations performed. As presented in [52] and [51], the SOE reconstruction method does not include a method for spectral isolation. In this chapter, an extension to the SOE method is made to include a mechanism for spectral isolation.

The performance of this method was then evaluated for isolating gamma-ray and neutron spectra. This technique was then applied to a measurement of three neutron and gamma-ray emitting sources including WGPu. The following sections are lightly edited excerpts from the paper [55], describing spectrum isolation with SOE and discrimination of category-I SNM. It should be noted that the results in this paper were obtained before the SOE reconstruction parameters for burn-in and number of total iterations were studied. However, the results and conclusions shown in this paper are not changed as the parameters used for reconstruction were similar to the optimized ones.

4.2 Method used for spectral isolation

For SOE spectral isolation, a histogram structure is created to record the number of origins that correspond to a particular pixel and energy bin. The total number of separate histogram bins corresponds to the number of pixels multiplied by the number of energy bins. The histograms are populated according to the numbers of origins contained within a particular pixel and energy bin for each image state.

After a sufficient number of iterations is performed to reach a stochastic steady-state for all histograms, various solutions can be created from the distributions that estimate the actual source location(s) and spectra. For example, an image for each energy bin can be created by taking the mean or the mode of the distribution for each pixel. These solutions can then be summed to form an image that includes all energies. An energy spectrum for each pixel is formed by using the mode of the distribution for each energy bin. The distributions are fit with a first-order Gaussian distribution using the built-in MATLAB function fit [108]. If the fitting fails or produces a fit with a negative mode, which occasionally occurs for bins with low numbers of origins, the value in the isolated spectrum is set to zero. A version of the MATLAB function used to perform image reconstruction with spectrum isolation is found in Appendix B.

4.3 Evaluation of spectral isolation

Three experiments were performed with the DPI to show the ability of the described SOE algorithm to isolate energy spectra when multiple sources are present. An experiment using ^{22}Na and ^{137}Cs showed the capabilities of gamma-ray spectrum isolation. An experiment using ^{252}Cf and PuBe was performed to show neutron spectrum isolation. Finally, an experiment with WGPu, ^{252}Cf, and AmBe demonstrated the ability to localize a neutron and gamma-ray SNM spectra in an environment with multiple sources emitting neutron and

gamma rays.

4.3.1 Gamma-ray spectral isolation

Two well-known gamma-ray sources were measured with the DPI to evaluate the quality of SOE reconstruction for distinct energy peaks. The setup, results, and a discussion of the experiment follow.

Experimental setup

^{22}Na and ^{137}Cs point sources were measured simultaneously with the DPI for 20 minutes. The ^{22}Na had angular coordinates of (116° azimuthal, 72° inclination) and was located 543 cm from the center of the DPI. The coordinate system was defined such that a source centered directly in front of the DPI has angular coordinates (90°, 90°). The ^{137}Cs was located at (57°, 104°) at a distance of 306 cm from the DPI. The experimental setup is shown in Figure 4.1. Activities of the sources were 3.27 MBq and 3.24 MBq for the ^{22}Na and ^{137}Cs respectively. The ^{22}Na signature consists of two gamma-ray energies at 0.511 MeV and 1.275 MeV. The ^{137}Cs gamma-ray emission of interest is at 0.662 MeV.

Results

In this experiment a total of 54,541 gamma-ray events were detected. An energy bin width of 10 keV and 1×10^6 iterations provided sufficient statistics for both isolated energy spectra. The histogram for each energy bin/pixel used a bin width of one origin.

The reconstructed image shown in Figure 4.2 has two clearly defined hot-spots. The ^{22}Na reconstructed to the pixel (115°, 75°) and the ^{137}Cs created a hot-spot occupying the pixels (55°, 105°) and (60°, 105°). Table 4.1 compares the angular location of the reconstructed hot-spot with the expected angular location of the hot-spot. To identify the expected location for the reconstructed hot-spot, the actual angular locations of the sources were rounded to

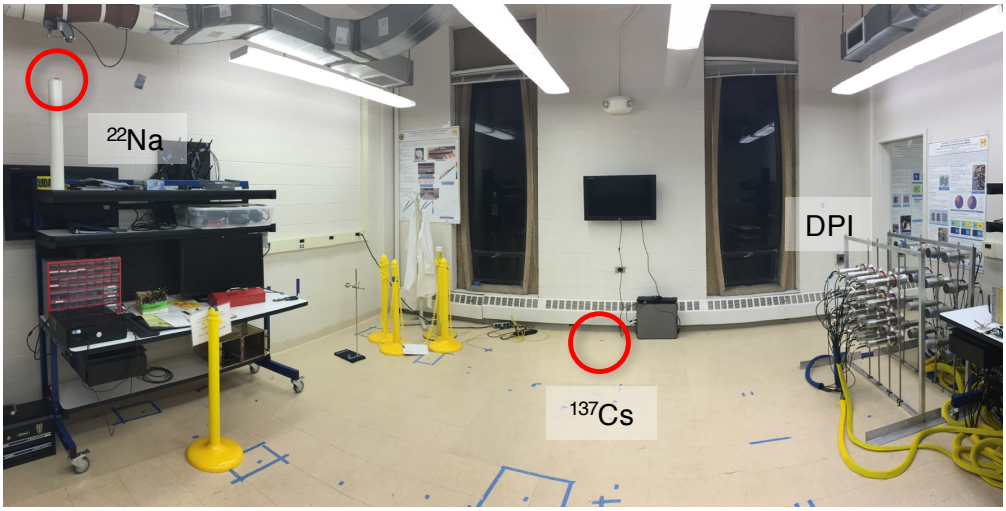

Figure 4.1: This photo shows the experimental setup for a measurement of ^{22}Na and ^{137}Cs. The sources positions are highlighted by red circles. The ^{22}Na was located at an angular coordinate of (116°, 72°), 543 cm from the DPI and the ^{137}Cs was located at (57°, 104°) at a distance of 306 cm. The DPI is seen at the right of the photo.

bin centers of the nearest pixel. The image was created using the mean value for each pixel over all image states. Because the ^{137}Cs was located near the edge of a pixel, contribution is seen in two pixels and makes the intensity appear lower than if the contribution were located in a single pixel such as for the ^{22}Na.

The isolated spectra shown in Figure 4.3 were created from a 3×3-pixel region surrounding the most intense pixel in the hot-spots. The nine pixel regions ensured that the full signal was captured when there was contribution in multiple pixels. For comparison, the reconstructed spectrum from all recorded events is shown on the same plot. In the total spectrum, the resolution of the 0.511-MeV, 0.662-MeV, and 1.275-MeV peaks were 10.6%, 9.4%, and 12.0% respectively. These resolutions were lower than the expected 15% for the 0.511-MeV peak and 13% for the 0.622-MeV peak. The resolution was greater than the expected 9% for the 1.275-MeV peak.

For the 3×3 ^{22}Na region (centered on pixel (115°, 75°)), the histogram corresponding to the energy bin 0.51 MeV is shown in Figure 4.4. The mode of the fitted distribution is

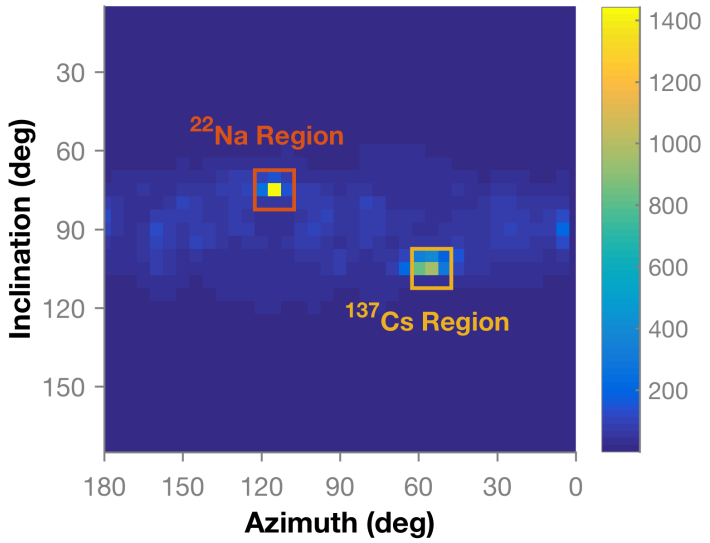

Figure 4.2: The reconstructed gamma-ray image shows two hot-spots which locate the ^{22}Na and ^{137}Cs sources. The ^{22}Na is located by the more intense pixel at top left. The ^{137}Cs hot-spot, in the lower right, appears less intense because it is split between two adjacent pixels.

105.5 origins, which is then used as the number of counts in the 0.51-MeV energy bin for the spectrum. For the 1.27-MeV energy bin, the mode of the fit, shown in Figure 4.4, was 30.5 origins. The uncertainty for each bin is given by the standard error of the fitted distribution. The resolution of the 0.511-MeV peak in the isolated spectrum was 11.1% and was 7.9% for the 1.275-MeV peak. The following section explains why the reconstructed images were created using mean values and the isolated spectra were created using the mode of the fitted histograms.

The histograms corresponding to the 0.66-MeV energy bin of the ^{137}Cs region is shown in Figure 4.5. For the 0.66-MeV energy bin the mode of the fit was 159.7 origins. The resolution of the isolated spectrum at 0.662 MeV, 10.1%, was similar to that of the peak in the aggregate spectrum.

The isolated ^{22}Na spectrum shows the two expected peaks at 0.511 MeV and 1.275 MeV

Table 4.1: The expected angular locations of the ^{22}Na and ^{137}Cs are compared to the locations of the most intense pixel in the reconstructed hot-spots. The angular distance from the expected source location to the reconstructed source location is given. The image pixels had a 5° width.

	^{22}Na		**^{137}Cs**	
	Azimuth	**Inclination**	**Azimuth**	**Inclination**
Expected location	115°	70°	55°	105°
Reconstructed location	115°	75°	55°	105°
Absolute difference	0°	5°	0°	0°

and the isolated ^{137}Cs spectrum shows the expected peak at 0.662 MeV. However, there is some contamination in each spectrum from the other spectrum. For example, a small peak can be seen in the ^{22}Na spectrum at 0.662 MeV and a small peak can be seen in the ^{137}Cs spectrum at 0.511 MeV. Contamination from the 1.275-MeV ^{22}Na peak is not seen in the isolated ^{137}Cs spectrum.

Discussion

In this experiment, spectrum isolation was evaluated for two sources emitting distinct gamma-ray decays energies. For this experiment and the following ones, the reconstructed images were created by using the mean value of the distributions while the values in the isolated spectra were populated using the mode of the distribution. For many bins, the mean and mode are the same because the distribution is well fit by a Gaussian. However, in distributions with a lower mean and mode, the data does not form the entire Gaussian distribution. In these cases, the mode of the data will be a smaller value than the mean. Using the mean values for image reconstruction produced less artifacts and noise than the mode values in all three experiments. A possible cause of the noise are poor fits for bins with small value modes. Peaks in the isolated spectra should be unaffected by poor fitting

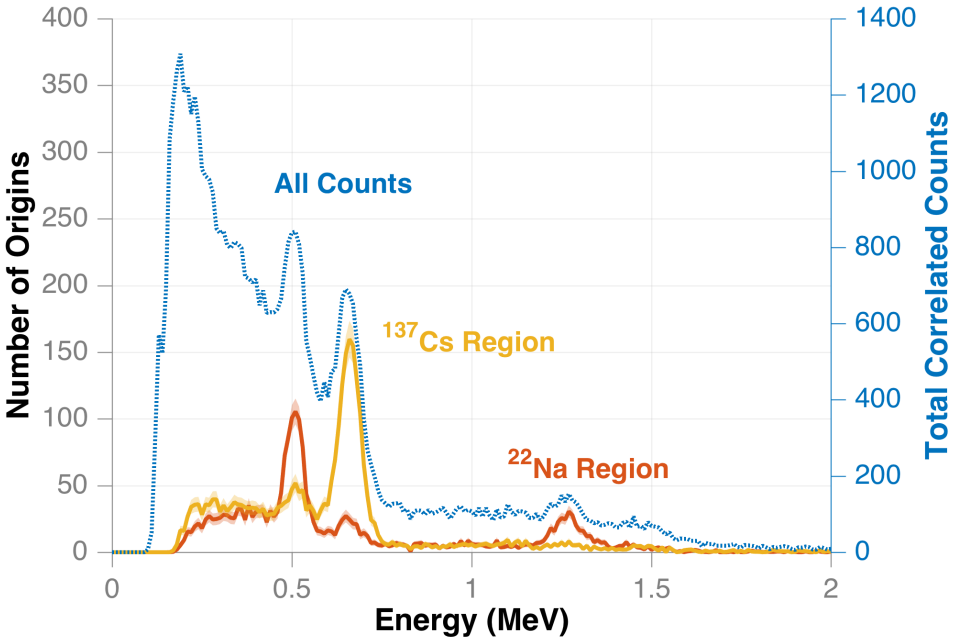

Figure 4.3: Two isolated spectra from the ^{22}Na and ^{137}Cs hot-spots are shown with the total measured spectrum. This figure shows that the total spectrum is the combination of a ^{22}Na and ^{137}Cs spectrum. The isolated spectra are plotted against the left axis while the total spectrum was plotted against the right axis. Each isolated spectrum was created from the 3×3-pixel region surrounding the brightest pixel in each hot-spot. The uncertainty is shown by the light shaded regions for the ^{22}Na and ^{137}Cs spectra although it is difficult to see because in most places it is not thicker than the line.

at low values because the peaks have large mode values.

The most intense peaks in ^{22}Na and ^{137}Cs were located at 0.511 MeV and 0.662 MeV respectively. The aggregate reconstructed spectrum from the measurement (Figure 4.3) showed that the DPI had sufficient resolution to resolve the two peaks. The measured resolution values were lower than expected based on the resolution functions for liquid and NaI(Tl) scintillators [72]. Uncertainty in the resolution of the liquid scintillators at low energies was likely the cause of the discrepancy. In [72], the lowest energy measured in the resolution function was about 250 keVee. The resolution function was extrapolated to lower values. Many of the measured events in the system had energy depositions in the liquid scintillators below 100 keVee. At these low energies, the extrapolated resolution function

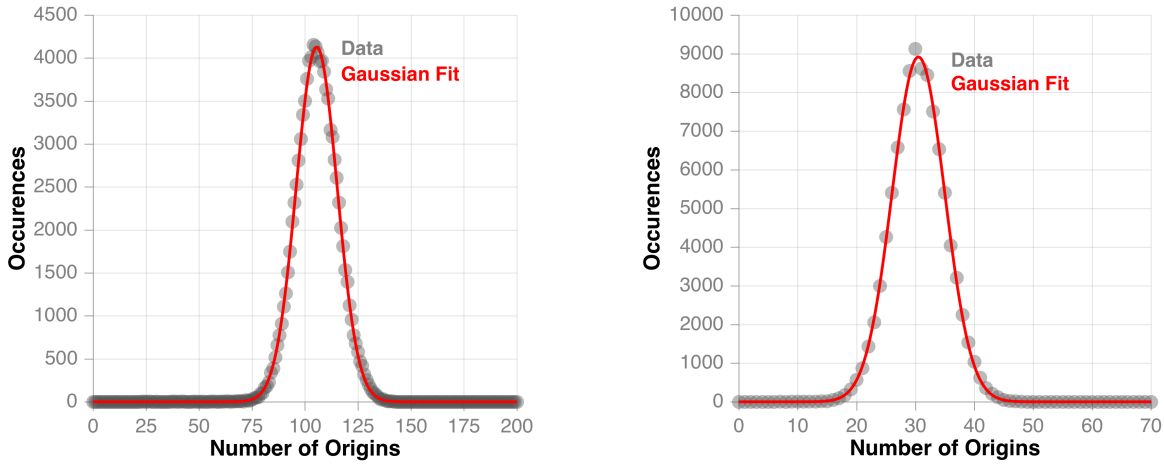

(a) (b)

Figure 4.4: Histograms from the 3×3-pixel ^{22}Na region for the 0.51-MeV (a) and 1.27-MeV (b) bins are fit well by a first order Gaussian. The histograms represent the number of occurrences for a specific number of origins from the 3×3 region from all 1×10^6 image states. The mode of the fit for the histogram from each energy bin is used to create the isolate spectrum with the standard deviation in each histogram representing the uncertainty.

likely has a large uncertainty.

The measured resolution in the aggregate spectrum was maintained in the isolated spectra. The resolution degraded in the isolated spectra for the 0.51-MeV and 0.662-MeV peaks by 0.5% and 0.6% respectively. These deviations are not believed to be significant but a more rigorous investigation including additional gamma-ray decay energies with higher statistics is warranted by the results from this experiment. For the 1.275-MeV peak the resolution was 12.0% in the aggregate spectrum but improved to 7.9% in the isolated spectrum. This difference is probably due to uncertainty in the calculated resolution in the aggregate spectrum. The peak was not much larger than the continuum. The resolution functions for the liquid and NaI(Tl) scintillators stipulate that resolution should be improved at higher energies. The 7.9% resolution calculated in the isolated spectrum is more in line with the expected 9% resolution.

The source localization was also good, with the most intense pixel in the ^{137}Cs hot-

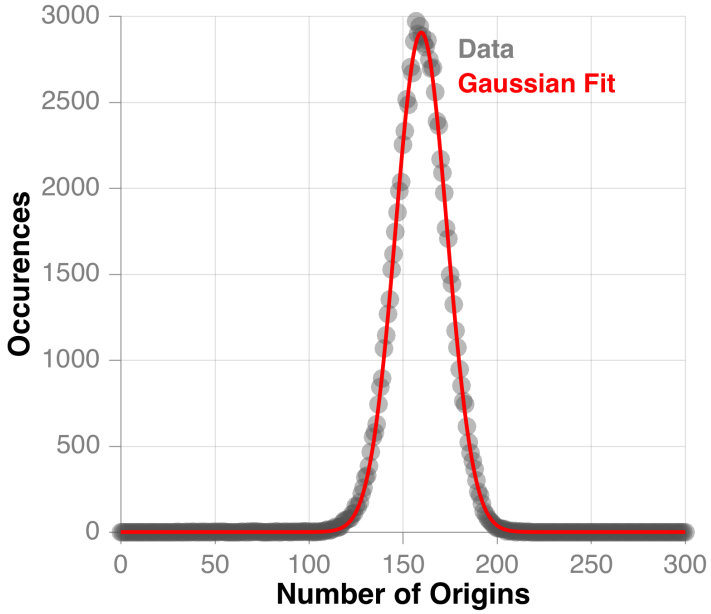

Figure 4.5: The histogram from the 3×3-pixel region surrounding the ^{137}Cs hot-spot for the 0.66-MeV energy bin was fit with a first order Gaussian. The mode of the fit was used for the 0.66-MeV bin in the isolated spectrum with the standard deviation of the fit representing the uncertainty.

spot reconstructing to the expected pixel. The most intense pixel in the ^{22}Na hot-spot reconstructed to the pixel directly below the expectation with a small contribution in the expected pixel. Because the simple backprojection image also has the most intense pixel in the ^{22}Na hot-spot in the same location, this suggests that the shift is attributable to other factors in the measurement, such as the uncertainty in the source positioning, and not the SOE algorithm.

While the energy resolution may suffer a small amount of degradation when isolated, the spatial resolution of the system was the cause for contamination of one spectrum into another. Small but statistically significant peaks are seen at 0.511 MeV in the ^{137}Cs spectrum and 0.662 MeV in the ^{22}Na spectrum (Figure 4.3). The contamination of events from the other source appearing in each isolated spectrum is because some of the cones defining possible source locations overlapped both actual source locations. The overlap allowed for

a single event to be sampled at either location and is attributable to the broadening of the cone, which represents the uncertainty of the events caused by system resolution. For a theoretical system with improved resolution, the cones would be less broad thereby lowering the probability of overlap between both sources locations.

The proximity of both sources will also factor into the amount of contamination. A small distance between the sources will increase the probability of cones overlapping both events. Quantification of the contamination in an isolated spectrum due to source proximity and system resolution is a topic that will be further studied in the future.

Another observation made in the isolated spectra was the absence of low-energy events that dominate the aggregate spectrum. The isolated spectrum only examines events from a region of interest, which suppresses events from the background radiation that is spread more evenly throughout the environment. This observation highlights one of the main advantages of radiation imaging compared to detection without localization, which is a greater signal-to-noise ratio in the region that the source is located compared to the entire environment.

4.3.2 Neutron spectral isolation

While many radioisotopes that emit gamma rays do so with distinct energy-peaks, neutron sources typically emit neutrons with a continuous energy spectrum. Two such sources, PuBe and ^{252}Cf were measured to evaluate performance of the algorithm.

Experimental setup

PuBe and ^{252}Cf point sources were measured simultaneously because they emit different neutron energy spectra. PuBe produces neutrons through the ^{9}Be(α,n) reaction. The emitted energy spectrum has a different shape and higher average energy than the neutrons emitted by spontaneous fission from ^{252}Cf. The PuBe was located at the angular coordinates (136°, 92°) at a distance of 344 cm from the DPI. The ^{252}Cf was placed at (71°, 90°) with a distance

of 419 cm from the DPI. Figure 4.6 shows the setup of the measurement. The PuBe had an activity of about 37 GBq and the ^{252}Cf had an activity of about 165 MBq. These activities corresponded to an approximate emission of 1.5×10^6 neutrons per second from the PuBe and 1.9×10^7 neutrons per second from the ^{252}Cf. Because the ^{252}Cf emitted many more neutrons per second than the PuBe, it was shielded with 23.5 cm of polyethylene to avoid masking the PuBe. The measurement time for this experiment was 45 minutes.

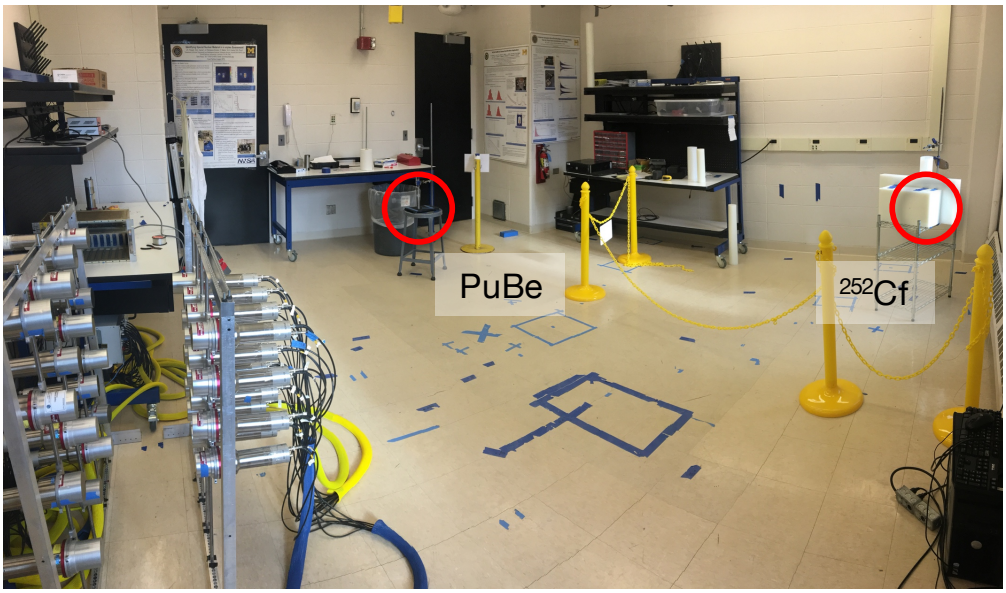

Figure 4.6: The experimental setup for the measurement of a ^{252}Cf and a PuBe source is shown in this photo. Both sources are highlighted by red circles. The ^{252}Cf was located at an angular coordinate of (71°, 90°) and distance of 419 cm from the DPI. A total thickness of 23.5 cm of polyethylene was used to shield the ^{252}Cf so the much greater neutron emission rate would not mask the PuBe source. The PuBe was located at (136°, 92°), 344 cm from the DPI. The DPI appears on the left side of the photo.

Results

In the experiment to demonstrate neutron spectrum isolation, a total of 17,298 neutron events were detected from the simultaneous measurement of PuBe and ^{252}Cf. Figure 4.7 shows the reconstructed neutron image as an average of all SOE image states. In this image, a distinct hot-spot for the PuBe in pixel (130°, 90°) is seen. However, because of

the large amount of polyethylene shielding used for the ^{252}Cf, the hot-spot is not as intense and occupies a much larger region. The maximum image value of the hot-spot is at the (80°, 90°) pixel. Table 4.2 shows a comparison between the expected hot-spot locations and reconstructed hot-spot locations. This image was created using 1×10^6 iterations and a 0.1-MeV energy bin width.

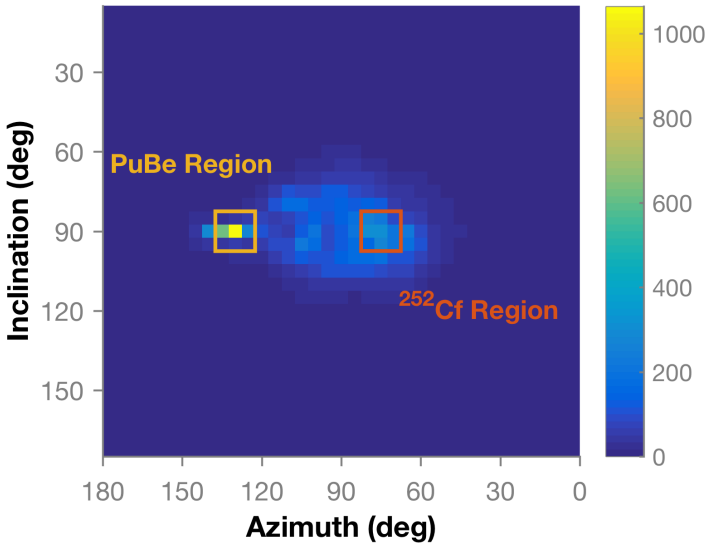

Figure 4.7: The reconstructed neutron image shows an intense hot-spot for the PuBe and a less intense, blurred hot-spot for the shielded ^{252}Cf. The ^{252}Cf hot-spot is blurred because 23.5 cm of polyethylene was used as shielding.

Figure 4.8 shows the isolated spectra for each source. The spectrum for the PuBe was created from the 3×3-pixel region surrounding (130°, 90°). The spectrum for the ^{252}Cf was from the 3×3 region centered at (80°, 90°). The histograms shown in Figure 4.9 correspond to the energy bin producing the maximum value for each region. For PuBe this bin was 2.6 MeV and for ^{252}Cf this bin was 2.4 MeV. Each isolated spectrum was normalized to an integral value of one for comparison, which is shown in Figure 4.10. The isolated PuBe spectrum had a larger portion at higher energies compared to the isolated ^{252}Cf spectrum as expected. The average energy of the isolated PuBe spectrum was 3.85 MeV and was 2.90

Table 4.2: The expected angular locations of the PuBe and ^{252}Cf sources are compared to the locations of the most intense pixel in the reconstructed hot-spot. The absolute difference between the two locations is given. The image pixels had a 5° width.

	^{252}Cf		**PuBe**	
	Azimuth	**Inclination**	**Azimuth**	**Inclination**
Expected location	135°	90°	70°	90°
Reconstructed location	130°	90°	75°	90°
Absolute difference	5°	0°	5°	0°

MeV for the isolated ^{252}Cf spectrum.

Discussion

The experiment with PuBe and ^{252}Cf showed the performance of spectrum isolation for two sources with different neutron spectra. There are two key differences in the analysis of this experiment compared to the prior ^{22}Na and ^{137}Cs experiment. First, the neutron spectra emitted by both sources are continuous unlike the gamma-ray spectra from ^{22}Na and ^{137}Cs. Second, there is very little environmental background present in the neutron signal.

The average energy calculated from the isolated ^{252}Cf spectrum was 2.90 MeV, which was higher than the 2.1-MeV average neutron energy emitted from ^{252}Cf. The spectrum in this experiment was also softened compared to the isolated ^{252}Cf spectrum in the WGPu, ^{252}Cf and AmBe experiment. The softened spectrum was caused by neutrons that had been moderated in the large amount of polyethylene shielding the source. Although the reconstructed energy spectrum was softened, the average energy calculated from the isolated spectrum is still larger than the expected average energy of emitted neutrons. A detection threshold for correlated events causes the overall hardening of the reconstructed spectra compared to the emitted spectra. The threshold for a detection in a liquid scintillator was set at 0.04 MeVee which corresponds to a neutron energy deposition of approximately 0.38

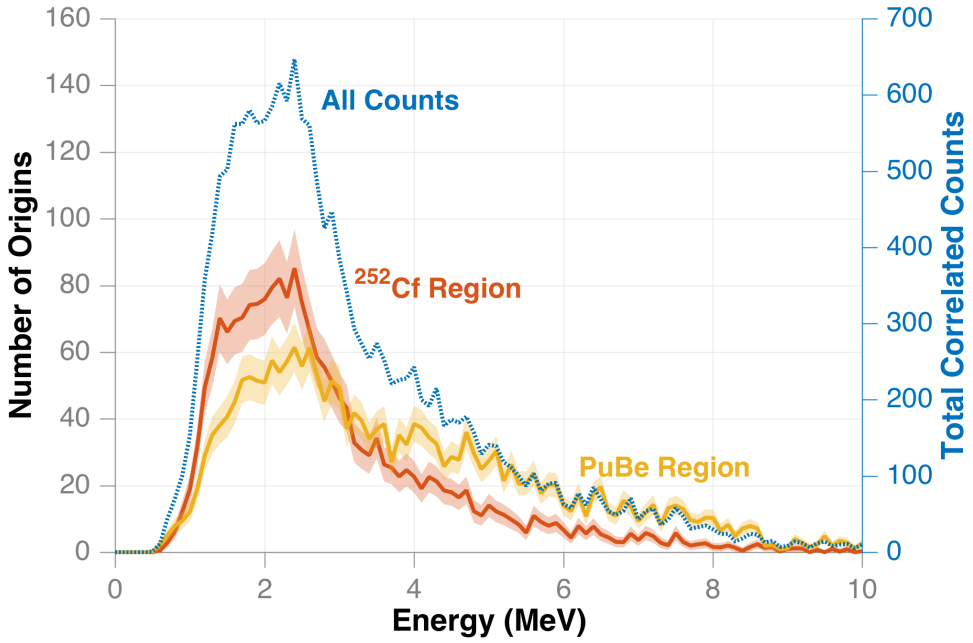

Figure 4.8: The isolated spectra for the PuBe and ^{252}Cf regions are shown in comparison to the total measured spectrum. The light shaded regions for the isolated spectra represent one-sigma uncertainty calculated from the solution histograms.

MeV. This threshold is required to achieve acceptable pulse shape discrimination between the neutron and gamma rays. Because a double scatter is required for detection, the minimum energy that can be detected by the DPI is 0.76 MeV. However, the probability of neutrons near this energy scattering such that the energy deposited is above threshold in both detectors is low. Methods to unfold these effects, which would produce a spectrum more representative of the emitted spectrum are under investigation.

Higher energy regions of the isolated spectra are also suppressed due to energy dependent efficiencies. This is especially apparent in the isolated PuBe spectrum which falls off at higher energies much quicker than the emitted spectrum. The DPI is most efficient at about 2.5 MeV after which neutrons of a higher energy are less likely to interact in the detectors. An upper limit also exists due to the 2-V dynamic range of the digitizer. For this experiment the upper threshold was 3.1 MeVee and for the ^{22}Na/^{137}Cs and the WGPu/^{252}Cf/AmBe

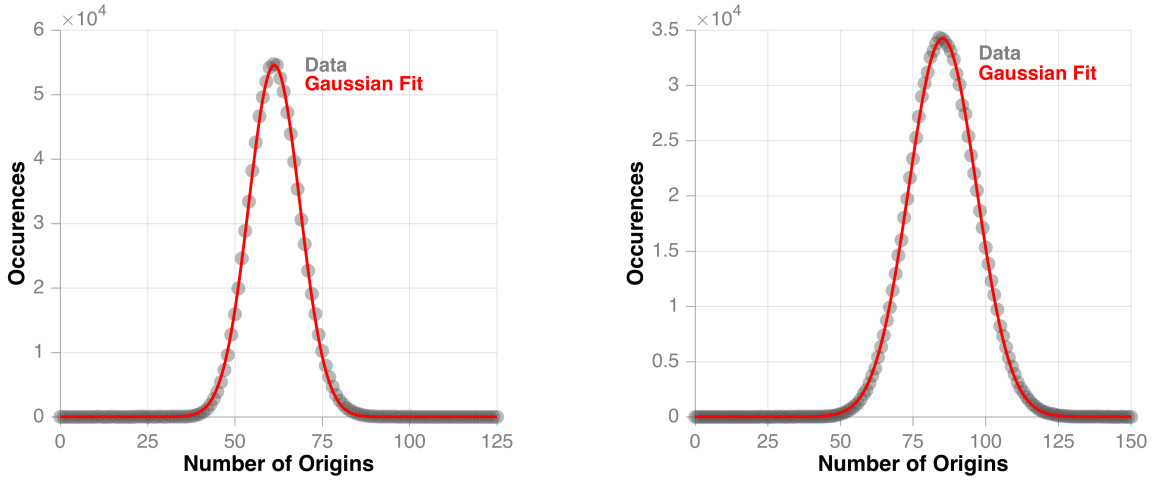

(a) (b)

Figure 4.9: A first order Gaussian was fit to the solution histograms for each energy bin in each 3×3-pixel region. The histograms for the energy bins 2.6 MeV (a) and 2.4 MeV (b) are shown for the PuBe and ^{252}Cf regions respectively. The mode and standard deviation of the fit for each energy bin was used to create both isolated spectra.

experiments the upper thresholds were 2.8 MeVee and 3.1 MeVee respectively. The different upper threshold in the ^{22}Na/^{137}Cs measurement was due a higher baseline used in waveform acquisition. Again, unfolding techniques may be able to remove this effect from the spectrum to better match the emitted spectrum.

Both sources were localized to the pixel adjacent to the expected pixel. For the PuBe, the most intense pixel in the SOE image hot-spot was in the same location in the simple backprojection image suggesting a bias or uncertainty in the measurement itself and not SOE. However, this is not the case for the ^{252}Cf hotspot although there is still a large contribution in the backprojection image in the same pixel where the SOE image located the source. The difference in location in this case may be due to the broadened hot-spot caused by the large amount of shielding used.

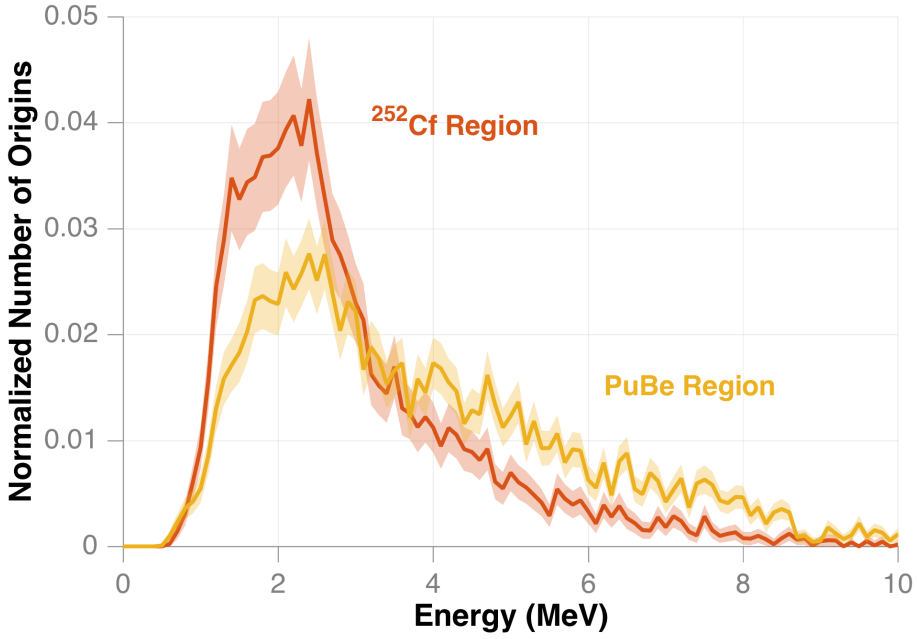

Figure 4.10: A comparison between the integral-normalized isolated spectra highlights the differences in shape. The ^{252}Cf spectrum has a greater fraction of neutrons at lower energies than the PuBe spectrum. A PuBe source emits a larger fraction of neutrons at greater energies than a ^{252}Cf source so this result was expected. The average reconstructed energy of the ^{252}Cf spectrum was 2.90 MeV and the average energy of the PuBe spectrum was 3.85 MeV.

4.4 Using spectral isolation to discriminate SNM

The two prior experiments showed that spectral isolation was effective for gamma-ray energy peaks and continuous neutron fission or (α,n) spectra. In this experiment, both gamma-ray and neutron spectral isolation are used to isolate the spectra from category-I SNM. Spectral features in the isolated spectra and how they differ from the other two non-SNM sources is discussed.

4.4.1 Experimental setup

To demonstrate gamma-ray and neutron spectrum isolation for category-I SNM, the DPI was used for experiments at the Device Assembly Facility (DAF) located within the Nevada

National Security Site [109]. The DAF provided a 4.1-kg disk of WGPu that measured 10.64 cm in diameter and had a thickness of 2.52 cm [110, 111]. The WGPu was measured in the presence of two other neutron and gamma-ray emitting sources. The WGPu had the coordinates (90°, 85°) and had an emission of approximately 5.2×10^5 neutrons per second. The ^{252}Cf was located at (90°, 109°) and had an emission rate of approximately 3×10^5 neutrons per second. The AmBe was placed at (141°, 85°) and emitted approximately 1×10^6 neutrons per second. The WGPu, ^{252}Cf, and AmBe sources were located 201 cm, 212 cm, and 207 cm from the DPI respectively and were measured for 850 minutes. Figure 4.11 shows the sources in relation to the DPI. A 1.3 cm lead shadow-shield was placed 30 cm in front of the WGPu to help reduce the large flux of low energy gamma rays particularly the 0.0595-MeV emission from built up ^{241}Am, which has a specific activity of 4.54×10^{10} gamma rays per second per gram. The AmBe was also shielded with about 10 cm of lead to accommodate another detection system that was measuring concurrently with the DPI.

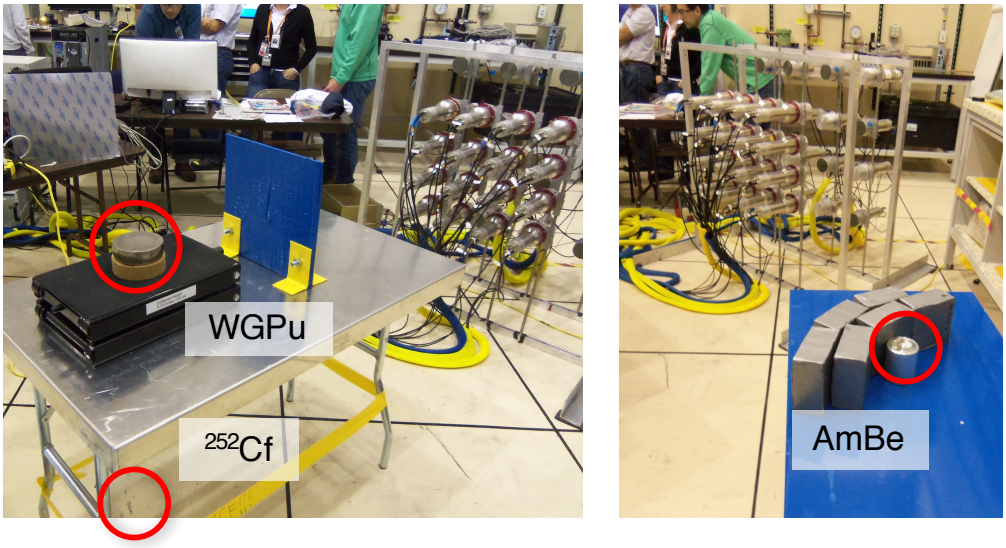

Figure 4.11: The three sources are highlighted by red circles in these pictures of the experimental setup. The WGPu had the angular coordinate (90°, 85°), the ^{252}Cf (90°, 109°), and the AmBe (141°, 87°). The three sources were located at distances of 201 cm, 212 cm, and 207 cm from the DPI respectively.

Results

The reconstructed neutron image shows three hot-spots in Figure 4.12. To generate this reconstruction, 1×10^5 iterations were used with 0.10-MeV energy bin widths and a total of 161,189 neutron events. Due to the closer proximity of the sources to the DPI, the long-distance approximation was not used for reconstruction in this experiment. Each cone was projected onto a sphere with a radius of 200 cm. The expected hot-spot locations are compared to their reconstructed locations in Table 4.3.

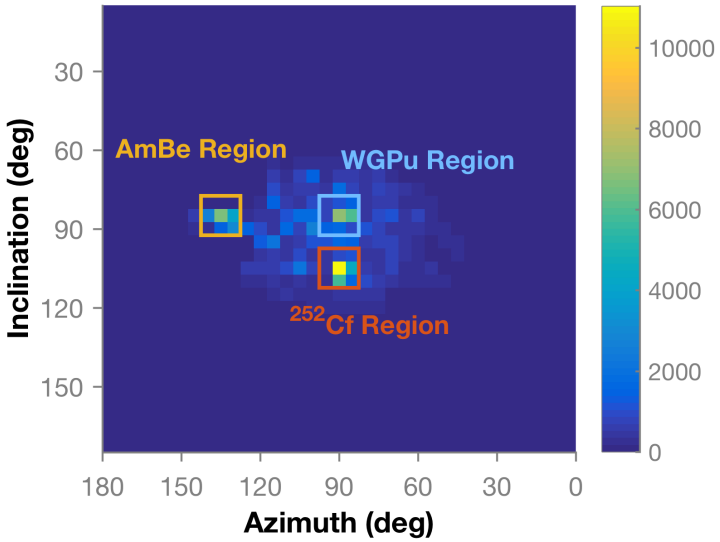

Figure 4.12: The reconstructed neutron image shows three hot-spots, localizing the WGPu, ^{252}Cf, and AmBe. The left-most hot-spot is the AmBe source, the upper-right most is the WGPu, and the lower-right most is the ^{252}Cf.

The isolated neutron spectra, shown in Figure 4.13, for each hot-spot for the WGPu, ^{252}Cf, and AmBe were generated from 3×3-pixel regions centered at (90°, 85°), (90°, 105°), and (135°, 85°) respectively. The spectra were normalized for comparison and are shown in Figure 4.13. The shapes for the WGPu and ^{252}Cf hot-spots are similar as expected, with average energies of 3.23 MeV and 3.20 MeV respectively, since both sources emit neutrons

Table 4.3: A comparison between the expected angular location for each source and the actual angular location is given. The absolute difference between the two locations is also shown. The image pixels had a 5° width.

	WGPu		**^{252}Cf**		**AmBe**	
	Azimuth	**Inclination**	**Azimuth**	**Inclination**	**Azimuth**	**Inclination**
Expected location	90°	85°	90°	110°	140°	85°
Reconstructed neutron location	90°	85°	90°	105°	135°	85°
Reconstructed gamma-ray location	90°	85°	90°	110°	N/A	N/A
Absolute difference (gamma rays)	0°	0°	0°	5°	5°	0°
Absolute difference (neutrons)	0°	0°	0°	0°	N/A	N/A

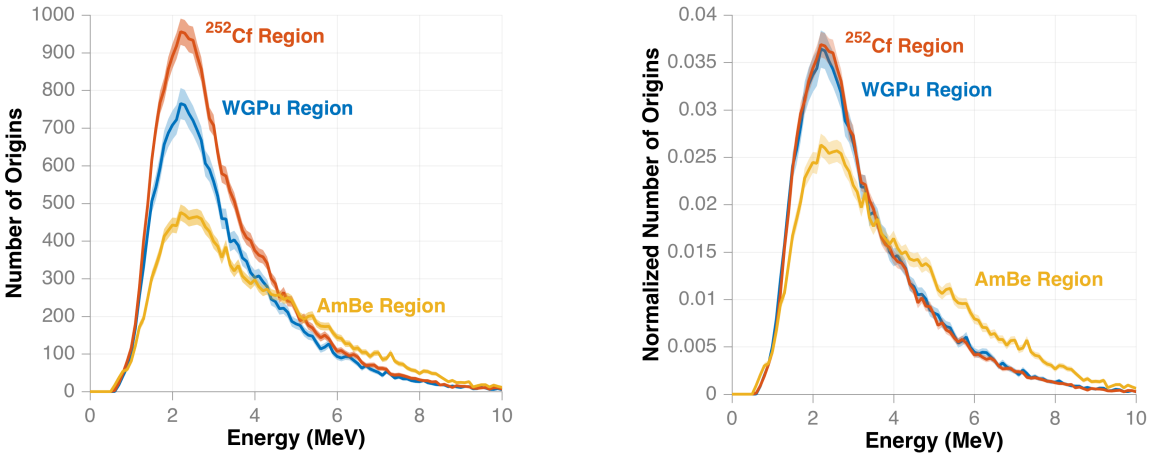

(a) (b)

Figure 4.13: The isolated neutron spectra for the 3×3-pixel regions surrounding each hot-spot are compared using absolute number of origins (a) and normalized number of origins (b) with the light shaded regions showing one-sigma uncertainty. The spectra for the WGPu and ^{252}Cf are similar because both sources emit neutrons in a Watt distribution. The average energies of the WGPu and ^{252}Cf spectra were 3.23 MeV and 3.20 MeV respectively. The average energy of the AmBe spectrum was greater as expected at 3.85 MeV.

in a Watt distribution. However, the AmBe spectrum has a different shape with a larger fraction of neutrons being emitted at higher energies and an average energy of 3.85 MeV.

The reconstructed gamma-ray image, in Figure 4.14, showed only two hot-spots, which located the WGPu and the ^{252}Cf. A hot-spot is not seen for the AmBe because of the 10-cm lead shield placed in between it and the DPI. A total of 1×10^5 iterations was used in the reconstruction.

The isolated spectra were taken from 33-pixel regions centered at (90°, 85°) and (90°, 110°) and are shown in Figure 4.15. Table 4.3 compares the actual source locations with the reconstructed hot-spot locations. A comparison of the normalized spectra is shown in Figure 4.15. The spectrum isolated from the WGPu showed a peak at 0.64 MeV that is less prominent in the isolated spectrum from ^{252}Cf. The peak in the WGPu spectrum is a result of decay gamma rays from ^{239}Pu and ^{241}Am, which were both isotopes present in the sample. The WGPu contained approximately 205 g of ^{240}Pu which has a specific activity of 1.05×10^3

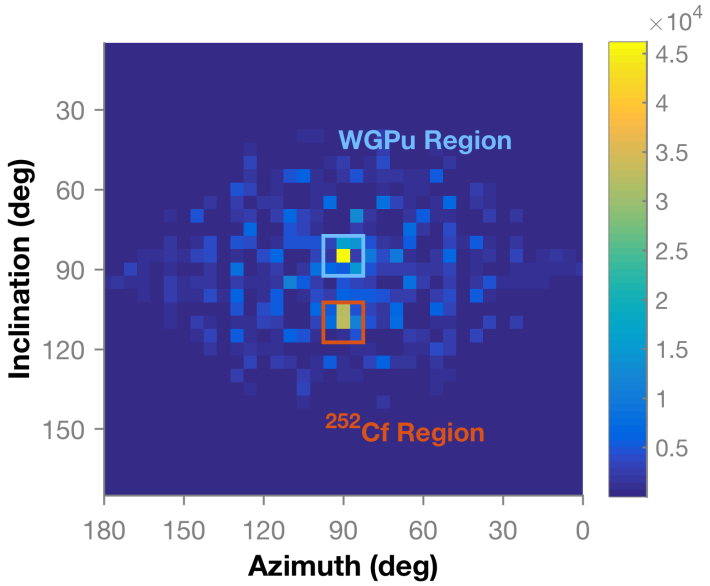

Figure 4.14: The reconstructed gamma-ray image shows two hot-spots for the WGPu (upper) and ^{252}Cf (lower). A hot-spot for the AmBe is not visible because 10 cm of lead was used to shield the source.

for the 0.642 keV gamma ray. The peak at 0.62 MeV in the ^{252}Cf spectrum was due to fission products that built up in the source and some contamination from origins that were actually produced from the WGPu. The ^{252}Cf had an approximate age of 10 years. A feature was also seen in the ^{252}Cf spectrum at about 0.48 MeV. This feature can be attributed to photon production from the (n,α) reaction on ^{10}B, which composed part of the optical windows in the EJ-309 liquid scintillators. This feature is not seen in the WGPu spectrum because the source-to-background ratio is larger so it is washed out and other gamma ray energies are present in this region.

Discussion

This experiment demonstrated that the SOE algorithm could be used as a first step towards discriminating and identifying SNM in an environment where other radioactive sources are present. In this case, it was significant to show that the neutron spectra for

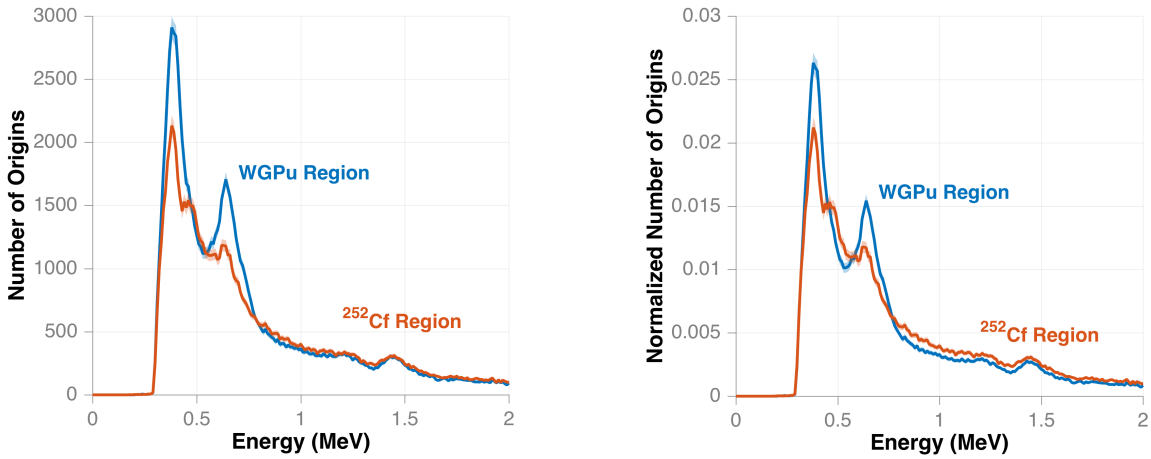

(a) (b)

Figure 4.15: A comparison between the isolated spectra from the 3×3-pixel regions for WGPu and ^{252}Cf is shown in absolute (a) and normalized (b) scales. The WGPu spectrum display two prominent peaks at 0.38 MeV and 0.64 MeV, which are characteristic of Pu and Am gamma-ray decay energies. The ^{252}Cf spectrum also has two peaks at these energies, likely due to the build-up of fissions products, but with much lower intensities than the peaks in the WGPu spectrum. The shoulder at 0.48 MeV in the ^{252}Cf spectrum is from the (n,α) reaction on ^{10}B. This feature is not seen in the WGPu spectrum because of other gamma-ray decay energies present near this energy and the source-to-background ratio is larger.

WGPu and ^{252}Cf had the same shape (Figure 4.13) and average energy. Of course further steps would be required to make a robust identification especially if shielding has changed the spectral shape. Unfolding the isolated spectra would be the another step in identification because it would remove the resolution and efficiency effects found in the reconstructed spectra. This would transform the isolated spectra into a closer representation of the actual emitted spectra.

This experiment also showed that a source completely invisible to gamma-ray detection by the DPI was detected and imaged using the neutron signal, which demonstrates the advantage of dual-particle sensitivity. A system detecting both particle types has a better chance of finding all present sources of SNM in an environment, especially if shielding is present.

Using the gamma-ray signal also allowed us to identify a difference in the signal produced by the WGPu and the ^{252}Cf. The normalized gamma-ray spectra (Figure 4.15) show features that can be used to identify and discriminate WGPu from other gamma-ray sources. Two large peaks are seen in the WGPu at 0.38 MeV and 0.640 MeV which are not prominent in the ^{252}Cf spectrum. There are two notable features seen in the ^{252}Cf spectrum that may make identification more difficult. The first is a shoulder at about 0.48 MeV from gamma rays created by the (n,α) reaction on ^{10}B, present in the liquid scintillator optical windows, and the second is a small peak at 0.62 MeV from built-up fission products and a contamination from WGPu origins. Due to the age of the source, ^{249}Cf is also present in the sample which emits a 0.388-MeV gamma ray with an intensity of 66%. Further characterization of the SOE algorithm may provide a method for quantification and subtraction of contamination of origins in the wrong spectrum. The effect of gamma-ray production from neutron interactions in the detectors when a large field of slower neutrons is present must also be further investigated.

4.5 Conclusions

The experiments detailed in this work demonstrate the powerful combination of SOE spectrum isolation for image reconstruction with the DPI. For non-proliferation applications, completeness (finding all sources) and characterization (identifying sources of interest) are essential. The modified SOE algorithm is able to successfully isolate spectra from multiple hot-spots in an image, which allows for further analysis to identify sources. The method was demonstrated with several experiments that included sources emitting both gamma rays and neutrons, including an experiment in which the spectra from WGPu was isolated from two other sources.

In our experiment measuring two gamma-ray sources, the 0.511-MeV and 0.662-MeV peaks were resolved from ^{22}Na and ^{137}Cs achieving 11.1% and 10.1% resolutions in the isolated spectra respectively. For neutron spectrum isolation, the average energy of the isolated ^{252}Cf spectrum was calculated as 2.90 MeV and a higher average energy of 3.85 MeV was calculated for the isolated PuBe spectrum. The average neutron spectra energies were again used for the final experiment with three sources, which included WGPu, to discriminate a ^{9}Be(α,n) neutron spectrum from a Watt fission neutron spectrum. The AmBe had an average energy of 3.85 MeV, which was higher than the average energies of the WGPu and ^{252}Cf spectra of 3.23 MeV and 3.20 MeV respectively. Due to the similar shape and average energies of the WGPu and ^{252}Cf neutron spectra, the isolated gamma-ray spectra were needed to discriminate the two sources. The isolated WGPu spectrum showed two prominent peaks at 0.38 MeV and 0.64 MeV which are consistent with decay energies from WGPu. The isolated ^{252}Cf spectrum did not feature these prominent peaks but was consistent with a gamma-ray spectrum from fission.

Chapter 5

Methods for characterizing highly enriched uranium using the DPI

Highly enriched uranium is involved in many pathways for the acquisition and use of a nuclear weapon. While HEU is typically regarded as a more difficult material to acquire than plutonium, weapon fabrication is easier and requires less advanced capabilities than would be required for plutonium [112]. Detecting HEU presents a unique set of challenges because the neutron emission rate is much lower than that of plutonium and the large amount of emitted low-energy (< 200 keV) gamma rays can be easily shielded. This chapter explores a technique known as active interrogation, which induces more neutron and gamma-ray emissions from the HEU by shooting other particles at it.

5.1 Difficulties associated with HEU detection

A typical definition for weapons-grade HEU is that ^{235}U exceeds 90% in a sample with the rest composed mostly of ^{238}U [112]. Other designations for uranium enrichment include non weapons-usable HEU from 20% to 90% ^{235}U, low-enriched uranium (LEU) with up to 5% ^{235}U, natural uranium with 0.7% ^{235}U, and depleted uranium (DU) with approximately 0.3% ^{235}U [2]. Both ^{235}U and ^{238}U undergo spontaneous fission, through which they emit neutrons and gamma rays. However, with longer half-lives and a lower probability of a fission

event per decay compared to ^{240}Pu, the neutron emission rate is much lower.

While the neutron emission rate is low, there is still a sizable emission of x-rays and gamma rays from ^{235}U. Most significant are a 13.0 keV x-ray and 19.55, 143.7, and 185.7 keV gamma rays. Photons with energies below 100 keV are very easily shielded by a thin metal sheet and scintillators typically provide poor resolution at these energies. Only semiconductor detectors such as high-purity germanium or CdZnTe have the necessary resolution to effectively measure these energies. The two other prominent gamma-ray energies are also relatively low and easily shielded compared to those emitted by other SNM such as WGPu. These energies are also relatively easily shielded and, for the DPI, fall near the double scatter energy threshold, described in Section 2.4.1, making detection less efficient.

The difficulties of HEU detection using photons and the low emission rate of neutrons makes passive detection impractical. For reliable detection of HEU, a technique known as active interrogation can be used to increase the emission rates of neutrons and gamma rays as well as the average energy of emitted gamma rays [113]. Active interrogation is a technique in which particles, typically neutrons or photons, are shot at a target to induce nuclear reactions in the material. For fissile materials, the interrogating particles will induce fission reactions, which creates a stronger signal for detection consisting of both prompt and delayed fission neutrons and photons. Interrogation sources are usually either radioisotopes or charged particle accelerators.

Photons used to interrogate an object are often bremsstrahlung photons created from an electron accelerator. A bremsstrahlung spectrum is exponential in shape with most photons being produced at low energies and the maximum energy possible being that of the accelerated electrons. Because photofission has a minimum energy threshold, 5.31 MeV for ^{235}U, much of the bremsstrahlung spectrum will fall below this energy and not induce the desired fission reactions [114]. Recent progress has been made towards the development of mono-energetic gamma-ray sources at energies above the photofission threshold [115].

Neutron sources used for active interrogation can be radioisotopes, (α,n) sources, or charged particle accelerators that create neutrons through fusion. A common radioisotope that emits neutrons through spontaneous fission is ^{252}Cf. Common (α,n) sources include an isotope that undergoes alpha decay with a lighter element such as Be or Li. These sources include PuBe, AmBe, and AmLi, all of which emit a continuous neutron spectrum [116]. Fusion reactions from a charged particle accelerator such as d(d,n)^{3}He (DD) and d(t,n)^{4}He (DT) will produce mono-energetic neutrons at energies of 2.5 and 14.1 MeV respectively [116].

Much of the available literature for active interrogation examines the increased count rates created by actively interrogated HEU over the background or active background count rates [116, 117]. In these cases, positive detection can be susceptible to large changes in the environmental or active background, which is the signal produced when no item is present for interrogation. For example, a system deployed outdoors would be affected by environmental background changes caused by weather. Active background can change based on the operating characteristics of a particle generator or the presence of other objects nearby that can scatter particles. In a treaty verification scenario, spoofing the system could be achieved by using another radioactive source located nearby to achieve the expected count rate from an actual item or from a hoax item instead.

5.2 Using imaging with active interrogation

Mating radiation imaging with active interrogation addresses the given issues by localizing the detected radiation. In this type of spoofing scenario, the particles that caused an increased count rate would be seen in a different location than the interrogated item. For a search scenario, localizing the emitted radiation will greatly increase the signal-to-background ratio, making a well characterized background much less important. In general,

imaging will provide greater assurance of a desired positive or negative detection than simple particle counting.

Some efforts to combine imaging and active interrogation have been made, such as the imaging of thermal neutrons in depleted uranium with a coded aperture camera [28]. A coded aperture camera was also used in [29] to detect HEU interrogated by a DT neutron generator with limited success. Only a couple attempts have been made using a scatter camera. The neutron scatter camera from Sandia National Laboratories (SNL) measured low-enriched uranium at the LANSCE facility[118], and the MINER system from SNL was used to create an image of HEU actively interrogated with AmLi [119].

Other active interrogation methods are the Nuclear Material Identification System and the Advanced Portable Neutron Imaging System both developed by Oak Ridge National Laboratory [120, 121]. These systems use a related technique know as associated particle imaging in which the direction of each interrogating neutron can be tracked.

5.3 Active interrogation methods and challenges

Several key physics principles are involved in the active interrogation of an object. It is critical to understand the characteristics of the interrogating particle, as well as which sources emit interrogating particles with the desired characteristics. The desired interaction for interrogation of fissile materials, such as HEU, is induced fission. However, the cross-sections of other interactions such as (n,Xn) will play a role. This section discusses the underlying physics principles of active interrogation with neutrons.

5.3.1 Induced fission in HEU

Practical detection of HEU using a neutron signal requires a larger emission rate than that which is passively produced. The specific activity of spontaneous ^{235}U neutron emission is

Table 5.1: A comparison of the half-lives, spontaneous fission rates, neutrons emitted per fission, and specific activity are given for ^{235}U, ^{238}U, and ^{240}Pu.

Isotope	**Half life**	**Fission prob. per decay**	**Neutrons per fission**	**Neutrons per g-s**
^{235}U	7.04×10^{8} years	2.0×10^{-9}	1.86	3.0×10^{-4}
^{238}U	4.47×10^{9} years	5.4×10^{-7}	2.07	0.0136
^{240}Pu	6569 years	5.0×10^{-8}	2.21	920

Source: [123]

two orders of magnitude lower than that or ^{238}U and six orders of magnitude lower than that of ^{240}Pu. Table 5.1 compares the specific activity of the isotopes. The number of neutrons emitted per g-s is much smaller than for the two other isotopes because the probability of spontaneous fission per decay is much lower. The number of neutrons emitted per fission from ^{235}U is also lower than for ^{238}U and ^{240}Pu. However, ^{235}U has a sizable cross-section for the (n,f) reaction that can be exploited through active interrogation with neutrons, to produce more emitted particles. For fast neutrons the cross-section, shown in Figure 5.1, is on the order of several barns and for slower and thermal neutrons it is several hundred to thousands of barns [122].

The neutrons released from an induced or spontaneous fission reaction can then undergo further interactions in the material or escape the material altogether. Possible interactions include elastic or inelastic scattering, radiative capture, (n,Xn), or fission to name a few of the major ones. The fast neutrons released from fission will be more likely to undergo elastic scattering or an (n,Xn) interaction in the ^{235}U than to induce a fission reaction [122]. However, having undergone a scatter the energy of the neutron will be diminished and therefore the (n,f) reaction become more probable than before. Once the resonance section is reached at about 2,200 eV, elastic scattering and (n,f) become equally likely. The (n,f) reaction becomes more probable at energies below 1eV. Figure 5.1 shows a comparison between the (n,f) and elastic scattering cross-sections. Instead of interacting in the material,

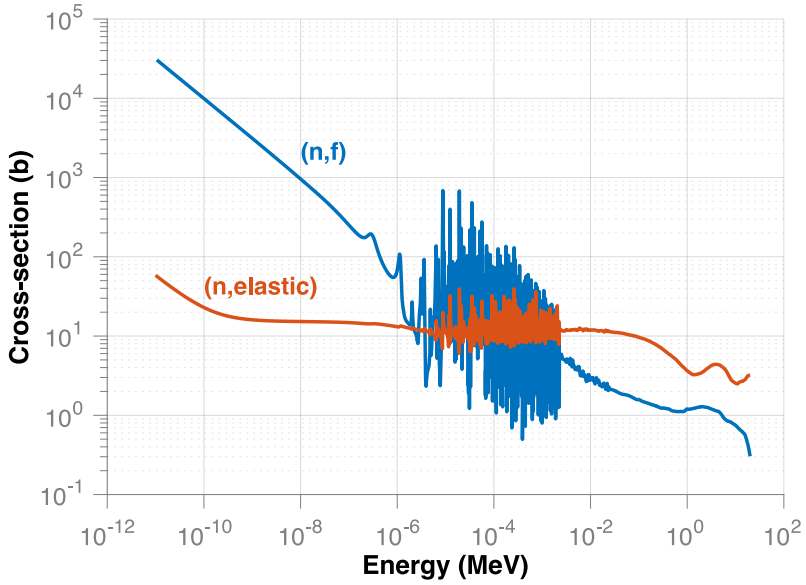

Figure 5.1: Cross-section for the (n,f) and (n,elastic) reactions on ^{235}U

neutrons can also escape altogether. The size and shape of the material play a role in determining the probability of a neutron escaping. In general, the larger the material, the lower the probability of escape [124].

The factors discussed above, including the isotopic composition, object size and shape, as well as the interrogating particles will define the make up of the fission chains created in the object. The length of a fission chain is defined by how many generations it lasts, with *generation one* consisting of the neutrons created in the initial fission, and *generation two* consisting of neutrons created from any fission induced by a neutron from *generation one*. Uranium with a large amount of ^{235}U encourages longer fission chains than for uranium with a lower enrichment because of the low (n,f) cross-section of ^{238}U. A larger mass of HEU will also create longer fission chains than a smaller mass because having more material present will make the escape of neutrons less likely. The surface area, defined by the shape of the object, also factors into the probability for a neutron to escape. A sphere minimizes the surface area for a given mass of material compared to a block for example. Therefore, all

things equal, a sphere of HEU would produce more and longer fission chain than a block of HEU with the same mass [124].

The quantity k_{eff}, known as the effective neutron multiplication factor, is defined as the number of neutrons present in the current generation divided by the number of neutrons present in the previous generation [123]. A $k_{eff} < 1$ means the fission chains will terminate because not enough neutrons are causing other fission events to sustain them. A critical mass has a $k_{eff} = 1$. The fission chains will be sustained meaning the number of neutrons produced in each generation is constant. Nuclear power plants are an example of a critical system. Finally, a $k_{eff} > 1$ is a super-critical system in which more neutrons are produced in each subsequent generation than the last. An example of a super-critical system is a nuclear weapon. Active interrogation increases the number of fission chains in a subcritical object with the neutrons escaping the material acting as a signal for detection. The neutron sources used for interrogation in the experiments in this chapter are described in the following section.

5.3.2 Challenges of active interrogation

A large challenge associated with active interrogation is the presence of active background. The radiation used to interrogate a sample can be detected by the measurement system and obscure the desired signal. In most cases, the flux emitted from the interrogating source is much larger than the signal produced from the item. This large flux is necessary to overcome distance or shielding present between the interrogating source and sample. At these large fluxes, detector performance can degrade or the high count rates can choke data throughput from digitized pulses.

This chapter looks at several methods to separate the HEU signal from the interrogating radiation. If a pulsed neutron generator is used, a time cut can be implemented that removes counts collected when the generator is emitting particles. If the generator is operated contin-

uously, using an energy threshold can discriminate particles from the neutron generator and high-energy particles created from induced fission. Finally, choosing an interrogation source with an energy spectrum that is not detectable by the measurement system ensures that any measured counts are from the sample. Data-acquisition techniques are also described to explain how acceptable data throughput rates were obtained in the high flux environment. What follows is a description of neutron sources that can be used for active interrogation and a description of experimental results detailing the discrimination methods discussed here.

5.3.3 Neutron sources

Radioisotopes: ^{252}Cf

The isotope ^{252}Cf has a large specific activity for neutrons emitted from spontaneous fission. It emits 2.3×10^{12} neutrons per s-g compared to 920 neutrons per s-g for ^{240}Pu [123]. The neutron energy spectrum has the shape of a Watt distribution and is shown in Figure 5.2 [83]. Because the spectral shape of ^{252}Cf is very similar to the induced fission spectrum from HEU, it is not an ideal source to use for interrogation. Many neutrons from the ^{252}Cf will be detected which will obscure the desired signal from HEU.

(α,n) sources: AmBe and AmLi

AmBe and AmLi both emit neutrons through the (α,n) reaction. The americium undergoes alpha-decay and the emitted alpha particles can collide with a low-Z element such as beryllium or lithium to release a neutron. The resulting fast neutron spectrum for AmBe and AmLi are very. AmBe produces a large fraction of higher energy neutrons compared to ^{252}Cf while the AmLi neutron spectrum is much softer compared to both ^{252}Cf and AmBe. The spectra from ^{252}Cf, AmBe, and AmLi are compared in Figure 5.2. AmLi is a more ideal source for this application because most of the spectrum falls below the detection thresh-

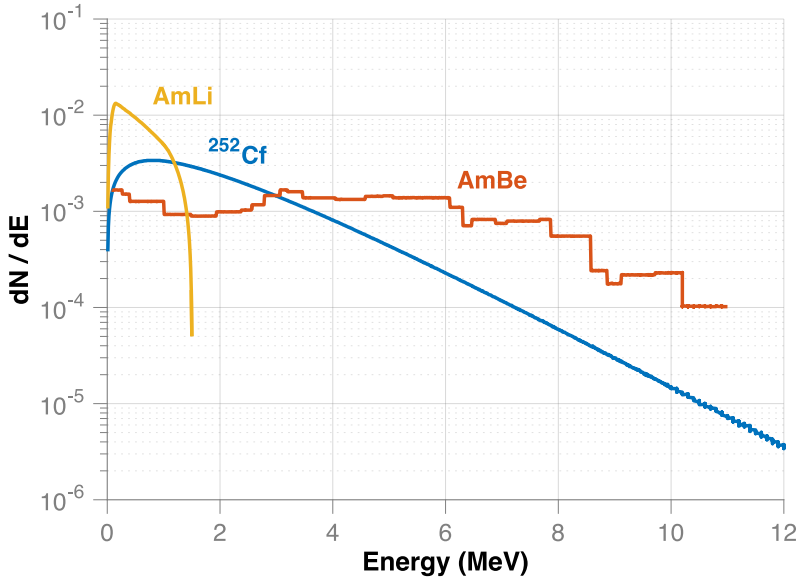

Figure 5.2: A comparison of the emitted neutron spectra from ^{252}Cf, AmBe, and AmLi. The data used in this plot was tallied from the sources available in MCNPX-PoliMi.

old, of approximately 1 MeV, for the DPI whereas a sizable portion of the ^{252}Cf and AmBe spectra lie above above this threshold.

Neutron generator: DD and DT

While radioisotopes and (α,n) sources produce continuous neutron spectra, neutron generators are capable of emitting a mono-energetic neutron spectrum. Two of the more popular reactions to produce neutrons from a generator are the DD and DT fusion reactions. The DD reaction fuses two deuterons, which creates a 2.45 MeV neutron and a ^{3}He particle. The DT reaction fuses a deuteron and triton, which releases a 14.1 MeV neutron and an alpha particle.

An attractive feature of neutron generators is that they can be pulsed to only emit neutrons in short bursts. This allows for detection systems to veto the time when the generator is operating so neutrons emitted from the generator are not detected. A typical pulse may last for several hundred microseconds with a repetition rate of several hundred

Table 5.2: The weight percentages for all present isotopes in Rocky Flats Shells, which were used as the HEU source for active interrogation experiments.

Isotope	**wt%**
^{233}U	Not Recorded
^{234}U	1.02
^{235}U	93.16
^{236}U	0.47
^{238}U	5.35

Source: The data is from the 1971 isotopics measurement provided in [125]

Hertz. These factors define the duty cycle which is the percentage of the time that the generator is producing neutrons.

5.4 Description of HEU samples used in experiments

Experiments with HEU were carried out at the DAF. The HEU samples used are known as the *Rocky Flats Shells* which consist of multiple hemispheres that can be configured to achieve different masses of HEU [125]. The sample was enriched to 93.16% ^{235}U. The full isotopic composition can be found in Table 5.2.

The experiments in this work used two configurations of the shells. The first used shells number one through 24, which when assembled created a solid sphere with a mass of 13.7 kg. Another assembly of the shells was used to evaluate a smaller mass. Shells 13 through 24 were assembled, which created a hollow sphere that had a mass of 10.0 kg. In both cases the outer radius of the sphere measured 5.7 cm and for the 10.0-kg configuration the inner radius was 3.7 cm. A picture of the shells being assembled can be seen in Figure 5.3.

Figure 5.3: Assembly of the Rocky Flats shells into a sphere.

Monte Carlo calculation of HEU multiplication

MCNP6 KCODE was used to evaluate the k_{eff} for both the 13.7-kg and 10.0-kg configurations of the HEU. For shells 1-24, which had a mass of 13.7-kg, k_{eff} was 0.649. When surrounded by a 3.8-cm thick polyethylene shell, with a 1.9-cm gap between the HEU and shell, k_{eff} increased to 0.764. For shells 13-24, with a mass of 10 kg, the k_{eff} was 0.392. These results demonstrate that a larger mass of HEU, in a solid sphere, will have a larger k_{eff} than a hollow sphere with a smaller mass. The results also confirmed that adding a low-Z moderator increased multiplication.

5.5 DD experiments

An active interrogation experiment was performed using a DD neutron generator to interrogate a bare 13.7-kg HEU sphere. The DD generator operated at an output of approximately 1×10^6 neutrons per second. Using the generator in pulse mode and a veto signal, further discussed in Section 5.6.1, did not produce enough neutron counts to create an image of the source. In a 41.5-minute measurement, a total of one correlated neutron count was observed. The DPI was located 116 cm from the HEU with angular coordinates

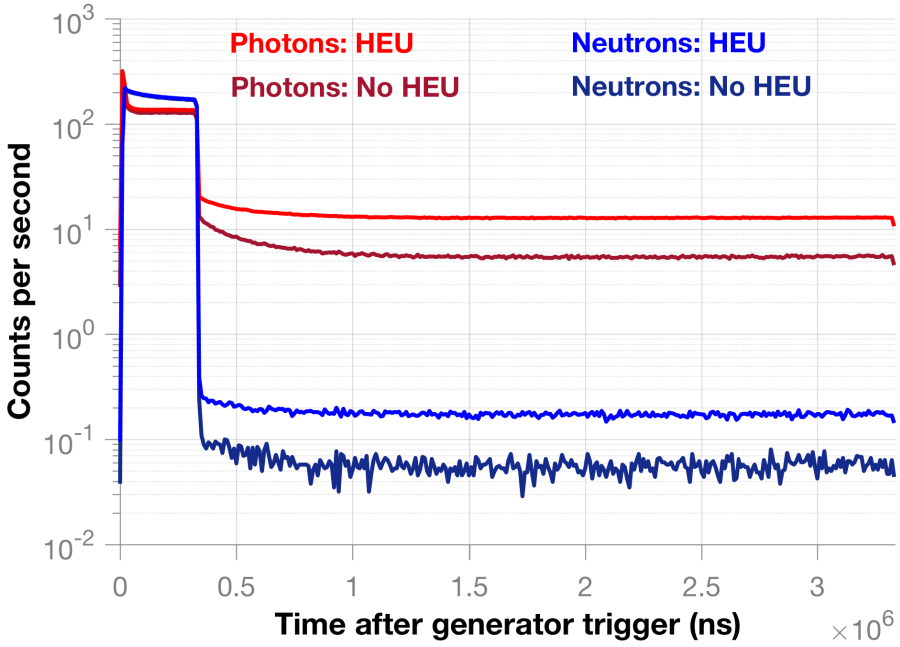

Figure 5.4: A comparison of the neutron and gamma-ray count-rates, as a function of time, during the DD generator pulse structure with no source and the HEU present

(90°, 85°). Figure 5.4 shows the counts rates as a function of the arrival time in the front plane detectors. Despite the increased neutron count rate with HEU present, it was not sufficient to produce enough correlated neutron counts for imaging.

Another attempt was made to image the HEU with the DD generator by running the generator continuously rather than pulsed, and using energy thresholds to remove the detected DD particles from the image. The reconstructed energy spectrum, in Figure 5.5, shows a peak for the 2.5-MeV neutrons from the generator with a long tail that presumably contains higher energy neutrons produced by induced fission in the HEU. However, simply imaging the neutrons above 4 MeV does not produce an image of the HEU. It is likely that system resolution caused a significant amount of 2.5-MeV neutrons from the generator to reconstruct to energies above 2.5 MeV.

One such way for this to occur is for an event to have a small measured time-of-flight (TOF) value, due to either time resolution or an accidental count in which two separate

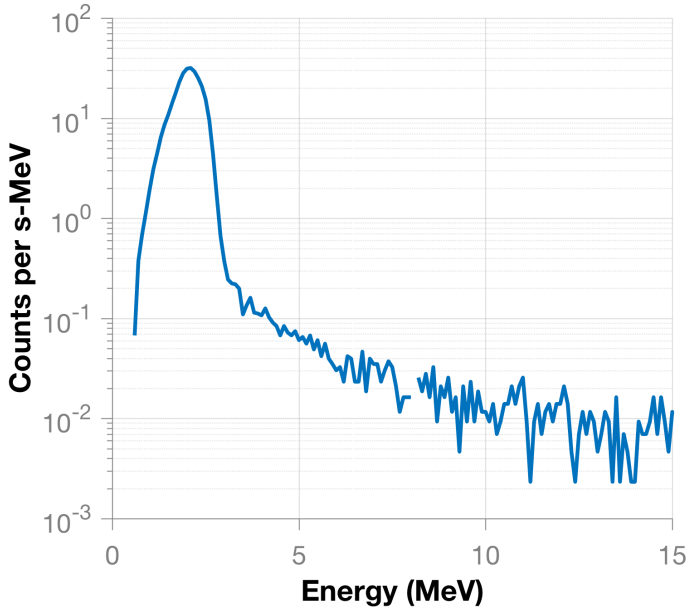

Figure 5.5: Reconstructed neutron spectrum from continuous DD interrogation of HEU. The red box shows the position of the DD generator and the green box shows the position of the HEU.

neutron detections appear as a single correlated count. After removing all counts with a TOF less than 35 ns and energy less than 4 MeV, the reconstructed backprojection image, in Figure 5.6, suggests that the neutrons are from the HEU and not DD. The red box shows the location of the DD generator and the green box shows the expected location of the HEU. However, with this cleaning, only 115 neutrons remain after beginning with a total of 127,342.

For gamma rays, applying a lower energy threshold of 2.5- MeV produced a good image of the HEU in Figure 5.7. A total of 7,511 counts remained after the threshold was applied. This threshold eliminate much of the active and environmental background that obscured the image with no energy threshold applied. The reconstructed SOE image clearly shows an image of the HEU and not the DD generator, which was located within the red box overlaid on the image. The reconstructed energy spectrum is shown in Figure 5.8.

While images of the HEU were produced using DD interrogation, the signal was very

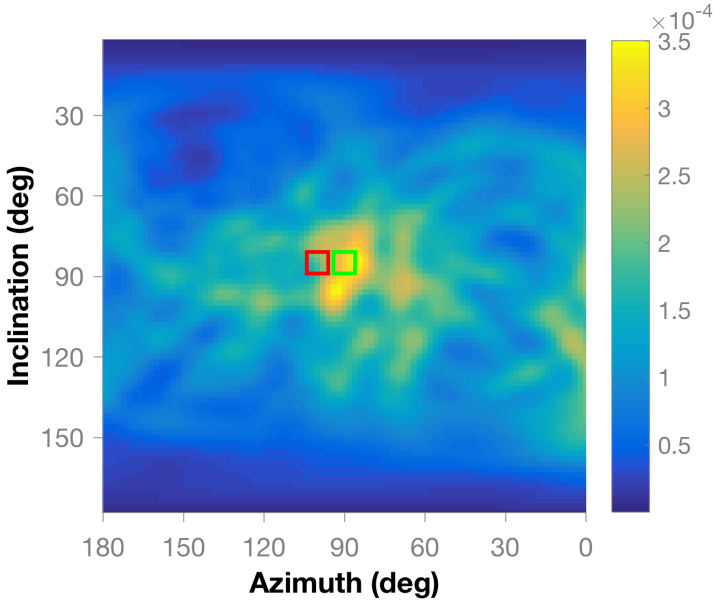

Figure 5.6: A reconstructed neutron image created from DD interrogation of HEU. Only neutrons with an energy above 4 MeV and a time-of-flight above 35 ns were included. The red box shows the position of the DT generator and the green box shows the position of the HEU.

small after removing the DD signal with time or energy cuts.

5.6 DT experiments

A series of experiments was carried out to evaluate the detection of HEU with the DPI when interrogated with a DT neutron source. The HEU was measured in bare and moderated configurations as well as being swapped out for a *hoax* sample made of tungsten instead of HEU.

5.6.1 Methods

The DT experiments used a Thermo Scientific MP 320 neutron generator to interrogate the HEU. The parameters used for the generator and the measurement configurations are

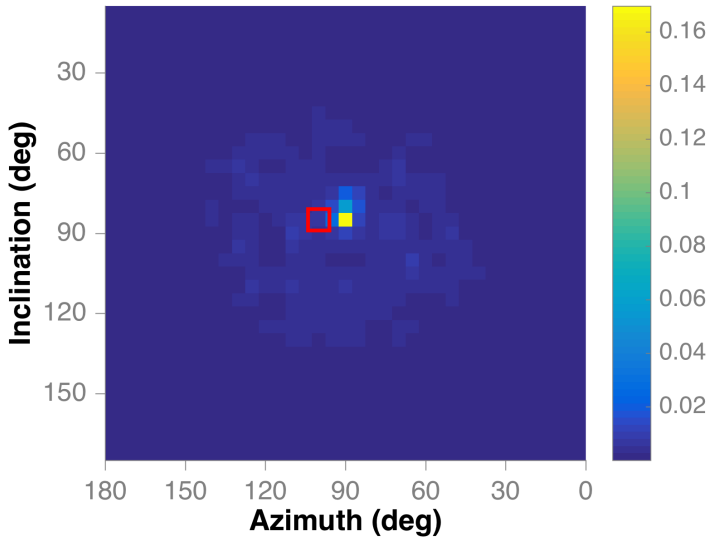

Figure 5.7: A reconstructed gamma-ray image created from DD interrogation of HEU. Only gamma rays with an energy above 2.5 MeV were included. The red box shows the position of the DT generator.

detailed in this section.

MP 320 neutron generator with DT target

The neutron generator was configured with the DT tube, which produced 14.1-MeV neutrons. The generator was set to a pulse length of 3.33 µs with a repetition rate of 300 Hz. These parameters defined the duty cycle to be 10%. Other generator settings were a current of ∼50 µA and a high voltage of 70 kV. The neutron emission rate was unknown at these settings.

The total emission rate is necessary to ensure that the simulations presented later in this chapter are an accurate reflection of the measurement. In the paper [126], Remetti et al. evaluate the anisotropy present in the neutron emission from an MP 320 operated in DT mode. They provide an estimate of the total emission, for different current and voltage settings, as well as the angular emission. Figure 5.9 shows a plot of the total neutron yield

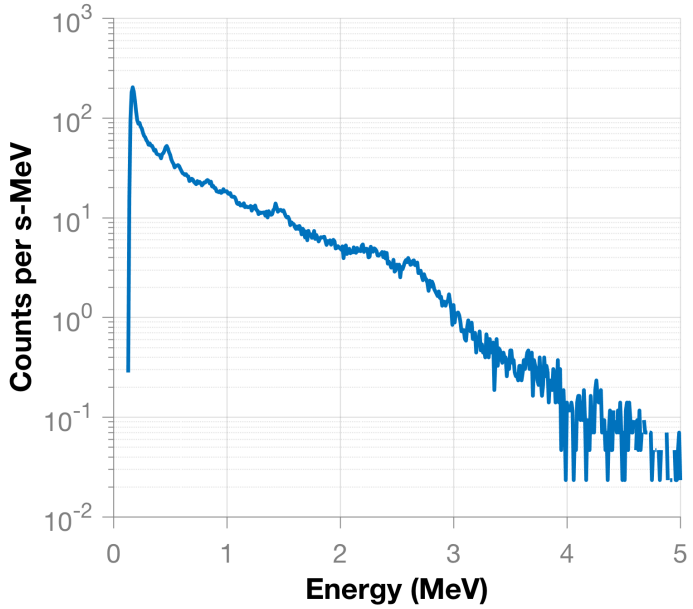

Figure 5.8: Reconstructed gamma-ray spectrum from continuous DD interrogation of HEU

that was reproduced from the plot and equations given in their paper. The plot suggests that a voltage of 70 kV and a current of 50 µA will produce a neutron yield of about 6×10^7 neutrons per second. By the coordinate definitions in the paper, the HEU sample was located at 0° for the following experiments, which was stated to have a 15% greater flux than the total emission. Based on these estimates, assuming an isotropic emission of approximately 7×10^7 neutrons per second produces the proper neutron flux in the direction of the HEU.

Veto pulse

The generator produced a TTL logic pulse that was fed into a signal generator. The pulse was converted to a positive, square pulse with a height of 1 V and the signal was connected to the digitizers so it was time synchronized with detector pulses. Acquisition was setup to acquire the leading edge of the pulse. Data was constantly acquired by the system, even when the generator was on, with a veto applied in post-processing.

To calculate the proper length for the veto, the arrival times of neutron and gamma-

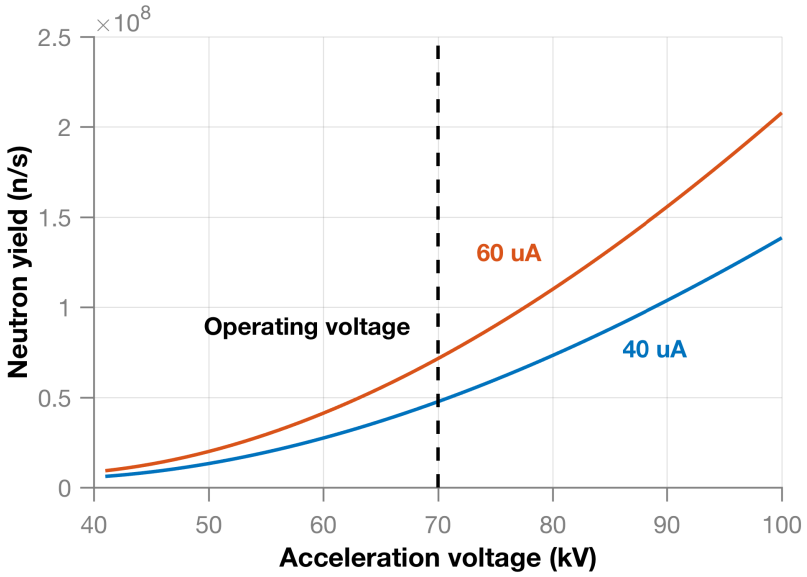

Figure 5.9: Estimated neutron yields from DT generator with different operational settings [126]

ray pulses in all front plane liquid scintillators had the start time of the prior veto pulses subtracted. The times were then histogrammed, which displayed the time structure of the generator pulse and allowed for the length of the veto pulse to be chosen. The entire time spectrum is shown in Figure 5.10 and a time spectrum with finer binning and chosen veto length of 335,700 ns is shown in Figure 5.11. The setup for this measurement is detailed in the next section. The case with no sample was used for this analysis.

Experimental configurations

The DT generator was placed on an aluminum table at a distance of 158 cm from the center of the DPI. It had angular coordinates of (100° , 86°). The sample being interrogated was placed on the table with the sample center at a distance of 155 cm and angular coordinates of (90° , 86°). Figure 5.12 shows the setup with the DPI, neutron generator, and sample. The sample was varied to represent different detection scenarios including shielded HEU and a sample representing a hoax. The experiments performed are listed in Table 5.3.

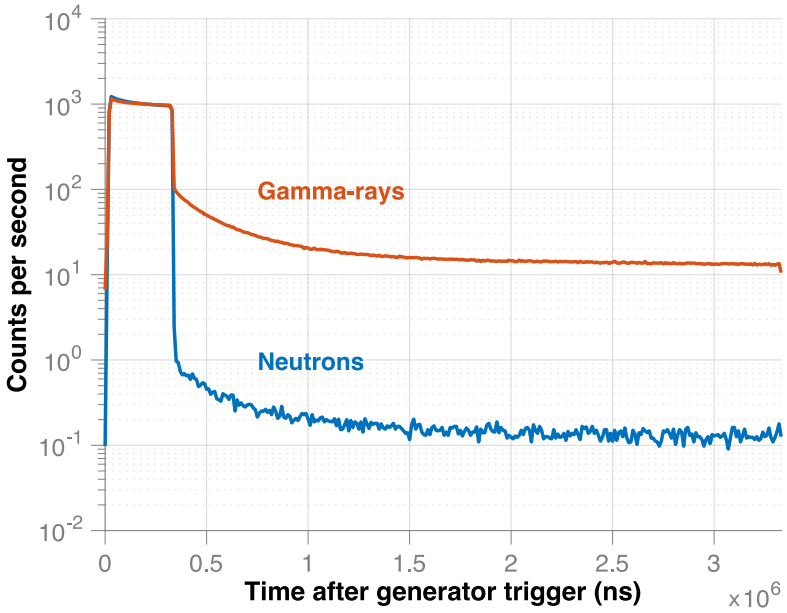

Figure 5.10: Time spectra of the neutron and gamma-ray pulses made by the DT generator.

A measurement was conducted with no sample to characterize the signal from the DT generator and to choose an appropriate veto length. The 13.7-kg configuration of the HEU was then interrogated with the same set-up for the DT generator and DPI. Experiments were also conducted to evaluate detection when the HEU was shielded with either low-Z polyethylene or high-Z tungsten. Finally, the HEU sample was swapped with a tungsten sphere, which represented a sample that is benign and could be used as a hoax.

5.6.2 Results and discussion

The experiments were characterized and compared in several different ways. Time spectra of singles count rates in the front plane liquid scintillators were created to provide an expectation of the correlated count rate. Images and spectra were also created using SOE. The location of the hot-spot is another method of ensuring that veto eliminates particles for the DT generator.

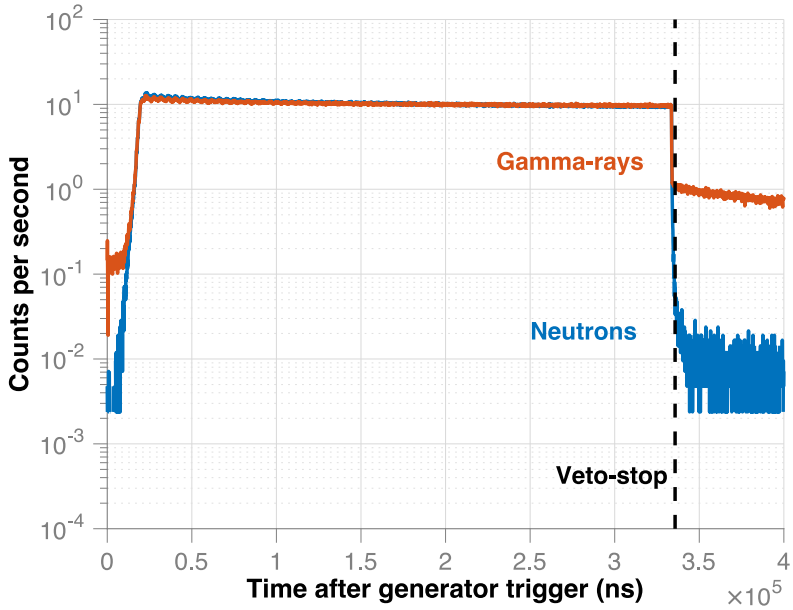

Figure 5.11: Time spectrum of the DT generator pulse with fine time binning and the chosen veto-stop time.

DT generator with no sample

To verify that an appropriate veto length was chosen, the data from the experiment with only the DT generator and no sample was processed with and without the veto applied. With no veto, a correlated count rate of 698 neutrons per second was observed. However, when the veto was applied the count rate dropped to almost zero, with only two correlated neutron events recorded in the full 7-minute measurement.

The reconstructed neutron image and spectrum are shown in Figure 5.13. While the hot-spot appears in the correct location, denoted by the overlaid red box on the image, the image is noisy surrounding the hot-spot. The many neutrons reconstructing to lower energies, as seen in the spectrum, contributes to image noise. This effect is likely due to the assumption that all correlated neutron events underwent a single elastic scatter on hydrogen in a front plane detector. At higher energies, carbon interactions such as elastic and inelastic scattering, as well as carbon breakup become more prevalent. Interactions on carbon produce

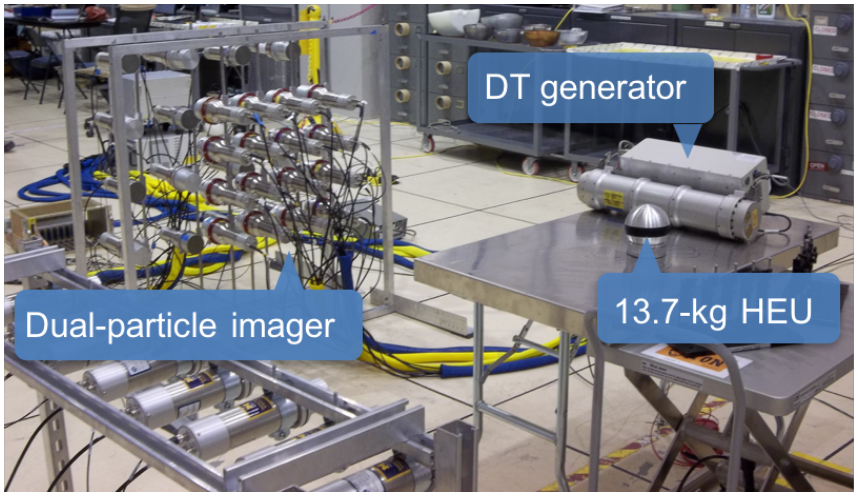

Figure 5.12: A picture of the experimental setup that shows the configuration used to measure the HEU interrogated by the DT generator.

less light in the detector, which results in a lower reconstructed energy if the particle does score in a correlated event.

A better image of the DT can be produced by only reconstructing the events that fall near 14.1 MeV. The image is improved because events that reconstruct to energies other than 14.1 MeV, will not be ideal events, and will likely have reconstructed to the wrong location. Neutrons that are down scattered by objects in the room and then detected are also removed using this energy window. Figure 5.14 shows the image with only events that reconstruct to an energy between 11 and 17 MeV. This removes the noise present in the previous image.

While a veto length of 335,700 ns eliminated virtually all of the neutron signal, the same veto reduced the gamma-ray count rate from 1,126 per second to 85.8 per second. A comparison of the spectra produced with and without the veto is shown in Figure 5.15. The counts being recorded after the veto are due to environmental background, as well as gamma-ray decays from materials inside the generator that have been activated.

The images reconstructed with and without the veto are compared in Figure 5.16. The images were created using a minimum energy threshold of 500 keV. Events at lower energies

Table 5.3: Summary of experiments using a DT neutron generator.

Sample	**Shielding**	**Meas. time**	**Notes**
None	N/A	7 min.	-
13.7 kg HEU	None	59 min.	-
13.7 kg HEU	Polyethylene	22 min.	3.81 cm thick hollow sphere of shielding w/ a 2-cm gap between HEU and shield
13.7 kg HEU	Tungsten	10 min.	2.54 cm thick hollow sphere of shielding w/ a 0.7-cm gap between HEU and shield
Tungsten sphere	None	10 min.	8.9-cm outer and 6.4-cm inner radius

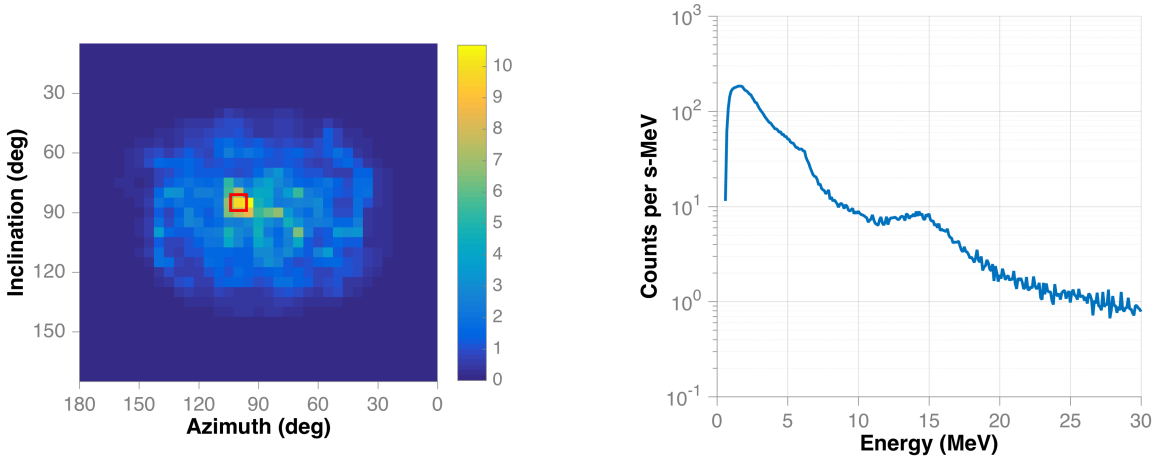

(a) (b)

Figure 5.13: The SOE neutron image (a) localizes the DT neutron source to the correct location, denoted by the red box overlaid on the image. The reconstructed spectrum (b) shows a peak at 14.1-MeV with many other events reconstructing to lower energies.

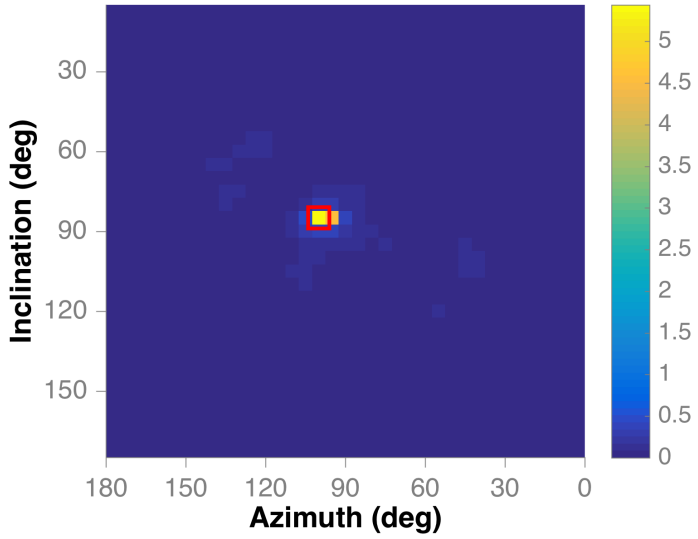

Figure 5.14: An SOE image of the DT source using only neutron events with reconstructed energies between 11 and 17 MeV. The red box shows the position of the DT generator.

including the peak seen at 0.478 keV, do not reconstruct to the correct location as explained in Section 5.16. The peak seen in the spectra, and seen in the gamma-ray spectra to follow, is produced from the ^{10}B(n,α)^{7}Li reaction, which occurs in the liquid scintillator optical windows, made of the borosilicate glass BK7. These events cannot be used for localization. It is evident that the veto eliminates much of the gamma-ray signal from the DT generator, when the images are compared using the same color scale.

Bare HEU

The bare HEU sphere was placed at a distance of 155 cm at an angular location of (90°, 94°) and measured for 59 minutes (setup shown in Figure 5.12). When the veto is applied, a count rate of 0.217 correlated neutrons per second is achieved (794 total counts). The red box superimposed on the reconstructed image, in Figure 5.17, shows the location of the DT generator and the green box shows the location of the HEU. It is clear that the

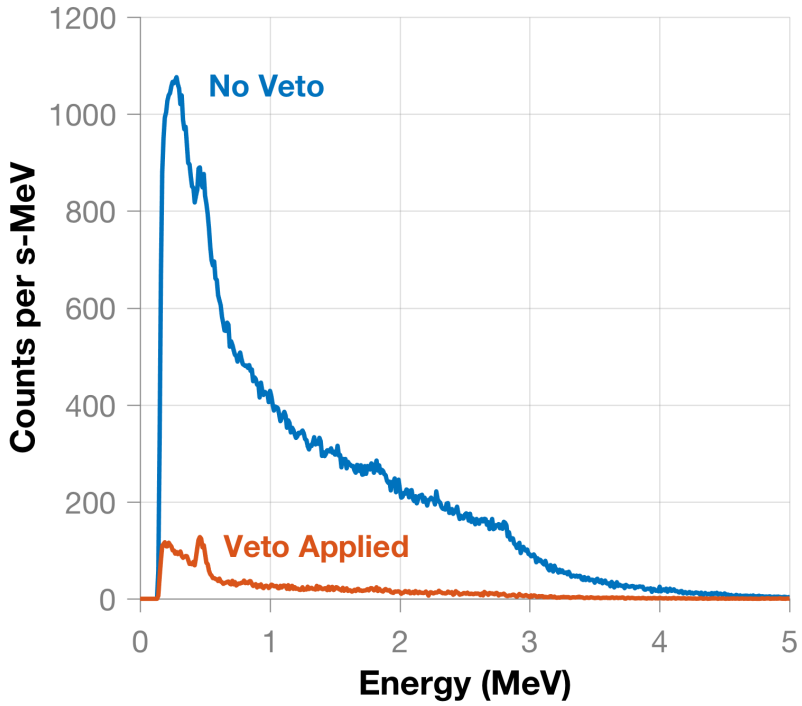

Figure 5.15: Comparison of the measured gamma-ray spectrum with and without the veto applied.

reconstructed hot-spot is not located at the location of the DT generator but is instead located at the expected position of the HEU. This image is compared to the neutron image created when no sample was interrogated. Both images are shown using the same scale and it is evident that the detected neutrons are from the HEU and not the DT neutron generator.

The reconstructed energy spectrum is shown in Figure 5.18, where it is compared to the other HEU configurations. The shape is suggestive of the expected induced fission Watt spectrum. In comparison with the other spectra, the bare HEU produced less measured counts than the poly moderated case and a similar amount to the tungsten moderated case. These configurations will be discussed in detail in the next sections.

To effectively image the gamma-ray signal from the HEU, an energy threshold had to be included to eliminate contribution from the environmental and active background. We found the best image, shown in Figure 5.19, was produced with a lower threshold of 2.5-MeV.

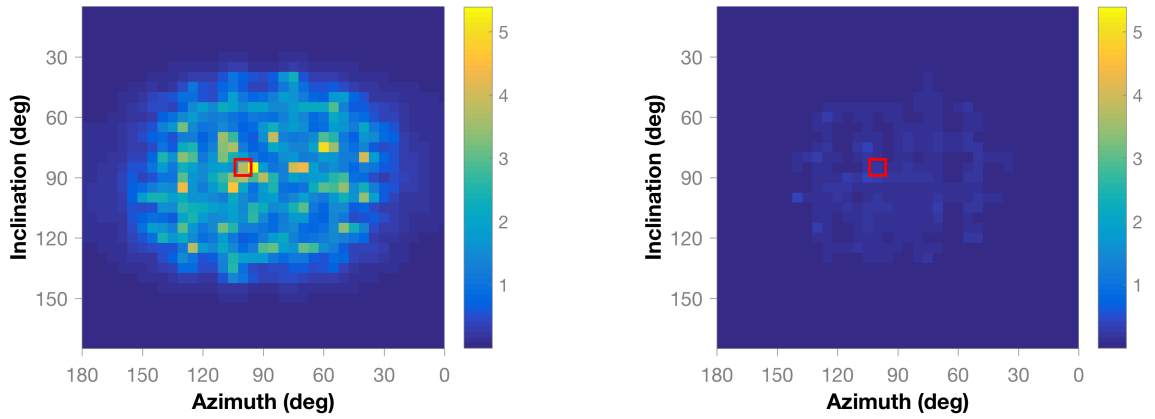

(a) (b)

Figure 5.16: The reconstructed gamma-ray images with no veto applied (a) and with the veto applied (b). when no sample was present.

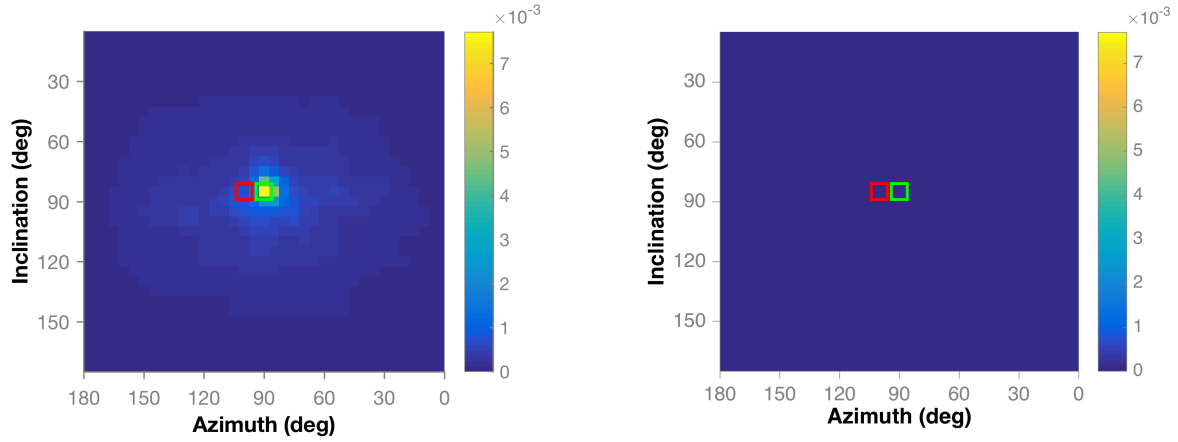

(a) (b)

Figure 5.17: The neutron image of the bare HEU interrogated with DT (a) and a comparison of an image created using the same parameters with no sample present (b). The red boxes show the position of the DT generator and the green boxes show the position of the HEU.

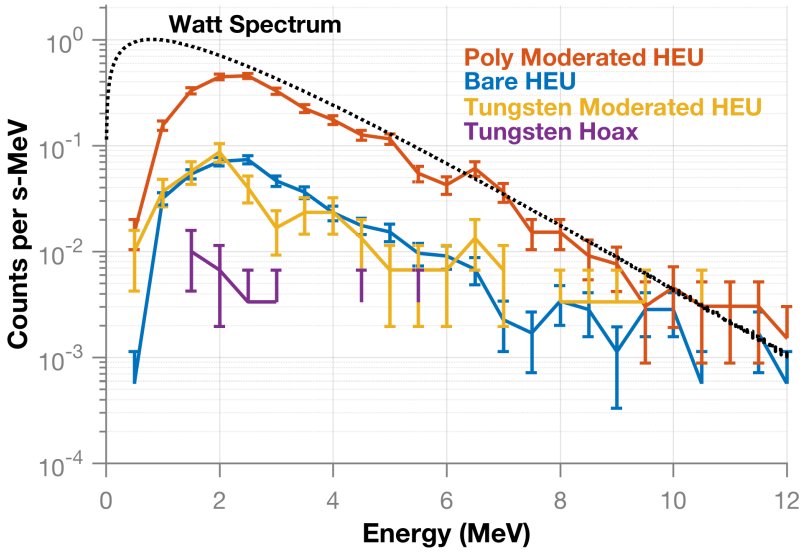

Figure 5.18: Comparison of reconstructed neutron spectra for DT experiments

Using this threshold also ensures that the image localizes high energy gamma rays that have been produced from fission, providing confidence that the interrogated item is in fact fissile material.

While the hot-spot is not located in the expected pixel, but rather the adjacent pixel, there is still high confidence that the localized gamma rays are from the HEU and not the active background. The same threshold was applied to create an image for the configuration in which no sample was present. This image, also shown in Figure 5.19 is noisy and does not localize a single source of gamma rays. The scales for both images, given in counts per second, are also different, with the hot-spot from the HEU showing 0.086 counts per second and the brightest spot in the background image showing 0.014 counts per second. By comparing this result with the gamma-ray image when the bare HEU was present, it can be concluded that the HEU was localized, but with a slight error in the location.

The reconstructed gamma-ray spectra for the bare configuration is compared to those for the other configurations in Figure 5.20. These spectra have the *background* case, in which no sample was present, subtracted. The gamma-ray spectrum for the bare HEU appears at

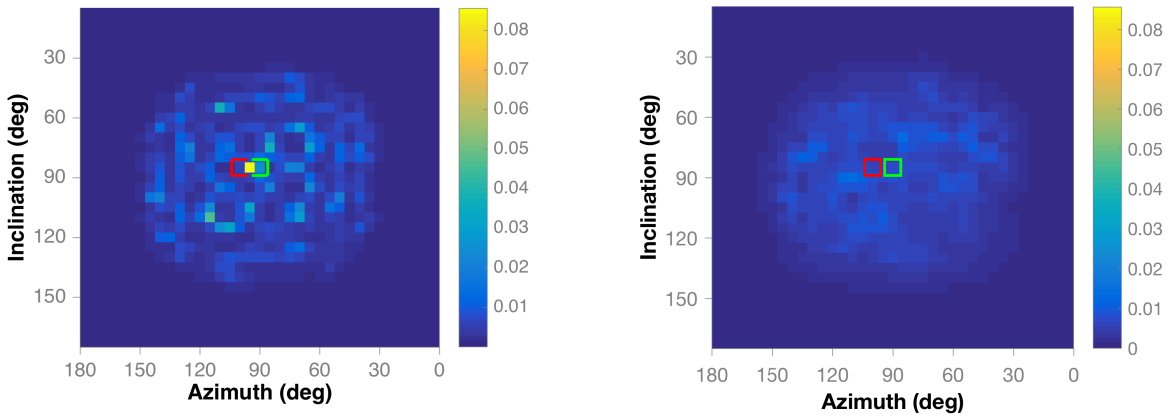

(a) (b)

Figure 5.19: The gamma-ray image of the bare HEU configuration (a) reconstructed with energies greater than 2.5 MeV. An image reconstructed with the same energies when no sample is present (b). The red boxes show the position of the DT generator and the green boxes show the position of the HEU.

a magnitude below the spectrum from the poly moderated HEU and above the spectrum from the tungsten moderator case.

Time spectra for detected counts, based on their arrival time in the system, can show the relation between count rates for each configuration as well. It is important to note that the count rate in this context is for single events, not correlated counts. Figure 5.21 shows a comparison between the counts rates with no item present, and the count rate during interrogation of the bare HEU. The count rate for single neutrons, after the pulse, is approximately double when the bare HEU is included. The gamma-ray count rate increases by a factor of 1.4.

Polyethylene moderator

Scenarios may exist in which the HEU is surrounded by low-Z material. In this case, moderation of the interrogating neutrons and emitted neutrons will occur. To evaluate this scenario, the HEU was placed in a polyethylene sphere that was 3.8-cm thick. A 1.9-cm

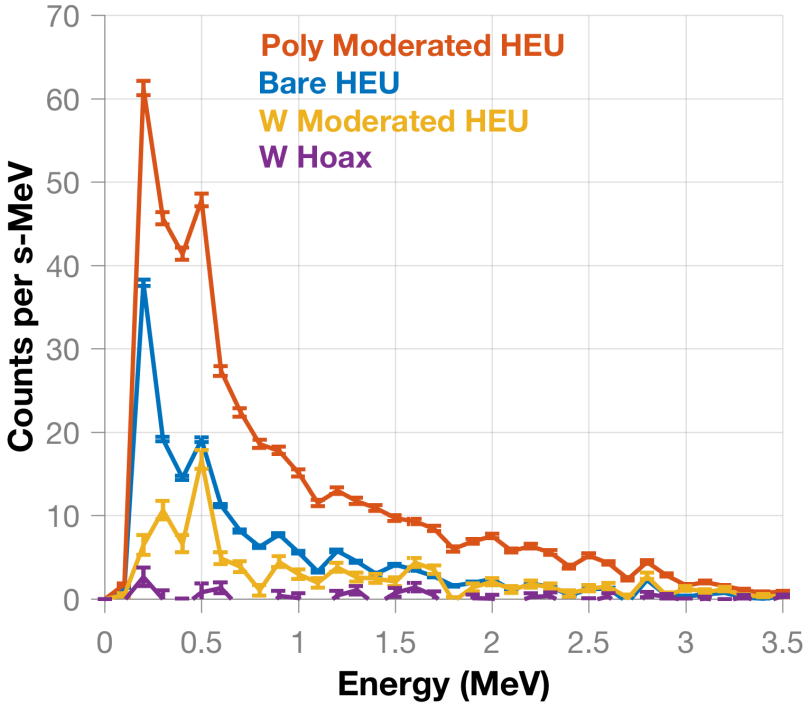

Figure 5.20: Comparison of reconstructed gamma-ray spectra for DT experiments

gap was present between the polyethylene and HEU. This configuration was measured for 22 minutes and produced a total of 1,769 neutron and 172,316 gamma-ray counts. This corresponded to counts rates of 1.34 and 130.5 per second respectively. The reconstructed spectra are shown in Figures 5.18 for neutrons and 5.20 for gamma rays (active background subtracted). In both cases, the spectra have the largest count rates out of all four cases.

The increased count rates for both particle types is due to an increases in the induced fission rate. The polyethylene shell will moderate some neutrons from the DT source, slowing them into the thermal range, which increases the (n,f) cross-section (Figure 5.1) by several orders of magnitude. Neutrons released through induced fission are also moderated by the shell and are reflected back into the HEU, which produces more fission reactions. The k_{eff} of this configuration was 0.764 compared to 0.649 for the bare configuration, which results in a total multiplication of 4.237 and 2.849 respectively.

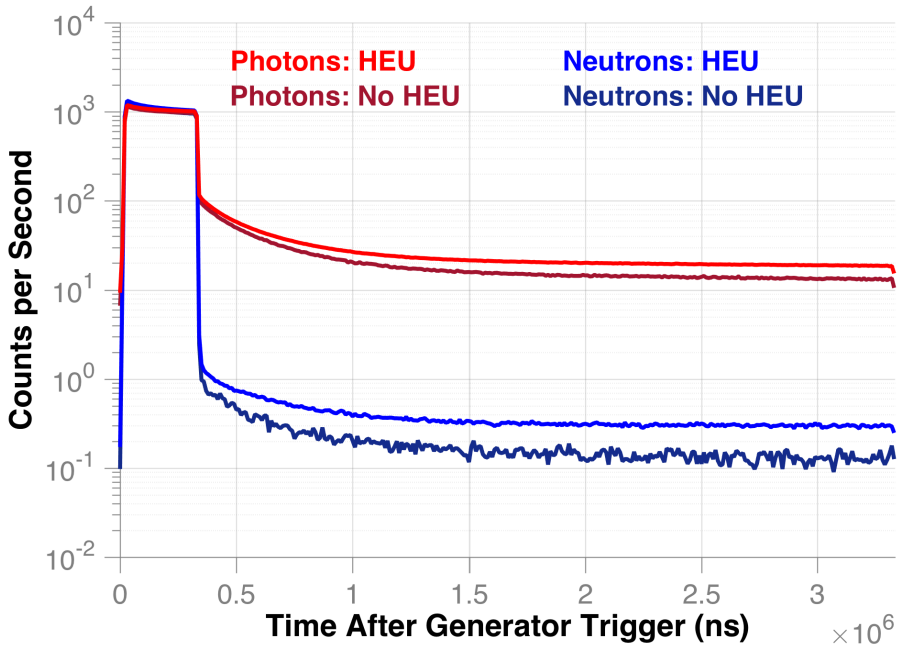

Figure 5.21: A comparison of the neutron and gamma-ray count-rates, as a function of time, during the DT generator pulse structure with and without the bare HEU present.

An increased count rate is also seen in the arrival times for neutrons in the front plane detectors. A similar analysis used for the no HEU and bare HEU cases was used to show the count rate as a function of particle arrival time in Figure 5.22. The most notable change in the structure of the arrival times is for neutrons. Immediately after the pulse, the count rate for neutrons is much higher than that of the bare HEU. About 1 ms after the pulse, the count rate is only slightly elevated compared to that of the bare HEU. The gamma-ray count rate is also slightly elevated compared to the bare HEU case, but without the dramatically increased rate directly proceeding the pulse.

The reconstructed neutron image is shown in Figure 5.23. Despite the low-z polyethylene that neutrons must travel through to be detected, the increased number of induced fission events create higher count rates which produces an image with a larger signal-to-noise ratio. This is also the case for the gamma-ray image, in Figure 5.23, which produces a clear hot-spot at the correct location. The gamma-ray image was created using a five-minute subset of

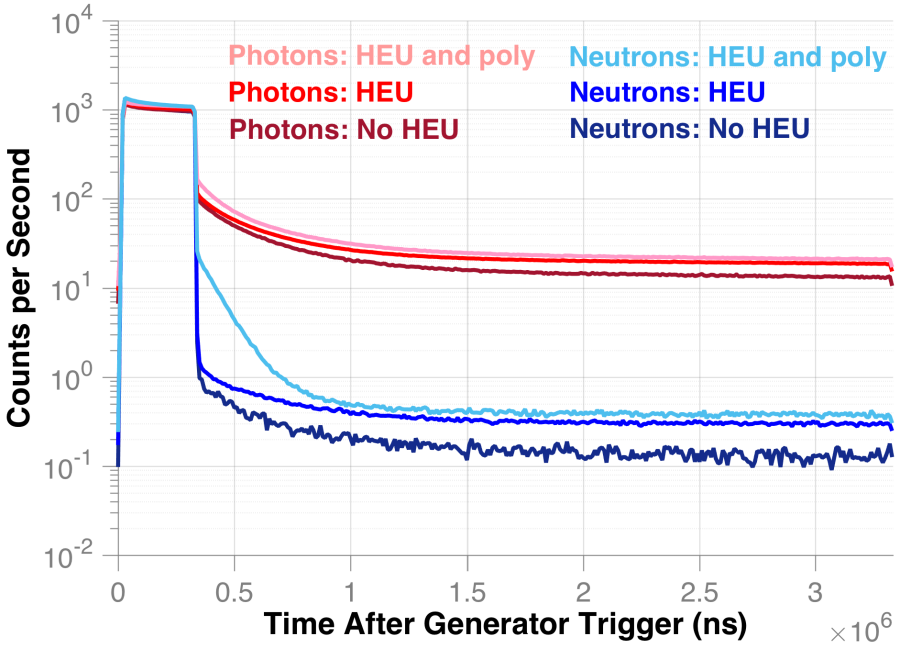

Figure 5.22: A comparison of the neutron and gamma-ray count-rates, as a function of time, during the DT generator pulse structure with no source, HEU, and polyethylene moderated HEU.

data and a 500 keV threshold, which corresponded to 23,638 events, to reduce reconstruction time.

Tungsten moderator

A tungsten moderator was used to evaluate the response to a high-z material moderating the DT neutrons and the HEU. A 10-minute measurement of this configuration was taken. The results of this measurement suffer from poor statistics but still allow some conclusions to be drawn. The correlated count rates were found to be 0.195 neutrons per second (117 total) and 95.8 for gamma rays (57,460 total). The neutron count rate is similar to the bare HEU configuration and the reconstructed spectrum is at similar magnitude in Figure 5.18 despite the limited statistics. For gamma rays, the count rate is slightly elevated from the case with no sample. Much of this increase comes from the peak at 478 keV, which is proportional

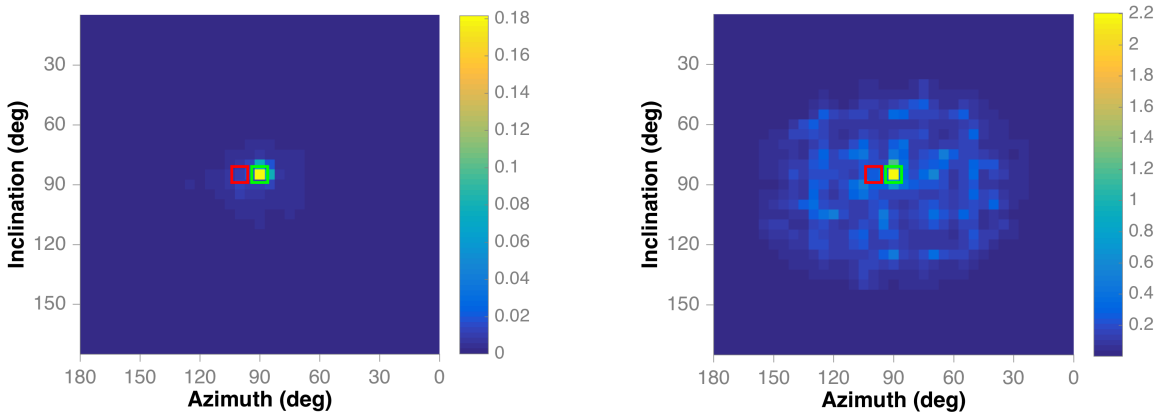

(a) (b)

Figure 5.23: The reconstructed neutron (a) and gamma-ray (b) images for the poly moderated HEU. The scale units are in counts per second. The red boxes show the position of the DT generator and the green boxes show the position of the HEU.

to the neutron flux incident on the DPI. Figure 5.20 shows that the peak for the bare HEU and tungsten moderated HEU is the same height, which supports the theory that the count increase is due to the gamma rays produced by neutron interactions in the detector optical windows. The count rates for particle arrival times in the front plane detectors gives the same conclusion as the spectra. Figure 5.24 shows that the neutron rate is similar to the bare configuration and that the gamma-ray rate is similar to the case with no sample.

The reconstructed neutron image, in Figure 5.25, shows that neutrons from the HEU, and not neutron generator are being detected. However, the limited number of total neutrons measured produces a low quality reconstructed image. Given a longer measurement time, the image would be expected to appear similar to the neutron image from the bare configuration (Figure5.17). The reconstructed gamma-ray image does not produce a hot-spot for the HEU and is similar to the configuration with no HEU sample.

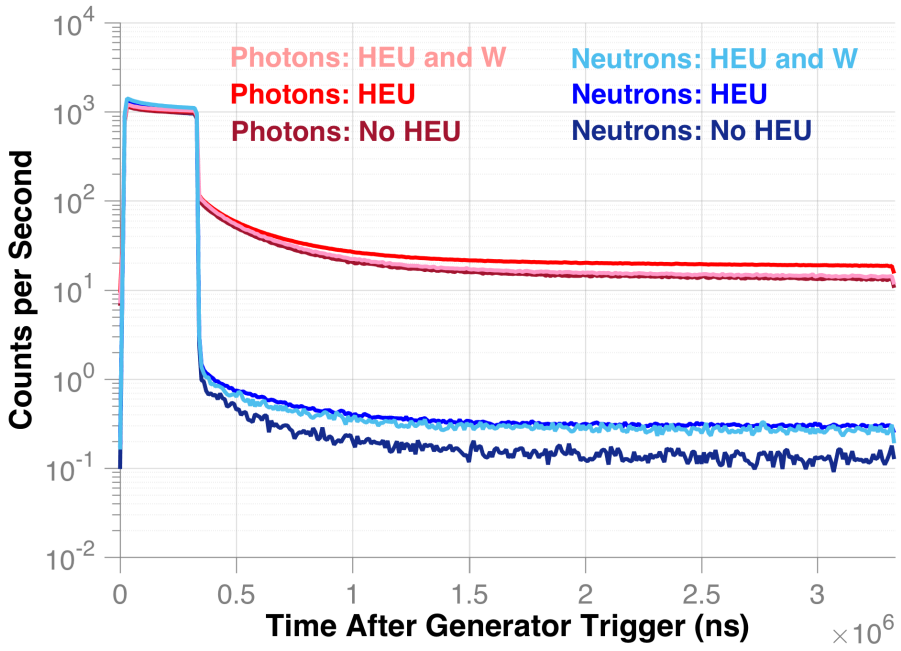

Figure 5.24: A comparison of the neutron and gamma-ray count-rates, as a function of time, during the DT generator pulse structure with no source, HEU, and tungsten-moderated HEU.

Tungsten "hoax" item

A heavy-metal "hoax" item was interrogated to show that the system will not produce a false positive. A hollow tungsten sphere with an 8.9-cm outer and 6.4-cm inner radius was measured in the same configuration as the HEU. A neutron count rate of 0.018 per second and gamma-ray count rate of 85.8 per second were recorded. These are the same count rates seen when no sample was interrogated. The time spectra for single counts, in Figure 5.26, shows that the tungsten hoax has the same rates as when no source is present. Matching correlated count rates and singles rates with the measurement of no sample provides confidence that a dense metal object cannot produce the same signal as HEU.

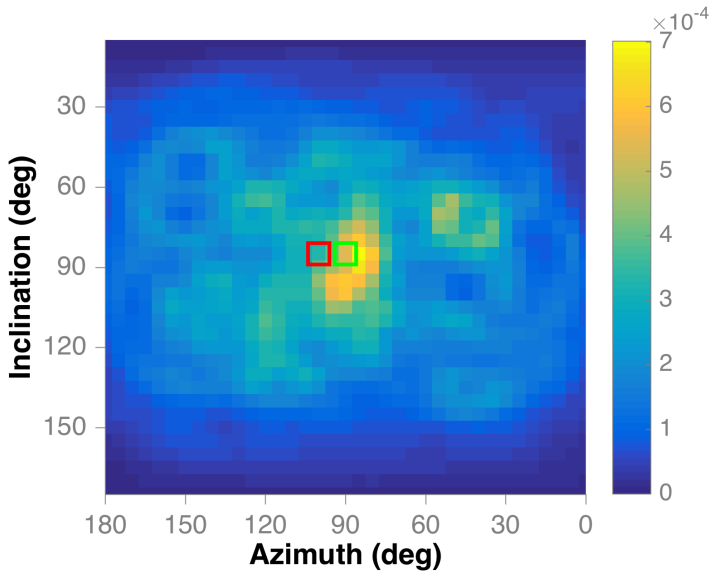

Figure 5.25: The neutron image of the tungsten-moderated HEU, interrogated with DT. The scale units are counts per second. The red box shows the position of the DT generator and the green box shows the position of the HEU.

5.6.3 DT experiment simulation

Access to large quantities of HEU for experimentation, especially for active interrogation, is expensive and difficult to obtain. As such, developing a trusted simulation tool allows for further research and characterization of active HEU detection using the DPI. The following is a description of how the above experiments were simulated using MCNPX-PoliMi with the parameters described in Chapter 2.

Simulation method

To simulate these experiments, the source neutrons from the DT generator must be distributed in time, matching the pulse structure of the generator. This requires the accurate simulation of delayed neutrons and gamma rays. The time distribution was accomplished by using the TME card with the the start and stop times for each pulse provided. To limit the

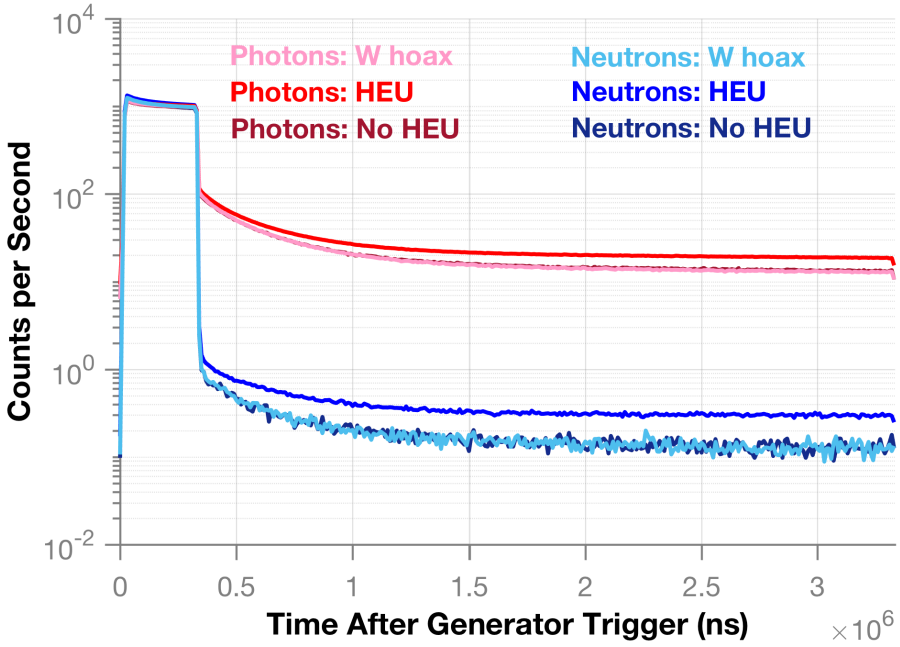

Figure 5.26: A comparison of the neutron and gamma-ray count-rates, as a function of time, during the DT generator pulse structure with no source, HEU, and a tungsten "hoax" item

number of source particles simulated, the 14.1-MeV neutrons were directed in a cone towards the HEU instead of isotropically. To achieve the full measurement time, multiple seeds were run, processed individually to create the response of the DPI, then summed. The delayed neutron option was turned on in the PHYS:N card and the 61c cross sections were used for all uranium isotopes. The delayed gamma rays were produced through use of the ACT card and run using the *group* option. Example input files for MCNPX-PoliMi and MPPost are shown in Appendix C.

Once the collision files were produced from MCNPX-PoliMi, the veto was applied by removing any interactions with a time stamp that occurred from the start of a pulse to 335,700 ns after the pulse. The collision files are then processed with MPPost to create the DPI response, with the results summed to produce the final simulated result.

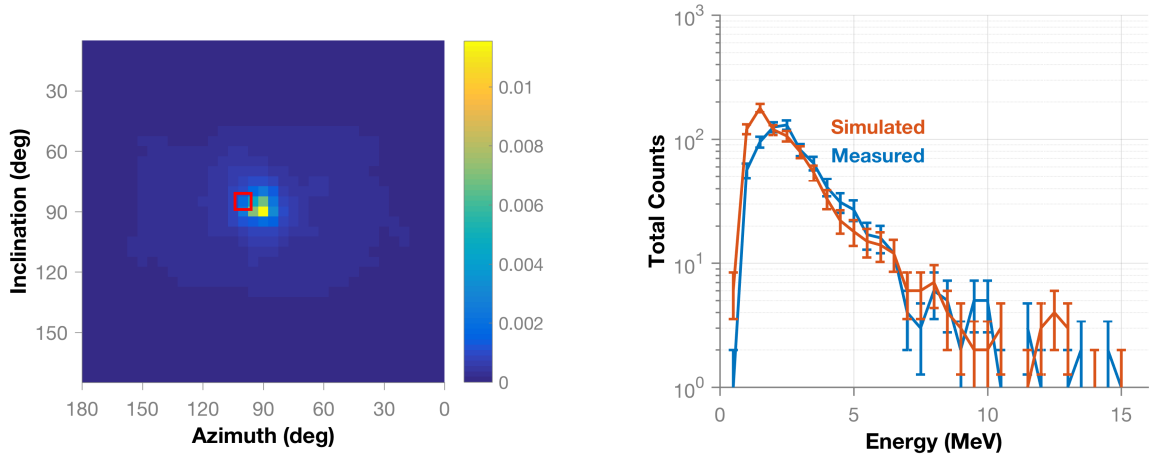

(a) (b)

Figure 5.27: The reconstructed image from the neutron simulation of DT interrogating bare HEU (a) shows a hot-spot that is similar to the measured image. The red box shows the position of the DT generator. The measured and simulated spectra are compared (b) and appear similar in shape and magnitude.

Simulated results

The above simulation method provided good agreement between measurement and simulation for neutrons. For the bare configuration, the simulated count rate, 0.239 per second, was within 10% of the measured count rate of 0.217 per second. The reconstructed image and a comparison of reconstructed energy spectra are shown in Figure 5.27. The image clearly shows a hot-spot from the HEU, and appears similar to the image reconstructed from measurement, in Figure 5.17. The green box showing the location of the HEU has been omitted for clarity because hot-spot appears one pixel below the expected location. This discrepancy may be explained by low statistics (less than 1000 total counts) or show that the experimental setup had small error in measuring the vertical position of the HEU. The reconstructed spectra, also shown in Figure 5.27, appear very similar, with the simulated spectra having a slightly increased count rate at lower energies compared to the measured spectrum.

Agreement was even better for the polyethylene configuration with a simulated neutron

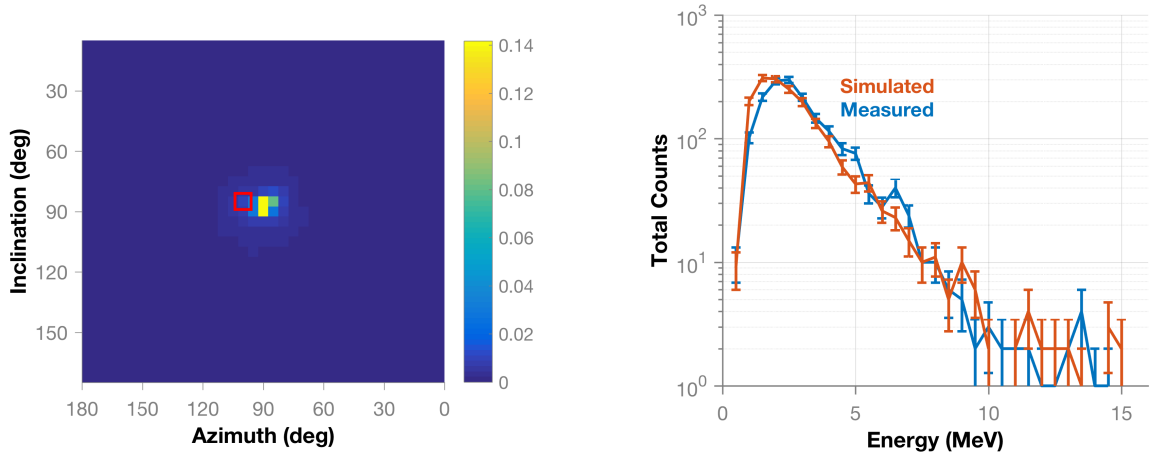

(a) (b)

Figure 5.28: The reconstructed image from the neutron simulation of DT interrogating polyethylene moderated HEU (a) shows a hot-spot that is similar to the measured image. The red box shows the position of the DT generator. The measured and simulated spectra are compared (b) and appear similar in shape and magnitude.

count rate of 1.37 per second, that was within 1.9% of the measured count rate 1.34 per second. Figure 5.28 shows the reconstructed image and a spectra comparison. The image shows a hot-spot from the HEU appears very similar to the measured image in Figure 5.23. The hot-spot skews towards the pixel below the HEU as well suggesting that there was systematic uncertainty in the vertical location of the HEU sphere. The simulated spectrum still shows a slightly higher contribution of lower energy neutrons than the measured spectrum as was also the case for the bare configuration.

For gamma rays, only the polyethylene configuration was simulated, because it was the only configuration to produce a distinct hot-spot using most of the energy range in the measurement results. The measured count rate was 44.7 per second once the active background was subtracted. The simulated count rate was 33.8 per second, which is a difference of 24%. Figure 5.29 shows the reconstructed image and a comparison of the spectra. The largest area of disagreement is at energies around 100 keV. The peak near 500 keV, from the neutron interaction in the detectors described earlier, agrees very well. At energies above 500

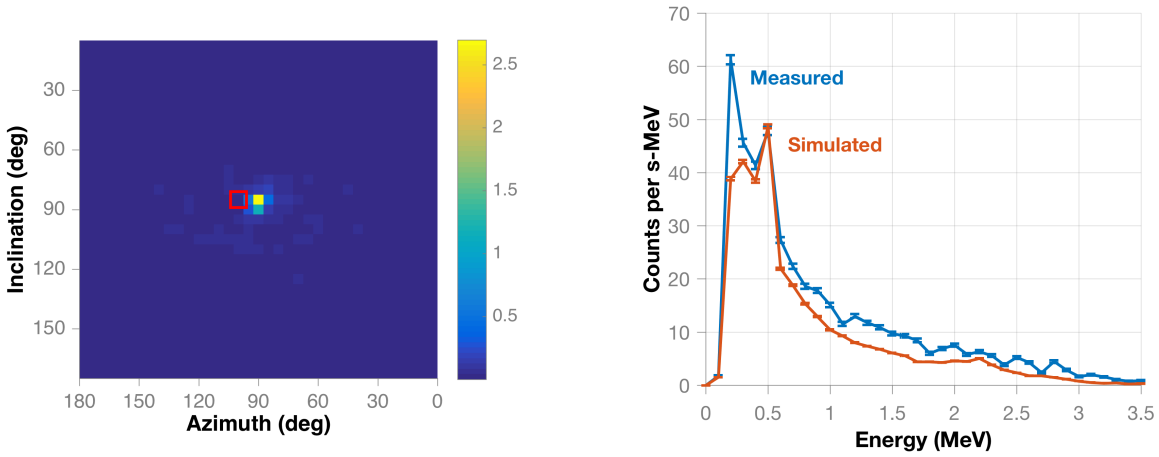

(a) (b)

Figure 5.29: The reconstructed image from the gamma-ray simulation of DT interrogating polyethylene moderated HEU (a). The measured and simulated spectra are compared (b).

keV, the measured spectrum is slightly larger. The low energy disagreement is likely due to down-scattered gamma rays in PMTs and building materials. While these features are included in the simulation, they are difficult to model due to their complexity.

The reconstructed image from the simulation does not contain the same amount of noise surrounding the hot-spot as is seen in the measured image (Figure 5.23) because the measured image includes counts recorded from both the environmental and active background.

In general, the neutron validation is sufficient to draw conclusions about quantities such as minimum detectable activities (MDA), as well as the signal-to-noise ratio expected in the image. For gamma rays, the agreement is such that simulations can be used to determine an approximate signal expected from the HEU. This valuable information can aid in measurement planning and be used to infer approximate system response. The agreement achieved is not good enough to reproduce images with the same signal-to-noise ratio or to quantify MDA. A better characterization of active and environmental background may be needed for validation improvement.

5.6.4 Neutron lifetime analysis

The neutron lifetime is a characteristic of fissile material that can be used to infer the multiplication of an item. An identical item consisting of DU or LEU by definition has a lower enrichment than HEU and thus will have a lower multiplication. Once localization has verified that neutron counts are from the interrogated item, the timing of single counts recorded in the liquid scintillators can be used to evaluate the leakage multiplication of the item. This technique has been successfully used for passive measurements of weapons grade plutonium, which showed that sources with different multiplication will produce a different neutron lifetime [127].

Measured results showing discrimination of bare and poly moderated HEU

To create the neutron time spectrum for each configuration, the detection times for neutrons detected in the 16 front-plane liquid scintillators are histogrammed based on the arrival time after the start of the generator pulse. Each spectra is normalized such that the last time bin of the pulse has a value of one. Figure 5.30 shows a comparison of the normalized spectra for different configurations. The main plot shows the neutron lifetime over the entire period after a pulse, with a bin width of 10 µs, while the inset plot shows the neutron decay within the first 3 µs after the pulse using 20 ns bins.

During the first 3 µs, the poly moderated HEU clearly decays at a slower rate than the bare HEU, tungsten hoax, and the active background when no item is present. Neutrons emitted by the HEU that are reflected by the poly back into the HEU, and create fission chains later after the DT pulse than the bare HEU does. However, the initial component of the decay does not appear sufficient to distinguish between the bare HEU, the hoax, or when there is no target. To discriminate the neutron lifetime in these cases, looking over the entire length of the entire pulse structure, shows a slower decay for the bare HEU than for the active background. Also encouraging is that the decay from the tungsten hoax follows

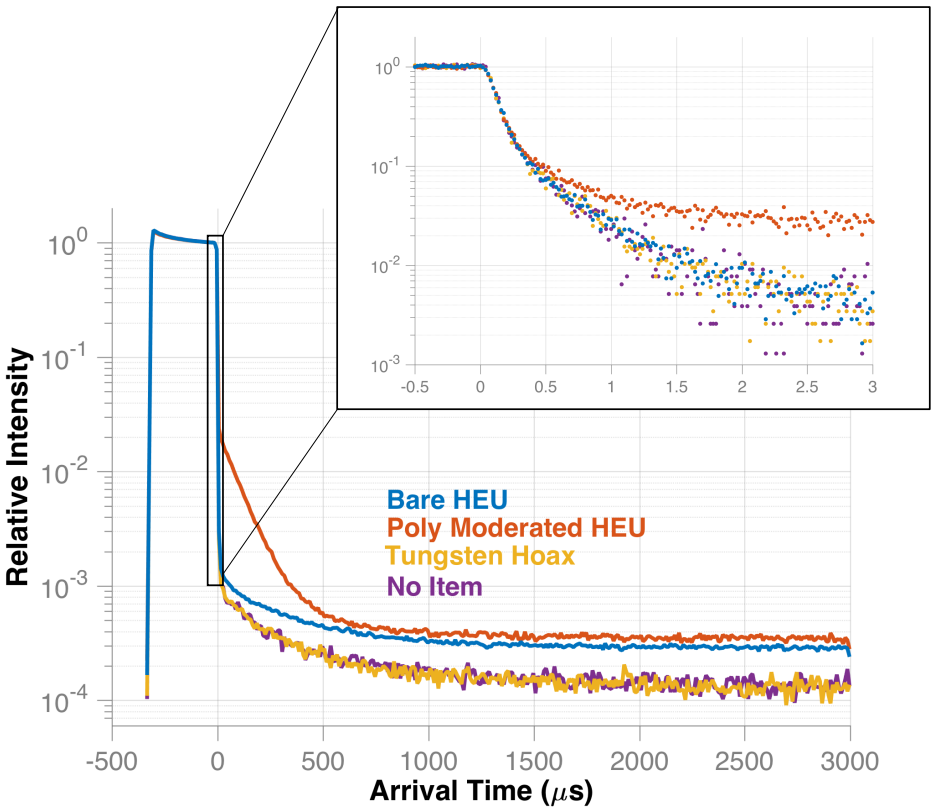

Figure 5.30: The neutron lifetime in measured configurations is compared. The main plot shows the entire structure of a pulse and the time between pulses while the inset plot shows the neutron decay behavior in the first 3 μs with a finer binning.

that of the active background, showing that no multiplication is occurring in the item.

Simulated results showing discrimination of HEU and depleted uranium

A DU sample was not available during the experiments. A large DU sphere would undergo induced fission, which would allow for localization and produce a neutron Watt spectrum. But, because the multiplication is much less in DU compared to HEU, the neutron lifetime will be different. An PoliMi simulation was performed using the experimental setup discussed previously in Section 5.6.2 with a 13.7-kg HEU sphere and a sphere of the same size substituted with DU. In both simulations, the spheres were moderated with poly to

accentuate the neutron decay. An MCNP6 KCODE calculation showed that the k_{eff} of the poly moderated DU sphere was 0.145 compared to 0.764 for the poly moderated HEU sphere.

A comparison of the neutron lifetime is shown in Figure 5.31. In the simulation, a cone of 14.1-MeV neutrons was focused on the target to improve simulation time compared to an isotropic source. As a result, neutrons detected by the DPI due to direct shine from the DT neutron generator are not included in the histogram. It is clear by examining both the first 3 µs and the entire histogram that the decay rate for HEU and DU, both moderated by poly, is distinctly different. In both cases, the HEU displays a longer neutron lifetime than the DU.

5.6.5 Conclusions from experimental and simulated DT results

A DT neutron generator was used to interrogate a 13.7-kg HEU sphere, with the neutrons and gamma rays produced from the induced fission reactions successfully imaged by the DPI. Several configurations were measured, including no sample present, bare HEU, polyethylene moderated, tungsten moderated, and a tungsten *hoax* item. It was confirmed through examination of the case with no sample, that a time veto could be used to eliminate the whole neutron signal from the generator and a large portion of the gamma-ray signal. For the bare configuration, a neutron image from the HEU was reconstructed to the correct location. The gamma-ray count rate was too small however to significantly stand out from the noise.

The polyethylene configuration produced the largest signal for both neutrons and gamma rays. Despite acting as a low-Z shield for neutrons leaving the HEU, the polyethylene also moderated neutrons interrogating the HEU, causing more induced fission chains to occur later after generator pulse. This effect was seen by examining the neutron lifetime for the polyethylene moderated and bare configuration (Figure 5.22). As expected, the tungsten

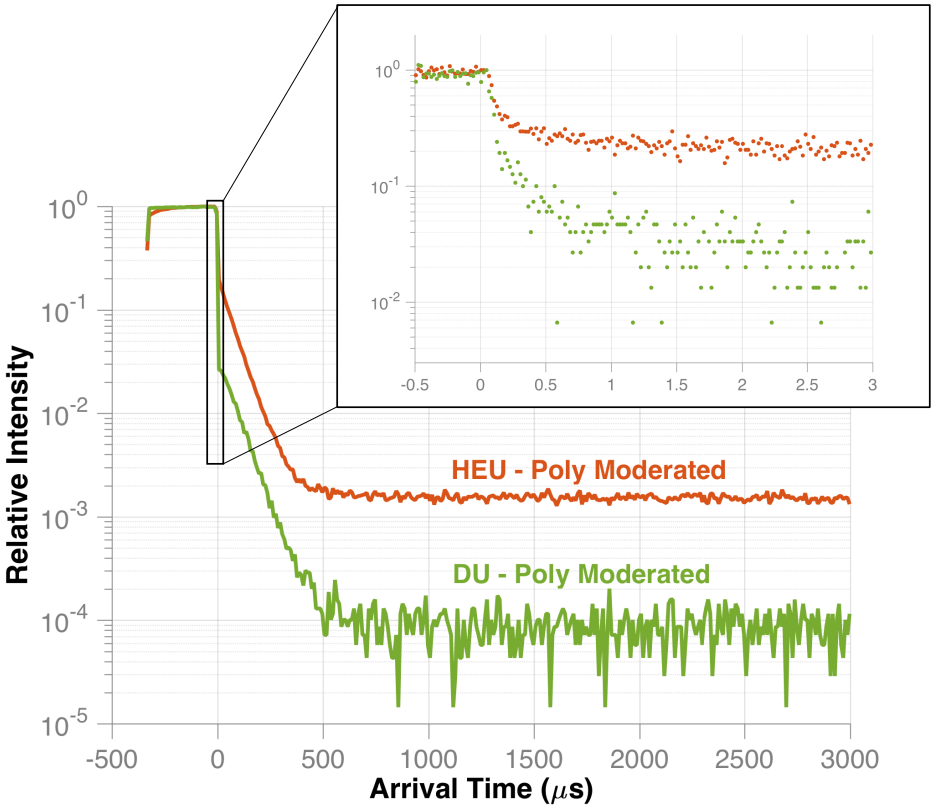

Figure 5.31: Simulated neutron lifetime is compared for HEU and DU, both moderated by poly. Both the entire pulse structure and the first 3 µs (inset) show a difference between the neutron lifetime for the HEU and DU. The HEU neutron population decays at a slower rate than the DU due to a higher probability of induced fission.

moderator eliminated the gamma-ray signal from the HEU but only caused a small decrease in the neutron signal. The measurement using the tungsten *hoax* appeared the same as when no sample was present, which provided more confidence that the measured signal was due to induced fission from the HEU and not due to other interactions in a heavy metal.

MCNPX-PoliMi was shown to produce a neutron simulation of the bare and polyethylene configurations that agreed very well with measurement, with both count rates agreeing within 10%. A simulation of the gamma-ray signal from the polyethylene configuration only agreed to within 25% of the measured result but contained the same shape and some spectral

features present in the measurement.

Finally, the neutron lifetime was examined to infer the relative multiplication between different configurations. Measured results showed that the poly moderated HEU with a larger multiplication will have a slower neutron decay than configurations with a smaller multiplication. A simulated result showed that this technique can be used to discriminate between HEU and DU.

5.7 AmLi experiments

The experiments with AmLi provided an opportunity to examine properties such as the induced fission spectrum and timing properties of the neutron events. The energy spectrum of neutrons emitted from AmLi, shown in Figure 5.2, is below the threshold detected by the system. As opposed to the continuous DD interrogations, the AmLi interrogation does not need energy thresholds to be used in the analysis. These experiments were permitted to dwell overnight, which provided excellent statistics.

5.7.1 Experimental setup

The HEU sphere was placed at a distance of 116 cm from the DPI with angular coordinates (90°, 85°). Surrounding the HEU were four cylindrical lead pigs with walls each 2.54-cm thick that housed four AmLi sources. Each AmLi source had a neutron emission of approximately 2.5×10^5 per second. Figure 5.32 shows the experimental setup. Rocky Flats shells 1-24, creating a mass of 13.1-kg were measured for 850 minutes, with shells 13-24, creating a 10-kg hollow sphere, measured for 850 minutes as well.

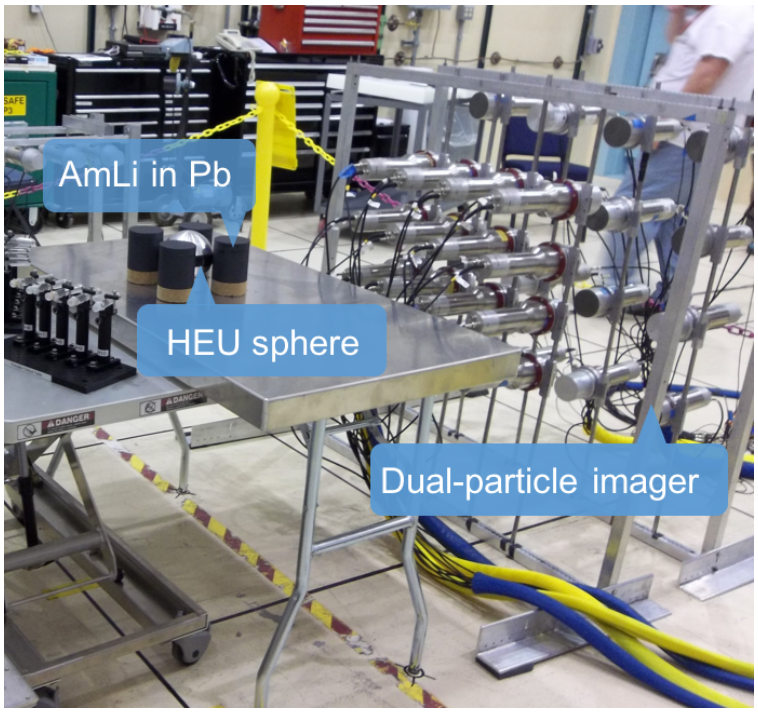

Figure 5.32: Experimental setup showing active interrogation of HEU with AmLi

5.7.2 Results

The neutron count rate measured for the 13.7-kg sphere was 0.512 per second. For the 10-kg mass the count rate was 0.296 per second. This result was expected due to the difference in mass and multiplicities of the configurations. With a multiplication of 0.649, the 13.7-kg mass was expected to produce more neutrons when interrogated compared to the 10-kg mass with a multiplication of 0.392. Both neutron images had hot-spots correctly locating the source and are shown in Figure 5.33. A comparison of the reconstructed neutron spectra is shown in Figure 5.34.

The gamma-ray count rate was the same between the two masses, with the 13.7-kg mass having a count rate of 23.5 per second and the 10-kg mass having a slightly higher count rate of 24.8 per second. A comparison of the spectra are shown in Figure 5.35. The rates are similar because gamma rays originating in the center of the more massive sphere are attenuated before escaping the sphere. Only gamma rays from a small part of the surface

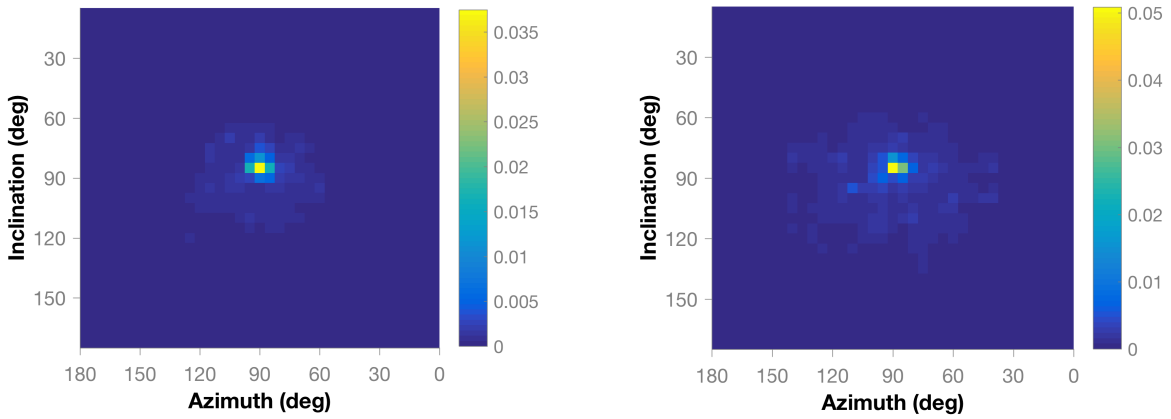

(a) (b)

Figure 5.33: Reconstructed neutron images from the 10-kg hollow HEU sphere (a) and 13.7-kg sphere (b). The scale units are counts per second.

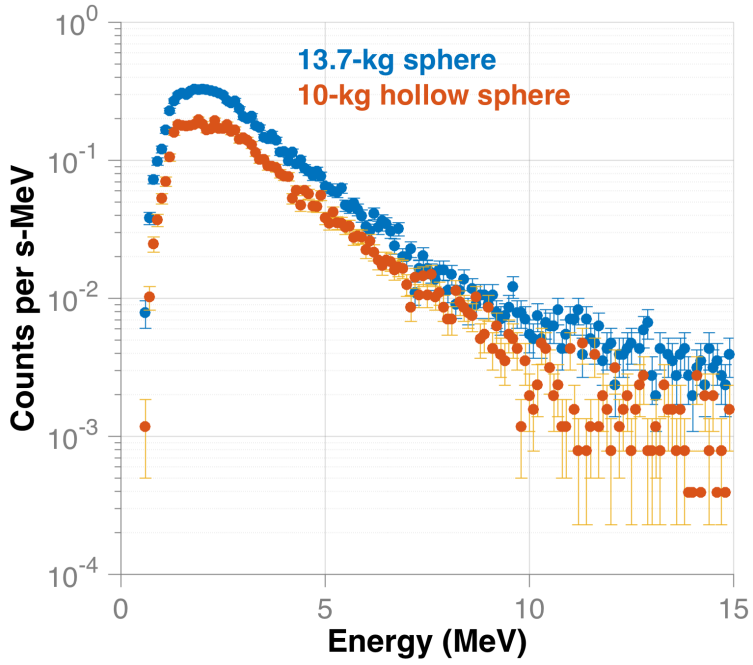

Figure 5.34: Comparison of reconstructed neutron spectra for the AmLi interrogation of 13.7 and 10-kg masses of HEU.

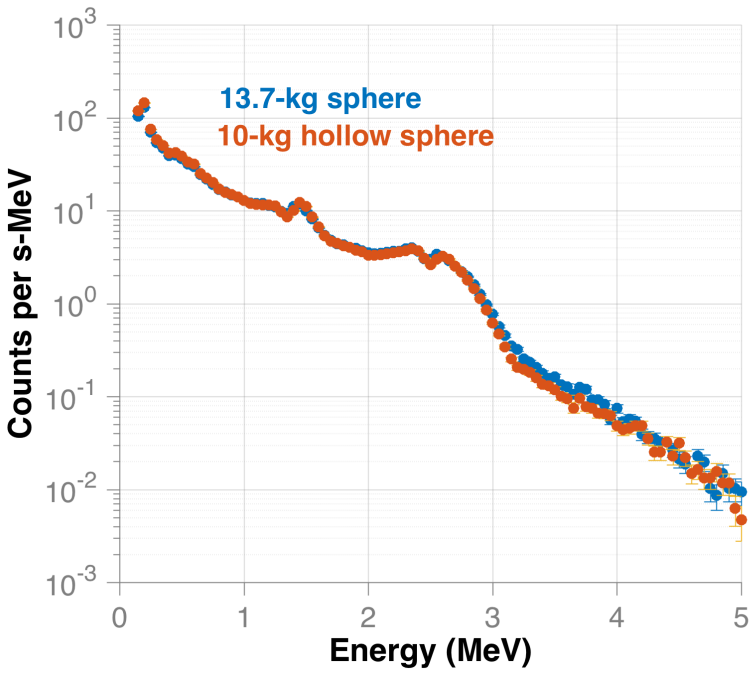

Figure 5.35: Comparison of reconstructed gamma-ray spectra for the AmLi interrogation of 13.7 and 10-kg masses of HEU.

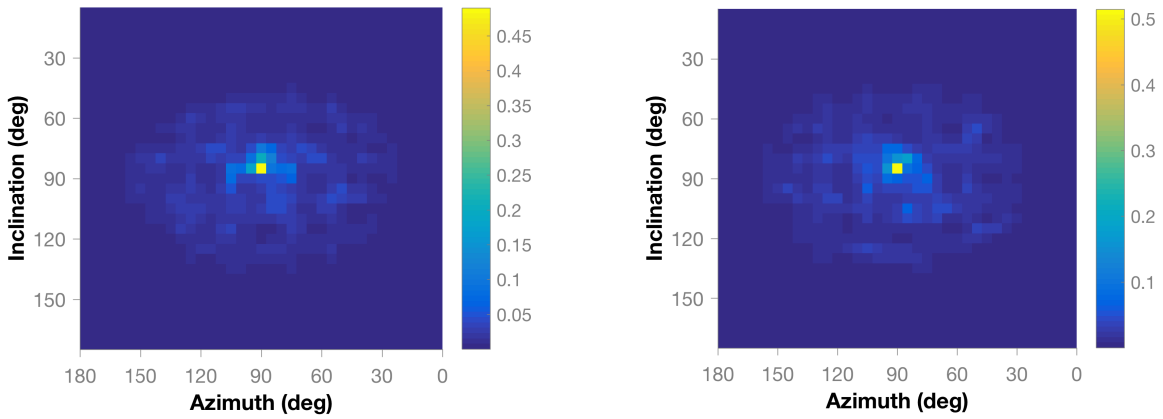

(a) (b)

Figure 5.36: Reconstructed gamma-ray images from the 10-kg hollow HEU sphere (a) and 13.7-kg sphere (b). The scale units are counts per second.

were detected. One explanation for the slightly larger count rate from the smaller mass is a slight difference in the measurement geometry between the two experiments. The setup was changed in between the measurements and a slightly different distance or a rearrangement of the AmLi sources may have caused the discrepancy. Both images are shown in Figure 5.36 and correctly located the source. Only 30 minutes of the measurements were used for the images to cut down on processing time and a 500 keV threshold was used in the images to improve quality.

Inferring multiplication

The AmLi experiments provided sufficient statistics to examine the neutron lifetime in both masses of HEU. Trahan demonstrated in [127] that liquid scintillators were capable of producing Rossi-alpha distributions for un-moderated fast neutrons. The Rossi-alpha technique was developed to examine the time properties of a fission chain by assuming that each detected neutron initiated a fission chain [128]. Type-I Rossi-alpha distributions were created for both AmLi experiments and compared to distributions for ^{252}Cf, a non-multiplying spontaneous fission source, and PuBe, in which the neutron emission is not correlated. The Rossi-alpha distributions were created using a window size of 0.05 seconds, with the maximum of each distribution normalized to one and the flat continuum at the end subtracted. Figure 5.37 shows a comparison of the four distributions. The two HEU masses and the ^{252}Cf were all measured at the same location, 116 cm from the system. The PuBe was measured slightly closer at a distance of 108 cm.

The distributions show a clear difference in the neutron lifetime from the correlated sources (HEU and ^{252}Cf) versus the PuBe, which produces uncorrelated neutrons. The more massive HEU has longer neutron lifetime than the smaller mass. This was expected based on the simulated multiplications calculated in Section 5.4. The spontaneous fission source ^{252}Cf follows the same decay rate as the 10-kg HEU mass For this source, the decay

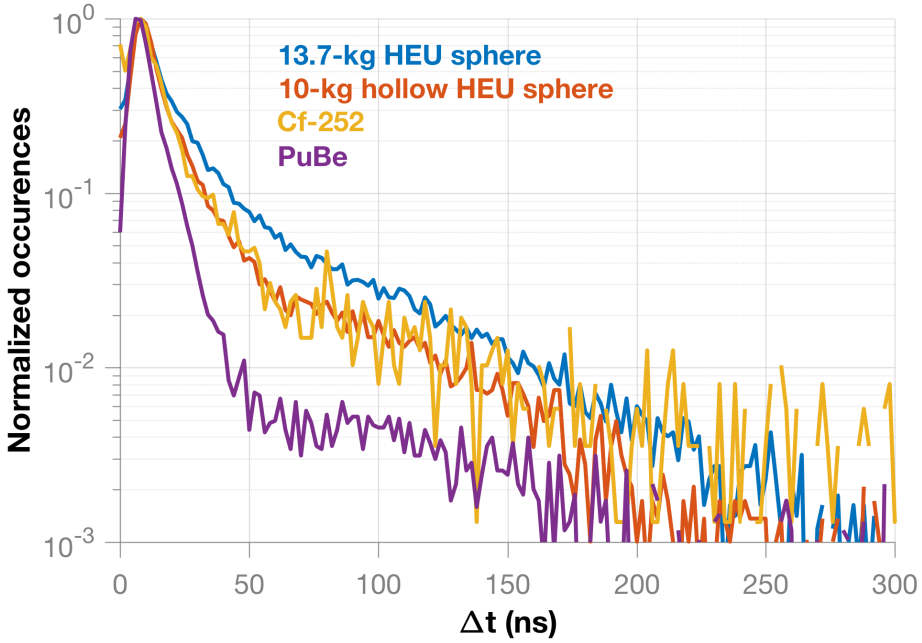

Figure 5.37: Rossi-alpha distributions for two different HEU masses, ^{252}Cf, and a PuBe source

characteristic is not a result of multiplication but occurs from correlated neutrons produced through spontaneous fission. The PuBe neutron lifetime decays very quickly as expected because the neutrons are uncorrelated.

5.7.3 Conclusions from AmLi experiments

These experiments showed that the DPI could detect neutrons and gamma rays from induced fission events in HEU by AmLi. Two configurations of HEU were compared through count rates and Rossi-alpha distributions. The larger mass, with a higher multiplication, gave a larger neutron count rate and had a longer neutron lifetime in the Rossi-alpha distribution than the smaller mass. The gamma-ray count rates were similar for both HEU masses. While a good hot-spot was produced using the gamma rays in images of both masses, similar count rates suggest that gamma rays from the AmLi may be a larger fraction of the total than gamma rays from induced fission.

5.8 Active interrogation conclusions

The largest neutron count rate for the 13.7-kg bare HEU configuration was produced by the AmLi interrogation. After an adjustment using the inverse square law, a count rate of 0.287 neutrons per second would be expected at a distance of 155 cm from the source. For comparison the same HEU mass interrogated by the DT generator produced a count rate of 0.217 neutrons per second at a distance of 155 cm. The gamma-ray image also produced a more distinct hot-spot without the need to create an energy threshold. While AmLi may be advantageous to use due to simplicity compared to a neutron generator, they must be placed very close to the target item which may not be practical. The use of a neutron generator allows for a larger standoff.

All three forms of active interrogation showed that the HEU could be localized with either a gamma ray or neutron image. All three cases used a different method to isolate the neutrons and gamma rays created from induced fission compared to the interrogating neutrons. For the DD experiments, an energy threshold and time-of-flight cutoff localized the neutrons from the HEU. An energy cutoff also produced a clear image of the gamma rays by eliminating low energy contributions from the continuously run generator. The DT experiments showed that a time veto used with a pulsed interrogating source successfully discriminated the 14.1-MeV neutrons produced from the DT neutron generator. Finally, the AmLi experiments demonstrated that using a low energy neutron source does not require any data cuts. These experiments all demonstrate successful localization and characterization of the HEU, providing more options to address the challenge of HEU detection for non-proliferation.

Chapter 6

Conclusions and future work

6.1 Summary and conclusions

Non-proliferation demands new methods for better material accountability to aid in the peaceful use of nuclear material. Radiation imaging is a desirable technology for this application because it provides the ability to localize sources of radiation and perform characterization. This work demonstrated the effectiveness of the DPI to both localize and characterize SNM. The system was designed to function as a fast neutron and gamma-ray imager while also providing spectroscopy. This unique combination of information provides a robust means of detecting shielded nuclear material because neutrons can effectively penetrate a high-Z shield and gamma rays can penetrate a low-Z shield.

The DPI was built using a two-plane design that combined a Compton and neutron scatter camera. Liquid organic scintillators proved a great choice for the scatter plane detectors because of their sensitivity to both neutrons and gamma rays while allowing the use of pulse shape discrimination to identify particle type. The back plane used more organic liquid scintillators as the second scatter plane for neutrons and NaI(Tl) scintillators as the absorption plane for gamma rays. An experiment using a ^{252}Cf source, a good surrogate for SNM, demonstrated that the DPI could accurately locate and reconstruct the energies of neutrons and gamma rays emitted through fission.

While source localization was achieved, conventional image reconstruction methods failed in two key areas. Backprojection produced images with artifacts and a low signal-to-noise ratio. MLEM greatly improved the image quality, but is an iterative method that requires a stopping condition to produce good image quality. To address these issues, the SOE method was applied to the DPI for both neutron and gamma-ray image reconstruction. Through evaluation of different source distributions, this method showed that image quality was generally improved compared to MLEM and that image quality was not heavily dependent on the number of iterations performed.

Because the SOE technique was previously only applied in medical imaging applications, no mechanism existed for isolating the energy spectra from a measurement containing multiple sources. This work designed a method that allowed isolated energy spectra, for both neutrons and gamma rays, to be extracted from any pixel in the image. An experiment with ^{22}Na and ^{137}Cs showed that individual gamma-ray spectra with unique energies could be isolated and used to identify each source. This same concept was tested with two neutrons sources, ^{252}Cf and PuBe, that emitted different neutron spectra. A comparison of the isolated spectra showed a clear difference and allowed the sources to be discriminated from one another. Finally, this method was tested for an experiment with a 4.1-kg disk of WGPu, ^{252}Cf, and AmBe. The results concluded that SOE spectrum isolation could be used to discriminate the AmBe neutron spectrum from the Watt spectrum produced by the other two sources, and that the isolated gamma-ray spectrum discriminated the WGPu from the ^{252}Cf.

To localize and characterize HEU, active interrogation was needed to produce a detectable signal. Experiments with a 13.7-kg HEU sample and three different neutron interrogation sources showed that three different methods were effective to discriminate the induced fission particles from the interrogating particles. For a continuously operated DD neutron generator, applying an energy and time-of-flight threshold eliminated the 2.5-MeV neutrons produced

by the neutron generator in the image, displaying only neutrons from induced fission. For experiments using a pulsed DT neutron generator, a veto was applied to eliminate particles detected during the pulse. This technique was used to measure bare and moderated configurations of HEU and a hoax item. When HEU was present it was localized and the neutron and gamma-ray spectra from induced fission were successfully reconstructed. The neutron lifetime also showed a difference between configurations with different multiplications. Simulated results showed that this method could be used to discriminate between HEU and DU samples. Finally, sensitivity of the DPI to the interrogating neutrons was avoided altogether by using AmLi sources. Localization and spectroscopy were achieved for the 13.7-kg HEU sample and a smaller 10-kg HEU sample and Rossi-alpha distributions were used to identify the more massive object.

6.2 Proposed future work

The DPI proved an effective tool for imaging neutrons and gamma rays as well as providing characterization of nuclear material. However, some future modifications to the system and further algorithm development can greatly improve performance. For example, the largest limitation to system resolution is the size of the detector cells. This has been addressed to create a smaller version of the DPI using stilbene pillars and silicon photomultipliers (SiPMs) [129]. Stilbene is still very expensive compared to organic liquid scintillators but SiPMs are inexpensive. Using an array of SiPMs to collect light created in liquid or segmented plastic scintillators could greatly improve image resolution and allow the shape of objects to be detected.

Modifications to the SOE algorithm may allow for better reconstructed image quality. The underlying Bayesian prior used to create the acceptance probability for origins can be further optimized depending on system parameters or application specific knowledge, such as

an expected source distribution [106]. Other efforts to improve SOE are focused on improving reconstruction time through parallelization of the algorithm [52, 107]. These techniques have examined handling iterative origin sampling in parallel using graphical processing units.

Furthermore, improvements can be made to the implementation of the SOE algorithm to improve spectral isolation if required by the application. As implemented in this work, SOE approximates a uniform efficiency across the image space. Using a simulated system response matrix that calculates spatially-dependent efficiencies can improve localization. Adjusting individual event probabilities based on these efficiencies would likely remove some artifacts primarily seen in the SOE gamma-ray images and improve the appearance of extended sources. The response matrix could also be used to unfold isolated spectra, which would improve the resolution and aid in isotopic identification. This technique was partially demonstrated in [130]. The robust energy information provided by the system and spectral isolation may also provide the necessary information to infer or quantify intervening material present between sources and the DPI.

Because SOE preserves the individual properties associated with each event, an opportunity exists to examine time spectra for double-scatter events. This would allow the neutron lifetime to be isolated for multiple sources to determine if the source is multiplying or not. Detection of a correlated neutron event with a gamma ray from the same fission or fission chain would also allow for time-correlated pulse-height analysis to be isolated for multiple sources [131].

Finally, improvements can be made to achieve better localization and characterization for HEU in active interrogation settings. Moving the system closer to the interrogated item would increase the source-to-background ratio for gamma rays, which could provide for more interesting analysis. To achieve better statistics, the use of a collimated DT source would allow for continuous interrogation (without pulsing) and all measured counts could be attributed to the HEU without use of a veto. Finally, a more rigorous characterization

of the neutron lifetime and Rossi-alpha spectra must be performed and tested with items of differing mass and enrichment, which would allow for conclusions to be drawn about the mass of ^{235}U in an item.

Appendix A

Contextual usage scenarios for gamma-ray imaging

VII. Annex: contextual usage scenarios

CUS	Category	Description	Drawbacks or limitations of the current method	What could be the advantage of the new method	Comment / Critical assumptions to be verified
CUS01	CA	The inspector enters room/lab full of cupboards, containing several rad sources. While carrying out interviews, he captures a gamma image of the room. He is able to verify the presence of SNM that may be masked by other rad sources before leaving the room, and reorient his inspection accordingly.	Time consuming Risk of false negative (masking)	Simultaneous localization of multiple SNM	Rather big to carry around; handheld would be more convenient. Sensitivity is questionable, especially in comparison with Backpack of HM-5. **Critical assumptions**: Robust to masking scenario (NM+background); counting discrete sources; robust to shielding.
CUS02	CA	The inspector enters room/lab full of cupboards. He leaves the camera operating during the rest of the CA and captures a gamma image of the room. He is able to verify the presence of NM before the end of the CA, and reorient his inspection accordingly.	Time consuming Risk of false negative (masking)	Use time during inspection to keep on integrating gamma measurements	Need tampering/video indications to remain unattended. Rather big to carry around; handheld would be more convenient. Sensitivity is questionable, especially in comparison with Backpack of HM5 **Critical assumptions**: same as CUS 1 (longer)

15

CUS10	Managed Access	The inspector captures a gamma image from behind the curtain, in an area where the access has been managed by the operator. Without capturing sensitive visual information, he is still able to verify the presence (or confirm absence) of NM	No possibility to make precise measurement, other than presence/absence of NM	Detailed localization of NM, partially confirming operator's declaration	Acceptability to be confirmed
CUS11	Managed Access	The inspector captures a gamma image from a room containing sensitive equipment that is not safeguards relevant, or from a room that he cannot/does not want to enter (clean room). He makes a gamma image, without capture sensitive visual information, or without entering the room,.		Document the presence of NM, without capturing sensitive information	
CUS13	Glovebox	A gamma image of a whole glovebox containing multiple small size containers is captured to assess the presence of SNM.	handling of each PU sample separately If multiple assets inside a glovebox, inspector might omit measuring some of them	Remote measurement, limited handling Several samples at a time Capture the whole glovebox content at once	In combination with neutron measurement method. **Critical assumptions**: counting of discrete sources behind shielding + background + discrimination
CUS14	Safety	During briefing or training, an image of the room along with the gamma sources is shown to inspectors. A map of the gamma radiation is provided to the inspectors. During site activities, the inspector remembers more vividly the safe areas and is able to limit their dose rates.		Knowing visually where the sources are located, in combination with using a dosimeter, is useful when we can act on them (shield or move them)	We are measuring gamma source location, not dose rate, which would be more relevant.

CUS15	Safety	Inspector captures a gamma image of the room where he is about to work. He quickly visualizes the source of irradiation and can determine a safe working area, with low gamma dose rates.			Contamination visualization is usually not possible Should be fast and handheld to be practical Dose reading is more relevant Alternative: HM-5, dosimeter See CUS14 for better scenario
CUS19	Waste	Wastes have been buried underground. A gamma image of the landscape is taken over a long exposure period. Anomalies/hotspots are identified and localized for further verifications.			very low activities Need tampering indication for unattended operation + outdoor operating capabilities (+batteries)
CUS20	Waste	Various wastes containing NM have been stored in a pit. A gamma picture is taken; spots with NM items are identified, enabling a general verification of NM declarations. Further detailed verifications are then carried out.	None available	Provide NM accountancy	Improving using 3D scanning?
CUS21	Waste	Wastes containing NM have been stored in a pit. A gamma picture is taken establishing a reference fingerprint used as C/S measure; the image is compared to a previous one and document any significant change that occurred between the inspections.	None available	Provide containment capabilities	Possibly use 3D scanning/visible image/thermal imaging to contain the well and prove that no changes have occurred. Automated comparison needs to match features, in order to cope with different viewpoints.

Appendix B

Example of SOE MATLAB code

```
function sol = SOE(particle,SM,meshSize,...
    histPct,histBinning,aFactor,numEvents,ergLow,ergHigh,phiROI,thetaROI)

% % particle: Specifiy 'n' or 'p' for neutron or gamma-ray
% % SM: System matrix of backprojected cones
% % meshSize: Desired size of image pixels
% % histPct: Pre-alocation size for energy spectrum histograms in fraction
%      of total counts (0.01 is usually a good value)
% % histBinning: Binning width for number of origins in a pixel/energy bin
% % aFactor: Used to adjust the acceptance factor, default is 1.0
% % numEvents: Number of events to use in reconstruction
% % ergLow: Lower energy threhold
% % ergHigh: Upper energy threshold
% % phiROI: Specify phi coordinates of a region of interest to
%      sum energy spectrum
% % thetaROI: Specify theta coordinates of a region of interest
%      to sum energy spectrum


%%%%%%%%%%%% Set random number generator to default seed %%%%%%%%%%%%%%%
rng('default')

%%%%%%%%%%%% Initialize varibles that were not specified %%%%%%%%%%%%%%%
if ~exist('numEvents','var') || isempty(numEvents)
    numEvents = [];
end

if ~exist('ROI','var') || isempty(ROI)
    ROI  = [];
end
```

```
if ~exist('histPct','var') || isempty(histPct)
    histPct = 1;
end

if ~exist('fits','var') || isempty(fits)
    fits = 0;
end

if ~exist('ergLow','var') || isempty(ergLow)
    ergLow = 0;
end

if ~exist('ergHigh','var') || isempty(ergHigh)
    ergHigh = 100000;
end

if ~exist('phiROI','var') || isempty(phiROI)
    phiROI = [];
end

if ~exist('thetaROI','var') || isempty(thetaROI)
    thetaROI = [];
end

neutronThreshold = 0;

if isempty(phiROI)
    clear phiROI
end

if isempty(thetaROI)
    clear thetaROI
end

%%%%%%%%%%%%% Load detected event data %%%%%%%%%%%%%%%
if particle == 'n'
    load('Correlated_events_n.mat');

end
if particle == 'p'
    load('Correlated_events_p.mat')
end

if isempty(numEvents)
    numEvents = length(events(:,1));
```

```
end

countsUsed = numEvents;

eventLength = length(events(1:numEvents,1));

if particle == 'n'
    totEvents = zeros(pointsPerCone * eventLength, 14);
end
if particle == 'p'
    totEvents = zeros(pointsPerCone * eventLength, 19);
end


for i = 1:pointsPerCone
    totEvents(eventLength*i-eventLength+1:eventLength*i,:)...
        = events(1:eventLength,:);
end

%%%%%%%%%%%% Load system matrix of backprojection cones %%%%%%%%%%%%%%%
load([SM,'.mat'])

display('Loaded System Matrix')

for i = 1:length(systemMatrix(1,:))
    if i == 1
        systemMatrix(:,i) = systemMatrix(:,i);
    else
        systemMatrix(:,i) = systemMatrix(:,i) + systemMatrix(:,i-1);
    end
end

for i = 1:length(systemMatrix(:,1))
    systemMatrix(i,:) = systemMatrix(i,:) ./ max(systemMatrix(i,:));
end

%%%%%%%%%%%% Modify event data to include only desired events %%%%%%%%%%
if particle == 'n'
    goodCount = 1;
    goodEvents = zeros(length(totEvents(:,1)),14);
    for i = 1:length(totEvents(:,1))
        if totEvents(i,3) == 1 && totEvents(i,1) > (ergLow./1000)...
                && totEvents(i,1) < (ergHigh./1000)
            goodEvents(goodCount,:) = totEvents(i,:);
            goodCount = goodCount + 1;
```

```
        end
    end
    totEvents = goodEvents(1:goodCount-1,:);
end

if particle == 'p'
    goodCount = 1;
    goodEvents = zeros(length(totEvents(:,1)),19);
    for i = 1:length(totEvents(:,1))
        if totEvents(i,3) == 1 && totEvents(i,2) > 0 && totEvents(i,1)...
               > (ergLow./1000) && totEvents(i,1) < (ergHigh./1000)
            goodEvents(goodCount,:) = totEvents(i,:);
            goodCount = goodCount + 1;
        end
    end
    totEvents = goodEvents(1:goodCount-1,:);
end

numEvents = length(totEvents(:,1));

eventData = zeros(numEvents,8); %Vx,Vy,Vz,theta,erg,phii,thetai

%%%%%%%%%%%% Specify and convert detector numbers to x,y,z coordinates %%%
frontPlane(1,1,1:3) = [-22.5 17.55 -22.5];
frontPlane(1,2,1:3) = [-22.5 17.55 -7.5];
frontPlane(1,3,1:3) = [-22.5 17.55 7.5];
frontPlane(1,4,1:3) = [-22.5 17.55 22.5];
frontPlane(2,1,1:3) = [-7.5 17.55 -22.5];
frontPlane(2,2,1:3) = [-7.5 17.55 -7.5];
frontPlane(2,3,1:3) = [-7.5 17.55 7.5];
frontPlane(2,4,1:3) = [-7.5 17.55 22.5];
frontPlane(3,1,1:3) = [7.5 17.55 -22.5];
frontPlane(3,2,1:3) = [7.5 17.55 -7.5];
frontPlane(3,3,1:3) = [7.5 17.55 7.5];
frontPlane(3,4,1:3) = [7.5 17.55 22.5];
frontPlane(4,1,1:3) = [22.5 17.55 -22.5];
frontPlane(4,2,1:3) = [22.5 17.55 -7.5];
frontPlane(4,3,1:3) = [22.5 17.55 7.5];
frontPlane(4,4,1:3) = [22.5 17.55 22.5];

backPlane(1,1,1:3) = [-37.5 -18.8 -37.5];
backPlane(1,2,1:3) = [-37.5 -18.8 -12.5];
backPlane(1,3,1:3) = [-37.5 -18.8 12.5];
backPlane(1,4,1:3) = [-37.5 -18.8 37.5];
backPlane(2,1,1:3) = [-12.5 -18.8 -37.5];
```

```
backPlane(2,2,1:3) = [-12.5 -18.8 -12.5];
backPlane(2,3,1:3) = [-12.5 -18.8 12.5];
backPlane(2,4,1:3) = [-12.5 -18.8 37.5];
backPlane(3,1,1:3) = [12.5 -18.8 -37.5];
backPlane(3,2,1:3) = [12.5 -18.8 -12.5];
backPlane(3,3,1:3) = [12.5 -18.8 12.5];
backPlane(3,4,1:3) = [12.5 -18.8 37.5];
backPlane(4,1,1:3) = [37.5 -18.8 -37.5];
backPlane(4,2,1:3) = [37.5 -18.8 -12.5];
backPlane(4,3,1:3) = [37.5 -18.8 12.5];
backPlane(4,4,1:3) = [37.5 -18.8 37.5];

phiBins = 0:meshSize:360-meshSize;
thetaBins = meshSize:meshSize:180-meshSize;
phiNumBins = numel(phiBins);
thetaNumBins = numel(thetaBins);
histBins = 0:histBinning:round(numEvents*histPct);
numPixels = length(thetaBins)*length(phiBins);
moves_pct = zeros(iterations,1);
maxChg = zeros(round(iterations./10000)-1,1);

if exist('phiROI','var')
    phiEdges = [-Inf, mean([phiBins(2:end); phiBins(1:end-1)]), +Inf];
    phiInds = discretize(phiROI,phiEdges);
    thetaEdges = [-Inf, mean([thetaBins(2:end); thetaBins(1:end-1)]), +Inf];
    thetaInds = discretize(thetaROI,thetaEdges);
    pixelInds = sub2ind([length(thetaBins) length(phiBins)]...
        ,thetaInds,phiInds);
end

%%%%%%%%%%%% Populate array with relevent data for each event %%%%%%%%%%
for i = 1:numEvents

    if particle == 'n'

        if totEvents(i,1) >= neutronThreshold

            det1 = [frontPlane(totEvents(i,5),totEvents(i,7),1)...
                frontPlane(totEvents(i,5),totEvents(i,7),2)...
                frontPlane(totEvents(i,5),totEvents(i,7),3)];
            det2 = [backPlane(totEvents(i,9),totEvents(i,11),1)...
                backPlane(totEvents(i,9),totEvents(i,11),2)...
                backPlane(totEvents(i,9),totEvents(i,11),3)];

            eventData(i,1) = det2(1) - det1(1);
```

```
            eventData(i,2) = det2(2) - det1(2);
            eventData(i,3) = det2(3) - det1(3);

            eventData(i,4) = totEvents(i,2);
            eventData(i,5) = totEvents(i,1);

        end

    end

    if particle == 'p'

        if (totEvents(i,3) == 1)

            det1 = [frontPlane(totEvents(i,5),totEvents(i,7),1)...
                frontPlane(totEvents(i,5),totEvents(i,7),2)...
                frontPlane(totEvents(i,5),totEvents(i,7),3)];
            det2 = [backPlane(totEvents(i,15),totEvents(i,17),1)...
                backPlane(totEvents(i,15),totEvents(i,17),2)...
                backPlane(totEvents(i,15),totEvents(i,17),3)];

            eventData(i,1) = det2(1) - det1(1);
            eventData(i,2) = det2(2) - det1(2);
            eventData(i,3) = det2(3) - det1(3);

            eventData(i,4) = totEvents(i,2);
            eventData(i,5) = totEvents(i,1);

        end
    end

end

clear events
numEvents = length(eventData(:,1));
points = zeros(3,1,numEvents);
zAxis = zeros(1,3,numEvents);
zAxis(1,3,:) = 1;
tempPoints = zeros(3,1,numEvents);


%%%%%% Define histograms for energy bins %%%%%%%%%%%%%
if particle == 'p'
    ergBinsP = 0:0.01:5;
end
```

```
if particle == 'n'
    ergBinsP = 0:0.1:15;
end

storedHists = zeros(numPixels,length(histBins),length(ergBinsP));
if exist('phiROI','var')
    roiCounts = zeros(iterations,length(ergBinsP),length(phiROI));
end


%%%%%% Assign each particle to an energy histogram bin
ergEdges = [-Inf, mean([ergBinsP(2:end); ergBinsP(1:end-1)]), +Inf];
eventData(:,8) = discretize(eventData(:,5),ergEdges);
SOEimageTot = zeros(thetaNumBins,phiNumBins,length(ergBinsP));
pixelInd = zeros(numPixels.*length(ergBinsP),1);
ergInd = zeros(numPixels.*length(ergBinsP),1);

for i = 1:length(ergBinsP)
    for j = 1:numPixels

        pixelInd((numPixels.*(i-1))+j) = j;
        ergInd((numPixels.*(i-1))+j) = i;

    end
end


%%%%% Create Initial Image State %%%%%%%%
tic;

pixelRand = rand(numEvents,1);
pixelSubtract = repmat(pixelRand,1,numPixels);
subtractedVals = abs(systemMatrix - pixelSubtract);
[~,sampledInds] = min(subtractedVals,[],2);
[thetai,phii] = ind2sub(size(SOEimageTot(:,:,1)),sampledInds);

eventData(:,6) = phii(:);
eventData(:,7) = thetai(:);

ergi = reshape(eventData(:,8),[1 1 length(eventData(:,8))]);
SOEimage = accumarray([thetai(:) phii(:) eventData(:,8)],1,...
    [thetaNumBins phiNumBins length(ergBinsP)]);

%%%%%%% Run Iterations %%%%%%%%
itCount = 0;
```

```
n=1;
nn = 1;
ii = 1;
checkFlag = true;
avgFlag = false;
display('Start of Iterations')
iterate = true;

while(iterate)

    %%%%%%%%%%% Sample origin positions based on probabilites
    %%%%%%%%%%% in system matrix
    pixelRand = rand(numEvents,1);
    logicalMatrix = bsxfun(@lt,systemMatrix,pixelRand);
    sampledInds = sum(logicalMatrix,2)+1;
    [thetai,phii] = ind2sub(size(SOEimageTot(:,:,1)),sampledInds);

    indOrig = sub2ind([thetaNumBins phiNumBins length(ergBinsP)]...
        ,eventData(:,7),eventData(:,6),eventData(:,8));
    combinedIndOrig = sub2ind([thetaNumBins phiNumBins]...
        ,eventData(:,7),eventData(:,6));
    indNew = sub2ind([thetaNumBins phiNumBins length(ergBinsP)]...
        ,thetai(:),phii(:),eventData(:,8));
    combinedIndNew = sub2ind([thetaNumBins phiNumBins],thetai(:),phii(:));
    combinedImage = sum(SOEimage,3);
    numPointsOrig = combinedImage(combinedIndOrig);
    numPointsNew = combinedImage(combinedIndNew);
    prob = min(1,((numPointsNew+1).*aFactor)./(numPointsOrig.*1.0));
    randNums = rand(numEvents,1,1);
    accept = randNums < prob;
    moves_pct(ii) = sum(accept) ./ length(accept);

    %%%%% Calculate origins in original and new pixels %%%%%%%%
    pixelRange = 1:1:numPixels*length(ergBinsP);
    eventData(accept,6) = phii(accept);
    eventData(accept,7) = thetai(accept);
    acceptedOrigInd = indOrig(accept);
    acceptedOrigIndHist = histo(acceptedOrigInd,pixelRange);
    acceptedNewInd = indNew(accept);
    acceptedNewIndHist = histo(acceptedNewInd,pixelRange);
    SOEimage(pixelRange) = SOEimage(pixelRange)...
        - acceptedOrigIndHist(pixelRange);
    SOEimage(pixelRange) = SOEimage(pixelRange)...
        + acceptedNewIndHist(pixelRange);
```

```
%%%%%%%%% Calculate the bur-in period and begin
%%%%%%%%% averaging solutions after complete
if ii > 100 * 2 && avgFlag == false
    pct_change = (mean(moves_pct(ii-100*2:ii-1-100))...
        - mean(moves_pct(ii-100:ii-1)))...
        ./ mean(moves_pct(ii-100*2:ii-1-100));
    if pct_change < 0
        avgFlag = true;
        avgSt = ii;
    end
end

if avgFlag
    SOEimageTot = SOEimageTot + SOEimage;
    SOEimageAvg = SOEimageTot./n;
    n = n + 1;

    if mod(ii,10000) == 0
        if checkFlag
            image1 = sum(SOEimageAvg,3);
            checkFlag = false;
        else
            image2 = sum(SOEimageAvg,3);
            good = image1 >= 0.01*sum(sum(image1))...
                & image2 >= 0.01*sum(sum(image2));
            if sum(sum(good)) < 1
                good = image1 >= 0.001*sum(sum(image1))...
                    & image2 >= 0.001*sum(sum(image2));
            end

            maxChg(nn) = max(abs(image1(good)-image2(good))...
                ./ image1(good));
            nn = nn + 1;
            image1 = sum(SOEimageAvg,3);
            sy = smooth(maxChg(1:nn-1),20);
            if nn > 2
                sy(nn-2)
                if sy(nn-2) <= 0.01
                    iterate = false;
                    iterations = ii;
                end
            end
        end
    end
```

```
        %%%%%%%%%%%% Populate histogram with updated image state %%%%%%%%
        countEdges = [-Inf, mean([histBins(2:end);...
            histBins(1:end-1)]), +Inf];
        I = discretize(SOEimage,countEdges);
        shapedImage = reshape(I,[numPixels length(ergBinsP)]);
        shapedImage = reshape(shapedImage,[numPixels.*length(ergBinsP) 1]);
        histInd = sub2ind([numPixels length(histBins) length(ergBinsP)],...
            pixelInd(:), shapedImage(:), ergInd(:));
        storedHists(histInd) = storedHists(histInd) + 1;

    end

    %%%%%%%%%%%% Sum pixels in the ROI %%%%%%%%%%%%%%%
    if exist('phiROI','var')
        totItCounts = zeros(1,1,length(ergBinsP));
        for iii = 1:length(phiInds)
            tempCounts = SOEimage(thetaInds(iii),phiInds(iii),:);
            roiCounts(ii,:,iii) = tempCounts;
        end

    end

    itCount = itCount+1;
    ii = ii + 1;

end

%%%%%% Average total image %%%%%%%%%
if iterations == 0
    SOEimageTot = sum(SOEimage,3);
end
eBinImages = SOEimageTot ./ (iterations - avgSt + 1);
avgImage = sum(SOEimageTot,3) ./ (iterations - avgSt + 1);

elapsed_time = toc;

%%%%%%%%%%%% Store information to data structure %%%%%%%%%%%%%%%
sol.particle = particle;
sol.meshSize = meshSize;
sol.iterations = iterations;
sol.avgSt = avgSt;
sol.PPC = pointsPerCone;
sol.numEvents = numEvents;
sol.avgImage = avgImage;
sol.phiBins = phiBins;
```

```
sol.thetaBins = thetaBins;
sol.runTime = elapsed_time;
sol.nThresh = neutronThreshold;
sol.histBins = histBins;
sol.storedHists = storedHists;
sol.eBinImages = eBinImages;
sol.ergBins = ergBinsP;
sol.ergLow = ergLow;
sol.ergHigh = ergHigh;
sol.aFactor = aFactor;
if exist('phiROI','var')
    sol.roiCounts = roiCounts;
    sol.phiROI = phiROI;
    sol.thetaROI = thetaROI;
end
sol.moves_pct = moves_pct;
sol.maxChg = maxChg;

%%%%%%%%%%%% Save final solution %%%%%%%%%%%%%%%
save(['sol_',particle,'_',num2str(meshSize),'deg_',num2str(iterations),...
    'it_',num2str(avgSt),'avgSt_',num2str(pointsPerCone),'ppc_',...
    num2str(countsUsed),'N_',num2str(thetaSampling),'th_',...
    num2str(ergLow),'_',num2str(ergHigh),'_erg.mat'],'sol','-v7.3')

%%%%%%%%%%%% Plot final image %%%%%%%%%%%%%%%
PlotLoadedSolution(sol,'avg')
```

Appendix C

Sample MCNPX-PoliMi and MPPost input files for the DPI

C.1 Example MCNPX-PoliMi input file

```
c DNNG DPI
c ~~~~~~~~~~~~~~~~~~~~~~~~~~~~~~~~
c  Cells
c ~~~~~~~~~~~~~~~~~~~~~~~~~~~~~~~~
c   Imager
c ~~~~~~~~~~~~~~~~~~~~~~~~~~~~~~~~
c Front plane liquid
111 1 -0.935 -10 13 14 imp:n,p=1
112 like 111 but trcl=112
113 like 111 but trcl=113
114 like 111 but trcl=114
121 like 111 but trcl=121
122 like 111 but trcl=122
123 like 111 but trcl=123
124 like 111 but trcl=124
131 like 111 but trcl=131
132 like 111 but trcl=132
133 like 111 but trcl=133
134 like 111 but trcl=134
141 like 111 but trcl=141
142 like 111 but trcl=142
143 like 111 but trcl=143
144 like 111 but trcl=144
c
c Front plane Al casing
```

```
150 9 -2.7 (-15:-16) 10 imp:n,p=1
151 like 150 but trcl=112
152 like 150 but trcl=113
153 like 150 but trcl=114
154 like 150 but trcl=121
155 like 150 but trcl=122
156 like 150 but trcl=123
157 like 150 but trcl=124
158 like 150 but trcl=131
159 like 150 but trcl=132
160 like 150 but trcl=133
161 like 150 but trcl=134
162 like 150 but trcl=141
163 like 150 but trcl=142
164 like 150 but trcl=143
165 like 150 but trcl=144
c
c Front plane PMT
411 4 -0.51498 -12:-11 imp:n,p=1
412 like 411 but trcl=112
413 like 411 but trcl=113
414 like 411 but trcl=114
421 like 411 but trcl=121
422 like 411 but trcl=122
423 like 411 but trcl=123
424 like 411 but trcl=124
431 like 411 but trcl=131
432 like 411 but trcl=132
433 like 411 but trcl=133
434 like 411 but trcl=134
441 like 411 but trcl=141
442 like 411 but trcl=142
443 like 411 but trcl=143
444 like 411 but trcl=144
c
c Back plane liquid
211 1 -0.935 -20 23 24 imp:n,p=1
212 like 211 but trcl=213
213 like 211 but trcl=222
214 like 211 but trcl=224
221 like 211 but trcl=231
222 like 211 but trcl=233
223 like 211 but trcl=242
224 like 211 but trcl=244
c
```

```
c Back plane casing
251 9 -2.7 -25 20 imp:n,p=1
252 like 251 but trcl=213
253 like 251 but trcl=222
254 like 251 but trcl=224
255 like 251 but trcl=231
256 like 251 but trcl=233
257 like 251 but trcl=242
258 like 251 but trcl=244
c
c Back plane PMT
511 4 -0.51498 -22:-21 imp:n,p=1
512 like 511 but trcl=213
513 like 511 but trcl=222
514 like 511 but trcl=224
521 like 511 but trcl=231
522 like 511 but trcl=233
523 like 511 but trcl=242
524 like 511 but trcl=244
c
c Back plane NaI
311 2 -3.67 -30 imp:n,p=1
312 like 311 but trcl=314
313 like 311 but trcl=321
314 like 311 but trcl=323
321 like 311 but trcl=332
322 like 311 but trcl=334
323 like 311 but trcl=341
324 like 311 but trcl=343
c
c Back plane NaI Casing
351 9 -2.7 -33 30 imp:n,p=1
352 like 351 but trcl=314
353 like 351 but trcl=321
354 like 351 but trcl=323
355 like 351 but trcl=332
356 like 351 but trcl=334
357 like 351 but trcl=341
358 like 351 but trcl=343
c
c Back plane NaI PMT
611 4 -0.51498 -32:-31 imp:n,p=1
612 like 611 but trcl=314
613 like 611 but trcl=321
614 like 611 but trcl=323
```

```
621 like 611 but trcl=332
622 like 611 but trcl=334
623 like 611 but trcl=341
624 like 611 but trcl=343
c
c Front plane Window
711 8 -2.51 -13:-14 imp:n,p=1
712 like 711 but trcl=112
713 like 711 but trcl=113
714 like 711 but trcl=114
721 like 711 but trcl=121
722 like 711 but trcl=122
723 like 711 but trcl=123
724 like 711 but trcl=124
731 like 711 but trcl=131
732 like 711 but trcl=132
733 like 711 but trcl=133
734 like 711 but trcl=134
741 like 711 but trcl=141
742 like 711 but trcl=142
743 like 711 but trcl=143
744 like 711 but trcl=144
c
c Back Plane Window
766 8 -2.51 -23:-24 imp:n,p=1
767 like 766 but trcl=213
768 like 766 but trcl=222
769 like 766 but trcl=224
776 like 766 but trcl=231
777 like 766 but trcl=233
778 like 766 but trcl=242
779 like 766 but trcl=244
c
c ~~~~~~~~~~~~~~~~~~~~~~~~~~~~~~~~
c  Floor and walls
c ~~~~~~~~~~~~~~~~~~~~~~~~~~~~~~~~
  903   10  -2.3  -500 -61 62 -63 65 -66 imp:n,p=1 $ concrete
  904   10  -2.3  -500 64 62 -63 65 -66 imp:n,p=1
  905   10  -2.3  -500 -62 65 -66       imp:n,p=1
  906   10  -2.3  -500 63 65 -66        imp:n,p=1
  907   10  -2.3  -500 -65         imp:n,p=1
  908   10  -2.3  -500 66          imp:n,p=1
  909   10  -2.3  -67              imp:n,p=1
c ~~~~~~~~~~~~~~~~~~~~~~~~~~~~~~~~
c  HEU
```

```
c ~~~~~~~~~~~~~~~~~~~~~~~~~~~~~~~~
801 13 -18.0038 -81              imp:n,p=1
802 3 -0.001205 81 -82           imp:n,p=1
803 5 -0.93 82 -83               imp:n,p=1 $Moderator
c ~~~~~~~~~~~~~~~~~~~~~~~~~~~~~~~~
c NCAI Mask $Poly mask from other measurement system present
c ~~~~~~~~~~~~~~~~~~~~~~~~~~~~~~~~
910 5  -0.93 -91 imp:n,p=1
920 14 -1.0 -92 imp:n,p=1
c ~~~~~~~~~~~~~~~~~~~~~~~~~~~~~~~~
c Environment
c ~~~~~~~~~~~~~~~~~~~~~~~~~~~~~~~~
901    3 -0.001205 -500 83 61 -64 62 -63 91 92 65 -66 67
       10 11 12 15 16 20 21 22 25 30 31 32 33
       #111 #112 #113 #114 #121 #122 #123 #124
       #131 #132 #133 #134 #141 #142 #143 #144
       #150 #151 #152 #153 #154 #155 #156 #157
       #158 #159 #160 #161 #162 #163 #164 #165
       #411 #412 #413 #414 #421 #422 #423 #424
       #431 #432 #433 #434 #441 #442 #443 #444
       #211 #212 #213 #214 #221 #222 #223 #224
       #251 #252 #253 #254 #255 #256 #257 #258
       #511 #512 #513 #514 #521 #522 #523 #524
       #311 #312 #313 #314 #321 #322 #323 #324
       #351 #352 #353 #354 #355 #356 #357 #358
       #611 #612 #613 #614 #621 #622 #623 #624
       #711 #712 #713 #714 #721 #722 #723 #724
       #731 #732 #733 #734 #741 #742 #743 #744
       #766 #767 #768 #769 #776 #777 #778 #779
       imp:n,p=1
999  0    500                 imp:n,p=0

c ~~~~~~~~~~~~~~~~~~~~~~~~~~~~~~~~
c  Surfaces
c ~~~~~~~~~~~~~~~~~~~~~~~~~~~~~~~~
c   Imager
c ~~~~~~~~~~~~~~~~~~~~~~~~~~~~~~~~
10  RCC -22.5 21.452 22.5  0.0 -6.3  0.0  3.81 $Front plane Liquid
11  RCC -22.5 22.087 22.5 0.0 6.5   0.0  3.81 $Front plane PMT Thick
12  RCC -22.5 28.587 22.5 0.0 17.2  0.0  2.94  $Front plane PMT skinny
13  RCC -22.5 21.452 22.5  0.0 -1.2  0.0  3.25  $Front plane window thick
14  RCC -22.5 21.452 22.5  0.0  0.635 0.0  3.9075 $Front plane window skinny
15  RCC -22.5 21.452 22.5  0.0 -.64  0.0  4.2995 $Casing Lip
16  RCC -22.5 21.452 22.5  0.0 -6.452 0.0 3.962 $Casing
c
```

```
20  RCC -37.5 -14.848 37.5  0.0  -9.2  0.0  3.81 $Middle Liquid scintillator
21  RCC -37.5 -24.683 37.5 0.0 -6.5  0.0  3.81 $Middle PMT thick
22  RCC -37.5 -31.183 37.5 0.0 -17.2 0.0  2.94  $Middle PMT skinny
23  RCC -37.5 -24.048 37.5  0.0  1.6  0.0  3.25  $Front plane window thick
24  RCC -37.5 -24.683 37.5 0.0  0.635 0.0  3.9075 $Front plane window skinny
25  RCC -37.5 -14.696 37.5  0.0  -9.352 0.0  3.962 $Casing
c
30  RCC -12.5 -16.748 37.5 0.0 -7.62 0.0 3.81 $NaI scintillator
31  RCC -12.5 -24.368 37.5 0.0 -4.0 0.0 3.81 $Front part of NaI PMT
32  RCC -12.5 -28.368 37.5 0.0 -14.0 0.0 2.94 $Back part of NaI PMT
33  RCC -12.5 -16.596 37.5 0.0 -7.772 0.0 3.962 $Casing
c
40  RCC  22.5 21.452  22.5  0.0  -9.2  0.0  3.81 $Front plane 3" liquid
41  RCC -22.5 22.087 22.5 0.0 6.5  0.0  3.81 $Front plane PMT Thick
42  RCC -22.5 28.587 22.5 0.0 17.2  0.0  2.94  $Front plane PMT skinny
43  RCC  22.5 21.452  22.5  0.0  -1.6  0.0  3.25 $Front plane 3" window thick
44  RCC  22.5 21.452  22.5  0.0  0.635 0.0  3.9075 $ Front plane 3" window skinny
45  RCC  22.5 21.452  22.5  0.0  -9.352 0.0  3.962 $Casing
c
c ~~~~~~~~~~~~~~~~~~~~~~~~~~~~~~~~
c  Environment
c ~~~~~~~~~~~~~~~~~~~~~~~~~~~~~~~~
500 RPP -525 475 -1150 650  -174 1100
c
c ~~~~~~~~~~~~~~~~~~~~~~~~~~~~~~~~
c Floor and walls
c ~~~~~~~~~~~~~~~~~~~~~~~~~~~~~~~~
 61 PZ    -74  $ Floor level
 62 PX    -425
 63 PX    375
 64 PZ    1000
 65 PY    -1050
 66 PY    550
 67 RPP 125 225 -1050 -650 -74 1000
c ~~~~~~~~~~~~~~~~~~~~~~~~~~~~~~~~
c    RF Shell
c ~~~~~~~~~~~~~~~~~~~~~~~~~~~~~~~~
81 SPH 0 155 11.5 5.6692 $shells 1 - 24, total 13.741 kg
c ~~~~~~~~~~~~~~~~~~~~~~~~~~~~~~~~
c    Moderator
c ~~~~~~~~~~~~~~~~~~~~~~~~~~~~~~~~
82 SPH 0 155 11.5 7.6
83 SPH 0 155 11.5 11.41
c ~~~~~~~~~~~~~~~~~~~~~~~~~~~~~~~~
c NCAI Mask
```

```
c ~~~~~~~~~~~~~~~~~~~~~~~~~~~~~~~~
91 RPP -40 40 242 247 -10 70
92 RPP -40 40 247 249 -10 70

c ~~~~~~~~~~~~~~~~~~~~~~~~~~~~~~~~
c Data
c ~~~~~~~~~~~~~~~~~~~~~~~~~~~~~~~~
c
c ~~~~~~~~~~~~~~~~~~~~~~~~~~~~~~~~
c Physics
c ~~~~~~~~~~~~~~~~~~~~~~~~~~~~~~~~
  MODE n p
  PHYS:N J 20 0 -1 J 1
  PHYS:P J 1 0 -1 1 0 1
  CUT:P 2J 0
  CUT:N 2J 0
  ACT FISSION=P NONFISS=P DG=MG
c ~~~~~~~~~~~~~~~~~~~~~~~~~~~~~~~~
c Source
c ~~~~~~~~~~~~~~~~~~~~~~~~~~~~~~~~
SDEF POS = -28 155 11.5 PAR=1 ERG=14.1 TME=D1 VEC=1 0 0 DIR=D2
SI2 0.92594 1
SP2 0 1
IPOL  0 J J J J 2 88 111 112 113 114 121 122 123 124
                   131 132 133 134 141 142 143 144
                   411 412 413 414 421 422 423 424
                   431 432 433 434 441 442 443 444
                   211 212 213 214 221 222 223 224
                   511 512 513 514 521 522 523 524
                   311 312 313 314 321 322 323 324
                   611 612 613 614 621 622 623 624
                   711 712 713 714 721 722 723 724
                   731 732 733 734 741 742 743 744
                   766 767 768 769 776 777 778 779
RPOL 0.001 0.001
NPS 7776300     $7776300 is 7e7 n/s isotropic w/ cos(theta) = 0.92594 for 3s
LCA 8J 1
FILES 21 DUMN1
DBCN
PRDMP 2J 1
PRINT
c ~~~~~~~~~~~~~~~~~~~~~~~~~~~~~~~~
c Materials
c ~~~~~~~~~~~~~~~~~~~~~~~~~~~~~~~~
c  EJ-309 liquid scintillator d=-0.916
```

```
c (Eljen Technologies, EJ-309 Fact Sheet)
c Liquid Scintillator
m1   NLIB=60c PLIB=04p
      1001   0.555443  $ H
      6000   0.444557  $ C
c
c NaI Scintillator
m2   NLIB=60c PLIB=04p
     11023 -0.153373  $ Na
     53127 -0.846627  $ I
c
c Air
m3    NLIB=60c PLIB=04p
      6000 -0.000124
      7014 -0.755268
      8016 -0.231781
      18000.59c -0.012827
c
c Homogenized PMT
m4   NLIB=60c PLIB=04p
      14000 -0.0933168  $Si
      8016  -0.1312437  $Oxy
      5010  -0.0079926  $B
     11023  -0.0096386  $Na
     13027  -0.0040993  $Al
     26056  -0.2481451  $Fe ONLY Fe-56
     28058  -0.5049603  $Ni ONLY Ni-58
      7014  -0.0005934  $N
c     18040 -1.008186e-5 $Ar-40 at 99.6035 percent of natural Ar
c     18036 -3.376699e-8 $Ar-36 at 0.3336 percent of natural Ar
c     18038 -6.366738e-9 $AR-38 at 0.00629 percent of natural Ar
c
c Poly
m5   NLIB=60c PLIB=04p
     1001   -0.14371    $H
     6000   -0.856284   $C
c
c Lead
m6 NLIB=60 PLIB=04p
c     82204 -0.014    $Pb
     82206 -0.241
     82207 -0.221
     82208 -0.524
c
c BK7
```

```
m8   NLIB=60c PLIB=04p
     14000 -0.323138999 $ Changed to natural
     8016  -0.483882614
     5011  -0.033384805
     56138 -0.027496631
     11023 -0.077153875
     19000 -0.052216449 $ Changed to natural
c    33075 -0.002726626
c ~~~~~~~~~~~~~~~~~~~~~~~~~~~~~~~~
c Aluminum table d=-2.70
c ~~~~~~~~~~~~~~~~~~~~~~~~~~~~~~~~
  m9  nlib=60c plib=04p
     13027    -1
c ~~~~~~~~~~~~~~~~~~~~~~~~~~~~~~~~
c Concrete (Mat. Compendium PNNL) d=-2.3
c (Mat. Compendium PNNL)
c ~~~~~~~~~~~~~~~~~~~~~~~~~~~~~~~~
  m10  nlib=60c plib=04p
      1001    -0.022100
      6000    -0.002484
      8016    -0.574930
     11023    -0.015208
     12000    -0.001266
     13027    -0.019953
     14000    -0.304627
     19000    -0.010045
     20000    -0.042951
     26000.50c    -0.006435
c ~~~~~~~~~~~~~~~~~~~~~~~~~~~~~~~~
c    Steel
c ~~~~~~~~~~~~~~~~~~~~~~~~~~~~~~~~
  m12 nlib=60c plib=04p
       6000 -0.005
       26000 -0.995
c ~~~~~~~~~~~~~~~~~~~~~~~~~~~~~~~~
c    HEU
c ~~~~~~~~~~~~~~~~~~~~~~~~~~~~~~~~
m13 nlib=61c plib=04p
       92235 -0.9316
       92238 -0.0535
       92234 -0.0102
       92236 -0.0047
m14 nlib=60c plib=04p
       1001 -0.125355
       5010 -0.02
```

```
      5011 -0.08
      6000 -0.774645
c ~~~~~~~~~~~~~~~~~~~~~~~~~~~~~~~~
c  Tallies
c ~~~~~~~~~~~~~~~~~~~~~~~~~~~~~~~~
c
c ~~~~~~~~~~~~~~~~~~~~~~~~~~~~~~~~
c  Translations
c ~~~~~~~~~~~~~~~~~~~~~~~~~~~~~~~~
c Front Plane Translations
tr112 15  0.0  0.0
tr113 30  0.0  0.0
tr114 45  0.0  0.0
tr121 0.0  0.0 -15
tr122 15  0.0 -15
tr123 30  0.0 -15
tr124 45  0.0 -15
tr131 0.0  0.0 -30
tr132 15  0.0 -30
tr133 30  0.0 -30
tr134 45  0.0 -30
tr141 0.0  0.0 -45
tr142 15  0.0 -45
tr143 30  0.0 -45
tr144 45  0.0 -45
c
c Back Plane Liquid Translations
tr213 50   0.0   0.0
tr222 25   0.0  -25
tr224 75   0.0  -25
tr231 0.0   0.0  -50
tr233 50   0.0  -50
tr242 25   0.0  -75
tr244 75   0.0  -75
c
c Back Plane NaI Translations
tr314 50   0.0    0.0
tr321 -25  0.0   -25
tr323 25   0.0   -25
tr332 0.0   0.0   -50
tr334 50   0.0   -50
tr341 -25  0.0   -75
tr343 25   0.0   -75
c
c ~~~~~~~~~~~~~~~~~~~~~~~~~~~~~~~~
```

```
SI1  0
     33333.333333
     333333.333333
     366666.666667
     666666.666667
     700000.000000
     1000000.000000
     1033333.333333
     .
     .
     .
     Additional time cards removed for brevity

SP1  0
     1
     0
     1
     0
     1
     0
     1
     .
     .
     .
     Additional time cards removed for brevity
```

C.2 Example MPPost input file

```
#
#~~~~~~~~~~~~~~~~~~~~~~~~~~~~~~~~~~~~~~~~~~~~~~~~~~~~~~~~~~~~~~~~~~~~~~~~~~~~~~~
# ~~~~~~~~~~~~~~~~~~~~~~~~~~~~~~~~~~~~~~~~~~~~~~~~~~~~~~~~~~~~~~~~~~~~~~~~~~~~~~~
#
#  Input file for MPPost
#
version              2.1.9
# ~~~~~~~~~~~~~~~~~~~~~~~~~~~~~~~~~~~~~~~~~~~~~~~~~~~~~~~~~~~~~~~~~~~~~~~~~~~~~~~
# ~~~~~~~~~~~~~~~~~~~~~~~~~~~~~~~~~~~~~~~~~~~~~~~~~~~~~~~~~~~~~~~~~~~~~~~~~~~~~~~

# ~~~~~~~~~~~~~~~~~~~~~~~~~~~~~~~~~~~~~~~~~~~~~~~~~~~~~~~~~~~~~~~~~~~~~~~~~~~~~~~
# GENERAL INFORMATION
# ~~~~~~~~~~~~~~~~~~~~~~~~~~~~~~~~~~~~~~~~~~~~~~~~~~~~~~~~~~~~~~~~~~~~~~~~~~~~~~~
title          TEST
username       MLR

# ~~~~~~~~~~~~~~~~~~~~~~~~~~~~~~~~~~~~~~~~~~~~~~~~~~~~~~~~~~~~~~~~~~~~~~~~~~~~~~~
```

```
# I/O FILE INFORMATION
# ~~~~~~~~~~~~~~~~~~~~~~~~~~~~~~~~~~~~~~~~~~~~~~~~~~~~~~~~~~~~~~~~~~~~~~~~~~~~
polimi_det_in         dumn1    # MCNP-PoliMi detector filename
import_pulses         no         # If processing pulse list (from measurements or
   simulation) turn to yes
output_file           MPP_Output # Desired output name
label_output          no         # Place labels at the top of the output files
separate_det_response no         # Print individual distributions for each
   detector
list_of_pulses        no         # Print a list mode file of all collected pulses
incident_light        no         # Data written to list of pulses no = incident
   energy (MeV)
                                 #    yes = write the max potential LIGHT (MeVee)
event_inventory_on    no         # Print out a table summarizing all events in the
    file
collision_history     no         # Print summary of how collisions make pulses in
   the detector
time_file_on          no         # Use TIME file to obtain start times for each
   history
time_file_name                   # Name of the TIME file
overwrite_files       yes        # Allow the code to overwrite old files
comma_delimited       yes         # Output files delimited by a comma

# ~~~~~~~~~~~~~~~~~~~~~~~~~~~~~~~~~~~~~~~~~~~~~~~~~~~~~~~~~~~~~~~~~~~~~~~~~~~~
# MEMORY
# ~~~~~~~~~~~~~~~~~~~~~~~~~~~~~~~~~~~~~~~~~~~~~~~~~~~~~~~~~~~~~~~~~~~~~~~~~~~~
division_size  16000  # MB, size of segments to divide the file
cushion        200    # number of lines added to the arrays to prevent
   overstepping arrays

# ~~~~~~~~~~~~~~~~~~~~~~~~~~~~~~~~~~~~~~~~~~~~~~~~~~~~~~~~~~~~~~~~~~~~~~~~~~~~
# DETECTOR INFORMATION
# ~~~~~~~~~~~~~~~~~~~~~~~~~~~~~~~~~~~~~~~~~~~~~~~~~~~~~~~~~~~~~~~~~~~~~~~~~~~~
time_dependent        yes             # Perform analysis by time instead of by
   history
NPS                   1              # NPS used in the MCNP run
detector_type         1 1 4 0 0 0 0 0 0 # Type of Detector - list for each cell
   number
                                     #   0 = Non Active Volume (i.e. PMT)
                                     #   1 = Liquid Organic Scintillator
                                     #   2 = He3 (Cannot be run with other types)
                                     #   3 = Plastic Organic Scintillator
                                     #   4 = NaI
                                     #   5 = CaF2
                                     #   6 = LaBr3
```

```
threshold         0.045 0.045 0.045    # MeVee, Threshold for event detection -
   list for each cell number
upper_threshold   2.8 2.8 2.8     # MeVee, the max acceptable light for event
   detection - list for each cell number
detector_cell_numbers ( 111 112 113 114 121 122 123 124 131 132 133 134 141 142
   143 144 ) &
   ( 211 212 213 214 221 222 223 224 ) &
   ( 311 312 313 314 321 322 323 324 ) &
   ( 411 412 413 414 421 422 423 424 431 432 433 434 441 442 443 444 ) &
   ( 511 512 513 514 521 522 523 524 ) &
   ( 611 612 613 614 621 622 623 624 ) &
   ( 711 712 713 714 721 722 723 724 731 732 733 734 741 742 743 744 ) &
   ( 766 767 768 769 776 777 778 779 )
# ~~~~~~~~~~~~~~~~~~~~~~~~~~~~~~~~~~~
# Capture Neutron Profile ( Works in CLYC cells)
# ~~~~~~~~~~~~~~~~~~~~~~~~~~~~~~~~~~~
ncp_on                       no     # yes/no, option to produce a phd based on
   the energy released in each capture (on automatically for clyc)
ncp_low                      0      # MeV, lower recorded neutron energy value
ncp_high                     5      # MeV, upper recorded neutron energy value
ncp_incr                     0.1    # MeV, bin width for recorded neutron energy
   values
capture_material     3007,5010     # List zaid for materials relevent caputre
   events can occur in, up to 10

# ~~~~~~~~~~~~~~~~~~~~~~~~~~~~~~~~~~~~~~~~~~~~~~~~~~~~~~~~~~~~~~~~~~~~~~~~~~~~~~~
# DETECTOR INFORMATION - Pulse Height
# ~~~~~~~~~~~~~~~~~~~~~~~~~~~~~~~~~~~~~~~~~~~~~~~~~~~~~~~~~~~~~~~~~~~~~~~~~~~~~~~
pulse_height_on   no               # Print pulse height distributions
sum_then_light    no                # Convert the sum of all contributing
   particles energy to light
cross_talk_on     no                # Eliminate histories with cross talk

# Pulse Generation Time - ns, Light collection time for a pulse
organic_liq_pgt   10
organic_pl_pgt    10
nai_pgt           10
caf2_pgt          10
labr3_pgt         10
clyc_pgt                     10

# Deadtime - ns, deadtime of the detector between pulses
organic_liq_dt     0
organic_pl_dt      0
nai_dt             0
```

```
caf2_dt            0
labr3_dt           0
clyc_dt               0

histogram_start    0     # MeVee, Min value for the pulse height distribution
histogram_stop    10    # MeVee, Max value for the pulse height distribution
bin_step          0.01     # MeVee, Bin step - top side of the bin

# ~~~~~~~~~~~~~~~~~~~~~~~~~~~~~~~~~~~
# ORGANIC SCINTILLATOR
# ~~~~~~~~~~~~~~~~~~~~~~~~~~~~~~~~~~~
calibration_regions 1   # Number of independently fit neutron light regions
region_type        3       # Specify which form for the coefficients, if multiple
   regions list selections
     # Type   Form      How to enter values on the neutron_calibration line
     #   1 = Ax^2+Bx+C -> E1 E2 A B C
     #   2 = Ax^2/(x+B) -> E1 E2 A B
     #   3 = A(Bx-C(1-exp(Dx^E))) -> E1 E2 A B C D E
     #   Where E1 and E2 are the lower and upper energy bounds respectivly in
         MeVee
neutron_calibration 0 50 1 0.6682 1.625 -0.3866 1.05
photon_calibration    1.000  0.000         # A,B: Parameters for photon light
   conversion - Ax+B
carbon_light_constant 0.02                  # Constant value for carbon light
   conversion
deuterium_fit_type    2                        # Specify which form for the
   coefficients for deuterium light conversion: 1 or 2
deuterium_calibration 1 0.74692 3.5522 -0.1977 1   # Enter coefficients for chosen
    deuterium fit type
    #   1 = Ax^4+Bx^3+Cx^2+Dx+E -> A B C D E
    #   2 = A(Bx-C(1-exp(Dx^E))) -> A B C D E
clyc_n_calib          .6465    # Constant value for light conversion for capture
   events in CLYC

# ~~~~~~~~~~~~~~~~~~~~~~~~~~~~~~~~~~~
# Energy Resolution
# ~~~~~~~~~~~~~~~~~~~~~~~~~~~~~~~~~~~
light_resolution_on    yes            # Turns on/off the a Gaussian Energy
   Broadening
organic_liq_p_lgt   9.8532 0 4738.66   # Coefficients A,B,C for Gaussian
   Broadening: A*LO+B*Sqrt(LO)+C
organic_liq_n_lgt   9.8532 0 4738.66
organic_pl_p_lgt    10.083 311.77 431.58
organic_pl_n_lgt    10.083 311.77 431.58
nai_lgt   0.0353099 147.455303 1423.525484       # For Inorganics leave blank to
```

```
   use defaults
caf2_lgt                          # or specify Coefficients as
labr3_low_lgt                     # Coefficients A,B,C for Gaussian Broadening:
    A*LO+B*Sqrt(LO)+C
labr3_high_lgt
clyc_lgt           3.6218 -79.1285 3092.1

# ~~~~~~~~~~~~~~~~~~~~~~~~~~~~~~~~~~
# Time Resolution
# ~~~~~~~~~~~~~~~~~~~~~~~~~~~~~~~~~~
tme_resolution_on yes               # Turns on time broadening
organic_liq_tme   1
organic_pl_tme    1
nai_tme           16
caf2_tme          24
labr3_tme         1
clyc_tme

# ~~~~~~~~~~~~~~~~~~~~~~~~~~~~~~~~~~
# Voxels
# ~~~~~~~~~~~~~~~~~~~~~~~~~~~~~~~~~~
cell_voxels_on yes
cells_to_voxel       111   211   311             # Cell numbers that are to be
   voxeled
xVox          -30 15 30  -50  25  50   -50  25  50       # Start, step, max for
   voxelation
yVox          15.152 6.3 21.452      -24.048  9.2 -14.848   -24.3680  7.62
   -16.748     #   for multiple cells repeat start,step,stop
zVox          -30 15 30  -50  25  50     -50  25  50    #   start1,step1,stop1,start2
   ,step2,stop2

# ~~~~~~~~~~~~~~~~~~~~~~~~~~~~~~~~~~~~~~~~~~~~~~~~~~~~~~~~~~~~~~~~~~~~~~~~~~~~~~~
# TIME-OF-FLIGHT, CORRELATION, and AUTOCORRELATION INFORMATION
# ~~~~~~~~~~~~~~~~~~~~~~~~~~~~~~~~~~~~~~~~~~~~~~~~~~~~~~~~~~~~~~~~~~~~~~~~~~~~~~~
tof_on               no     # yes/no, Turn on TOF distributions (cannot have a
   start detector)
cross_correlation_on  no     # yes/no, Turn on cross correlation function
auto_correlation_on   no     # yes/no, Turn on auto correlation function
start_detector       100    # Cell number of the start detector
time_start           -100.5 # ns, time for the correlation plot to start (NOTE:
   there has to be a decimal point, even if it is just 100.0)
time_stop            100.5  # ns, time for the correlation plot to stop (NOTE:
   there has to be a decimal point, even if it is just 100.0)
time_increment       1      # ns, time increment between the bins - top side of
   the bin
```

```
cc_window_incr       1000   # ns, time window for correlation events for time
   dependent analysis
# ~~~~~~~~~~~~~~~~~~~~~~~~~~~~~~~~~~
# Pulse Height Correlation
# ~~~~~~~~~~~~~~~~~~~~~~~~~~~~~~~~~~
pulse_correlation_on no      # yes/no, turn on pulse height correlation analysis
pc_min               0       # MeVee, Minimum value for pulse height binning
pc_max               5       # MeVee, Maximum value for pulse height binning
pc_incr              0.05    # MeVee, increment for pulse height binning
stop_pulse_only      yes     # Ignore start detector pulse height
# ~~~~~~~~~~~~~~~~~~~~~~~~~~~~~~~~~~
# CAPTURE GATED DETECTORS
# ~~~~~~~~~~~~~~~~~~~~~~~~~~~~~~~~~~
capture_gate_on   no         # Run the capture gated detector response
cap_low           0          # ns, start time for binning the time to capture
   histogram
cap_high          2000       # ns, stop time for binning the time to capture
   histogram
cap_incr          10         # ns, bin size the time to capture histogram

# ~~~~~~~~~~~~~~~~~~~~~~~~~~~~~~~~~~~~~~~~~~~~~~~~~~~~~~~~~~~~~~~~~~~~~~~~~~~~~~~~
# IMAGING SYSTEM
# ~~~~~~~~~~~~~~~~~~~~~~~~~~~~~~~~~~~~~~~~~~~~~~~~~~~~~~~~~~~~~~~~~~~~~~~~~~~~~~~~
imaging_system_on yes     # yes/no, turn on the imaging system
longdistance     yes      # yes/no, turn on long distance
window_front     5      # Time window used to discriminate double scatters in
   plane 1 for neutrons
                         # (implemented before and after the trigger)
window_start     5       # Start of time window used to correlate neutrons
window_end       100     # Time window used to correlate neutrons
window_gamma     25      # Time window used to correlate gammas
                         # (implemented before and after the trigger)
backprojection   no     # yes/no, run back projection algorithm
sphere_center    0 0 0   # X, Y, and Z coordinates of the center of the back
   projection sphere
sphere_radius    500   # Radius of the back projection sphere
sphere_mesh      2       # Degrees per mesh point
cone_thickness   2       # Thickness of the back projection cones
mlem_input_data  no     # yes/no, outputs data to use with MLEM algorithm
mlem_angle_bin   10      # Angle binning used for MLEM
p_emin           0       # Min cutoff energy in MeVee
p_ebin           0.05       # Energy Binning in MeVee
p_emax           6       # Max cutoff energy in MeVee
n_emin           0       # Min cutoff energy in MeVee
n_ebin           0.25       # Energy Binning in MeVee
```

```
n_emax           15       # Max cutoff energy in MeVee
uncertaintythickness no  # yes/no
distancecheck      no    # yes/no

# ~~~~~~~~~~~~~~~~~~~~~~~~~~~~~~~~~~~~~~~~~~~~~~~~~~~~~~~~~~~~~~~~~~~~~~~~~~~~
# He3 MODULE
# ~~~~~~~~~~~~~~~~~~~~~~~~~~~~~~~~~~~~~~~~~~~~~~~~~~~~~~~~~~~~~~~~~~~~~~~~~~~~
he3_multiplicity   no    # yes/no: Turn on the He3 module
number_of_windows  256   # Number of windows to evaluate
window_increment   16    # Window increment in microseconds
deadtime_type      1     # Control which model is applied for dead time
                         #   1 = Type I, applied to each tube only
                         #   2 = Type II, applied to each tube then fed into an
                             amplifier
                         #   3 = Type III, AWCC style, detector, into amp, into
                             OP amp
detector_deadtime  4     # Detector dead time in microseconds
amplifier_deadtime 0.5   # Level I amplifier dead time in microseconds
amp_2_deadtime     0.03  # Level II amplifier dead time in microseconds
max_multiplicity   500   # Maximum multiplicity expected (for array size handling
   )
trigger_type       1     # Control how the multiplicity windows are triggered
                         #   1 = Constant window
                         #   2 = Open on trigger (Reverse)
                         #   3 = Open on trigger (Forward)
pre_delay          4.5   # Predelay after event trigger in microseconds
long_delay         1024  # Delay between R+A window and A window in microseconds
run_time           105.33 # Time the source is distributed over in seconds
output_style       3     # Controls what data is printed to a file
                         #   1 = All multiplicity distributions + Feynman-Y + S,D
                             ,T
                         #   2 = Last multiplicity distribution + S,D,T rates
                         #   3 = Last multiplicity distribution + Mean, Variance,
                              Feynman-Y
generation_analysis_on yes # yes/no, analysis of the neutron generations captured
paralyzable       no     # yes/no, yes treats He-3 detectors as paralyzable, no
   treated as non-paralyzable
# ~~~~~~~~~~~~~~~~~~~~~~~~~~~~~~~~~~
# Select Capture Event Type
# ~~~~~~~~~~~~~~~~~~~~~~~~~~~~~~~~~~
output_sort_file  no     # Print out a file with all sorted events
sort_ipt          1      # Particle type to sort by, set -1 to ignore
sort_nxs          2003   # Material of interaction to sort by, set to -1 to
   ignore
sort_ntyn         0      # Interaction type to sort by, set to -1 to ignore
```

```
# ~~~~~~~~~~~~~~~~~~~~~~~~~~~~~~~~~~~~~~~~~~~~~~~~~~~~~~~~~~~~~~~~~~~~~~~~~~~~
# Scintillator Multiplicity MODULE
# ~~~~~~~~~~~~~~~~~~~~~~~~~~~~~~~~~~~~~~~~~~~~~~~~~~~~~~~~~~~~~~~~~~~~~~~~~~~~
scint_mult        no     # Turn on Scintillator Multiplicity
neutrons_only     no     # Only process neutron multiplicities (i.e. np -> n and
   nnppp -> nn)
digitizer_window  480    # ns, Length of the digitizer window
digitizer_gap     16     # ns, Delay between successive digitizer windows
digitizer_end     220    # ns, Time at end of digitizer window where pulses are
   not seen
digitizer_lag     80     # ns, Time at the beginning of digitizer window before a
    pulse can be seen
sm_dist_on        yes    # yes/no, Pulse height distributions for each
   multiplicity combination

# ~~~~~~~~~~~~~~~~~~~~~~~~~~~~~~~~~~~~~~~~~~~~~~~~~~~~~~~~~~~~~~~~~~~~~~~~~~~~
# Variance Reduction
# ~~~~~~~~~~~~~~~~~~~~~~~~~~~~~~~~~~~~~~~~~~~~~~~~~~~~~~~~~~~~~~~~~~~~~~~~~~~~
apply_weight      no    # yes/no, use the non-unity weights of particles
```

Bibliography

[1] United States Nuclear Regulatory Commission, "Safeguard Categories of SNM," 2017.

[2] International Atomic Energy Agency, "IAEA Safeguards Glossary," tech. rep., 2001.

[3] "Treaty Between The United States Of America And The Union Of Soviet Socialist Republics On The Elimination Of Their Intermediate-Range And Shorter-Range Missiles," 1987.

[4] "Treaty Between The United States of America and The Russian Federation on Measures for the Further Reduction and Limitiation of Strategic Offensive Arms," 2010.

[5] "Treaty on the Non-Proliferation of Nuclear Weapons," 1970.

[6] R. Ewing and K. W. Marlow, "A fast-neutron detector used in verification of the INF Treaty," *Nuclear Inst. and Methods in Physics Research, A*, vol. 299, pp. 559–561, 1990.

[7] J. Yan and A. Glaser, "Nuclear Warhead Verification: A Review of Attribute and Template Systems," *Science & Global Security*, vol. 23, no. 3, pp. 157–170, 2015.

[8] S. Fetter, V. A. Frolov, M. Miller, R. Mozley, O. F. Prilutsky, S. N. Rodionov, and R. Z. Sagdeev, "Detecting nuclear warheads," *Science & Global Security*, vol. 1, no. 3-4, pp. 225–253, 1990.

[9] National Nuclear Security Administration Office of Nonproliferation and Arms Control and United Kingdom Ministy of Defense, "Joint U.S.-U.K. Report on Technical Cooperation for Arms Control," tech. rep., 2015.

[10] International Atomic Energy Agency, "The Structure and Content of Agreements Between the Agency and States Required in Connection wth the Treaty on the Non-Proliferation of Nuclear Weapons," tech. rep., 1972.

[11] International Atomic Energy Agency, "Safeguards Techniques and Equipment: 2011 Edition," *International Nuclear Verification Series No I*, 2011.

[12] L. E. Smith, E. K. MacE, A. C. Misner, and M. W. Shaver, "Signatures and methods for the automated nondestructive assay of UF 6 cylinders at uranium enrichment plants," *IEEE Transactions on Nuclear Science*, vol. 57, no. 4, pp. 2247–2253, 2010.

[13] H. O. Menlove, "Description and operation manual for the active well coincidence counter," tech. rep., Las Alamos National Laboratory, 1979.

[14] Provided by Arden Dougan of the National Nuclear Security Administration, "Contextual usage scenarios for gamma-ray imaging."

[15] R. W. Todd, J. M. Nightingale, and D. B. Everett, "A proposed γ camera," *Nature*, vol. 251, no. 5471, pp. 132–134, 1974.

[16] D. Herzo, R. Koga, W. A. Millard, S. Moon, J. Ryan, R. Wilson, A. D. Zych, and R. S. White, "A large double scatter telescope for gamma rays and neutrons," *Nuclear Instruments and Methods*, vol. 123, no. 3, pp. 583–597, 1975.

[17] D. Everett, J. Fleming, R. Todd, and J. Nightingale, "Gamma-radiation imaging system based on the Compton effect," *Proceedings of the Institution of Electrical Engineers*, vol. 124, no. 11, p. 995, 1977.

[18] M. Singh, "An electronically collimated gamma camera for single photon emission computed tomography. Part I: Theoretical considerations and design criteria.," *Medical physics*, vol. 10, no. 4, pp. 421–7, 1983.

[19] V. Schonfelder, R. Diehl, G. G. Lichti, H. Steinle, B. N. Swanenburg, A. J. M. Deerenberg, H. Aarts, J. Lockwood, W. Webber, J. Macri, J. Ryan, G. Simpson, B. G. Taylor, K. Bennett, and M. Snelling, "The Imaging Compton Telescope Comptel on the Gamma Ray Observatory," *IEEE Transactions on Nuclear Science*, vol. 31, no. 1, pp. 766–770, 1984.

[20] G. W. Phillips, "Gamma-ray imaging with Compton cameras," *Nuclear Inst. and Methods in Physics Research, B*, vol. 99, no. 1-4, pp. 674–677, 1995.

[21] Y. Du, Z. He, G. F. Knoll, D. K. Wehe, W. Li, R. B. James, and R. C. Schirato, "Evaluation of a Compton scattering camera using 3D position-sensitive CdZnTe detectors," vol. 3768, pp. 228–238, 1999.

[22] S. T. Brown, Y. A. Boucher, J. Mann, Y. Zhu, and Z. He, "Thermal neutron source location using a 3-D position-sensitive CdZnTe detector array," *2013 IEEE Nuclear Science Symposium and Medical Imaging Conference (2013 NSS/MIC)*, pp. 1–5, 2013.

[23] P. E. Vanier and L. Forman, "Demonstration of a directional fast neutron detector," in *IEEE Nuclear Science Symposium Conference Record*, vol. 1, pp. 116–119, 2005.

[24] U. Bravar, P. J. Bruillard, E. O. Flückiger, J. S. Legere, J. R. Macri, A. L. MacKinnon, P. Mallik, M. L. McConnell, M. R. Moser, B. Pirard, J. M. Ryan, and R. S. Woolf, "Design optimization and performance capabilities of the Fast Neutron Imaging Telescope (FNIT)," in *IEEE Nuclear Science Symposium Conference Record*, vol. 1, pp. 264–269, 2007.

[25] N. Mascarenhas, J. Brennan, K. Krenz, P. Marleau, and S. Mrowka, "Results with the neutron scatter camera," in *IEEE Nuclear Science Symposium Conference Record*, vol. 56, pp. 3368–3371, 2008.

[26] J. Brennan, E. Brubaker, R. Cooper, M. Gerling, C. Greenberg, P. Marleau, N. Mascarenhas, and S. Mrowka, "Measurement of the fast neutron energy spectrum of an 241Am-Be source using a neutron scatter camera," *IEEE Transactions on Nuclear Science*, vol. 58, no. 5 PART 2, pp. 2426–2430, 2011.

[27] M. D. Gerling, J. E. M. Goldsmith, and J. S. Brennan, "MINER - A mobile imager of neutrons for emergency responders," *2014 IEEE Nuclear Science Symposium and Medical Imaging Conference, NSS/MIC 2014*, 2016.

[28] P. E. Vanier, L. Forman, and D. R. Norman, "Thermal neutron imaging in an active interrogation environment," in *AIP Conference Proceedings*, vol. 1099, pp. 583–586, 2009.

[29] P. Hausladen and M. Blackston, "Passive and Active Fast-Neutron Imaging in Support of AFCI Safeguards Campaign," Tech. Rep. August, Oak Ridge National Laboratory, 2009.

[30] P. Hausladen, J. Newby, F. Liang, and M. Blackston, "The Deployable Fast-Neutron Coded- Aperture Imager: Demonstration of Locating One or More Sources in Three Dimensions," *ORNL/TM-2013/446, Oak Ridge National Laboratory*, 2013.

[31] S. Zelakiewicz, R. Hoctor, A. Ivan, W. Ross, E. Nieters, W. Smith, D. McDevitt, M. Wittbrodt, and B. Milbrath, "SORIS - A standoff radiation imaging system," *Nuclear Instruments and Methods in Physics Research, Section A: Accelerators, Spectrometers, Detectors and Associated Equipment*, vol. 652, no. 1, pp. 5–9, 2011.

[32] B. R. Kowash, D. K. Wehe, and J. A. Fessler, "A rotating modulation imager for locating mid-range point sources," *Nuclear Instruments and Methods in Physics Research, Section A: Accelerators, Spectrometers, Detectors and Associated Equipment*, vol. 602, no. 2, pp. 477–483, 2009.

[33] J. Brennan, E. Brubaker, A. Nowack, J. Steele, M. Sweany, and D. Throckmorton, "Bubble masks for time-encoded imaging of fast neutrons," tech. rep., Sandia National Laboratory, 2013.

[34] P. Marleau, J. Brennan, E. Brubaker, M. Gerling, A. Nowack, P. Schuster, and J. Steele, "Time encoded fast neutron/gamma imager for large standoff SNM detection," *IEEE Nuclear Science Symposium Conference Record*, pp. 591–595, 2012.

[35] H. H. Barrett, T. White, and L. C. Parra, "List-mode likelihood," *Journal of the Optical Society of America A*, vol. 14, no. 11, p. 2914, 1997.

[36] D. Xu, S. Member, Z. He, and S. Member, "Gamma-ray Energy-imaging Integrated Deconvolution," in *2005 IEEE Nuclear Science Symposium Conference Record Gamma-ray*, no. 1, pp. 882–886, 2005.

[37] D. Xu and Z. He, "Gamma-ray energy-imaging integrated spectral deconvolution," *Nuclear Instruments and Methods in Physics Research, Section A: Accelerators, Spectrometers, Detectors and Associated Equipment*, vol. 574, no. 1, pp. 98–109, 2007.

[38] W. Wang, C. G. Wahl, J. M. Jaworski, and Z. He, "Maximum-likelihood deconvolution in the spatial and spatial-energy domain for events with any number of interactions," *IEEE Transactions on Nuclear Science*, vol. 59, no. 2, pp. 469–478, 2012.

[39] J. K. Polack, *A Maximum-Likelihood Approach for Localizing and Characterizing Special Nuclear Material with a Dual-Particle Imager*. PhD thesis, University of Michigan, 2016.

[40] J. K. Polack, A. Poitrasson-Rivière, M. C. Hamel, K. Ide, M. L. Kyle, S. D. Clarke, M. Flaska, and S. A. Pozzi, "Dual-Particle Imager for Standoff Detection of Special Nuclear Material," *IEEE Nuclear Science Symposium Conference Record*, no. 1, pp. 1494–1500, 2011.

[41] M. C. Hamel, A. Poitrasson-Rivière, J. K. Polack, S. D. Clarke, M. Flaska, and S. A. Pozzi, "Design and Analysis of a Two-Plane Dual-Particle Imaging System," in *Proceedings of the INMM 54th Annual Meeting*, 2013.

[42] J. M. Ryan, C. Bancroft, P. Bloser, D. Fourguette, L. Larocque, J. Legere, A. Madden, M. L. McConnell, J. Pavlich, G. Ritter, G. Wassick, and M. Rousseau, "An imaging neutron/gamma-ray spectrometer," vol. 8509, p. 850905, 2012.

[43] A. C. Madden, P. F. Bloser, D. Fourguette, L. Larocque, J. S. Legere, M. Lewis, M. L. McConnell, M. Rousseau, and J. M. Ryan, "An imaging neutron/gamma-ray spectrometer," *Proc. SPIE 8710, Chem. Biol. Radiol. Nucl. Explos. Sens.*, vol. 8710, 2013.

[44] A. Poitrasson-Rivière, *Development of a Dual-Particle Imaging System for Nonproliferation Applications*. PhD thesis, University of Michigan, 2016.

[45] A. Poitrasson-Rivière, B. A. Maestas, M. C. Hamel, S. D. Clarke, M. Flaska, S. A. Pozzi, G. Pausch, C. M. Herbach, A. Gueorguiev, M. F. Ohmes, and J. Stein, "Monte Carlo investigation of a high-efficiency, two-plane Compton camera for long-range localization of radioactive materials," *Progress in Nuclear Energy*, vol. 81, pp. 127–133, 2015.

[46] A. Poitrasson-Rivière, M. C. Hamel, J. K. Polack, M. Flaska, S. S. D. Clarke, and S. S. A. Pozzi, "Dual-particle imaging system based on simultaneous detection of photon and neutron collision events," *Nuclear Instruments and Methods in Physics*

Research, Section A: Accelerators, Spectrometers, Detectors and Associated Equipment, vol. 760, pp. 40–45, 2014.

[47] A. Poitrasson-Rivière, J. K. Polack, M. C. Hamel, D. D. Klemm, K. Ito, A. A. T. McSpaden, M. Flaska, S. S. D. Clarke, S. S. A. Pozzi, A. Tomanin, and P. Peerani, "Angular-resolution and material-characterization measurements for a dual-particle imaging system with mixed-oxide fuel," *Nuclear Instruments and Methods in Physics Research, Section A: Accelerators, Spectrometers, Detectors and Associated Equipment*, vol. 797, pp. 278–284, 2015.

[48] S. Wilderman, N. Clinthorne, J. Fessler, and W. Rogers, "List-mode maximum likelihood reconstruction of Compton scatter camera images in nuclear medicine," *1998 IEEE Nuclear Science Symposium Conference Record*, vol. 3, pp. 1716–1720, 1998.

[49] N. Bissantz, B. A. Mair, and A. Munk, "A multi-scale stopping criterion for MLEM reconstructions in PET," *2006 IEEE Nuclear Science Symposium Conference Record*, vol. 6, pp. 3376–3379, 2006.

[50] N. Bissantz, B. A. Mair, and A. Munk, "A statistical stopping rule for MLEM reconstructions in PET," *IEEE Nuclear Science Symposium Conference Record*, no. m, pp. 4198–4200, 2008.

[51] A. Sitek, "Representation of photon limited data in emission tomography using origin ensembles.," *Physics in medicine and biology*, vol. 53, no. 12, pp. 3201–3216, 2008.

[52] A. Andreyev, A. Sitek, and A. Celler, "Fast image reconstruction for Compton camera using stochastic origin ensemble approach.," *Medical physics*, vol. 38, no. 1, pp. 429–438, 2011.

[53] D. Mackin, S. Peterson, S. Beddar, and J. Polf, "Evaluation of a stochastic reconstruction algorithm for use in Compton camera imaging and beam range verification from secondary gamma emission during proton therapy," *Physics in Medicine and Biology*, vol. 57, no. 11, pp. 3537–3553, 2012.

[54] J. C. Polf, S. Avery, D. S. Mackin, and S. Beddar, "Imaging of prompt gamma rays emitted during delivery of clinical proton beams with a Compton camera: feasibility studies for range verification," *Phys Med Biol*, vol. 60, no. 18, pp. 7085–7099, 2015.

[55] M. C. Hamel, J. K. Polack, A. Poitrasson-Rivière, M. Flaska, S. D. Clarke, S. A. Pozzi, A. Tomanin, and P. Peerani, "Stochastic image reconstruction for a dual-particle imaging system," *Nuclear Instruments and Methods in Physics Research, Section A: Accelerators, Spectrometers, Detectors and Associated Equipment*, vol. 810, pp. 120–131, 2016.

[56] M. C. Hamel, J. K. Polack, S. D. Clarke, and S. A. Pozzi, "Localization and spectral isolation of special nuclear material using stochastic image reconstruction," *Nuclear Inst. and Methods in Physics Research, A*, vol. 841, no. August 2016, pp. 24–33, 2017.

[57] R. C. Runkle, "Neutron sensors and their role in nuclear nonproliferation," *Nuclear Instruments and Methods in Physics Research, Section A: Accelerators, Spectrometers, Detectors and Associated Equipment*, vol. 652, no. 1, pp. 37–40, 2011.

[58] A. Poitrasson-Rivière, M. C. Hamel, J. K. Polack, K. L. Mcmillan, K. Ide, S. D. Clarke, M. Flaska, and S. A. Pozzi, "Design considerations of a dual-particle imager for nonproliferation applications," in *Proceedings of INMM 52nd Annual Meeting*, 2011.

[59] J. K. Polack, A. Poitrasson-Rivière, M. C. Hamel, M. F. Becchetti, K. Ide, S. D. Clarke, M. Flaska, S. A. Pozzi, M. L. Kyle, S. D. Clarke, M. Flaska, S. A. Pozzi, M. F. Becchetti, K. Ide, S. D. Clarke, M. Flaska, and S. A. Pozzi, "Image reconstruction using a three-plane, dual-particle imager for standoff detection of special nuclear material," in *IEEE Nuclear Science Symposium Conference Record*, no. 1, pp. 118–121, 2012.

[60] S. A. Pozzi, S. D. Clarke, M. Flaska, A. Poitrasson-Rivière, J. K. Polack, and K. Ide, "Dual Particle Imaging System for Standoff SNM Detection in High Background Radiation Environments," 2012.

[61] J. K. Polack, A. Poitrasson-Rivière, M. C. Hamel, K. Ito, S. D. Clarke, M. Flaska, S. A. Pozzi, A. Tomanin, and P. Peerani, "Image reconstruction of shielded mixed-oxide fuel using a dual-particle imaging system," *2014 IEEE Nuclear Science Symposium and Medical Imaging Conference, NSS/MIC 2014*, pp. 1–4, 2014.

[62] S. A. Pozzi, M. C. Hamel, J. K. Polack, M. L. Ruch, T. L. Beams-Canivet, and S. D. Clarke, "Dual Particle Imaging for Treaty Verification," in *Proceedings of INMM 57th Annual Meeting*, 2016.

[63] G. F. Knoll, *Radiation Detection and Measurement*. John Wiley & Sons, 4th ed., 2010.

[64] R. Batchelor, W. B. Gilboy, J. B. Parker, and J. H. Towle, "The response of organic scintillators to fast neutrons," *Nuclear Instruments and Methods*, vol. 13, no. 3, pp. 70–82, 1961.

[65] R. Winyard, J. Lutkin, and G. McBeth, "Pulse Shape Discrimination in Inorganic and Organic Scintillators. I," *Nuclear Instruments and Methods in Physics Research Section A*, vol. 95, no. 1, pp. 141 – 153, 1971.

[66] S. Marrone, D. Cano-Ott, N. Colonna, C. Domingo, F. Gramegna, E. M. Gonzalez, F. Gunsing, M. Heil, F. Käppeler, P. F. Mastinu, P. M. Milazzo, T. Papaevangelou, P. Pavlopoulos, R. Plag, R. Reifarth, G. Tagliente, J. L. Tain, and K. Wisshak, "Pulse shape analysis of liquid scintillators for neutron studies," *Nuclear Instruments and Methods in Physics Research, Section A: Accelerators, Spectrometers, Detectors and Associated Equipment*, vol. 490, no. 1-2, pp. 299–307, 2002.

[67] M. Flaska and S. A. Pozzi, "Identification of shielded neutron sources with the liquid scintillator BC-501A using a digital pulse shape discrimination method," *Nuclear Instruments and Methods in Physics Research, Section A: Accelerators, Spectrometers, Detectors and Associated Equipment*, vol. 577, no. 3, pp. 654–663, 2007.

[68] I. A. Pawełczak, S. A. Ouedraogo, A. M. Glenn, R. E. Wurtz, and L. F. Nakae, "Studies of neutron-γ pulse shape discrimination in EJ-309 liquid scintillator using charge integration method," *Nuclear Instruments and Methods in Physics Research, Section A: Accelerators, Spectrometers, Detectors and Associated Equipment*, vol. 711, pp. 21–26, 2013.

[69] A. C. Kaplan, M. Flaska, A. Enqvist, J. L. Dolan, and S. A. Pozzi, "EJ-309 pulse shape discrimination performance with a high gamma-ray-to-neutron ratio and low threshold," *Nuclear Instruments and Methods in Physics Research, Section A: Accelerators, Spectrometers, Detectors and Associated Equipment*, vol. 729, pp. 463–468, 2013.

[70] J. Polack, M. Flaska, A. Enqvist, C. Sosa, C. Lawrence, and S. Pozzi, "An algorithm for charge-integration, pulse-shape discrimination and estimation of neutron/photon misclassification in organic scintillators," *Nuclear Instruments and Methods in Physics Research Section A: Accelerators, Spectrometers, Detectors and Associated Equipment*, vol. 795, pp. 253–267, sep 2015.

[71] P. Schuster and E. Brubaker, "Investigating the Anisotropic Scintillation Response in Anthracene through Neutron, Gamma-Ray, and Muon Measurements," *IEEE Transactions on Nuclear Science*, vol. 63, no. 3, pp. 1942–1954, 2016.

[72] A. Enqvist, C. C. Lawrence, B. M. Wieger, S. A. Pozzi, and T. N. Massey, "Neutron light output response and resolution functions in EJ-309 liquid scintillation detectors," *Nuclear Instruments and Methods in Physics Research, Section A: Accelerators, Spectrometers, Detectors and Associated Equipment*, vol. 715, pp. 79–86, 2013.

[73] M. A. Norsworthy, A. Poitrasson-Rivière, M. L. Ruch, S. D. Clarke, and S. A. Pozzi, "Evaluation of neutron light output response functions in EJ-309 organic scintillators," *Nuclear Instruments and Methods in Physics Research Section A: Accelerators, Spectrometers, Detectors and Associated Equipment*, vol. 842, no. October 2016, pp. 20–27, 2016.

[74] J. B. Birks, *The Theory and Practice of Scintillation Counting*, vol. 148. Elsevier, 1964.

[75] S. Ahlen, B. G. Cartwright, and G. Tarle, "Return to unsaturated response of polymeric scintillators excited by relativistic heavy ions," *Nuclear Instruments and Methods*, vol. 147, no. 2, pp. 321–328, 1977.

[76] M. A. Norsworthy, "Private Communications," 2017.

[77] H. O. Anger and D. H. Davis, "Gamma-ray detection efficiency and image resolution in sodium iodide," *Review of Scientific Instruments*, vol. 35, no. 6, pp. 693–697, 1964.

[78] A. Di Fulvio, T. H. Shin, M. C. Hamel, and S. A. Pozzi, "Digital pulse processing for NaI(Tl) detectors," *Nuclear Instruments and Methods in Physics Research, Section A: Accelerators, Spectrometers, Detectors and Associated Equipment*, vol. 806, pp. 169–174, 2015.

[79] CAEN, "720 Digitizer Family Data Sheet," 2013.

[80] CAEN, "730 Digitizer Family Data Sheet," 2015.

[81] L. S. Waters, "MCNPX User's manual version 2.3.0," 2002.

[82] S. A. Pozzi, E. Padovani, and M. Marseguerra, "MCNP-PoliMi: A Monte-Carlo code for correlation measurements," *Nuclear Instruments and Methods in Physics Research, Section A: Accelerators, Spectrometers, Detectors and Associated Equipment*, vol. 513, no. 3, pp. 550–558, 2003.

[83] S. A. Pozzi, S. D. Clarke, W. J. Walsh, E. C. Miller, J. L. Dolan, M. Flaska, B. M. Wieger, A. Enqvist, E. Padovani, J. K. Mattingly, D. L. Chichester, and P. Peerani, "MCNPX-PoliMi for nuclear nonproliferation applications," *Nuclear Instruments and Methods in Physics Research, Section A: Accelerators, Spectrometers, Detectors and Associated Equipment*, vol. 694, pp. 119–125, 2012.

[84] E. Padovani, S. A. Pozzi, S. D. Clarke, and E. C. Miller, "MCNPX PoliMi V2.0 Users Manual," 2012.

[85] S. A. Pozzi, M. Flaska, A. Enqvist, and I. Pázsit, "Monte Carlo and analytical models of neutron detection with organic scintillation detectors," *Nuclear Instruments and Methods in Physics Research, Section A: Accelerators, Spectrometers, Detectors and Associated Equipment*, vol. 582, no. 2, pp. 629–637, 2007.

[86] E. C. Miller, S. D. Clarke, M. Flaska, S. Prasad, S. A. Pozzi, and E. Padovani, "MCNPX-PoliMi Post-processing Algorithm for Detector Response Simulations," *Journal of Nuclear Materials Management*, vol. XL, no. 2, pp. 34–41, 2012.

[87] E. C. Miller, A. P. Riviere, A. Enqvist, J. L. Dolan, S. Prasad, M. M. Bourne, K. Weinfurther, and S. D. Clarke, "MCNPX PoliMi Post Processor (MPPost) Manual," 2012.

[88] C. E. Ordonez, A. Bolozdynya, and W. Chang, "Dependence of angular uncertainties on the energy resolution of Compton cameras," *Nuclear Science Symposium, 1997. IEEE*, vol. 2, pp. 1122–1125 vol.2, 1997.

[89] C. E. Ordonez, "Angular uncertainties due to geometry and spatial resolution in compton cameras," *IEEE Transactions on Nuclear Science*, vol. 46, no. 4 PART 2, pp. 1142–1147, 1999.

[90] N. Mascarenhas, J. Brennan, K. Krenz, J. Lund, P. Marleau, J. Rasmussen, J. Ryan, and J. Macri, "Development of a Neutron Scatter Camera for Fission Neutrons," *2006 IEEE Nuclear Science Symposium Conference Record*, vol. 2, no. 2, pp. 185–188, 2006.

[91] M. Frandes, B. Timar, and D. Lungeanu, "Image Reconstruction Techniques for Compton Scattering Based Imaging: An Overview [Compton Based Image Reconstruction Approaches]," *Current Medical Imaging Reviews*, vol. 12, no. 2, pp. 95–105, 2016.

[92] L. A. Shepp and Y. Vardi, "Maximum Likelihood Reconstruction for Emission Tomography," *IEEE Transactions on Medical Imaging*, vol. 1, no. 2, pp. 113–122, 1982.

[93] J. K. Polack, M. C. Hamel, A. Poitrasson-Rivière, P. A. Marleau, M. Flaska, and S. A. Pozzi, "Spectrum Isolation in Multi Source Image Reconstruction Using a Dual Particle Imager," in *Proceedings of INMM 56th Annual Meeting*, 2015.

[94] J. Dutta, S. Ahn, and Q. Li, "Quantitative statistical methods for image quality assessment," *Theranostics*, vol. 3, no. 10, pp. 741–756, 2013.

[95] W. K. Hastings, "Monte Carlo sampling methods using Markov chains and their applications," vol. 57, no. 1, pp. 97–109, 1970.

[96] A. Sitek, "Comment on 'Imaging of prompt gamma rays emitted during delivery of clinical proton beams with a Compton camera: feasibility studies for range verification'," *Phys Med Biol*, vol. 61, no. 18, pp. 8941–8944, 2016.

[97] J. C. Polf, S. Avery, D. S. Mackin, and S. Beddar, "Reply to Comment on 'Imaging of prompt gamma rays emitted during delivery of clinical proton beams with a Compton camera: feasibility studies for range verification'," *Phys Med Biol*, vol. 61, pp. 8945–8946–7099, 2016.

[98] A. Andreyev, A. Celler, and A. Sitek, "Resolution recovery for compton camera using origin ensemble algorithm," *IEEE Nuclear Science Symposium Conference Record*, pp. 2774–2778, 2012.

[99] H. Kesten, "Accelerated Stochastic Approximation," *The Annals of Mathematical Statistics*, vol. 29, no. 1, pp. 41–59, 1958.

[100] J. C. Spall, "Implementation of Simultaneous Perturbation Algorithm for Stochastic Optimization," *Proceedings of Models and Technologies for Intelligent Transportation Systems (MT-ITS)*, vol. 34, no. 3, pp. 817–823, 1996.

[101] N. Toft, G. T. Innocent, G. Gettinby, and S. W. J. Reid, "Assessing the convergence of Markov Chain Monte Carlo methods: An example from evaluation of diagnostic tests in absence of a gold standard," *Preventive Veterinary Medicine*, vol. 79, no. 2-4, pp. 244–256, 2007.

[102] S. P. Brooks, P. Giudici, and G. O. Roberts, "Efficient construction of reversible jump Markov chain Monte Carlo proposal distributions," vol. 65, no. 1, pp. 3–55, 2003.

[103] W. A. Link and M. J. Eaton, "On thinning of chains in MCMC," *Methods in Ecology and Evolution*, vol. 3, no. 1, pp. 112–115, 2012.

[104] D. B. Barber, "PuBe MRC 270 Documentation," 1964.

[105] J. L. Richmond, "Shipping Data: Plutonium Neutron Source," 1958.

[106] A. Sitek, *Statistical Computing in Nuclear Imaging*. CRC Press, 2014.

[107] F. X. Avila-Soto, A. N. Beri, E. Valenzuela, A. Wudenhe, A. R. Blenkhorn, J. S. Graf, S. Khuvis, M. K. Gobbert, and J. Polf, "Parallelization for Fast Image Reconstruction using the Stochastic Origin Ensemble Method for Proton Beam Therapy," no. September, 2015.

[108] MATLAB, *version 8.6.0 (R2015b)*. The Mathworks, Inc., 2015.

[109] J. Mattingly, J. Hutchinson, C. Sullivan, J. Stinnett, M. Kamuda, M. Alamaniotis, B. Sims, J. Mueller, J. Newby, J. Linkous, S. Pozzi, K. Polack, M. Hamel, A. Poitrasson-Rivière, S. Clarke, Z. He, D. Goodman, and M. Streicher, "CNEC and CVT Subcritical Experiments with Category I Special Nuclear Material at the Nevada National Security Site Device Assembly Facility Gamma Spectroscopic Identification of SNM Isotopic Composition," in *Proceedings of INMM 57th Annual Meeting*, 2016.

[110] R. B. Kidman, "Reckoning THOR," tech. rep., 1972.

[111] G. E. Hansen and H. C. Paxton, "Thor, A Thorium Reflected Plutonium Metal Critical Assembly," *Nuclear Science and Engineering*, vol. 71, no. 3, pp. 287–293, 1979.

[112] M. Bunn, "Terrorist Nuclear Weapon Construction: How Difficult?," *The ANNALS of the American Academy of Political and Social Science*, vol. 607, no. September, pp. 133–149, 2006.

[113] T. Gozani, "Active Nondestructive Assay of Nuclear Materials," tech. rep., National Technical Information Service, U.S. Department of Commerce, 1981.

[114] H. Yang, "Active Interrogation methods for detection of special nuclear material," p. 216, 2009.

[115] A. Persaud, J. W. Kwan, M. Leitner, K. N. Leung, B. Ludewigt, N. Tanaka, W. Waldron, S. Wilde, A. J. Antolak, D. H. Morse, and T. Raber, "A tandem-based compact dual-energy gamma generator," *Review of Scientific Instruments*, vol. 81, no. 2, pp. 2–6, 2010.

[116] R. C. Runkle, D. L. Chichester, and S. J. Thompson, "Rattling nucleons: New developments in active interrogation of special nuclear material," *Nuclear Instruments and Methods in Physics Research, Section A: Accelerators, Spectrometers, Detectors and Associated Equipment*, vol. 663, no. 1, pp. 75–95, 2012.

[117] D. L. Chichester and E. H. Seabury, "Using electronic neutron generators in active interrogation to detect shielded fissionable material," in *IEEE Nuclear Science Symposium Conference Record*, pp. 3361–3367, 2008.

[118] J. Brennan, R. Cooper, M. Gerling, P. Marleau, N. Mascarenhas, and S. Mrowka, "Results with a 32-element dual mode imager," *IEEE Nuclear Science Symposium Conference Record*, pp. 1634–1639, 2010.

[119] J. E. M. Goldsmith, J. S. Brennan, M. D. Gerling, P. A. Marleau, and M. Monterial, "Additional Capabilities of a Compact Neu tron Scatter Camera: Active Interrogation, Time-Correlated Pulse-Height Multiplication Measurements, and Gamma Imaging," in *Nuclear Science Symposium and Medical Imaging Conference (NSS/MIC), 2015 IEEE*, (San Diego, CA, USA), 2015.

[120] P. Hausladen, M. Blackston, J. Mullens, S. McConchie, J. Mihalczo, P. Bingham, M. Ericson, and L. Fabris, "Induced-Fission Imaging of Nuclear Material," in *INMM 51st Annual Meeting*, no. January, (Baltimore, MD, USA), pp. 1–10, 2010.

[121] A. Swift, *Materials and Configuration from NMIS Type Neutron Imaging and Gamma Spectroscopy*. PhD thesis, Oak Ridge National Laboratory, 2012.

[122] M. B. Chadwick, M. Herman, P. Obložinský, M. E. Dunn, Y. Danon, a. C. Kahler, D. L. Smith, B. Pritychenko, G. Arbanas, R. Arcilla, R. Brewer, D. a. Brown, R. Capote, a. D. Carlson, Y. S. Cho, H. Derrien, K. Guber, G. M. Hale, S. Hoblit, S. Holloway, T. D. Johnson, T. Kawano, B. C. Kiedrowski, H. Kim, S. Kunieda, N. M. Larson, L. Leal, J. P. Lestone, R. C. Little, E. a. McCutchan, R. E. MacFarlane, M. MacInnes, C. M. Mattoon, R. D. McKnight, S. F. Mughabghab, G. P. a. Nobre, G. Palmiotti, A. Palumbo, M. T. Pigni, V. G. Pronyaev, R. O. Sayer, a. a. Sonzogni, N. C. Summers, P. Talou, I. J. Thompson, A. Trkov, R. L. Vogt, S. C. van der Marck, A. Wallner, M. C. White, D. Wiarda, and P. G. Young, "ENDF/B-VII.1 nuclear data for science and technology: Cross sections, covariances, fission product yields and decay data," *Nuclear Data Sheets*, vol. 112, no. 12, pp. 2887–2996, 2011.

[123] J. K. Shultis and R. E. Faw, *Fundamentals of Nuclear Science and Engineering*. CRC Press, 2nd ed., 2008.

[124] N. L. Pruvost and H. C. Paxton, "Nuclear Criticality Safety Guide," tech. rep., Los Alamos National Laboratory, 1996.

[125] R. E. Roth, "Extrapolated Experimental Critical Parameters of Unreflected and Steel-Reflected Massive Enriched Uranium Metal Spherical and Hemispherical Assemblies," tech. rep., United States Department of Energy, 1997.

[126] R. Remetti, L. Lepore, and N. Cherubini, "Development and experimental validation of a monte carlo modeling of the neutron emission from a d-t generator," *Nuclear Inst. and Methods in Physics Research, A*, vol. 842, no. March 2016, pp. 7–13, 2017.

[127] A. Trahan, *Utilization of the Differential Die-Away Self-Interrogation Technique for Characterization and Verification of Spent Nuclear Fuel*. PhD thesis, University of Michigan, 2016.

[128] G. E. Hansen, "The Rossi Alpha Method," tech. rep., Los Alamos National Laboratory, 1985.

[129] M. L. Ruch, M. Flaska, and S. A. Pozzi, "Pulse shape discrimination performance of stilbene coupled to low-noise silicon photomultipliers," *Nuclear Instruments and Methods in Physics Research Section A: Accelerators, Spectrometers, Detectors and Associated Equipment*, vol. 793, pp. 1–5, sep 2015.

[130] M. C. Hamel, J. K. Polack, A. Poitrasson-Rivière, D. D. Klemm, M. Flaska, S. D. Clarke, S. A. Pozzi, A. Tomanin, and P. Peerani, "Time-of-flight neutron spectrum unfolding for mixed-oxide nuclear fuel and plutonium metal using a dual-particle imager," *2014 IEEE Nuclear Science Symposium and Medical Imaging Conference, NSS/MIC 2014*, pp. 2–6, 2014.

[131] M. Monterial, P. Marleau, M. Paff, S. Clarke, and S. Pozzi, "Multiplication and Presence of Shielding Material from Time-Correlated Pulse-Height Measurements of Subcritical Plutonium Assemblies," *Nuclear Instruments and Methods in Physics Research Section A: Accelerators, Spectrometers, Detectors and Associated Equipment*, vol. 851, no. September 2016, pp. 50–56, 2017.